Republic of Iraq
Ministry of Higher Education
and Scientific Research
University of Misan
College of Science
Department of Chemistry

Study of Photocatalytic Degradation and Adsorption Properties of Some New Nanocomposites for Removal of Methylene Blue Dye from Aqueous Solutions

Thesis Submitted to
The College of Science / University of Misan as Partial Fulfillment
of the Requirements for the Master Degree of Science in Chemistry

By

Muntazir Tahsin Ali

B.Sc. Chemistry College of Science / University of Misan (2020)

Supervisor

Assistant Professor

Safaa Sabri Najim

2024 **1446**

بِسْمِ اللَّهِ الرَّحْمَنِ الرَّحِيمِ

قُلْ هَلْ يَسْتَوِي الَّذِينَ يَعْلَمُونَ وَالَّذِينَ لَا يَعْلَمُونَ إِنَّمَا

يَتَذَكَّرُ أُولُو الْأَلْبَابِ

سورة الزمر/ اية (٩)

صدق الله العلي العظيم

Supervisor Certificate

I am the supervisor of **Mr. Muntazer Tahsin Ali,** certify that the thesis (**Study of Photocatalytic Degradation and Adsorption Properties of Some New Nanocomposites for Removel of Methylene Blue Dye from Aqueous Solution)** was done and written under my supervision as a fulfillment of the requirement for the master degree of science in chemistry.

Signature……

Assistant Professor
Safaa Sabri Najim
College of Science
Misan University

Date: /10/2024

Head of Chemistry Department Recommendation

According to the recommendation of the supervisor, this thesis is forwarded to the examination committee for approval.

Signature……
Dr. Mohammed Abdul raheem Saeed
H*ead of Chemistry Department*
College of Science
Misan University

Date: /10/2024

Dedication

To **The Sun and Moon Which Lighting my Life by Pave the Way my Success…**

My Father & My Mother

To **Those who have Supported me and are Waiting for my Success…**

My Sisters & My Close Friends

To The one who gave me his **Time and Knowledge…**

My Supervisor

Acknowledgement

Firstly, very much blessing to ***Allah*** the most merciful for his blessings who gave me health, strength, and facilitated the ways to accomplish this work and the prayer and peace of Allah be upon our Master and prophet Muhammad and his divine good family.

To my supervisor ***Asst. Prof. Safaa Sabri Najim,*** there are no words can match my gratitude, I thank you so much for you interest in my thesis, assistance and constructive guidance, I totally appreciate it; I can hardly express my gratitude.

My appreciation also goes to ***Asst. Prof. Dr. Osamah Ali Muhsen*** the previous head of chemistry department, ***Asst. Prof. Dr. Munther Abdul-Hasen*** and ***Asst. Prof. Dr. Diaah Bader Habesh*** for their support and advice.

Muntazir

Abstract

The water pollution problem is widespread throughout the world. Nowadays, growing industrial activities have resulted in the generation of huge amounts of hazardous; untreated industrial effluents and uncontrolled pollutants that are released into environmental water. Among them, dyes from textile industries generate a large amount industrial wastewater due to the huge water demand and frequently discharge into the environment throughout the production process and has a direct impact on human health , as a result, water pollution remediation is one of the imperative issues which the scientific community has given significant attention to with the primary goal of safeguarding and conserving natural water resources. This study includes three parts; Synthesis, Characterization and application of nano graphitic carbon nitride(g-C_3N_4), nano bismuth oxide (Bi_2O_3), nano-graphene oxide (NGO) composites for the removal of methylene blue dye.

Part one contains the synthesis of nano graphitic carbon nitride(g-C_3N_4), nano bismuth oxide (Bi_2O_3) and nano-graphene oxide (NGO). Binary nanocomposites were synthesized by high calcination method, including (20%) g-C_3N_4 -Bi_2O_3, (40%) g-C_3N_4 -Bi_2O_3, (60%) g-C_3N_4 -Bi_2O_3, and (80%) g-C_3N_4 -Bi_2O_3. Novel ternary nanocomposites were synthesized by high calcination method, BiC_{80}/GO (10 mg), BiC_{80}/GO (20 mg), BiC_{80}/GO (30 mg) and BiC_{80}/GO (40 mg).

Part two includes the characterization of these composites by ((XRD) to find out the particles size through Debye-Scherrer equation, (FT-IR), (UV–Vis) spectroscopy, PL, TGA to study the thermal stability of samples, FESEM and EDS to study the surface morphology of the composites

Part three contains the application of these composites for water treatment in order to remove the organic pollutants (methylene blue dye MB) Through two methods; first method Photocatalytic Degradation, The degradation efficiency D% was for (g-C_3N_4), (Bi_2O_3) and (NGO) (93.34%,0.95% and 98.335%) respectively, under the visible light irradiation in a time period of 180 min. The degradation efficiency D% for binary nanocomposites (20%) g-C_3N_4 -Bi_2O_3 , (40%) g-C_3N_4 -Bi_2O_3 , (60%) g-C_3N_4 -Bi_2O_3, (80%) g-C_3N_4 -Bi_2O_3, (21.77%, 35.4%, 41.48% and 98.38%) respectively, under the visible light irradiation in a

time period of 180 min, the optimum conditions obtained for the best efficient of (80%) g-C_3N_4 -Bi_2O_3 was (catalyst weight =50 mg, dye concentration= 5 mg.L^{-1} , temperature= 25℃, pH =14). The degradation efficiency D% for novel ternary nanocomposites, BiC_{80}/GO (10 mg), BiC_{80}/GO (20 mg), BiC_{80}/GO (30 mg) and BiC_{80}/GO (40 mg) (88.98%,97.81% ,96.65 and 91.58%) respectively, under visible light irradiation in a time period of 180 min. Optimum conditions obtained for ternary nanocomposites BiC_{80}/GO (20 mg), are (catalyst weight =50 mg, dye concentration= 5 mg.L^{-1}, temperature = 35℃, pH =12).

Second method includes fabricated, g-C_3N_4, Bi_2O_3 and NGO by vacuum filtration method. The removal efficiencies R% of methylene blue dye was, (62.872%, 34.434% and 51.673%) respectively. Binary nanocomposites, (20%) g-C_3N_4 -Bi_2O_3, (40%) g-C_3N_4 -Bi_2O_3, (60%) g-C_3N_4 -Bi_2O_3, (80%) g-C_3N_4 -Bi_2O_3 were fabricated as membranes by vacuum filtration, the removal R% was (33.268%, 36.995%, 52.436% and 70.819%) respectively. Ternary nanocomposites BiC_{80}/GO (10 mg), BiC_{80}/GO (20 mg), BiC_{80}/GO (30 mg) and BiC_{80}/GO (40 mg) were fabricated as membranes by vacuum filtration, the removal R% are (42.418%, 48.438%, 49.265% and 44.440%) respectively.

Contents

Subject	*Page*
Abstract	III
List of Tables	VIII
List of Figures	XI
Abbreviations	XVI
Chapter one Introduction	
1.1 Nano materials	**1**
1.2 Synthesis of nanomaterials	**1**
1.2.1 Top-down approach	**1**
1.2.1.1 Ball milling through Mechanical method	**2**
1.2.1.2 Electrospinning method	**3**
1.2.1.3 Lithography method	**4**
1.2.1.4 Sputtering method	**5**
1.2.1.5 The arc discharge method	**6**
1.2.1.6 Laser ablation method	**7**
1.2.2 Bottom-up approach	**8**
1.2.2.1 Chemical vapor deposition (CVD) method	**8**
1.2.2.2 Solvothermal and hydrothermal methods	**9**
1.2.2.3 The sol–gel method	**10**
1.2.2.4 Soft and hard templating methods	**11**
1.3 Pollution	**13**
1.3.1 Air pollution	**13**
1.3.2 Soil pollution	**13**
1.3.3 Water pollution	**14**
1.4 Types of Pollutants	**14**
1.4.1 Inorganic Pollutants	**14**
1.4.2 Organic Pollutants	**14**
1.4.2.1 Dyes	**14**

Chapter one Introduction	*Page*
1.4.2.2 Methylene blue dye (MB)	**15**
1.4.2.3 Applications of methylene blue dye	**15**
1.4.2.4 Toxicity of methylene blue dye	**16**
1.5 Photocatalysis	**16**
1.5.1 Photodegradation of Methylene Blue	**17**
1.5.2 Factors Affecting Methylene Blue Photodegradation	**17**
1.5.2.1 Effect of pH	**17**
1.5.2.2 Effect of MB dye concentration	**18**
1.5.2.3 Effect of Irradiation Time	**18**
1.5.2.4 Effect of different photocatalysts	**18**
1.5.2.5 Effect of catalyst Weight	**19**
1.6 Catalysts	**19**
1.6.1 Graphitic Carbon Nitride (g-C_3N_4)	**19**
1.6.2 Graphene Oxide (NGO) Nano-Sheets	**20**
1.6.3 Bismuth oxide (Bi_2O_3)	**22**
1.6.4 Nanocomposites	**22**
1.6.4.1 g-C_3N_4/Bi_2O_3 binary nanocomposites	**22**
1.6.4.2 Ternary nanocomposites	**23**
1.7 Membrane Filtration	**24**
1.7.1 Types of Nano-porous Membranes	**24**
1.8 The Aims of this study	**25**
Chapter Two Experimental	
2.1 Instruments and Chemicals	**26**
2.2 Synthesis of Graphitic Carbon Nitride g-C_3N_4	**27**
2.3 Synthesis of Nano Bismuth Oxide (Bi_2O_3)	**28**
2.4 Synthesis of Nano Graphene Oxide (NGO)	**28**
2.5 Synthesis of binary nanocomposites g-C_3N_4/Bi_2O_3	**30**
2.6 Synthesis ternary nanocomposites BiC_{80}/GO (x mg)	**30**

Chapter Two Experimental	*Page*
2.7 Sample Preparation	**30**
2.7.1 Stock solution of Methylene blue dye (1000 mg.L^{-1})	**30**
2.8 Photo catalytic degradation of the MB dye	**31**
2.8.1 Photocatalytic Degradation of the MB dye by Nano g-C_3N_4, Bi_2O_3, binary nano composites g-C_3N_4/Bi_2O_3, ternary nanocomposites BiC_{80}/GO (x mg)	**31**
2.8.2 Photo catalytic degradation of MB dye by NGO	**32**
2.9 Optimum conditions for the photocatalytic degradation of MB dye by binary nanocomposite 80%g-C_3N_4/Bi_2O_3 and ternary nanocomposite BiC80/GO (20 mg)	**32**
2.9.1 Effect of catalyst weight	**32**
2.9.2 Effect of MB dye concentration	**32**
2.9.3 Effect of temperature	**33**
2.9.4 Effect of pH	**33**
2.10Membranes Synthesis method	**34**
2.10.1 g-C_3N_4 , Bi_2O_3 ,NGO g-C_3N_4/Bi_2O_3 and BiC_{80}/GO (x mg) Membranes	**34**
2.11 Applications of Membranes	**35**
2.11.1 Separation of MB Dye by g-C_3N_4, NGO, Bi_2O_3, g-C_3N_4/Bi_2O_3 and BiC_{80}/GO (x mg) membranes	**35**
Chapter Three Results and Discussion	
3.1. Spectral Characterization of g-C_3N_4, Bi_2O_3, NGO, g-C_3N_4-Bi_2O_3 and BiC_{80} -GO (X mg) composites	**36**
3.1.1 X-Ray Diffraction Spectroscopy (XRD)	**36**
3.1.2 Fourier transform infrared spectrophotometry (FT-IR)	**41**
3.1.3 Ultraviolet - visible spectrophotometry	**44**
3.1.4 Photoluminescence Spectral Analysis (PL)	**47**
3.1.5 Thermogravimetric Analysis (TGA)	**50**
3.1.6 Field Emission Scanning Electron Microscopy (FESEM)	**53**
3.2 Photocatalytic degradation of the methylene blue (MB)	**65**
3.2.1 Photocatalytic degradation of the MB dye by g-C_3N^4, Bi_2O_3 and NGO	**65**
3.2.2 Photocatalytic degradation of the MB dye by g-C_3N_4 -Bi_2O_3 binary nanocomposites	**68**
3.2.3 Photocatalytic degradation of the MB dye by novel BiC_{80}/GO(x) ternary nanocomposites	**71**

Chapter Three Results and Discussion	*Page*
3.2.4 Recycle process	**73**
3. 3 Optimum conditions of photocatalytic degradation of MB	**75**
3.3.1 Effect of catalyst weight	**75**
3.3.2 Effect of the MB dye concentration	**79**
3.3.3 Effect of Temperature	**83**
3.3.4 Effect of pH	**87**
3.4 Energy gap	**94**
3.5 Photocatalytic mechanism of nanocomposites	**99**
3.5.1 Electron transfer mechanism of catalytic binary nanocomposites	**99**
3.5.2 Electron transfer mechanism of catalytic ternary nanocomposites	**100**
3.6 Kinetics of photocatalytic degradation of MB dye	**101**
3.7 Membrane synthesis	**103**
3.7.1 Separation of MB dye by g-C_3N_4, Bi_2O_3 and NGO membranes	**103**
3.7.2 Separation of MB dye by (20%) g-C_3N_4 -Bi_2O_3, (40%) g-C_3N_4 - Bi_2O_3, (60%) g-C_3N_4 -Bi_2O_3 and (80%) g-C_3N_4 -Bi_2O_3 binary nanocomposites	**104**
3.7.3 Separation of MB Dye by BiC_{80}/GO (10 mg), BiC_{80}/GO (20 mg), BiC_{80}/GO (30 mg) and BiC_{80}/GO (40 mg) ternary nanocomposites	**105**
Conclusion	**107**
Recommendations	**108**
References	**109**

Tables

Table	*Page*
Table (2-1) Instruments used in study, models, companies and origin	**26**
Table (2-2) Chemicals used, chemical formula, company and origin	**27**
Table (3-1) Particle size by Debye- Scherrer equation	**40**
Table (3-2) The major peak bands of g-C_3N_4	**41**
Table (3-3) The major peak bands of Bi_2O_3	**41**
Table (3-4) The major peak bands of NGO	**41**

Table	*Page*
Table (3-5) The major peak bands of (20%) g-C_3N_4 -Bi_2O_3, (40%) g- C_3N_4 – Bi_2O_3, (60%) g-C_3N_4 -Bi_2O_3 and (80%) g-C_3N_4 -Bi_2O_3 binary nanocomposites	**43**
Table (3-6) The major peak bands of BiC_{80}/GO (10 mg), BiC_{80}/GO (20 mg), BiC_{80}/GO (30 mg) and BiC_{80}/GO (40 mg) ternary nano composites	**44**
Table (3-7) Photocatalytic degradation of MB (10 mg.L^{-1}), Vol.=50 ml by g-C_3N_4 wt.=50 mg	**66**
Table (3-8) Photocatalytic degradation of MB (10 mg.L^{-1}), Vol.=50 ml by Bi_2O_3 wt.=50 mg	**66**
Table (3-9) Photocatalytic degradation of MB (100 mg.L^{-1}), Vol.=50 ml by NGO wt.=50 mg	**69**
Table (3-10) Photocatalytic degradation of MB (10 mg.L^{-1}), Vol.=50 ml by (20%) g-C_3N_4- Bi_2O_3 wt.=50 mg	**68**
Table (3-11) Photocatalytic degradation of MB (10 mg.L^{-1}), Vol.=50 ml by (40%) g-C_3N_4- Bi_2O_3 wt.=50 mg	**69**
Table (3-12) Photocatalytic degradation of MB (10 mg.L^{-1}), Vol.=50 ml by (60%) g-C_3N_4- Bi_2O_3 wt.=50 mg	**69**
Table (3-13) Photocatalytic degradation of MB (10 mg.L^{-1}), Vol.=50 ml by (80%) g-C_3N_4- Bi_2O_3 wt.=50 mg	**69**
Table (3-14) Photocatalytic degradation of MB (10 mg.L^{-1}), Vol.=50 ml by BiC_{80}/GO (10mg) wt.=50 mg	**71**
Table (3-15) Photocatalytic degradation of MB (10 mg.L^{-1}), Vol.=50 ml by BiC_{80}/GO (20mg), wt.=50 mg	**71**
Table (3-16) Photocatalytic degradation of MB (10 mg.L^{-1}), Vol.=50 ml by BiC_{80}/GO (30mg), wt.=50 mg	**72**
Table (3-17) Photocatalytic degradation of MB (10 mg.L^{-1}), Vol.=50 ml BiC_{80}/GO (40mg), wt.=50 mg	**72**
Table (3-18) Photocatalytic degradation of MB (10 mg.L^{-1}), Vol.=50 ml by (80%) g-C_3N_4 - Bi_2O_3 wt.=40 mg binary nanocomposite at 25^{o}C	**76**
Table (3-19) Photocatalytic degradation of MB (10 mg.L^{-1}), Vol.=50 ml by (80%) g-C_3N_4 - Bi_2O_3 wt.=50 mg binary nanocomposite at 25^{o}C	**76**
Table (3-20) Photocatalytic degradation of MB (10 mg.L^{-1}), Vol.=50 ml by (80%) g-C_3N_4 - Bi_2O_3 wt.=60 mg binary nanocomposite at 25^{o}C	**76**
Table (3-21) Photocatalytic degradation of MB (10 mg.L^{-1}), Vol.=50 ml by BiC_{80}/GO (20 mg) wt.=40 mg ternary nanocomposite at 25^{o}C	**78**
Table (3-22) Photocatalytic degradation of MB (10 mg.L^{-1}), Vol.=50 ml by BiC_{80}/GO (20 mg) wt.=50 mg ternary nanocomposite at 25^{o}C	**78**
Table (3-23) Photocatalytic degradation of MB (10 mg.L^{-1}), Vol.=50 ml by BiC_{80}/GO (20 mg) wt.=60 mg ternary nanocomposite at 25^{o}C	**78**
Table (3-24) Photocatalytic degradation of MB (5 mg.L^{-1}),Vol.=50 ml by (80%) g-C_3N_4 -Bi_2O_3 wt.=50 mg binary nanocomposite at 25^{o}C	**80**

Table	*Page*
Table (3-25) Photo catalytic degradation of MB (10 mg.L^{-1}), Vol.=50 ml by (80%) g-C_3N_4 - Bi_2O_3 wt.=50 mg binary nanocomposite at 25^oC	**80**
Table (3-26) Photo catalytic degradation of MB (15 mg.L^{-1}), Vol.=50 ml by (80%) g-C_3N_4 - Bi_2O_3 wt.=50 mg binary nanocomposite at 25^oC	**80**
Table (3-27) Photocatalytic degradation of MB (5 mg.L^{-1}), Vol.=50 ml by BiC_{80}/GO (20 mg), wt.=50 mg ternary nanocomposite at 25^oC	**82**
Table (3-28) Photo catalytic degradation of MB (10 mg.L^{-1}), Vol.=50 ml by BiC_{80}/GO (20 mg) wt.=50 mg ternary nanocomposite at 25^oC	**82**
Table (3-29) Photo catalytic degradation of MB (15 mg.L^{-1}), Vol.=50 ml by BiC_{80}/GO (20 mg) wt.=50 mg ternary nanocomposite at 25^oC	**82**
Table (3-30) Photocatalytic degradation of MB (10 mg.L^{-1}), Vol.=50 ml by (80%) g-C_3N_4 - Bi_2O_3 wt.=50 mg binary nanocomposite at 25^oC	**84**
Table (3-31) Photocatalytic degradation of MB (10 mg.L^{-1}), Vol.=50 ml by (80%) g-C_3N_4 - Bi_2O_3 wt.=50 mg binary nanocomposite at 35^oC	**84**
Table (3-32) Photocatalytic degradation of MB (10 mg.L^{-1}), Vol.=50 ml by (80%) g-C_3N_4 - Bi_2O_3 wt.=50 mg binary nanocomposite at 40^oC	**84**
Table (3-33) Photocatalytic degradation of MB (5 mg.L^{-1}), Vol.=50 ml by BiC_{80}/GO (20 mg), wt.=50 mg ternary nanocomposite at 25^oC	**86**
Table (3-34) Photocatalytic degradation of MB (5 mg.L^{-1}), Vol.=50 ml by BiC_{80}/GO (20 mg) wt.=50 mg ternary nanocomposite at 35^oC	**86**
Table (3-35) Photo catalytic degradation of MB(5ppm), Vol.=50 ml by BiC_{80}/GO (20 mg) wt.=50 mg ternary nanocomposite at 40^oC	**86**
Table (3-36) Photocatalytic degradation of MB (10 mg.L^{-1}) at pH= 2, Vol.=50 ml by (80%) g- C_3N_4 -Bi_2O_3 wt.=50 mg binary nanocomposite at 25^oC	**89**
Table (3-37) Photocatalytic degradation of MB (10 mg.L^{-1}) at pH= 4, Vol.=50 ml by (80%) g- C_3N_4 -Bi_2O_3 wt.=50 mg binary nanocomposite at 25^oC	**89**
Table (3-38) Photocatalytic degradation of MB (10 mg.L^{-1}) at pH= 6, Vol.=50 ml by (80%) g- C_3N_4 -Bi_2O_3 wt.=50 mg binary nanocomposite at 25^oC	**89**
Table (3-39) Photocatalytic degradation of MB (10 mg.L^{-1}) at pH= 8, Vol.=50 ml by (80%) g- C_3N_4 -Bi_2O_3 wt.=50 mg binary nanocomposite at 25^oC	**90**
Table (3-40) Photocatalytic degradation of MB (10 mg.L^{-1}) at pH= 10, Vol.=50 ml by (80%) g-C_3N_4 -Bi_2O_3 wt.=50 mg binary nanocomposite at 25^oC	**90**
Table (3-41) Photocatalytic degradation of MB (10 mg.L^{-1}) at pH=12, Vol.=50 ml by (80%) g- C_3N_4 -Bi_2O_3 wt.=50 mg binary nanocomposite at 25^oC	**90**
Table (3-42) Photocatalytic degradation of MB (10 mg.L^{-1}) at pH=14, Vol.=50 ml by (80%) g- C_3N_4 -Bi_2O_3 wt.=50 mg binary nanocomposite at 25^oC	**90**
Table (3-43) Photocatalytic degradation of MB (10 mg.L^{-1}) at pH=2, Vol.=50 ml by (BiC_{80}/GO-20 mg), wt.=50 mg ternary nanocomposite at 25^oC	**92**

Table	*Page*
Table (3-44) Photocatalytic degradation of MB (10 mg.L^{-1}) at pH= 4, Vol.=50 ml by (BiC_{80}/GO-20 mg), wt.=50 mg ternary nanocomposite at 25^{o}C	**92**
Table (3-45) Photocatalytic degradation of MB (10 mg.L^{-1}) at pH= 6, Vol.=50 ml by (BiC_{80}/GO-20 mg), wt.=50 mg ternary nanocomposite at 25^{o}C	**92**
Table (3-46) Photocatalytic degradation of MB (10 mg.L^{-1}) at pH= 8, Vol.=50 ml by (BiC_{80}/GO-20 mg), wt.=50 mg ternary nanocomposite at 25^{o}C	**93**
Table (3-47) Photocatalytic degradation of MB(10 mg.L^{-1}) at pH=10, Vol.=50 ml by (BiC_{80}/GO-20 mg), wt.=50 mg ternary nanocomposite at 25^{o}C	**93**
Table (3-48) Photocatalytic degradation of MB(10 mg.L^{-1}) at pH=12, Vol.=50 ml by (BiC_{80}/GO-20 mg), wt.=50 mg ternary nanocomposite at 25^{o}C	**93**
Table (3-49) Energy gap of g-C_3N_4, Bi_2O_3 and NGO	**95**
Table (3-50) Energy gap of (20%) g-C_3N_4 -Bi_2O_3, (40%) g-C_3N_4 -Bi_2O_3, (60%) g- C_3N_4 -$B_{i2}O_3$ and (80%) g-C_3N_4 -Bi_2O_3 binary nanocomposites	**97**
Table (3-51) Energy gap values of BiC_{80}/GO (10 mg), BiC_{80}/GO (20 mg), BiC_{80}/GO (30 mg) and BiC_{80}/GO (40 mg) ternary nanocomposites	**98**

Figures

Figure	*Page*
Fig. (1-1) The synthesis of nanomaterials via top-down and bottom-up approaches	**2**
Fig. (1- 2) The principle of the ball milling method	**3**
Fig. (1- 3) A schematic diagram of the coaxial electrospinning technique	**4**
Fig. (1-4): Nanosphere lithography process (NSL)	**5**
Fig. (1-5) A schematic diagram of the DC magnetron sputtering process	**6**
Fig. (1-6) A schematic illustration of the formation mechanisms of carbon nanomaterial on the inner wall of the chamber using different gases via a DC arc discharge approach	**7**
Fig (1-7) Sketch of the main experimental parameters of laser ablation synthesis in liquid solution	**8**
Fig. (1-8) A schematic diagram of the growth of in-plane graphene and hBN heterostructures via various techniques: (A) simultaneous in situ CVD growth, (B) sequential in situ CVD growth, (C) lithography-assisted growth, and (D) conversion growth	**9**

Figure	*Page*
Fig. (1-9) A general-purpose hydrothermal autoclave. The hydrothermal reactions occur inside the Teflon container	**10**
Fig (1-10) An overview showing two sol–gel method synthesis examples: (a) films from a colloidal sol and (b) powder from a colloidal sol transformed into a gel	**11**
Fig. (1-11) A schematic representation of the synthesis of materials using different types of templates	**12**
Fig. (1-12) Methylene blue molecular structure	**15**
Fig. (1-13) Various g-C_3N_4 precursors and the corresponding temperatures for their thermal condensation into g-C_3N_4	**20**
Fig. (1-14) Tri-s-triazine-based two-dimensional structure of g-C_3N_4. Color scheme: C, gray; N, blue	**20**
Fig. (1-15) Mechanism of graphene oxide synthesis	**21**
Fig. (2-1): The flow chart of the synthesis nano Graphitic Carbon Nitride	**28**
Fig. (2-2): The flow chart of the synthesis nano graphene oxide	**29**
Fig. (2-3) Hotplate with magnetic stirrer under Tungsten lamp- 300 watt	**31**
Fig. (2-4) (A) g-C_3N_4 membrane (B) Bi_2O_3 membrane, (C) NGO membrane, (D) g-C_3N_4/Bi_2O_3 membrane, (E) BiC_{80}/GO(x) membrane on substrate (cellulose nitrate)	**34**
Fig. (2-5) BiC80/GO(x) membrane (A) before, (B) after separation of MB dye(C) Vacuum filtration pump	**35**
Fig. (3-1) XRD patterns of g-C_3N_4, Bi_2O_3 and NGO	**36**
Fig. (3-2) XRD patterns of (20%) g-C_3N_4 -Bi_2O_3, (40%) g-C_3N_4 -Bi_2O_3, (60%) g-C_3N_4 – Bi_2O_3 and (80%) g-C_3N_4 -Bi_2O_3 binary nanocomposites	**38**
Fig. (3-3) XRD patterns of BiC_{80}/GO (10 mg), BiC_{80}/GO (20 mg), BiC_{80}/GO (30 mg) and BiC_{80}/GO (40 mg) ternary nano composites	**39**
Fig. (3-4) FT-IR spectrums of g-C_3N_4, Bi_2O_3 and NGO	**42**
Fig. (3-5) FT-IR spectrum of (20%) g-C_3N_4 -Bi_2O_3, (40%) g-C_3N_4 -Bi_2O_3, (60%) g-C_3N_4 - Bi_2O_3 and (80%) g-C_3N_4 -Bi_2O_3 binary nanocomposites	**43**
Fig. (3-6) FT-IR spectrum of BiC_{80}/GO (10 mg), BiC_{80}/GO (20 mg), BiC_{80}/GO (30 mg) and BiC_{80}/GO (40 mg) ternary nanocomposites	**44**
Fig. (3-7) Absorption spectrums of (A)g-C_3N_4, (B) Bi_2O_3 and(C) NGO	**45**
Fig. (3-8) Absorption spectrums of (20%) g-C_3N_4 -Bi_2O_3, (40%) g-C_3N_4 - Bi_2O_3, (60%) g- C_3N4-Bi_2O_3 and (80%) g-C_3N_4 -Bi_2O_3 binary nanocomposites	**46**
Fig. (3-9) Absorption spectrums of BiC_{80}/GO (10 mg), BiC_{80}/GO (20 mg), BiC_{80}/GO (30 mg) and BiC_{80}/GO (40 mg) ternary nanocomposites	**47**

Figure	*Page*
Fig. (3-10) Photoluminescence (PL) spectra of g-C_3N_4, Bi_2O_3 and NGO	**48**
Fig. (3-11) Photoluminescence (PL) spectra of (20%) g-C_3N_4 -Bi_2O_3, (40%) g-C_3N_4 -Bi_2O_3, (60%) g-C_3N_4 -Bi_2O_3 and (80%) g-C_3N_4 -Bi_2O_3 binary nanocomposites	**49**
Fig. (3-12) Photoluminescence (PL) spectra of BiC_{80}/GO (10 mg), BiC_{80}/GO (20mg), BiC_{80}/GO (30 mg) and BiC_{80}/GO (40 mg) ternary nanocomposites	**50**
Fig. (3-13) Thermogravimetric analysis (TGA) of g-C_3N_4, Bi_2O_3 and NGO	**51**
Fig. (3-14) Thermogravimetric analysis (TGA) of (20%) g-C_3N_4 -Bi_2O_3, (40%) g-C_3N_4 – Bi_2O_3, (60%) g-C_3N_4 -Bi_2O_3 and (80%) g-C_3N_4 -Bi_2O_3 binary nanocomposites	**52**
Fig. (3-15) Thermogravimetric analysis (TGA) of BiC_{80}/GO (10 mg), BiC_{80}/GO (20 mg), BiC_{80}/GO (30 mg) and BiC_{80}/GO (40 mg) ternary nanocomposites	**53**
Fig. (3-16) (A) FESEM images of g-C_3N_4, (B) Size distribution	**54**
Fig. (3-17) EDS spectrum of g-C_3N_4	**54**
Fig. (3-18) (A) FESEM images of Bi_2O_3, (B) Size distribution	**55**
Fig. (3-19) EDS spectrum of Bi_2O_3	**55**
Fig. (3-20) (A) FESEM images of NGO, (B) Size distribution	**56**
Fig. (3-21) EDS spectrum of NGO	**56**
Fig. (3-22) (A) FESEM images of (20%) g-C_3N_4 - Bi_2O_3 binary nanocomposite ,(B) Size distribution	**57**
Fig. (3-23) EDS spectrum of (20%) g-C_3N_4 - Bi_2O_3 binary nanocomposite	**57**
Fig. (3-24) (A) FESEM images of (40%) g-C_3N_4 - Bi_2O_3 binary nanocomposite ,(B) Size distribution	**58**
Fig. (3-25) EDS spectrum of (40%) g-C_3N_4 - Bi_2O_3 binary nanocomposite	**58**
Fig. (3-26) (A) FESEM images of (60%) g-C_3N_4 - Bi_2O_3 binary nanocomposite ,(B) Size distribution	**59**
Fig. (3-27) EDS spectrum of (60%) g-C_3N_4 - Bi_2O_3 binary nanocomposite	**59**
Fig. (3-28) (A) FESEM images of (80%) g-C_3N_4 - Bi_2O_3 binary nanocomposite ,(B) Size distribution	**60**
Fig. (3-29) EDS spectrum of (80%) g-C_3N_4 - Bi_2O_3 binary nanocomposite	**60**
Fig. (3-30) (A) FESEM images of BiC_{80}/GO (10 mg) ternary nanocomposite ,(B) Size distribution	**61**

Figure	*Page*
Fig. (3-31) EDS spectrum of BiC_{80}/GO (10 mg) ternary nanocomposite	**61**
Fig. (3-32) (A) FESEM images of BiC_{80}/GO (20 mg) ternary nanocomposite ,(B) Size distribution	**62**
Fig. (3-33) EDS spectrum of BiC_{80}/GO (20 mg) ternary nanocomposite	**62**
Fig. (3-34) (A) FESEM images of BiC_{80}/GO (30 mg) ternary nanocomposite ,(B) Size distribution	**63**
Fig. (3-35) EDS spectrum of BiC_{80} /GO (30 mg) ternary nanocomposite	**63**
Fig. (3-36) (A) FESEM images of BiC_{80}/GO (40 mg) ternary nanocomposite ,(B) Size distribution	**64**
Fig. (3-37) EDS spectrum of BiC_{80}/GO (40 mg) ternary nanocomposite	**64**
Fig. (3-38) Absorption spectrum of MB dye (10 $mg.L^{-1}$)	**66**
Fig. (3-39) Photocatalytic degradation efficiency of MB dye by g-C_3N_4, Bi_2O_3 and NGO under visible light irradiation	**67**
Fig. (3-40) MB dye before and after Photocatalytic degradation by (A) g-C_3N_4, (B) Bi_2O_3(C) NGO	**68**
Fig. (3-41) Photocatalytic degradation of MB dye by (20%) g-C_3N_4 -Bi_2O_3, (40%) g-C_3N_4 – Bi_2O_3, (60%) g-C_3N_4 -Bi_2O_3 and (80%) g-C_3N_4 – Bi_2O_3 binary nanocomposites	**70**
Fig. (3-42) MB dye before and after photocatalytic degradation by (80%) g-C_3N_4 -Bi_2O_3 binary nanocomposite	**70**
Fig. (3-43) Photocatalytic degradation MB dye by of BiC_{80}/GO (10 mg), BiC_{80}/GO (20 mg), BiC_{80}/GO (30 mg) and BiC_{80}/GO (40 mg) ternary nanocomposites under visible light irradiation	**72**
Fig. (3-44) MB dye before and after photocatalytic degradation by BiC_{80}/GO (20 mg) ternary nanocomposite under visible light irradiation	**73**
Fig. (3-45) Recycle process of (80%) g-C_3N_4 -Bi_2O_3 binary nanocomposite against MB dye for two cycles	**74**
Fig. (3-46) Recycle process of BiC_{80}/GO (20 mg) ternary nanocomposite against MB dye for two cycles	**75**
Fig. (3-47) Effect of catalyst weight on photocatalytic degradation of MB dye by (80%) g- C_3N_4 -Bi_2O_3 binary nanocomposite (composite weight=40, 50 and 60 mg)	**77**
Fig. (3-48) Effect of catalyst weight on photocatalytic degradation of MB dye by BiC_{80}/GO (20 mg) ternary nanocomposite (composite weight=40, 50 and 60 mg)	**79**
Fig. (3-49) Effect of MB dye concentrations on photocatalytic degradation by (80%) g-C_3N_4-Bi_2O_3, wt.=50 mg binary nanocomposite (MB dye concentration = 5,10 and 15 $mg.L^{-1}$)	**81**
Fig. (3-50) Effect of MB dye concentration on photocatalytic degradation of BiC_{80}/GO (20 mg) ternary nanocomposite, (MB dye concentration = 5,10 and 15 $mg.L^{-1}$)	**83**

Figure	*Page*
Fig. (3-51) Effect of temperature on photocatalytic degradation of MB(10mg.L^{-1}) by (80%) g- C_3N_4 -Bi_2O_3 binary nanocomposite at 25,35 and 40^oC	**85**
Fig. (3-52) Effect of temperature on photocatalytic degradation of MB by BiC_{80}/GO (20 mg) ternary nanocomposite at 25,35 and 40^oC	**87**
Fig. (3-53) Absorption spectrums of MB dye (10 mg.L^{-1}) at pH 2-14	**88**
Fig.(3-54)Effect of pH(2-14) on photocatalytic degradation of MB dye10 mg.L^{-1}, by (80%) g-C_3N_4 -Bi_2O_3 (50 mg) binary nanocomposite	**91**
Fig. (3-55) Effect of the pH (2-14) on the photocatalytic degradation of MB dye by (BiC_{80}/GO-20 mg) ternary nanocomposite	**94**
Fig. (3-56) Tauc plot for band gap energy of g-C_3N_4	**95**
Fig. (3-57) Tauc plot for band gap energy of Bi_2O_3	**96**
Fig. (3-58) Tauc plot for band gap energy of NGO	**96**
Fig. (3-59) Tauc plots for band gap energy of (20%) g-C_3N_4-Bi_2O_3, (40%) g-C_3N_4-Bi_2O_3, (60%) g-C_3N_4-Bi_2O_3 and (80%) g-C_3N_4-Bi_2O_3 binary nanocomposites	**97**
Fig. (3-60) Tauc plot for band gaps energy of BiC_{80}/GO (10 mg), BiC_{80}/GO (20 mg), BiC_{80}/GO (30 mg) and BiC_{80}/GO (40 mg) ternary nanocomposites	**98**
Fig. (3-61) Proposed mechanism for the photodegradation of MB dye by g-C_3N_4 -Bi_2O_3 binary nanocomposite catalyst	**100**
Fig. (3-62) Proposed mechanism for the photodegradation of MB dye by (BiC_{80}/GO (x mg) ternary nanocomposite catalyst	**101**
Fig. (3-63) First-order plots for photocatalytic degradation of MB dye (5-15 mg.L^{-1}) by 50 mg of (80%) g-C_3N_4 - Bi_2O_3 binary nanocomposite catalyst	**102**
Fig. (3-64) First-order plots for photocatalytic degradation of MB dye (5-15 mg.L^{-1}) by50 mg of BiC_{80}/GO (20 mg)ternary nanocomposite catalyst	**103**
Fig. (3-65) Removal percentage of MB dye by g-C_3N_4, Bi_2O_3 and NGO membranes	**104**
Fig. (3-66) Removal percentage of MB dye by (20%) g-C_3N_4 -Bi_2O_3, (40%) g-C_3N_4 -Bi_2O_3, (60%) g-C_3N_4 -Bi_2O_3 and (80%) g-C_3N_4 -Bi_2O_3 binary nanocomposites membranes	**105**
Fig. (3-67) Removal percentage of MB dye by BiC_{80}/GO (10 mg), BiC_{80}/GO (20 mg), BiC_{80}/GO (30 mg) and BiC_{80}/GO (40 mg) ternary nanocomposite membranes	**106**

List of Abbreviations

Abbreviation	Key
AOP	Advanced oxidation process
Bi_2O_3	Bismuth oxide
CCM	Colloidal crystal mask
CB	Conduction band
CVD	Chemical vapor deposition
CNTs	Carbon nanotubes
D%	Degradation efficiency
EDS	Energy Dispersion X-ray
FLG	Few-layer graphene
β	Full width at half maximum (FWHM)
FT-IR	Fourier transform infrared spectrophotometry
FESEM	Field Emission Scanning Electron Microscopy
g-C_3N_4	Graphitic Carbon Nitride
NGO	Graphene Oxide Nano-Sheets
g-C_3N_4-Bi_2O_3	Graphitic Carbon Nitride- Bismuth oxide
BiC_{80}/GO (x mg)	Graphitic Carbon Nitride- Bismuth oxide- Graphene Oxide Nano-Sheets
HCP	Hexagonal-close-packed
MB	Methylene blue dye
NSL	Nanosphere lithography
NF	Nano-filtering
DMF	N, N-di methyl formamide
PES	Polyether sulfone
PVDF	Polyvinylidene fluoride
PTFE	Polytetrafluoroethylene
PVA	Polyvinyl alcohol
D	Particle size
PL	Photoluminescence Spectral Analysis

Abbreviation	Key
RO	Reverse osmosis
R%	Removal efficiency
K	Scherrer's constant equal 0.9
THMs	Trihalomethanes
TGA	Thermogravimetric Analysis
UF	Ultra-Filtration
UV–Vis	Ultraviolet - visible spectrophotometry
VOCs	Volatile organic compounds
VB	Valence band
λ_{max}	Wavelength maximum
XRD	X-Ray Diffraction Spectroscopy

Chapter one
Introduction

1.1 Nanomaterials

An intriguing new class of materials known as nanomaterials is in great demand for a wide range of real-world uses. Five silicon atoms or ten hydrogen atoms lined up, each measuring one nanometer, can be used to illustrate the length of a nanometer. If a material's size or one of its dimensions falls between 1 and 100 nm, it is considered a nanomaterial[1]. They are smaller than their bulk materials and have high surface/volume ratios[2]. The quantity of component atoms surrounding a particle's surface grows as its size decreases. This leads to the development of highly reactive particles with distinct chemical, optical, physical, and electronic properties. The field of nanotechnology is one that is developing quickly and has a lot of applications in the chemical, pharmaceutical, engineering, and food processing industries[3],[4]. First used, the name "nanometer" was in 1914 which coined by Richard Adolf Zsigmondy [5]. In 1959, during the annual meeting of the American Physical Society, the specific notion of nanotechnology was introduced by Nobel Prize-winning American physicist Richard Feynman. This is regarded as the first lecture on nanotechnology given by an academic[5].

1.2 Synthesis of nanomaterials

Two main approaches are used for the synthesis of nanomaterials (Fig. 1-1): top-down approaches and bottom-up approaches:

1.2.1 Top-down approach

In top-down approaches, bulk materials are divided to produce nanostructured materials. Top-down methods include mechanical milling, laser ablation, etching, sputtering, and electro-explosion.

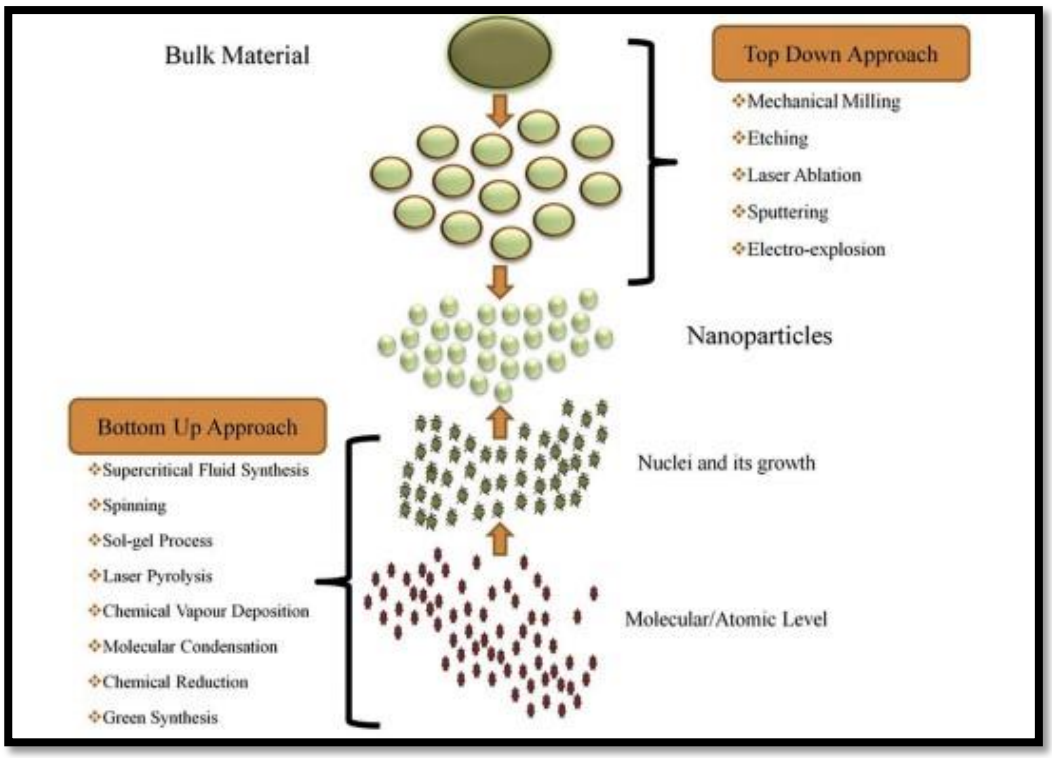

Fig.(1-1)The synthesis of nanomaterial's via top-down and bottom-up approaches[6]

1.2.1.1 Ball milling through Mechanical method

One economical way to convert bulk materials into nanoscale materials is by mechanical milling. Blends of various phases can be produced efficiently using mechanical milling, which also aids in the creation of nanocomposites. Fig. (1-2)[7] illustrates the ball milling method the basic idea. Ball-milled carbon nanomaterial's are thought to be a novel class of nanomaterial that offers the chance to meet the needs of energy conversion, energy storage, and environmental cleanup [8]. Mechanical milling involves the use of a high energy mill with a suitable milling medium and a powder charge (usually an elemental blend). Reducing particle size and mixing of particles in new phases are the goals of milling. Different ball milling techniques that impact the powder charge can be employed to synthesize nanomaterials[9].

The balls have two possible outcomes: either they fall freely and hit the powder and balls below, or they roll down the chamber's surface in a succession of parallel layers. It is more cost-effective to use mechanical millings for large-scale manufacturing of grain of nano size [10].

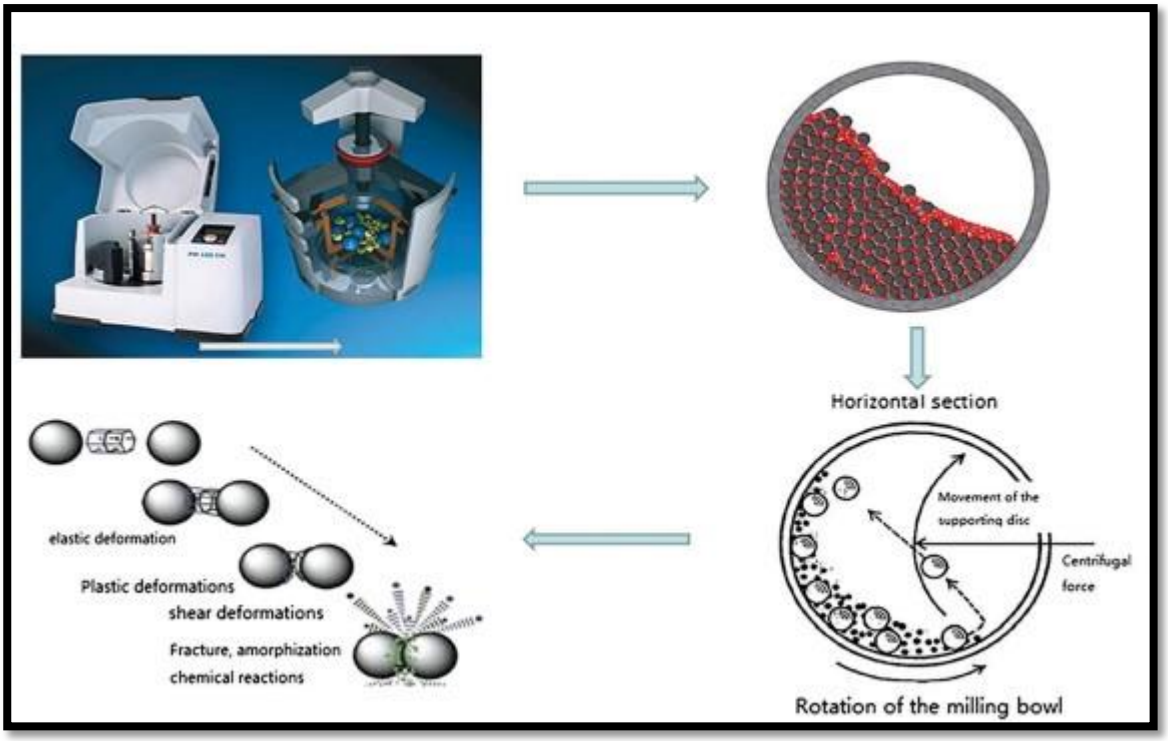

Fig.(1- 2)The principle of the ball milling method [7]

1.2.1.2 Electrospinning method

One of the most straightforward top-down techniques for creating nanostructured materials is Electrospinning. Generally speaking, it is employed to create nanofibers from a wide range of materials, most commonly polymers[11]. Coaxial electrospinning was one of the significant advances in electrospinning. The spinneret in coaxial electrospinning consists of two coaxial capillaries. Core–shell nanoarchitectures in an electric field can be formed in these capillaries using two viscous liquids, i.e., a viscous liquid as the shell and a non-viscous liquid as the core. An efficient and straightforward top-down method for producing core-shell ultrathin fibers on a big scale is coaxial electrospinning. These incredibly thin nanomaterials may be stretched to several centimeters in length. This process has been applied to the creation of inorganic, organic, hybrid, core-shell, and hollow polymer structures [12].

Fig.(1-3)[13] shows a schematic diagram of the coaxial electrospinning technique.

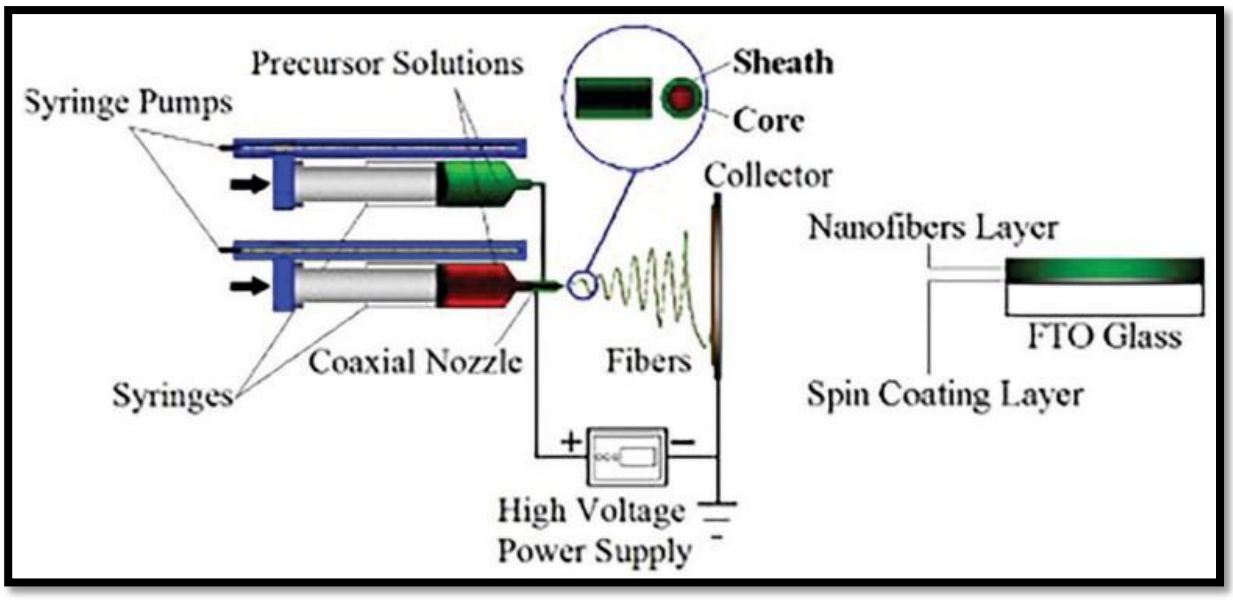

Fig.(1-3) A schematic diagram of the coaxial electrospinning technique [13]

1.2.1.3 Lithography method

A concentrated light or electron beam can be utilized to create nanoarchitectures through the use of lithography. There are two primary categories of lithography, both maskless and masked lithography[14]. Using a particular mask or template, nanopatterns are transmitted across a sizable surface area in masked nanolithography. Photolithography, Nanoimprint Lithography, and Soft Lithography are examples of Masked Lithography[15]. Electron beam lithography, focused ion beam lithography, and scanning probe lithography are examples of maskless lithography. A mask is not used in the arbitrary nanopattern writing process of maskless lithography, 3D freeform micro-nano-fabrication can be accomplished by combining wet chemical etching with focused ion beam implantation[16]. One promising low-cost method for creating consistent, homogenous arrays of nanoparticles of varying sizes is nanosphere lithography (NSL). The benefits of both top-down and bottom-up approaches are combined in this method. The procedure is broken down into two parts, mask preparation being the first Fig. (1-4). A suspension of monodisperse spherical colloids, such as polystyrene, is applied to the flat substrate following a chemical treatment to improve its hydrophilic properties. A colloidal crystal mask [17] (CCM) is a hexagonal-close-packed (HCP) monolayer or bilayer that forms after drying. Following the removal of the mask (lift-off), an array of ordered nanodots is left on the substrate's surface by either stripping or sonification in a suitable solvent.

In certain cases, crystallizing the sample or causing a crystallographic phase transition requires an annealing step[18].

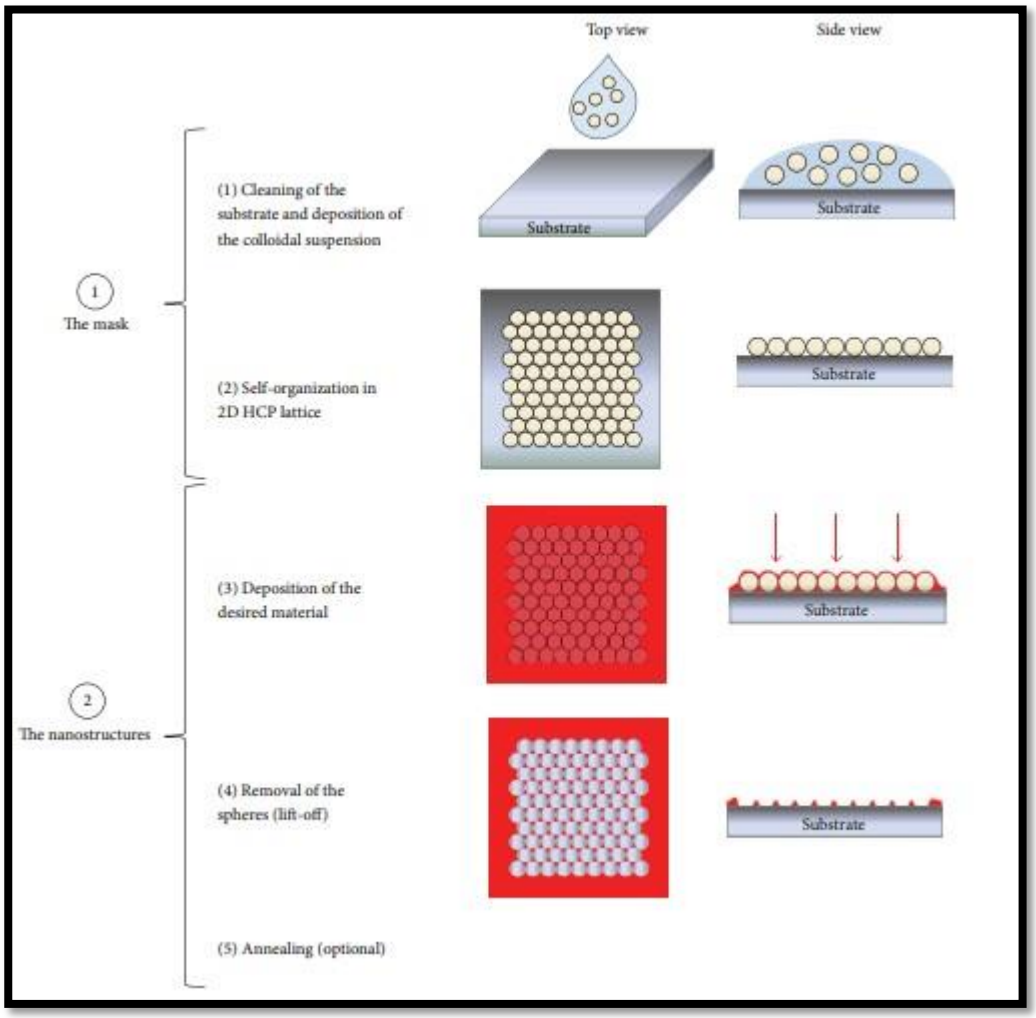

Fig. (1-4) Nanosphere lithography process (NSL)

1.2.1.4 Sputtering method

The technique of sputtering involves subjecting solid surfaces to high-energy particles like gas or plasma in order to create nanomaterials. Sputtering is thought to be a useful technique for creating thin nanomaterial films[19]. Depending on the incident gaseous-ion energy, tiny atom clusters are physically ejected off the target surface during the sputtering deposition process due to the bombardment of intense gaseous ions Fig.(1-5)[20]. There are various methods for carrying out the sputtering process, including magnetron, radio-frequency diode, and DC diode sputtering. Forty Sputtering is typically done in an evacuated chamber that has been supplied with sputtering gas. Free electrons clash with the gas when a high voltage is supplied to the cathode target, producing gas ions.

The ions that are positively charged rapidly accelerate in the these ions' electric field toward the cathode target repeatedly struck, causing atoms to be ejected off the target's surface[21]. To create WSe_2-layered nanofilms on SiO_2 and carbon paper substrates, magnetron sputtering is employe[22]. The sputtering approach is intriguing because it is less expensive than electron-beam lithography and produces nanomaterials with a composition that is identical to the target material but contains fewer contaminants[23].

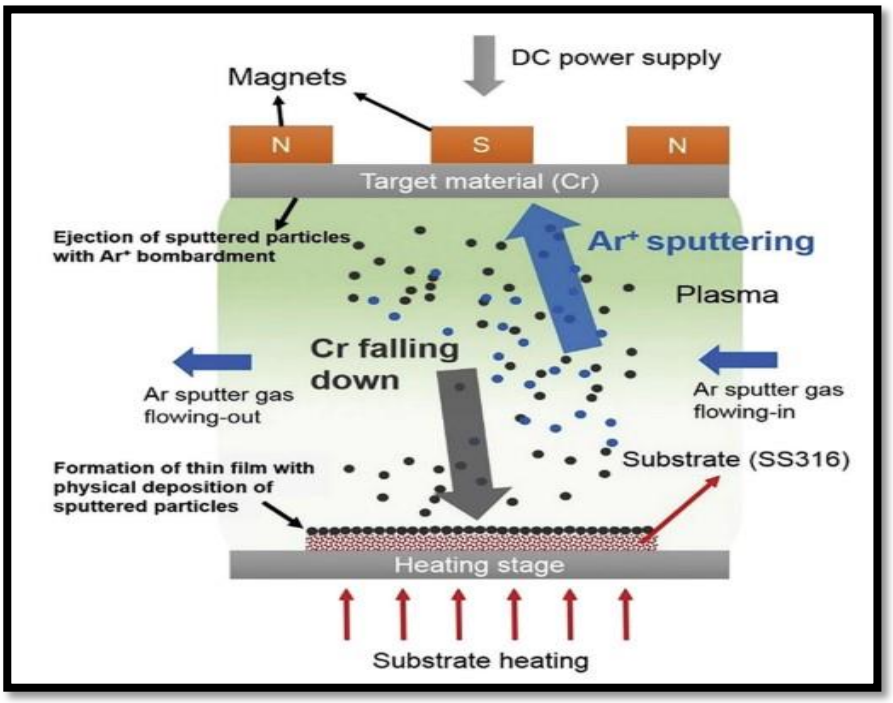

Fig.(1-5) A Schematic Diagram of the DC Magnetron Sputtering Process[20]

1.2.1.5 The arc discharge method

Arc discharge is a valuable technique for producing diverse nanostructured materials. It is well recognized for creating materials based on carbon, like amorphous spherical carbon nanoparticles, few-layer graphene (FLG), carbon nanotubes, fullerenes, and carbon nanohorns [24]. The production of fullerene nanomaterials greatly benefits from the use of the arc discharge technique. Two graphite rods are adjusted in a chamber that maintains a specific helium pressure during the formation process. It is crucial to fill the chamber completely with helium since fullerene synthesis is inhibited by oxygen or moisture. Arc discharge between the graphite rod ends propels the vaporization of carbon rods[25].

The creation of novel nanomaterials is greatly influenced by the circumstances surrounding arc discharge. Fig. (1-6) describes the circumstances in which various carbon-based nanomaterials are created using the arc discharge approach. Because different carbon-based nanomaterials have different development methods, they are gathered from various positions during the arc discharge method[24].

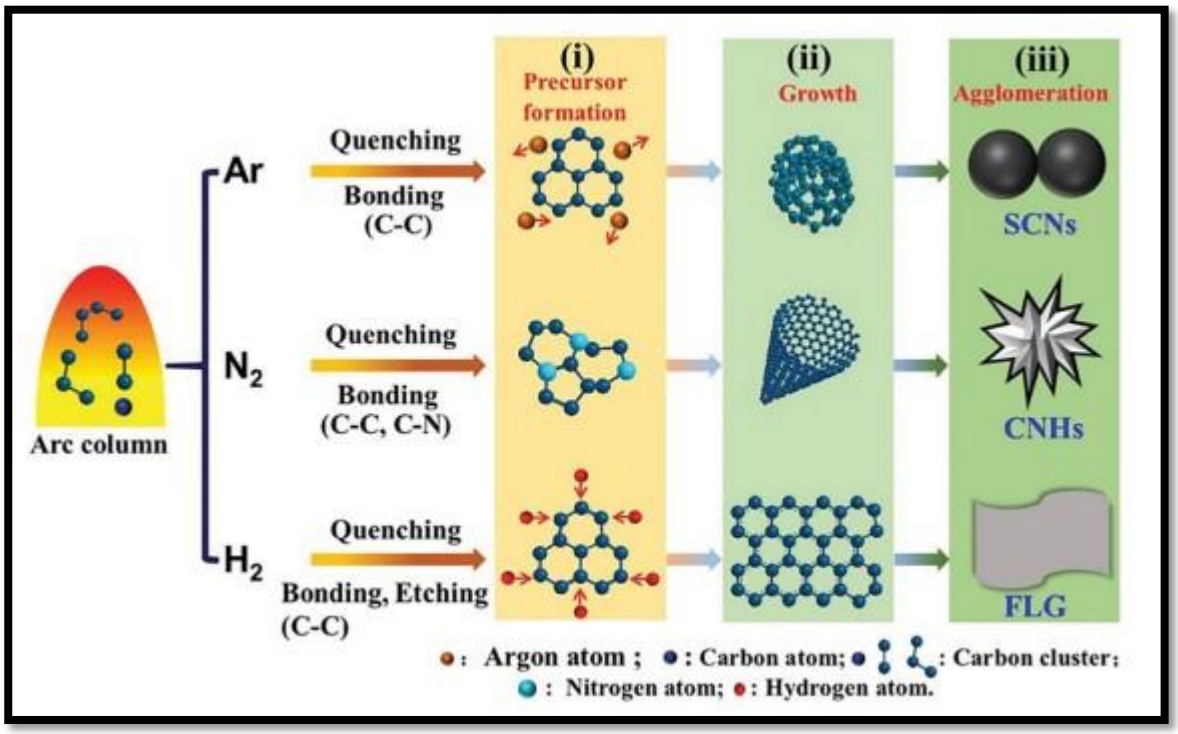

Fig. (1-6) A schematic Illustration of the Formation Mechanisms of Carbon anomaterial on the Inner wall of the Chamber using Different gases via a DC arc Discharge approach[24]

1.2.1.6 Laser ablation method

Using a strong laser beam to strike the target material, laser ablation synthesis creates nanoparticles. Because of the high energy of the laser irradiation during the laser ablation process, the source material or precursor vaporizes, forming nanoparticles. Since no additional chemicals or stabilizing agents are required for the production of noble metal nanoparticles using laser ablation, this method can be regarded as environmentally friendly[26].This approach can be used to manufacture a wide spectrum of nanomaterials, including oxide composites [27], metal nanoparticles [28],[29], carbon nanomaterials and ceramics [30],[29]. By focusing laser pulses on a bulk target submerged in a liquid solution, NMs are produced in laser ablation synthesis in liquid solution Fig. (1-7)[26].

While the dynamics of the synthetic process remain the same, the target can be either a single piece or crushed powder. Different mechanisms, such as nucleation and growth or ejection of hot droplets and solid pieces from the target, can lead to the production of nanoparticles [31].

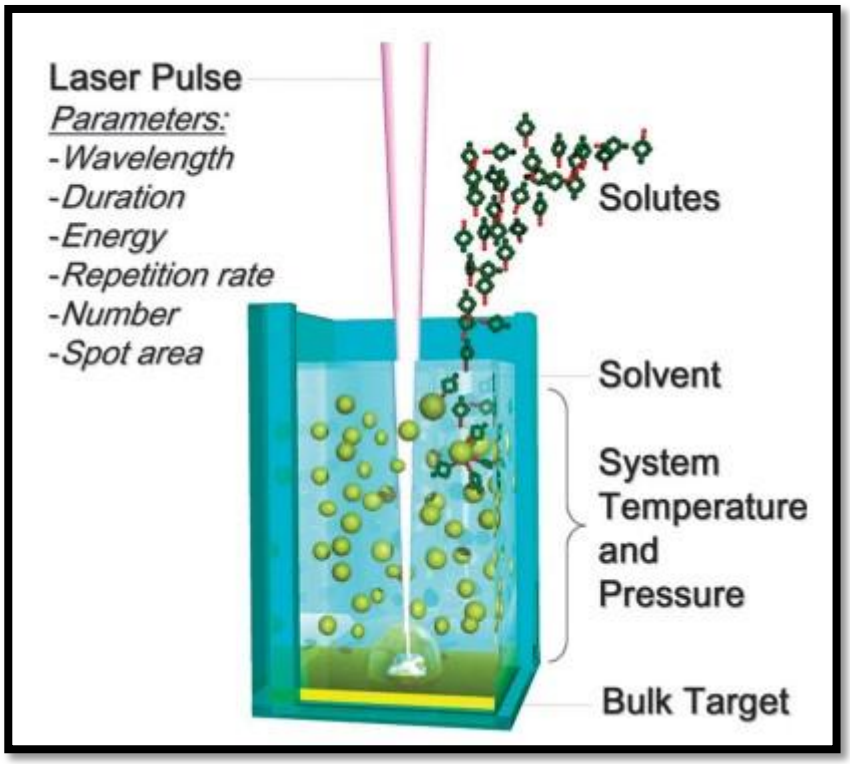

Fig (1-7) Sketch of the main experimental parameters of laser ablation synthesis in liquid solution[26]

1.2.2 Bottom-up approach

1.2.2.1 Chemical vapor deposition (CVD) method

When creating carbon-based nanomaterials, chemical vapor deposition techniques are crucial. In CVD, vapor-phase precursors react chemically to generate a thin coating on the substrate surface[32]. If a precursor has sufficient volatility, high chemical purity, good stability during evaporation, low cost, non-hazardous nature, and a long shelf life, it is deemed appropriate for CVD. Furthermore, there shouldn't be any leftover contaminants after its breakdown[32]. For example, high temperatures are applied to a substrate in an oven during the CVD process to produce carbon nanotubes. A carbon-containing gas, such as hydrocarbons, is then gradually added to the system as a precursor.

Carbon atoms are released during the breakdown of the gas at high temperatures, and these atoms then recombine to form carbon nanotubes on the substrate [33]. Nonetheless, the kind and form of the resulting nanomaterial are greatly influenced by the catalyst of choice. Ni and Co catalysts produce multilayer graphene in the CVD-based method of graphene synthesis, while a Cu catalyst produces monolayer graphene [34]. All things considered, CVD is a great way to create high-quality nanomaterials [35], and it's particularly well-known for creating two-dimensional nanomaterials Fig.(1-8) [36].

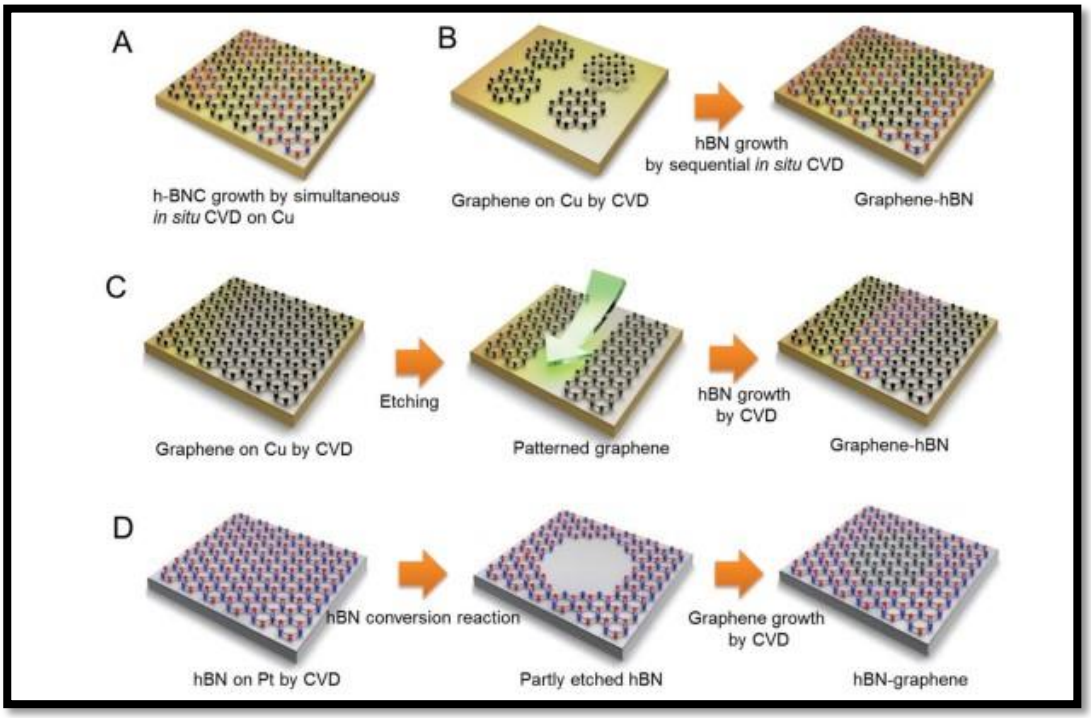

Fig. (1-8) A schematic diagram of the growth of in-plane graphene and hBN heterostructures via various techniques: (A) simultaneous in situ CVD growth, (B) sequential in situ CVD growth, (C) lithography-assisted growth, and (D) conversion growth[36]

1.2.2.2 Solvothermal and hydrothermal methods

One of the most well-known and widely applied processes for creating nanostructured materials is the hydrothermal process[37],[38]. By using a heterogeneous reaction in an aqueous medium at high pressure and temperature near the critical point in a sealed vessel, the hydrothermal technique produces nanostructured materials[39]. The hydrothermal method and the solvothermal method are similar. The fact that it is done in a non-aqueous liquid is the only distinction. Most solvothermal and hydrothermal techniques are used in closed systems[40]. The technique of crystallizing materials directly from solutions using hydrothermal/solvothermal processes typically entails two steps: crystal

nucleation and subsequent growth. The final products might be manufactured with the appropriate particle sizes and morphologies by adjusting processing factors like temperature, pH, reactant concentrations, and additives. The mechanisms that underlie the process-variable-tuned control over size and morphology are the supersaturation-dependent overall nucleation and growth rates [41]. The majority of hydrothermal and solvothermal reactions take place in sealed reactors, sometimes referred to as high-pressure bombs, pressure vessels, or autoclaves. Hydrothermal/solvothermal reactors are typically metal autoclaves lined with Teflon or alloy, or they may include an additional Teflon, platinum, gold, or silver can, beaker, or tube to shield the autoclave body from the extremely corrosive solvent that is maintained at high pressure and temperature. Sometimes .Figure(1-9) shows the most popular general-purpose autoclave used in laboratories[42].

Fig. (1-9) A general-purpose Hydrothermal autoclave. The Hydrothermal reactions occur inside the Teflon container[42]

1.2.2.3 Sol-gel method

The sol-gel method is a widely utilized wet chemical process in the synthesis of nanomaterials. This process is employed in the creation of several types of superior metal-oxide-based nanomaterials. This process is known as the "sol-gel method" because, in the process of creating the metal-oxide nanoparticles, the liquid precursor changes into a sol, which is then transformed again into a network structure known as a gel[43]. Metal alkoxides are the typical precursors used in the sol-gel process to create nanomaterials. There are multiple processes involved in the creation of nanoparticles using the sol-gel technique. In order to create a sol, the metal oxide is first hydrolyzed in water or with the help of alcohol. The following stage involves condensation, which raises the solvent's viscosity and creates porous structures that are then allowed to mature.

Metal–hydroxo– or metal–oxo–polymer formation in solution is the result of hydroxo– (M–OH–M) or oxo– (M–O–M) bridges forming during the condensation or polycondensation process[44]. Aging-related polycondensation results in modifications to the structure, characteristics, and porosity. The porosity reduces and the spacing between the colloidal particles widens with age. Following the aging phase, the gel is dried, removing any remaining water and organic solvents. Finally, the process of calcination is used to produce nanoparticles[45]. Sol-gel film and powder production is demonstrated in Fig.(1-10) [46]. The final product formed by the sol-gel process depends on a number of parameters, including the kind of precursor, pH, aging period, rate of hydrolysis, and molar ratio of the precursor to H_2O[47].

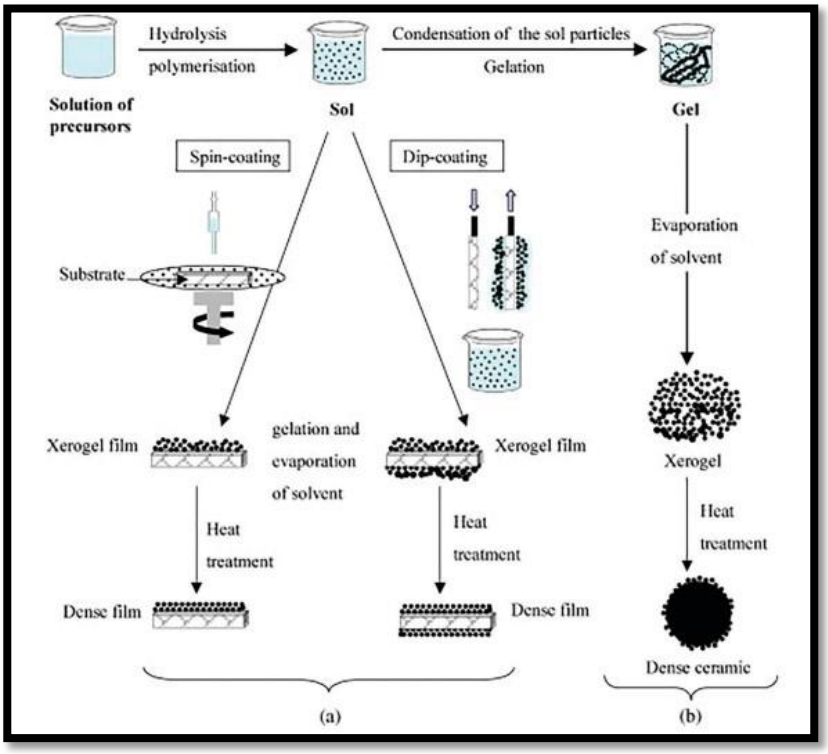

Fig. (1-10) An overview showing two sol–gel method synthesis examples: (a) Films from a colloidal sol and (b) Powder from a colloidal sol transformed into a gel [46]

1.2.2.4 Soft and hard templating methods

Production of nanoporous materials involves considerable use of both soft and hard template methods. A straightforward traditional technique for creating nanostructured materials is the soft template method. The discovery of materials with a variety of morphologies, easy implementation, and comparatively moderate testing conditions have all contributed to the perceived benefits of the soft template method[48]. Many soft templates, including anionic, cationic, and non-ionic surfactants, flexible organic molecules, and block copolymers, are used

in the soft templating approach to create nanoporous materials[49]. The three main ways that the soft templates and the precursors interact are through electrostatic, van der Waals, and hydrogen bonding interactions[50].Generally, two procedures known as cooperative self-assembly and "true" liquid-crystal templating are used for the soft templating approach of producing ordered mesoporous materials[49]. The quantities of surfactant and precursor, the ratio of surfactant to precursor, the structure of the surfactant, and the surrounding conditions are some of the variables that might impact the mesoporous material structures that are produced from 3D organized micelles[48].Another name for the hard template technique is nano-casting. To create nanostructures for the necessary applications, well-designed solid materials are utilized as templates. The solid template pores are then filled with precursor molecules Fig.(1-11)[50].The synthetic process for creating nanostructures using templating techniques consists of three key phases. The right original template is created or chosen in the first stage. The template mesopores are then filled with a specific precursor to turn them into an inorganic solid. To create the mesoporous replica, the original template is eliminated in the last phase[51]. A variety of unique structured nanomaterials, including nanowires, nanorods, 3D nanostructured materials, nanostructured metal oxides, and many more nanoparticles, can be produced by using mesoporous templates[52]. This brief discussion makes clear that both soft and hard template methods can be used to produce a wide range of unique structured nanomaterials.

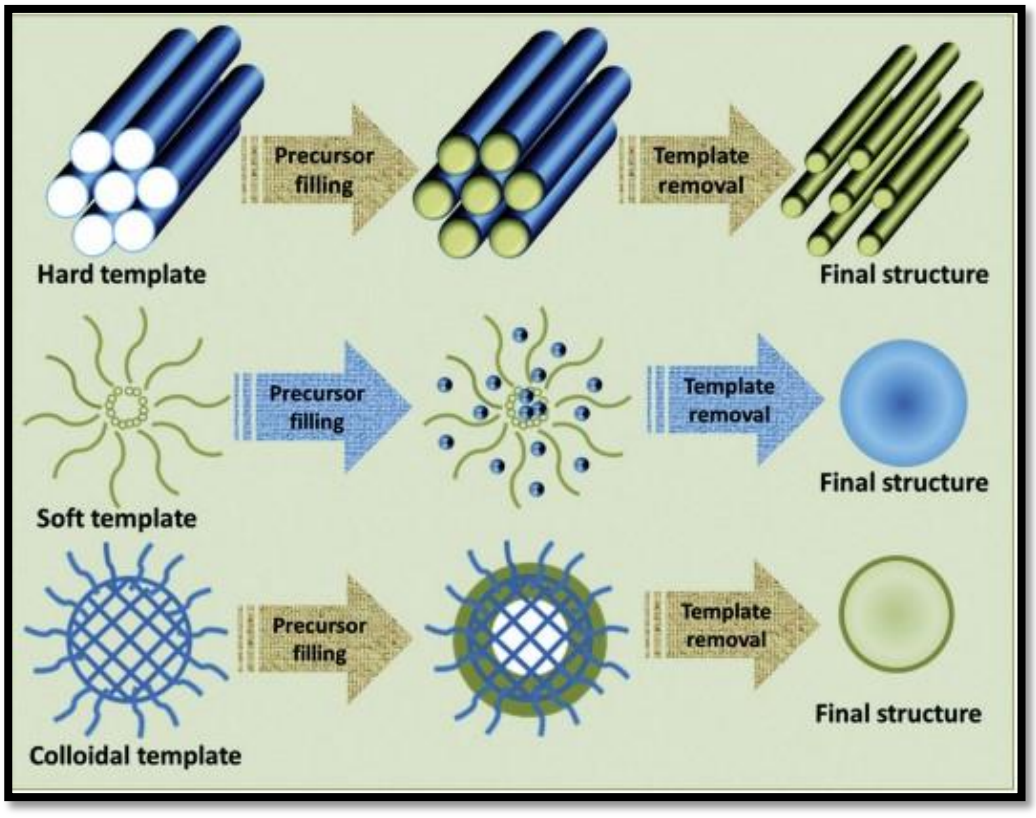

Fig. (1-11) A schematic representation of the synthesis of materials using different types of templates[50]

1.3 Pollution

The processes of transportation, manufacturing, construction, mining, petroleum refining, and urbanization are all part of the ongoing industrialization and urbanization that depletes natural resources and produces large amounts of hazardous wastes that pollute the air, water, and soil, endangering public health and environmental security. The produced wastes are discharged into the environment in a variety of ways. For instance, atmospheric pollutants can be made up of suspended airborne particles, volatile organic compounds (VOCs), and toxic gases such as nitrogen oxides, sulfur oxides, carbon oxides, and ozone. Meanwhile, soil and water pollutants can include microbial pathogens, heavy metals, organic materials (such as pesticides, insecticides, phenols, and hydrocarbons), and heavy metals (such as lead, cadmium, arsenic, and mercury). These contaminants in the environment have a significant potential to negatively impact human health [53].

1.3.1 Air pollution

One of the biggest issues facing the world today is air pollution, which is defined as the introduction of chemical, physical, or biological substances into the atmosphere through emissions from geogenic, anthropogenic, or biogenic sources, changing the atmosphere's natural composition. The ecosystem (plants and other living things) and human health are negatively impacted by poor air quality, as it may lead to a number of deadly diseases as cancer, respiratory disorders, and cardiovascular diseases[54].

1.3.2 Soil pollution

Hazardous substances in the natural soil environment are the source of soil pollution. The most common sources of contaminated soil are mining, manufacturing, landfill sites, especially those that accept industrial wastes (such as paint residues, batteries, electrical wastes, etc.), and municipal or industrial sludge. Heavy metals are common soil pollutants and can occur naturally in soil, though rarely at toxic levels. With the exception of mercury and selenium, which can be changed and volatile by microorganisms, heavy metals are thought to be among the more difficult soil pollutants because they are nondegradable and remain in the contaminated environment once they are present. Large-scale soil pollution can be handled either in situ, or on the spot, or ex situ, or removed and treated off-site. Nevertheless, conventional techniques of treating contaminated soil are prohibitively expensive and very challenging[55]. Therefore, the best strategy to safeguard the environment is to either stop heavy metal pollution from occurring or use immobilization techniques to stop the spread of heavy metals in soil [56].

1.3.3 Water pollution

Life depends on water, and while water covers over 70% of the Earth's surface, just 2.5% of that water is freshwater suitable for supporting terrestrial life[57]. Worldwide, water contamination is a major problem. This issue is caused by geological or anthropogenic (man-made) contamination [58]. Human activities such industrial, agricultural, commercial, residential, and waste disposal systems, as well as the usage of medications and personal care items, are the sources of anthropogenic pollutants[59]. Pollutants can be classified as either organic or inorganic.

1.4 Types of Pollutants

1.4.1 Inorganic Pollutants

The main sources of inorganic pollutants in water are both man-made and natural. The primary inorganic water contaminants are heavy metals, the phosphate and nitrate groups, and other elements including fluoride and chloride groups.[58].

1.4.2 Organic Pollutants

Organic compounds, whether man-made or naturally occurring, are present in almost every ecosystem and may be the main source of water contamination. Industrial developments are increasing the amount of synthetic organic chemicals, which raises the health risks associated with their presence in water [60]. Trihalomethanes (THMs) [61], volatile organic chemicals (VOCs) [58], pesticides, raw materials used in plastic manufacturing [62], medications, personal care products [63], and dyes were among the most prevalent organic pollutants. The dye is discussed in this thesis as a major pollutant.

1.4.2.1 Dyes

One of the many new compounds that might be applied to a wide range of industrial processes was the development of organic dyes. These dyes are widely used in industries and have become a crucial component of industrial effluent. In actuality, throughout the manufacturing and application procedures, almost 11% of the 450,000 tons of organic dyes generated each worldwide are lost in effluents [64]. Removing these dyes from industrial effluents poses a serious environmental risk because the majority of them are poisonous and may cause cancer[65]. While pigments remain in particle form and are insoluble, dyes are synthetic organic chemicals that dissolve in water or oil[66].

Complex unsaturated chemical compounds called dyes absorb light and give the visible region its color[67]. A number of techniques, including membranes, coagulation, adsorption, advanced oxidation process (AOP), and biodegradation,

have been proposed to address the removal of dyes from water[68],[69]. The chromophore, auxochrome, and matrix are the three fundamental groups that make up the molecules of dyes, which are actually organic compounds [70]. The dye's chromophore, or active site, is a summary of the spatial location of the atoms that absorb light energy[71].The most prevalent atom groups that make up the chromophore are nitro (─NO_2), azo(─N═N─), nitroso (─N═O), thiocarbonyl (─C═S), carbonyl (─C═O), and alkenes (─C═C─). The electrons in a molecule are excited, which causes the chromophore to absorb electromagnetic waves [70]. They cause the molecule containing them to turn chromogenic [72]. The only way to dye a chromogenic molecule is to add additional atom groups known as "auxochrome"[72]. These auxochromic groups can change the dye's color and enable the fixing of the dyes. They can be basic (NH_2, NHR, and NR_2) or acidic (COOH, SO_3, and OH). The third component of the dye, the matrix, is made up of the remaining atoms in the molecule [70]. Functional compounds included in textile dyes, such as carboxylic, amine, and azo groups, are difficult to handle using traditional techniques [73].

1.4.2.2 Methylene blue dye (MB)

A heterocyclic aromatic chemical molecule with a planar structure is methylene blue dye [74].Its molecular weight is 319.85 g/mol, and its chemical formula was $C_{16}H_{18}N_3S_l$ Fig. (1-12) [75]. The textile industry has extensively used MB dye, a common blue, cationic, thiazine dye, as a fiber coloring agent [76], [77], also as staining agents, as well as for preventative and therapeutic uses in the medical field [76],[78],[79].

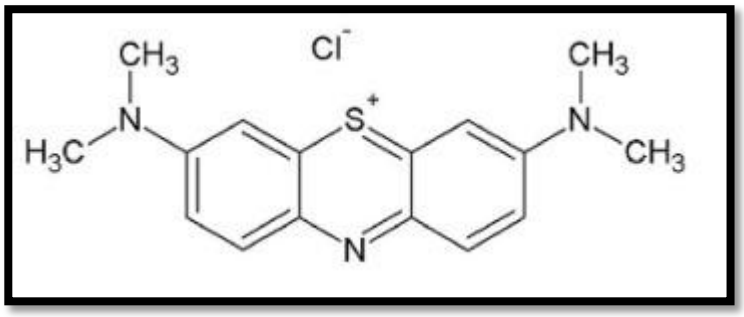

Fig. (1-12) Methylene blue molecular structure[75]

1.4.2.3 Applications of methylene blue dye

MB has a wide range of uses. Methylene blue was one of the first antimalarial medications to be synthesized and studied in medicine at the end of the 1800s [80].

Additionally, it was used with amodiaquine and found to be efficacious against falciparum malaria, particularly in adult and pediatric African patients[80], [81]. Additionally, methylene blue is widely used in medicine, where it is recommended for the treatment of individuals in both adult and pediatric stages who have been diagnosed with methemoglobinemia, a blood condition characterized by an abnormally high production of methemoglobin [82].

1.4.2.4 Toxicity of methylene blue dye

Even while MB was relevant in many different areas, its presence could seriously endanger both human health and the environment if it is not regulated in an environmentally responsible way [83]. It has been reported that this chemical molecule is teratogenic and embryotoxic. An exposure study of MB to rats and angelfish, respectively, verified the harmful effects [82]. A significant number of materials used in the manufacturing of textiles, paints, pharmaceuticals, cosmetics, and other items that use dyes, including MB, may be released into the environment as waste. According to a report, the textile industries account for roughly 67% of the dyestuff market and/or consumption [84].

1.5 Photocatalysis

Photocatalysis for water splitting is comprised of an intricate sequence of photophysical and electrocatalytic procedures[85].Mass transfer of the reactants and products, photon absorption, exciton separation, carrier diffusion, carrier transport, and catalytic efficiency are some of the components that make up photocatalytic reactions. Although carrier diffusion and carrier transport can occur simultaneously and coherently, they are separated here for ease of understanding[85].Photon absorption starts nonequilibrium photochemical and photophysical reactions. An electron-hole pairs, are produced on the femtosecond scale following photon absorption when an electron in the valence band (VB) is excited to the conduction band (CB) [86]. Following the exciton's defeat of the exciton binding energy determined by the electronic structure, the exciton is typically separated [87]. The electron and hole recombination needs to be prevented if a photocatalyzed reaction is desired.

The main goals of this process are to carry out a reaction between an oxidant and activated electrons to produce a reduced product, and a reaction between produced holes and a reductant to produce an oxidized product [88], [89].

1.5.1 Photodegradation of Methylene Blue

One essential method for removing the dye from industrial effluent is to oxidize MB to H_2O and CO_2 using a photocatalyst [90]. Photodegradation is an oxidation process where complex compounds break down chemically to become fragments with a reduced molecular weight that are straightforward, safe, and exposed to light [91]. This is a new and exciting technology for treating waste effluent that can break down dye molecules into simpler, non-toxic inorganic species like CO_2 and H_2O, thus decolorizing them [92]. The photocatalyst, a semiconductor substance that is activated by adsorbing photons and can speed up a reaction without being consumed, is used in this technique [93]. MB has the ability to absorb light in the 500–700 nm range, generate singlet and triplet species through intersystem crossing and electronic transition, and partially undergo self-decomposition [94]. Since the MB dye is photolyzed in the atmosphere, oxygen is necessary for the degradation to occur. $^{\bullet}OH$ radicals are created in basic media when MB^+ radicals are monoelectronically reduced by OH^-. $^{\bullet}OH$ combines with one another to form H_2O_2, a crucial active species in the processes of degradation. In a similar manner, excited MB^* radicals and O_2 combine to generate $O_2^{\bullet-}$. Equations (1-3), as follow:

$$\mathbf{MB^+ + OH^- \rightarrow MB^* + OH^{\bullet} \ldots\ldots\ldots\ldots\ (1\text{-}1)}$$

$$\mathbf{2OH^{\bullet} \rightarrow H_2O_2 \ldots\ldots\ldots\ldots\ldots\ldots\ (1\text{-}2)}$$

$$\mathbf{MB^* + O_2 \rightarrow MB^+ + O_2^{\bullet-} \ldots\ldots\ldots\ldots\ (1\text{-}3)}$$

All these reactive radical species take part in the direct photolysis of MB dye [95]. Photodegradation of MB dye in % can be calculated from the Equation:

$$\mathbf{Degradation\ rate\ (\%) = (C_0 - C/\ C_0) \times 100 \ldots\ldots\ldots\ldots\ (1\text{-}4)}$$

where, C_0 represents the initial concentration of dye, C stands for dye concentration after the reaction[96].

1.5.2 Factors Affecting Photodegradation of Methylene Blue

1.5.2.1 Effect of pH

The pH is one of the important factors for photocatalytic dye decolorization since it has a variety of effects on dye reaction rates. The adsorption of dye on the surface of semiconductors can be impacted by pH, as the catalyst surface charge is contingent upon the pH of the particular solution [97]. Being a cationic dye,

MB will adsorb on a photocatalyst that is extremely negatively charged [98]. The medium's pH could be adjusted to control the photodegradation of MB [99]. Because of the growing electrostatic attraction, the photocatalyst in a basic solution tends to pick up a negative charge, which increases the adsorption of positively charged dyes [100]. Lower pH (acidic fluids) cause less MB molecule adsorption on the photocatalyst surface because H^+, the dominating species, competes with the cationic MB dye. The reaction between the $^{\bullet}OH$ and MB is lessened because MB does not adsorb on the photocatalyst surface. Higher pH values prevent OH^- and MB from competing because OH^- will be repelled by the negatively charged surface of the photocatalyst and will persist in the mixture in significant amounts[101],[102].

1.5.2.2 Effect of MB dye concentration

A dye's rate of photodegradation is determined by its concentration, kind, and coexistence with other substances in the solution [103]. Because there were more active sites on the surface of the photocatalyst at lower concentrations, the MB dye has a higher adsorption capacity [104]. When the original dye concentration is increased to a certain point, the photodegradation rate of MB increases; beyond that point, it decreases [105]. The rise in the reaction probability between the dye molecules and the $^{\bullet}OH$ radical may be the cause of the initial increase in the MB dye degradation rate with increasing initial dye concentration [106].

1.5.2.3 Effect of irradiation time

The most important factors influencing photodegradation were the irradiation duration and the adsorption equilibrium between MB and a photocatalyst [107]. Degradation increases because the irradiation period has a direct relationship with the degree of MB degradation. when the irradiation time increases [108], [109]. As reaction times rise, the characteristic absorption peak of MB spectra eventually diminishes. It exhibits a color shift from blue to colorless, and the drop in absorption spectra is most likely due to the reduction of MB chromophore [110],[111] .After a certain amount of time, the photodegradation of MB becomes constant after first growing steadily with increasing irradiation time [96].

1.5.2.4 Effect of Different Photocatalysts

Impurities on the photocatalyst surface affect the adsorption behavior of the effluent as well as the lifetime and recombination rate of electron-hole pairs. Different photocatalysts photodegrade differently depending on variations in lattice mismatch and BET surface. Large surface area can play a significant role

in some photodegradation reactions. However, depending on the particle size, the electron-hole recombination mechanism can change [112].
To fully utilize the capabilities of photocatalysts, a great deal of work has been done to enhance their particular surface area [113].

1.5.2.5 Effect of Catalyst Weight

Numerous findings indicate that in photocatalytic degradation, the amount of catalyst is a crucial factor in the decomposition of organic compounds or dyes. The ideal loading must be determined for the effective removal of dye or organic component in order to prevent the usage of excess catalyst. Thus, in order to get the maximum photocatalytic activity, the amount of catalyst must be optimized[114]. In order to achieve complete absorption of sun photons and prevent needless surplus catalyst, the right catalyst must be supplied for effective photocatalytic degradation. Although intriguing, these results are predicated on the supposition that the catalyst particles were uniformly and equally lit, had the same size, and had the same optical characteristics[115].

1.6 Catalysts

1.6.1 Graphitic Carbon Nitride (g-C_3N_4)

With an appropriate bandgap energy of 2.7 eV and a graphene-like structure made up of nitrogen and carbon atoms bound by sp^2 bonds, g-C_3N_4 is a polymeric nanosheet with an abundance of amino groups on its surface [116]. Because of the sp^2 electronic band structure in g-C_3N_4, hybridization, it is regarded as a photon-harvesting semiconductor material that is essential for photoelectrochemical biosensors to detect biomolecules [117]. Graphitic carbon nitride (g-C_3N_4) has garnered significant interest due to its high absorption efficiency of visible light and its high activity. It comprises only the earth-abundant elements (carbon and nitrogen), great chemical and thermal stability due to the strong covalent link between carbon and nitrogen atoms in the conjugated layer structure. Moreover, its moderate bandgap energy of 2.7 eV (460 nm) allows it to capture visible light and has an ideal CB and VB edge position for both oxidation and reduction of water [118]. As a result, g-C_3N_4 quickly rises to prominence in the field of photocatalysis as a green photocatalyst. Furthermore, the fact that g-C_3N_4 may be produced using readily accessible, affordable precursors in a straightforward synthesis process accounts for its extensive use as a visible light-driven photocatalyst [119],[120]. A number of precursors have been suggested for the thermal condensation synthesis of g-C_3N_4. These substances, which include dicyandiamide, urea, cyanamide, and thiourea, are high in nitrogen and have a tri-s-triazine ring structure [121]. For example, if cyanamide is used as the precursor, thermal heating produces g-C_3N_4, melamine, melem, and dicyanamide, in that

order.Fig. (1-13) shows the g-C_3N_4 precursors' molecular structures and the matching temperatures at which their thermal condensation occurs[122].

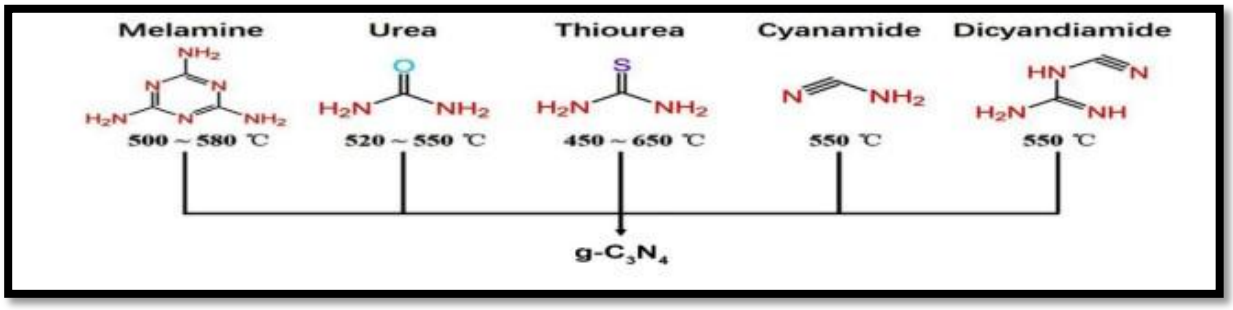

Fig. (1-13) Various g-C_3N_4 precursors and the corresponding temperatures for their thermal condensation into g-C_3N_4 [122]

Moreover, graphitic stacking of C_3N_4 layers, joined by tertiary amines Fig. (1-14) [123], gives g-C_3N_4 its distinct delocalized conjugated structure and strong electronic conductivity [124], [125].

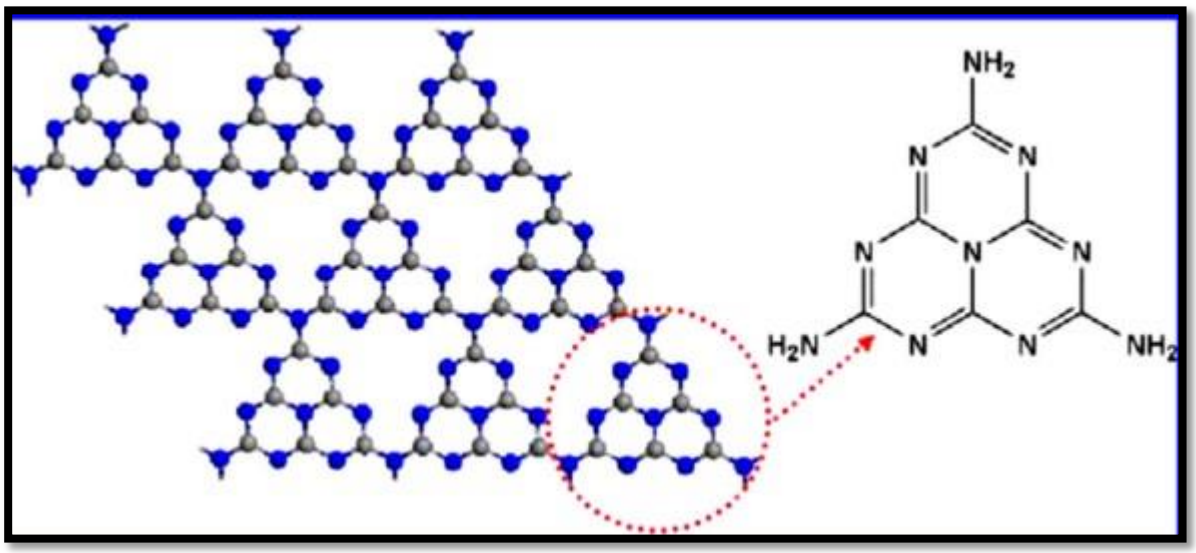

Fig. (1-14) Tri-s-triazine-based two-dimensional structure of g-C_3N_4. Color scheme: C, gray; N, blue [123]

1.6.2 Graphene Oxide (NGO) Nanosheets

Graphene, a two-dimensional material derived from three-dimensional graphite, has a large specific surface area and resembles a honeycomb structure composed of a connected carbon atom lattice with sp^2 hybridization[126]. The lattice structure of graphene is hexagonal and flat. Each carbon atom has four valence electrons, which are composed of three electrons (2s, $2p_x$, and $2p_y$) that form plane sp^2 hybrid orbitals. The orbital electron that is left behind creates a sizable π bond and is free to go throughout the plane. Because of their distinctive structural

and morphological characteristics, graphene and graphene oxide have superior electrical, mechanical, and thermal properties[127],[128]. NGOs can be created in a number of ways, such as the ways described by Brodie and Hummer[129]. As illustrated in Fig(1-15)., graphite can be oxidized to create pure NGO with plenty of hydroxyl (−OH), carbonyl (−CO), epoxy (−COC), and carboxyl (−COOH) groups[130]. Because of its unique characteristics, such as its high specific surface area, abundance of oxygen functional sites with both hydrophilic and hydrophobic groups, and strong thermal and chemical durability, graphene oxide has a high adsorption capacity[131]. Because of its adsorption qualities, graphene oxide can be utilized to clean up wastewater by eliminating one or more harmful substances. Additionally, because of its graphene skeleton and oxygen presence, NGO has appealing electrical, optical, and chemical properties. Metal ions can be bound by these oxygen groups [129].

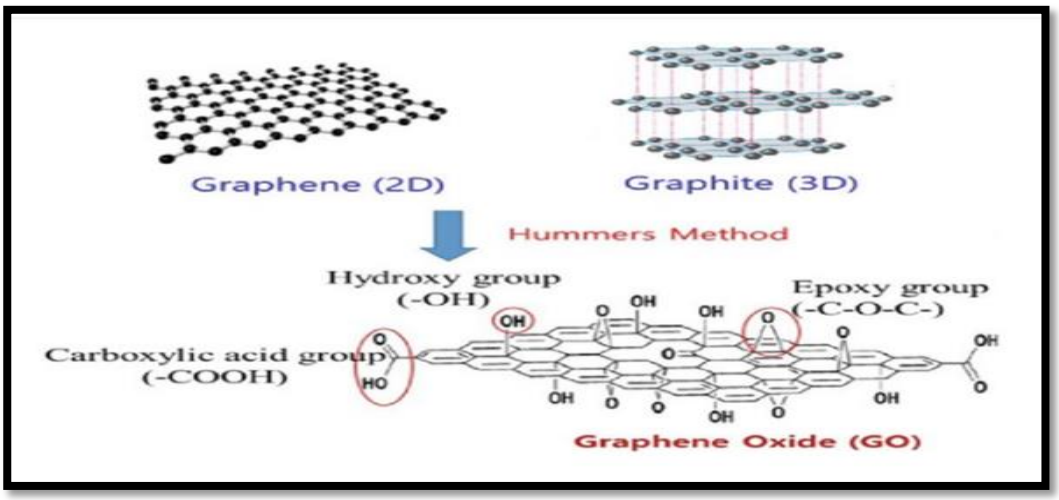

Fig. (1-15): Mechanism of Graphene Oxide Synthesis[130]

1.6.3 Bismuth Oxide (Bi_2O_3)

One of the heterogeneous components is bismuth oxide (Bi_2O_3), which has superior optical conductivity, a low band gap (2 to 3.96 eV), a high refractive index, non-toxic qualities, and significant photocatalytic activity [132],[133]. Bi_2O_3 is utilized in applications like water filtration, fuel cells, and gas detection because of these qualities [134]. α- (monoclinic), β- (tetragonal), γ- (body-centered cubic), δ- (face-centered cubic), and ε- (triclinic) are the five fuzzy shapes that Bi_2O_3 takes on [135]. The forms of Bi_2O_3 that have a metastable phase are α-Bi_2O_3, which is known to be the constant phase at low temperatures, and δ-Bi_2O_3, which is the stable phase at high temperatures (729 ◦C). It has been observed lately that β-Bi_2O_3, a metastable phase, exhibits superior photocatalytic activity in comparison to α-Bi_2O_3. Because β-Bi_2O_3 has the lowest band gap (2.4 eV) and performs best photocatalytically when exposed to visible light radiation, it has the largest absorption in the visible light area. β-Bi_2O_3 can serve as an electron donor in photocatalytic processes since it is an intrinsic p-type semiconductor with high mobility[136].

1.6.4 Nanocomposites

Nanocomposites are multiphase solids in which one of the phases has dimensions of less than 100 nm, or all three have dimensions of less than 100 nm [137],[138]. Polymer matrix nanocomposites, polymer-layered silicate nanocomposite, ceramic-polymer nanocomposites, inorganic–organic polymer nanocomposites, and inorganic–organic hybrid polymer nanocomposites are the further classifications for it[139]. Materials known as polymer matrix nanocomposites require the dispersion of inorganic nanoparticles with one dimension within the 10-100A^o range. When compared to ordinary polymer composites or pure polymers, these composites significantly improve the mechanical and physical properties [139].

1.6.4.1 g-C_3N_4-Bi_2O_3 Binary Nanocomposites

When it comes to the creation of the composite, g-C_3N_4 and bismuth oxide (Bi_2O_3) pair well because of their similar band gap edges. It is commonly recognized that matched-band gap energy may offer a practical path for charge carriers produced by photosynthesis. [140], [141]. By suppressing charge carrier recombination and promoting broader visible light absorption, the synthesis of

Bi_2O_3-g-C_3N_4 composite may produce heterojunction and increase the photocatalytic activity of g-C_3N_4 [142],[141],[143]. Band bending and the creation of an internal electric field are caused by the heterojunction (g-C_3N_4-Bi_2O_3) that is thus created. This heterojunction reduces the recombination of the photogenerated electrons and holes in addition to tuning dimensionality. When compared to other semiconductor materials, the composite's capacity to trap light is improved by the band gap's narrowing [144]. Bi_2O_3 and g-C_3N_4 also satisfy the requirements of an effective catalyst, which include being readily available, inexpensive, non-toxic, and having a simple synthesis process. [145],[146].

1.6.4.2 Ternary Nanocomposites

In an effort to improve the performance of nanomaterials, researchers have developed this binary nano-system into a new ternary nanostructure system (noble metal/metal/semiconductors or noble metal/semiconductors/semiconductors). The resulting new ternary nanostructures effectively show high efficiency with newly generated properties in comparison to the binary [147],[148]. Though the created nanostructures are important, not enough research has been done in this field; only a few varieties of ternary noble metal/semiconductors nanostructures have been examined for example (Au/CdS/TiO_2), (Pt/TiO_2/CdS), (Ag/TiO2/ZnO). In this research, ternary Nano composites were prepared by Graphitic Carbon Nitride (g-C_3N_4), Bismuth oxide (Bi_2O_3) and Graphene Oxide (NGO) Nano-Sheets(g-C_3N_4-Bi_2O_3-NGO).

1.7 Membrane Filtration

Compared to other water treatment technologies, membrane filtration has received greater attention. In many areas of wastewater treatment, membrane technique is thought to be a cost-effective and efficient method; nevertheless, the selectivity and permeability of the membrane materials greatly influence the membrane's ability to function. High energy consumption from membrane fouling and other issues prevented this approach from being widely adopted. The method is prone to clogging and has a high initial cost. Another drawback of this procedure is the need for frequent membrane replacement. This approach works well if the wastewater has a low dye concentration. It is possible for membrane filtration to function in conjunction with additional effluent treatments. This technique is not limited to the presence of organic contaminants and microbes in wastewater; it can also be applied to salts membrane filtering, which is utilized, among other things, for latex recovery, color removal, BOD reduction, and salt reduction. Although the process is temperature-resistant, microorganisms can negatively affect the membrane filtration. The remainder. Reverse osmosis (RO), Nano-filtering (NF), Ultra-Filtration (UF), and Micro-Filtration (MF) are the common membrane filtering types. The necessary quality of the final effluent influences the membrane process selection [149]. Numerous investigations have revealed that adding carbonaceous nanoparticles to membranes can enhance their selectivity, permeability, and fouling resistance. The applications of microporous membranes in water purification are limited since they are only effective in filtering particles with a size of 1–10 μm. Their pore size ranges from 0.1 to 5 μm. In the meantime, nanoporous membranes performed exceptionally well in the filtration of water. They are capable of filtering out of wastewater the majority of contaminants (1–10 nm), including salts, organic compounds, metallic ions, and microorganisms[150],[151]. Many types of inorganics, organic, and inorganic-organic hybrid materials have been used to construct high performance nano-porous membranes for water filtration. One example is the desalination of water using single-layer nanoporous graphene [152].

1.7.1 Types of Nano-Porous Membranes

Based on their material composition, nanoporous membranes for water purification can be broadly classified into three types: inorganic, organic, and inorganic-organic hybrid membranes. Ceramics are the primary material used to make inorganic membranes (Al_2O_3, TiO_2, ZrO_2, SiO_2, TiO_2-SiO_2, TiO_2-ZrO, Al_2O_3-SiC)) [153], graphene [154], and carbon nanotubes (CNTs) [155].

Polymeric materials, including polyvinyl alcohol (PVA), polyimide, polypropylene, polyethersulfone (PES), cellulose acetate, cellulose nitrates, polysulfone (PSU), polyvinylidene fluoride (PVDF), polyacrylonitrile, polytetrafluoroethylene (PTFE), and biomacromolecules, are the primary constituents of organic membranes [156]. Typically, inorganic elements (metals, metal oxides, or carbon-based compounds) are incorporated into a polymeric matrix system to create inorganic-organic hybrid membranes [157].

1.8 The Aims of This Study

1. Enhance the photocatalytic degradation properties of Bi_2O_3 by synthesis the binary composites; (20% g-C_3N_4-Bi_2O_3, 40% g-C_3N_4-Bi_2O_3, 60% g-C_3N_4-Bi_2O_3 and 80% g-C_3N_4-Bi_2O_3) and novel ternary composites BiC_{80}/GO (10 mg), BiC_{80}/GO (20 mg), BiC_{80}/GO (30 mg) and BiC_{80}/GO (40 mg), used high temperature calcination method.
2. Synthesis membranes; g-C_3N_4, Bi_2O_3, NGO, binary composites (20% g-C_3N_4-Bi_2O_3, 40% g-C_3N_4-Bi_2O_3, 60% g-C_3N_4-Bi_2O_3,80% g-C_3N_4-Bi_2O_3) and novel ternary composites BiC_{80}/GO (10 mg), BiC_{80}/GO (20 mg), BiC_{80}/GO (30 mg) and BiC_{80}/GO (40 mg), by vacuum filtration method in order to separate water pollutants.

Chapter Two

EXPERIMENTAL

2.1 Instruments and Chemicals

The instruments used in the present study and their models, companies and origin are listed in Table (2-1), the chemicals listed in Table (2-2).

Table (2-1): Instruments used in study, models, companies and origin

Ser.	Device	Company	Origin	Laboratory
1	UV-Vis. Spectrophotometer, UV-1800	Shimadzu	Japan	University of Misan /College of Science/ Chemistry Dept.
2	RF5301pc Spectrofluorophotometer	Shimadzu	Japan	University of Misan / College of Science/ Chemistry Dept.
3	FT-IR Spectrophotometer, FT-IR-1800	Shimadzu	Japan	BPC Analysis Center Adhamiya/ Baghdad
4	X-Ray Diffraction (XRD), PW1730	Philips	Holland	Tehran / Iran
5	Thermogravimetric (TG) SDT Q600 V20.9 Build 20	TA Instruments	USA	BPC Analysis Center Adhamiya/ Baghdad
6	Muffle Furnace	LAC	Czech Republic	University of Misan / College of Science/ Chemistry Dept.
7	Probe Ultrasonicator, FSFJY92-IIN	Sino Sonics	China	University of Misan / College of Science/ Biology Dept.
8	Field Emission Scanning Electronic Microscope (FESEM), 5 KV	Zeiss	Germany	Tehran University/ Advanced Materials Characterization Institute
9	Ultrasonic Bath Sonicator, WHC-A10H	Daihan Scientific	China	University of Misan / College of Science/ Chemistry Dept.
10	Vacuum Pump	Value	China	University of Misan / College of Science/ Chemistry Dept.
11	pH-meter, pH 7110	Inolab	Germany	University of Misan / College of Science/ Chemistry Dept.
12	Stirring water bath, KBLEE 2010	Daiki	Japan	University of Misan / College of Science/ Chemistry Dept.

Table (2-2): Chemicals used, chemical formula, company and origin

Ser.	Chemicals	Chemical Formula	Company	Origin	Purity
1	Urea	$CO(NH_2)_2$	Romil	UK	99%
2	Bismuth (III) nitrate pentahydrate	$BiN_3O_9.5H_2O$	Sigma-Aldrich	USA	98%
3	Graphite	C	CDH	India	99.5%
4	Sodium nitrate	$NaNO_3$	Thomas Baker	India	98%
5	Hydrogen peroxide	H_2O_2	Panreac applab	Spain	50%
6	Sulphuric acid	H_2SO_4	Chem Lab	UK	97%
7	Potassium permanganate	$KMnO_4$	GCC	UK	99%
8	Cellulose nitrate membrane filters	$(C_6H_{11}N_2O_{10})_n$	Fiscger	India	
9	Methylene Blue	$C_{16}H_{18}ClN_3S.xH_2O(x=2,3)$	Thomas Baker	India	99%
10	Dimethyl Formamide (DMF)	$HCON(CH_3)_2$	Thomas Baker	India	99.5%
11	Sodium hydroxide	NaOH	Chem Lab	UK	98%
12	Hydrochloric acid	HCl	Applichem	USA	97%

2.2 Synthesis of Graphitic Carbon Nitride g-C_3N_4

Place 10 g of urea powder into a covered ceramic crucible, close the cover, place the crucible in a muffle furnace set to 550 °C for four hours with a heating rate 15 °C per minute. The resulting yellowish powder was collected and used right away without any additional care. After the finished product had reached room temperature, they were pounded coarsely in a mortar and pestle Fig. (2-1)[158],[159].

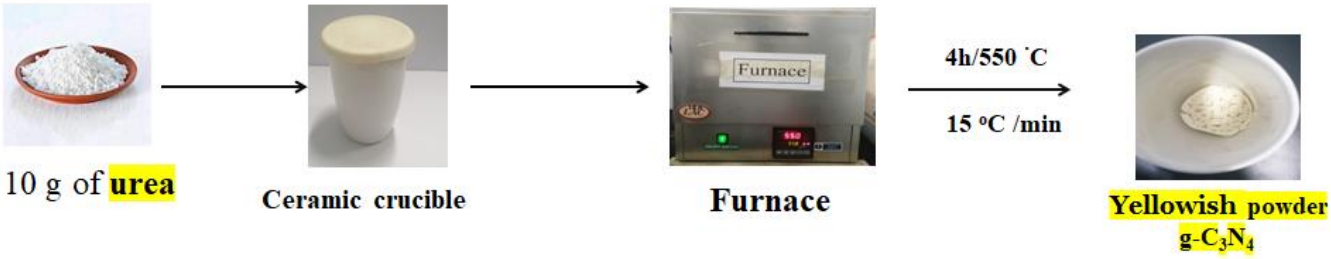

Fig. (2-1): The flow chart of the synthesis nano Graphitic Carbon Nitride

2.3 Synthesis of Nano Bismuth Oxide (Bi_2O_3)

Nano Bi_2O_3 crystals were synthesis by a solid-state decomposition reaction, 5 g of Bi $(NO_3)_3.5H_2O$ heated to 500 ^oC for 4 hrs. at heating rate of 10 ^oC /min. the produce was washed with 50 ml of distilled water (five times 10 ml each) and dried in oven at 80 ^oC for 6 hrs.[160].

2.4 Synthesis of Nano Graphene Oxide (NGO)

Nano graphene oxide synthesized by modified Hummer's method[129],[161]. Added 0.60 g graphite and 0.50 g sodium nitrate, dissolved in 23 mL cooled (0º C) concentrated sulphuric acid in beaker onto ice bath, stirring for 15 min. Added gradually 3.0 g potassium permanganate to the suspension (black color), continuous stirring to keep the reaction temperature below 20 ºC onto ice bath for 30 min. The reaction beaker placed in stirring water bath at 35 ºC for 2 hrs. (the suspension changed to dark brown). Added 50 ml deionized water gradually (by dropper) into the suspension over a hot plate with a magnetic stirrer, the temperature kept below 98 ºC, for 15 min, added 100 mL of warm deionized water, added 10 mL of hydrogen peroxide 30% gradually (by dropper) for 15 min. The suspension separated by centrifuge (4000 rpm for 5 min), the precipitate washed with warm hydrochloric acid (5% v/v) to remove sulphate ions (test by $BaCl_2$), the precipitate washed with deionized water until the pH of washing solution became 7.0.

The product (graphene oxide) dried in oven at 60 ºC for 1 hr. Added 0.5 g of Graphene oxide to 50 mL of N, N-di methyl formamide and sonicated by Probe ultrasonicator for 30 min, the suspension separated by centrifuge (4000 rpm for

10 min) the separated residue dried in oven at 60 ºC for 1 hr. as shown in Fig. (2-2).

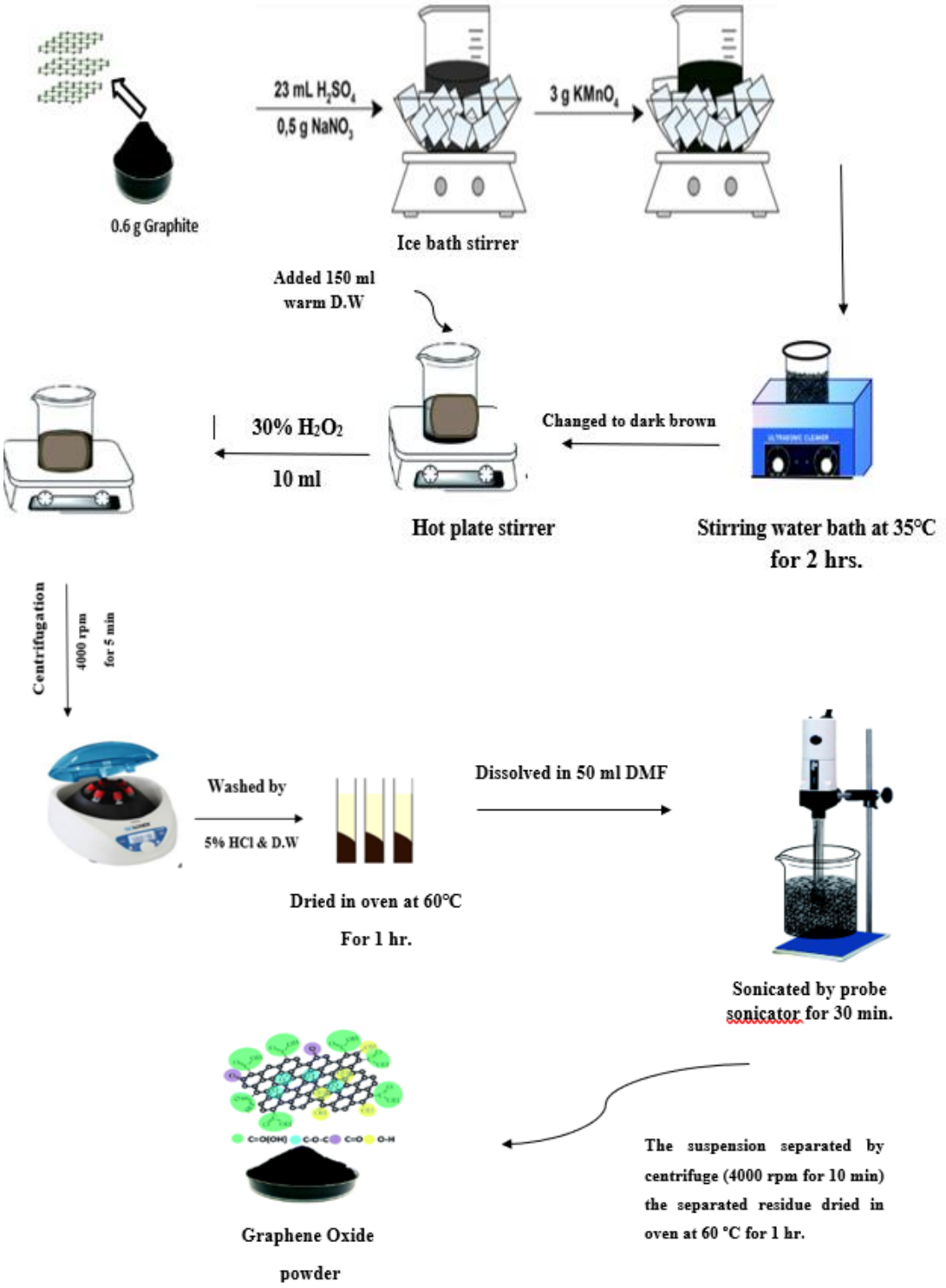

Fig. (2-2): The flow chart of the synthesis nano graphene oxide

2.5 Synthesis of binary nanocomposites g-C_3N_4/Bi_2O_3

The g-C_3N_4/Bi_2O_3 was prepared by different ratios (20% g-C_3N_4/Bi_2O_3, 40% g-C_3N_4/Bi_2O_3, 60% g-C_3N_4/Bi_2O_3 and 80% g-C_3N_4/Bi_2O_3). To prepare 20% g-C_3N_4/Bi_2O_3, 0.02 g of g-C_3N_4 with 0.08 g of Bi_2O_3 grind them well together using ceramic mortar and pestle, the resultant mixed powder was put in to a ceramic crucible with a cover and heated to 400 ^oC in a muffle furnace for 4 hrs. with heating rate 20 ^oC/min .The same process was followed to prepare 40% g-C_3N_4/Bi_2O_3(0.04g. g-C_3N_4+0.06Bi_2O_3), 60% g-C_3N_4/Bi_2O_3(0.06 g, g-C_3N_4+0.04g Bi_2O_3), 80% g-C_3N_4/Bi_2O_3 (0.08 g g-C_3N_4+0.02 g Bi_2O_3)[160].

2.6 Synthesis ternary nanocomposites BiC_{80}/GO (x mg)

Ternary Nano composites BiC_{80}/GO(x) were prepared by varying amount of GO(x=10,20,30 and 40 mg) as follows, the synthesis process (80% g-C_3N_4-Bi_2O_3)was added 0.08 g of g-C_3N_4 with 0.02 g of Bi_2O_3 subsequently with different amount of GO (10,20.30 and 40 mg)was added each time, grind them well together using mortar and pestle then the resultant mixed powder was put into a crucible with a cover, heated at 400 ^oC in a muffle furnace for 4 hrs. with heating rate of 20 ^oC/min.

The ternary nano composites are named as BiC_{80}/GO (10 mg), BiC_{80}/GO (20 mg), BiC_{80}/GO (30 mg) and BiC_{80}/GO (40 mg) respectively for 10, 20, 30 and 40 mg of GO added in the synthesis process.

2.7 Sample Preparation

2.7.1 Stock solution of methylene blue (1000 mg.L^{-1})

A stock solution of methylene blue (MB) (M. Wt. = 319.86 g/mol.) was prepared by dissolving 100 mg of the MB dye in deionized water into beaker, transferred quantitatively to volumetric flask (100 ml), filled up to the mark with deionized water. The working standard solutions were prepared by serial dilution of stock solution.

2.8 Photocatalytic Degradation of the MB dye

2.8.1 Photocatalytic Degradation of the MB dye by Nano g-C_3N_4, Bi_2O_3, binary nano composites g-C_3N_4/Bi_2O_3, ternary nanocomposites BiC_{80}/GO (x mg)

MB dye solution (10 mg.L^{-1}) was prepared in a volumetric flask (50 ml), the absorbance measured by using UV-Vis spectrophotometer at λ_{max}(664.50 nm) MB dye solution poured into a beaker (250 ml), put on a hotplate with a magnetic stirrer (700 rpm) , added 50mg of the catalyst g-C_3N_4, kept on the hot plate with a magnetic stirrer for 30 min. in the dark, withdrew 4ml of the solution by a syringe, the catalyst was separated by centrifuge (5000 rpm for 5 min. twice) then absorbance measured at λ_{max} (664.50 nm), kept the solution on the hot plate with a magnetic stirrer for 180 min. under the light (Tungsten lamp 300 watt), the absorbance measured at λ_{max}(664.50 nm), at intervals time (30,60,90,120,150 and 180 min.) respectively, withdrew 4ml of the solution by a syringe, the catalyst was separated by centrifuge (5000 rpm for 5 min twice) nm each time . The same procedure was followed for each Bi_2O_3 , binary nano composites (20% g-C_3N_4/Bi_2O_3, 40% g-C_3N_4/Bi_2O_3, 60% g-C_3N_4/Bi_2O_3 and 80% g-C_3N_4/Bi_2O_3)and ternary nanocomposites BiC_{80}/GO (10 mg), BiC_{80}/GO (20 mg), BiC_{80}/GO (30 mg) and BiC_{80}/GO (40 mg)as shown in Fig.(2-3)[162].

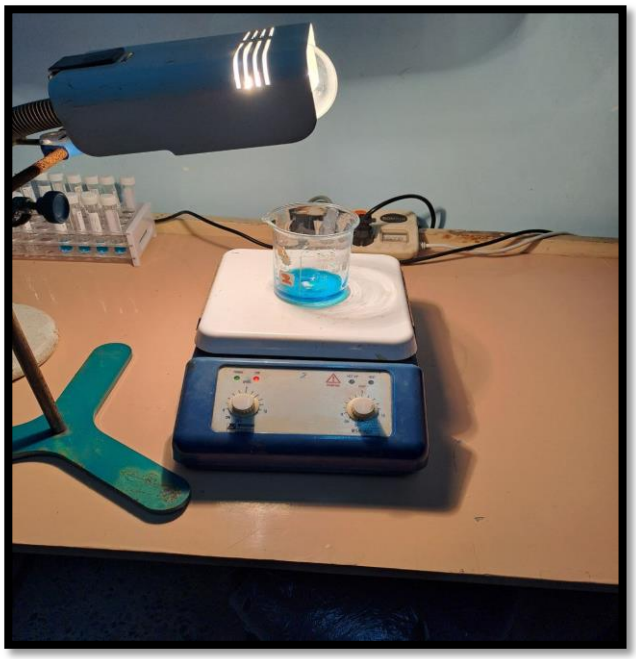

Fig. (2-3) Hotplate with magnetic stirrer under Tungsten lamp- 300 watt

2.8.2 Photocatalytic degradation of MB dye by NGO

MB dye solution (100 mg.L^{-1}) in a volumetric flask (50 ml) was prepared, the absorbance measured by using UV-Vis spectrophotometer at λ_{max} (664.50 nm). MB dye solution poured into beaker (250 ml) on a hot plate with a magnetic stirrer (700 rpm), added 50mg of NGO catalyst, left for 30 min. in the dark, withdrew 4ml of the solution by syringe, the catalyst was separated by centrifuge (5000 rpm for 5 min twice), absorbance measured at λ_{max} (664.50 nm) switched on the (Tungsten lamp-300 watt) for 180 min. the absorbance measured at λ_{max}(664.50 nm) intervals time (30,60,90,120,150 and 180 min.) each time respectively, withdrew 4ml of the solution by a syringe, the catalyst was separated by centrifuge (5000 rpm for 5 min. twice) each time[162] .

2.9 Optimum conditions for the photocatalytic degradation of MB dye by binary nanocomposite 80%g-C_3N_4/Bi_2O_3 and ternary nanocomposite BiC_{80}/GO (20 mg)

2.9.1 Effect of catalyst weight

MB dye solution (10 mg.L^{-1}) in a volumetric flask (50 ml) was prepared ,the absorbance measured at λ_{max}(664.50 nm), poured into a beaker (250 ml) put on a hot plate with a magnetic (700 rpm) , added (40,50 and 60 mg) of the catalyst 80% g-C_3N_4/Bi_2O_3 respectively to each solution, left for 30 min. in the dark withdrew 4ml of the solution by a syringe, the catalyst was separated by centrifuge (5000 rpm for 5 min twice), absorbance measured at λ_{max}(664.50 nm) , switched on the (Tungsten lamp 300 watt) for 180 min. the absorbance measured at λ_{max}(664.50 nm), at intervals time (30,60,90,120,150 and 180 min) for each solution respectively, withdrew 4ml of the solution by a syringe, the catalyst was separated by centrifuge (5000 rpm for 5 min twice) each time The same procedure was followed for BiC_{80}/GO(20 mg) ternary nanocomposite [162].

2.9.2 Effect of MB dye concentration

The effect of concentration of MB dye on the Photo catalytic degradation of the 80%g-C_3N_4-Bi_2O_3 binary nano composites was studied by preparing series concentration of the MB dye (5 mg.L^{-1},10 mg.L^{-1} and15 mg.L^{-1}) in each a volumetric flask (50 ml) ,the absorbance measured at λ_{max}(664.50 nm), poured

the MB dye solution into beakers (250 ml), put on a hot plate with a magnetic stirrer (700 rpm) , added 50mg of the catalyst 80%g-C_3N_4-Bi_2O_3, left for 30 min in the dark, withdrew 4ml of the solution by a syringe, the catalyst was separated by centrifuge (5000 rpm for 5 min twice), absorbance measured at λ_{max}(664.50 nm), switched on the (Tungsten lamp-300 watt) for 180 min, the absorbance measured λ_{max}(664.50 nm) at intervals time (30,60,90,120,150 and 180 min.) respectively, withdrew 4ml of the solution by a syringe, the catalyst was separated by centrifuge (5000 rpm for 5 min twice) each time. The same procedure was followed for BiC_{80}/GO(20 mg) ternary nanocomposite [162].

2.9.3 Effect of temperature

The effect of temperature on the photo catalytic degradation process was studied,50 ml aqueous solution of MB dye (10 $mg.L^{-1}$) in a volumetric flask was prepared , poured the MB dye solution into beaker (250 ml), put on a hot plate with magnetic stirrer, thermometer used to measure the temperature at (25 ˚C,35 ˚Cand 40 ˚C) (700 rpm) , added 50mg of the catalyst 80%g-C_3N_4-Bi_2O_3 left for 30 min. in the dark , withdrew 4ml of the solution by a syringe, the catalyst was separated by centrifuge (5000 rpm for 5 min twice), absorbance measured at λ_{max}(664.50 nm). Switched on the (Tungsten lamp-300 watt) for 180 min. the absorbance measured at λ_{max}(664.50 nm) for intervals time (30,60,90,120,150 and 180 min.) respectively, withdrew 4ml of the solution, by a syringe, separated the catalyst by centrifuge (5000 rpm for 5 min twice) each time. The same procedure was followed for BiC_{80}/GO(20 mg) ternary nanocomposite [162].

2.9.4 Effect of pH

Beaker contains 50 ml 0f MB dye (10 $mg.L^{-1}$), the pH of solution was set by using (0.1M HCl) and (0.1M NaOH) at pH values (2,4,6,8,10,12 and 14) by using pH-meter. The absorbance measured at λ_{max} (664.50 nm) then poured the MB dye solution into beaker (250 ml) put on a hot plate with a magnetic stirrer (700 rpm), added 50mg of the catalyst 80%g-C_3N_4-Bi_2O_3 to the solution for 30 min. in the dark, withdrew 4ml of the solution by a syringe, the catalyst was separated by centrifuge (5000 rpm for 5 min twice), the absorbance measured at λ_{max}(664.50 nm), switched on the (Tungsten lamp-300 watt) for 180 min. measured the absorbance at λ_{max}(664.50 nm) at intervals time (30,60,90,120,150 and 180 min) respectively withdrew 4ml of the solution by a syringe each time, the catalyst was separated by centrifuge (5000 rpm for 5 min twice). The same procedure was followed for BiC_{80}/GO(20 mg) ternary nanocomposite [162].

2.10 Membrane synthesis method

2.10.1 g-C_3N_4 , Bi_2O_3 ,NGO g-C_3N_4/Bi_2O_3 and BiC_{80}/GO (x mg) Membranes

The solution of g-C_3N_4 (100 mg.L^{-1}) was prepared by adding 5 mg of g-C_3N_4 powder to 50 ml deionized water, sonicated by bath sonicator for 2 min. at 32 ℃ for dispersion, poured on a cellulose nitrate substrate membrane into a filtering cup, switched on the vacuum pump (-15 psi), g-C_3N_4 membrane formed on the cellulose nitrate substrate membrane. (pores 0.22 µm), The same procedure was followed for each Bi_2O_3 ,NGO**,** binary nano composites (20% g-C_3N_4/Bi_2O_3, 40% g-C_3N_4/Bi_2O_3, 60% g-C_3N_4/Bi_2O_3 and 80% g-C_3N_4/Bi_2O_3)and ternary nanocomposites BiC_{80}/GO (10 mg), BiC_{80}/GO (20 mg), BiC_{80}/GO (30 mg) and BiC_{80}/GO (40 mg) as shown in Fig. (2-4) [163].

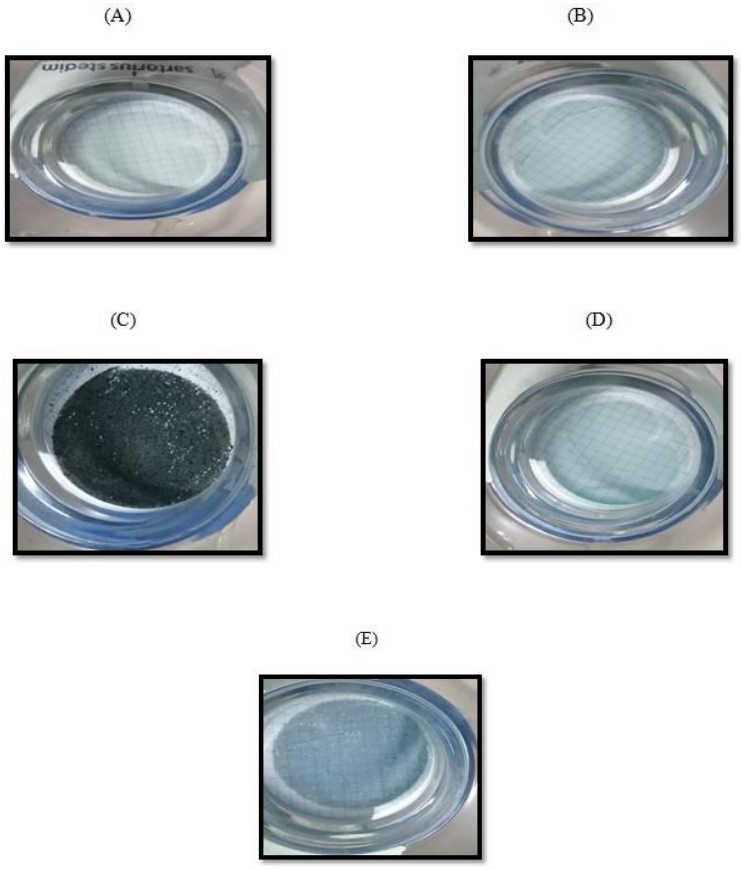

Fig. (2-4): (A) g-C_3N_4 membrane (B) Bi_2O_3 membrane, (C) NGO membrane, (D) g-C_3N_4/Bi_2O_3 membrane, (E) BiC_{80}/GO(x) membrane on substrate (cellulose nitrate)

2.11Applications of Membranes

2.12.1 Separation of MB dye by g-C_3N_4, NGO, Bi_2O_3, g-C_3N_4/Bi_2O_3 and BiC_{80}/GO (x mg) membranes

Standard solution 100 ml of MB dye 10 mg.L^{-1} was prepared, the absorbance measured at λ_{max} (664.50 nm). Poured 10 ml of MB dye solution on each membrane (g-C_3N_4, NGO, Bi_2O_3, g-C_3N_4/Bi_2O_3, BiC_{80}/GO(x mg)) respectively, filtered by using the vacuum filtration, the absorbance of the filtered solution measured at the same wavelength [163].

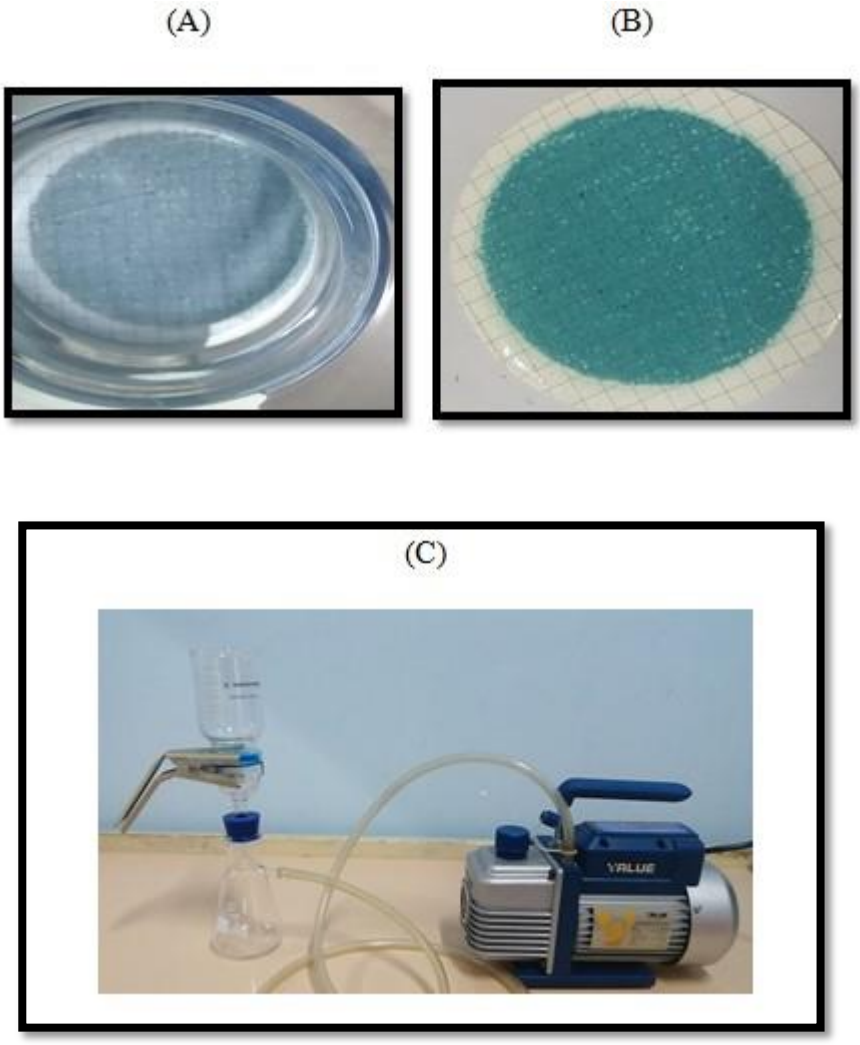

Fig. (2-5) BiC_{80}/GO(x) membrane (A) Before, (B) After separation of MB dye (C) Vacuum filtration pump

Chapter Three

Results and Discussion

3.1. Spectral characterization of g-C_3N_4, Bi_2O_3, NGO, and g-C_3N_4-Bi_2O_3, BiC_{80} -GO (X mg) composites

3.1.1 X-Ray Diffraction Spectroscopy (XRD)

The XRD spectrum measured in a range (5°-60°) of 2θ at 0.154 nm (copper source). The XRD analysis spectrum of the synthesized g-C_3N_4 gave excellent diffraction peaks at 2θ values of 13.9122°, 27.9907° respectively, which can be ascribed to the corresponding planes (hkl) (100), (002) respectively which match well with JCPDF No. 50- 1250[164]. The XRD analysis spectrum of Bi_2O_3 gave excellent diffraction peaks at 2θ values of 26.1695° , 27.8227° , 33.5340° and 46.7237° respectively, which can be ascribed to the corresponding planes (hkl)(111) ,(120) ,(200) and (041) respectively which match well with JCPDS No. 41-1449[165].The XRD analysis spectrum of the synthesized NGO gave excellent diffraction peaks at 2θ value of 11.1297° , which can be ascribed to the corresponding planes (hkl) (002) [166] as show in Fig. (3-1).

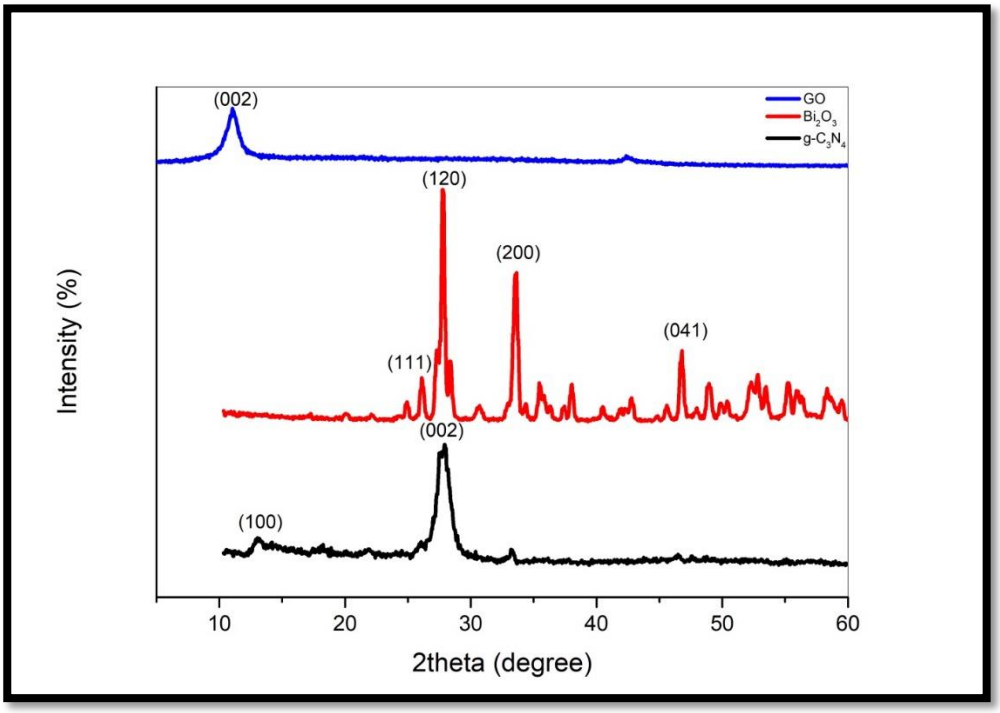

Fig. (3-1) XRD patterns of g-C_3N_4, Bi_2O_3 and NGO

The XRD analysis spectrum of the synthesized (20%)g-C_3N_4 - Bi_2O_3 binary nano composite gave excellent diffraction peaks at 2θ values of (2θ=25.9262°) low intensity with interlayer spacing of (d=3.4338 A°) , (2θ=27.6620°) high intensity corresponding to interlayer spacing of (d=3.23022 A°), (2θ=33.4385°) medium intensity corresponding to interlayer spacing of (d=2.6842 A°) and (2θ=46.5562°) low intensity with interlayer spacing of (d=1.9491 A°) as shown in Fig. (3-2).

The XRD analysis spectrum of the synthesized (40%)g-C_3N_4 - Bi_2O_3 binary nano composite gave excellent diffraction peaks at 2θ values of (2θ= 25.9830°) low intensity with interlayer spacing of (d= 3.4265 A°) , (2θ= 27.6398°) high intensity corresponding to interlayer spacing of (d= 3.2247 A°), (2θ= 33.4856°) medium intensity corresponding to interlayer spacing of (d= 2.6805 A°) and (2θ= 46.5855°) low intensity with interlayer spacing of (d= 1.9480 A°) as shown in Fig. (3-2).

The XRD analysis spectrum of (60%)g-C_3N_4 - Bi_2O_3 binary nano composites gave excellent diffraction peaks at 2θ values of (2θ= 25.9907°) low intensity with interlayer spacing of (d= 3.4340 A°) , (2θ= 27.5718°) high intensity corresponding to interlayer spacing of (d= 3.23255 A°), (2θ= 33.4077 °) medium intensity corresponding to interlayer spacing of (d= 2.6866 A°) and (2θ= 46.5265°) low intensity with interlayer spacing of (d= 1.9503 A°) as shown in Fig. (3-2).

The XRD analysis spectrum of (80%)g-C_3N_4 - Bi_2O_3 binary nano composites gave excellent diffraction peaks at 2θ values of (2θ= 25.9758°) low intensity with interlayer spacing of (d= 3.4359 A°) , (2θ= 27.5699°) high intensity corresponding to interlayer spacing of (d= 3.2327 A°), (2θ= 33.3800 °) medium intensity corresponding to interlayer spacing of (d= 2.6821 A°) and (2θ= 46.6257°) low intensity with interlayer spacing of (d= 1.9512 A°) as shown in Fig. (3-2).

The XRD analysis spectrum of the synthesized BiC_{80}/GO(10 mg) ternary nano composite gave excellent diffraction peaks at 2θ values of (2θ= 25.9585°) low intensity with interlayer spacing of (d= 3.4296 A°) , (2θ= 27.7880°) high intensity corresponding to interlayer spacing of (d= 3.2078 A°), (2θ= 33.1320°) medium intensity corresponding to interlayer spacing of (d= 2.7083A°) and (2θ= 46.2794°) low intensity with interlayer spacing of (d= 1.9601 A°) as show in Fig. (3-3).

The XRD analysis spectrum of the synthesized BiC_{80}/GO(20 mg) ternary nano composite gave excellent diffraction peaks at 2θ values of (2θ= 25.9458 °) low intensity with interlayer spacing of (d= 3.4313 A°) , (2θ= 27.6602°) high intensity corresponding to interlayer spacing of (d= 3.22242 A°), (2θ= 33.3794 °) medium

intensity corresponding to interlayer spacing of (d= 2.6822 A°) and (2θ= 46.6117 °) low intensity with interlayer spacing of (d= 1.9469 A°) as show in Fig. (3-3).

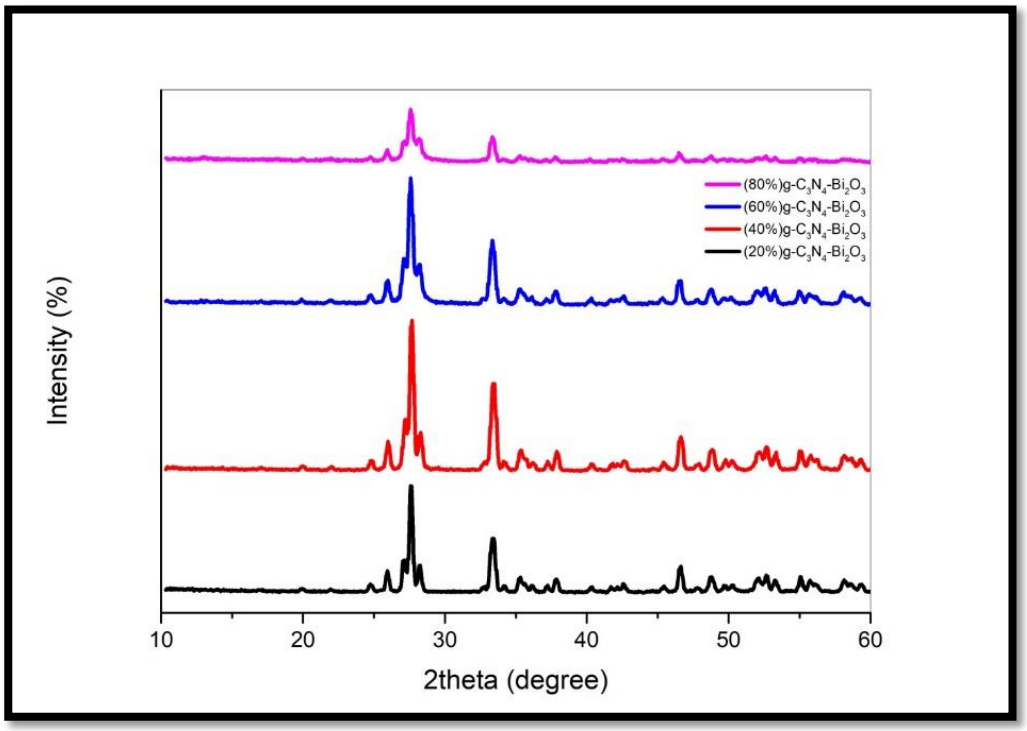

Fig. (3-2) XRD patterns of (20%) g-C_3N_4 -Bi_2O_3, (40%) g-C_3N_4 -Bi_2O_3, (60%) g-C_3N_4 – Bi_2O_3 and (80%) g-C_3N_4 -Bi_2O_3 binary nanocomposites

The XRD analysis spectrum of the synthesized BiC_{80}/GO(30 mg) ternary nano composite gave excellent diffraction peaks at 2θ values of (2θ= 26.4722°) low intensity with interlayer spacing of (d= 3.3642 A°) , (2θ= 27.7770°) high intensity corresponding to interlayer spacing of (d= 3.2091A°), (2θ= 33.4346°) medium intensity corresponding to interlayer spacing of (d= 2.6845A°) and (2θ= 46.5828 °) low intensity with interlayer spacing of (d= 1.9529 A°) as show in Fig. (3-3).

The XRD analysis spectrum of the synthesized BiC_{80}/GO (40 mg) ternary nano composites gave excellent diffraction peaks at 2θ values of (2θ= 25.8482 °) low intensity with interlayer spacing of (d= 3.4526 A°), (2θ= 27.8941°) high intensity corresponding to interlayer spacing of (d= 3.19593 A°), (2θ= 33.3448°) medium intensity corresponding to interlayer spacing of (d= 2.6849 A°) and (2θ= 46.5706 °) low intensity with interlayer spacing of (d= 1.9486 A°) as show in Fig. (3-3).

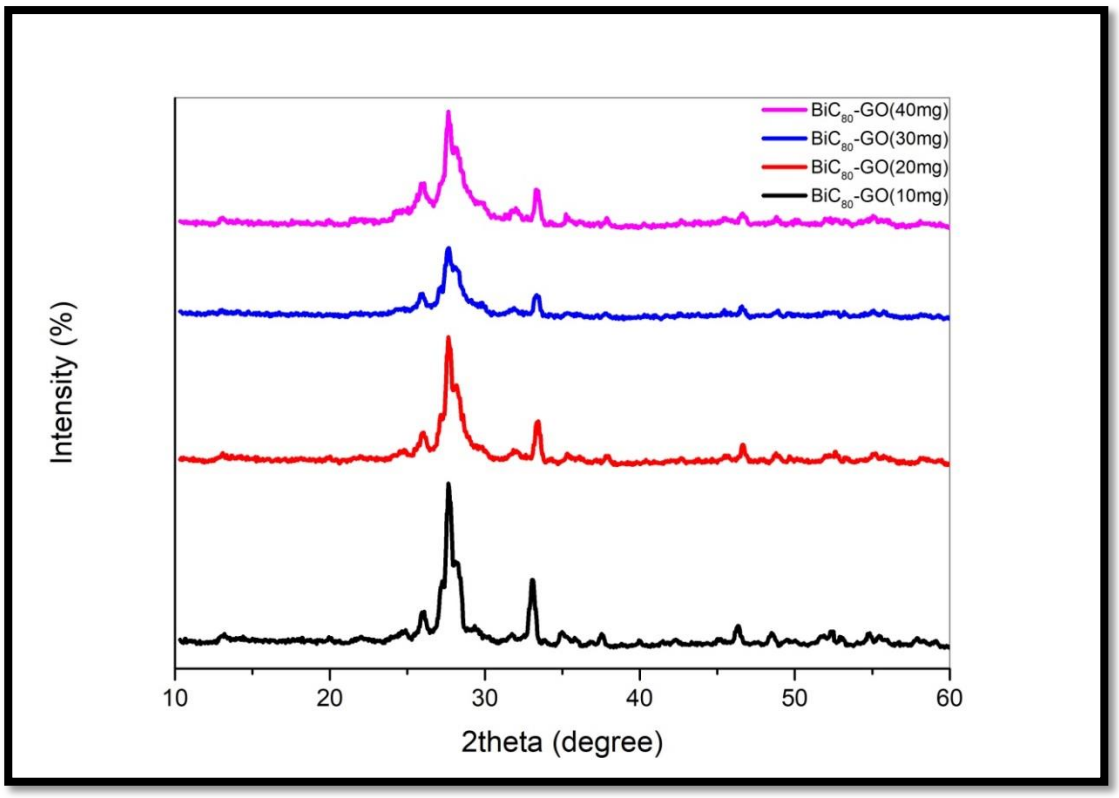

Fig. (3-3) XRD patterns of BiC_{80}/GO (10 mg), BiC_{80}/GO (20 mg), BiC_{80}/GO (30 mg) and BiC_{80}/GO (40 mg) ternary nano composites

The particle size calculated by Debye-Scherrer Equation(3-1)[167]

$$\boldsymbol{D = \frac{K\lambda}{\beta \cos \theta}} \text{ ..... (3-1)}$$

Where: D particle size, K Scherrer's constant equal 0.9, λ wave length of x-ray radiation source**,** β full width at half maximum (FWHM), θ X-ray diffraction angle in radians. The average particles size of synthesized g-C_3N_4, $Bi_2O_3$and NGO (5.209, 24.972 and 6.476 nm) respectively. Binary nanocomposites (20%) g-C_3N_4 -Bi_2O_3. (40%) g-C_3N_4 -Bi_2O_3, (60%) g-C_3N_4 -Bi_2O_3,(80%) g-C_3N_4 -Bi_2O_3 (29.775, 28.306, 24.245 and 29.533 nm) respectively. Ternary nano composites are BiC_{80}/GO (10 mg), BiC_{80}/GO (20 mg), BiC_{80}/GO (30 mg) and BiC_{80}/GO (40 mg) (17.468, 18.169, 21.097 and 20.397 nm) respectively, as shown in Table (3-1).

Table (3-1) Particle size by Debye- Scherrer equation

Compound	2 Theta (2θ) (degree)	FWHM (β) (degree)	Theta (θ) (radians)	β (radians)	D (nm)	D average (nm)	D (nm) In references
g-C_3N_4	13.9122°	3.6678	0.1213	0.0639	2.169	5.209	5.49 [168]
	27.9907°	0.9633	0.2441	0.0168	8.250		
Bi_2O_3	26.1695°	0.3035	0.2282	0.0052	26.654	24.972	69.5 [169]
	27.8227°	0.3927	0.2426	0.0068	20.382		
	33.5340°	0.3554	0.2924	0.0061	22.721		
	46.7237°	0.2685	0.4075	0.0046	30.131		
NGO	11.1297°	1.2312	0.0970	0.0214	6.476	6.476	7.4 [163]
(20%) g-C_3N_4 - Bi_2O_3	25.9262°	0.2527	0.2261	0.0044	31.500	29.775	16.51[170]
	27.6620°	0.2446	0.2412	0.0042	33.000		
	33.4385°	0.3484	0.2916	0.0060	23.100		
	46.5562°	0.2532	0.4060	0.0044	31.500		
(40%) g-C_3N_4 - Bi_2O_3	25.9830°	0.2554	0.2266	0.0044	31.500	28.306	19.55 [170]
	27.6398°	0.2800	0.2410	0.0048	28.875		
	33.4856°	0.3527	0.2920	0.0061	22.721		
	46.5855°	0.2686	0.4063	0.0046	30.131		
(60%) g-C_3N_4 - Bi_2O_3	25.9907°	0.3605	0.2266	0.0062	22.355	24.245	15.36 [170]
	27.5718°	0.3108	0.2404	0.0054	25.666		
	33.4077 °	0.4009	0.2913	0.0069	20.087		
	46.5265°	0.2763	0.4058	0.0048	28.875		
(80%) g-C_3N_4 - Bi_2O_3	25.9758°	0.2418	0.2265	0.0042	33.002	29.533	19.55 [170]
	27.5699°	0.3615	0.2404	0.0063	22		
	33.3800°	0.2653	0.2911	0.0046	30.130		
	46.6257°	0.2448	0.4066	0.0042	33		
BiC_{80}/GO (10 mg)	25.9585°	0.7421	0.2264	0.0129	10.744	17.468	This Work
	27.7880°	1.0163	0.2423	0.0177	7.830		
	33.1320°	0.4039	0.2889	0.0070	19.800		
	46.2794°	0.2574	0.4036	0.0044	31.500		
BiC_{80}/GO (20 mg)	25.9458 °	1.7917	0.2263	0.0312	4.423	18.169	This Work
	27.6602°	0.7209	0.2412	0.0125	11.088		
	33.3794 °	0.3129	0.2911	0.0054	25.666		
	46.6117 °	0.2534	0.4065	0.0044	31.500		
BiC_{80}/GO (30 mg)	26.4722°	4.0000	0.2308	0.0697	1.988	21.097	This Work
	27.7770°	0.7282	0.2422	0.0127	10.913		
	33.4346°	0.1921	0.2916	0.0033	42		
	46.5828 °	0.2718	0.4063	0.0047	29.490		
BiC_{80}/GO (40 mg)	25.8482 °	1.2691	0.2254	0.0221	6.271	20.397	This Work
	27.8941°	1.7834	0.2432	0.0311	4.456		
	33.3448°	0.3060	0.2908	0.0053	26.151		
	46.5706 °	0.1799	0.4061	0.0031	44.710		

Note: rad = (π/180) * degree

3.1.2 Fourier Transform Infrared Spectrophotometry (FT-IR)

The g-C_3N_4 FT-IR spectra are displayed in Fig. (3-4). The breathing mode of the heptazine ring system is assigned by the absorption band at 810.10 cm^{-1}, the deformation mode of N–H is assigned by the absorption band at 889.18 cm^{-1}, the stretching mode of C–N heterocycles as either trigonal C–N(–C)–C or bridging C–NH–C units is assigned by the absorption bands in the range of 1100–1700 cm^{-1}, and the broad bands in the range of the 3000–3700 cm^{-1} region are assigned to the adsorbed H_2O molecules and N–H vibration [158] as shown in Table (3-2).

Table (3-2) The major peak bands of g-C_3N_4

Functional Group	**Wavenumber (cm^{-1})**	**Functional Group**	**Wavenumber (cm^{-1})**
N–H, O-H	3000–3700	deformation mode of N–H	889.18
C–N(–C)–C, C–NH–C	1100–1700	heptazine ring system	810.10

The FT-IR spectrum of Bi_2O_3 as show in Fig. (3-4), the peaks at 503.42 and 542 cm^{-1} were associated with the Bi–O bending of BiO_6 units, while the band at 1379.10 cm^{-1} was assigned to the Bi–O stretching modes [171]. as shown in Table (3-3).

Table (3-3) The major peak bands of Bi_2O_3

Functional Group	**Wavenumber (cm^{-1})**	**Functional Group**	**Wavenumber (cm^{-1})**
Bi–O bending	503.42 and 542	Bi–O stretching	1379.10

The FT-IR spectrum of nano graphene oxide (NGO) as shown in Fig. (3-4) broad band observed at 3000-3700 cm^{-1}represents the stretching vibration of -OH in carboxylic and alcohol groups[129], peaks appeared at 1716.65 $cm^{-1}$and 1575.84 cm^{-1} which can be assigned to vibration stretching C=O of carboxylic groups and C=C on the basal plan of NGO sheets respectively. The peaks appeared 1521.84 cm^{-1} refers to epoxy group C-O-C as shown in Table (3-4).

Table (3-4) The major peak bands of NGO

Functional Group	**Wavenumber (cm^{-1})**	**Functional Group**	**Wavenumber (cm^{-1})**
OH	3000-3700	C=C	1575.84
C=O	1716.65	C-O-C	1521.84

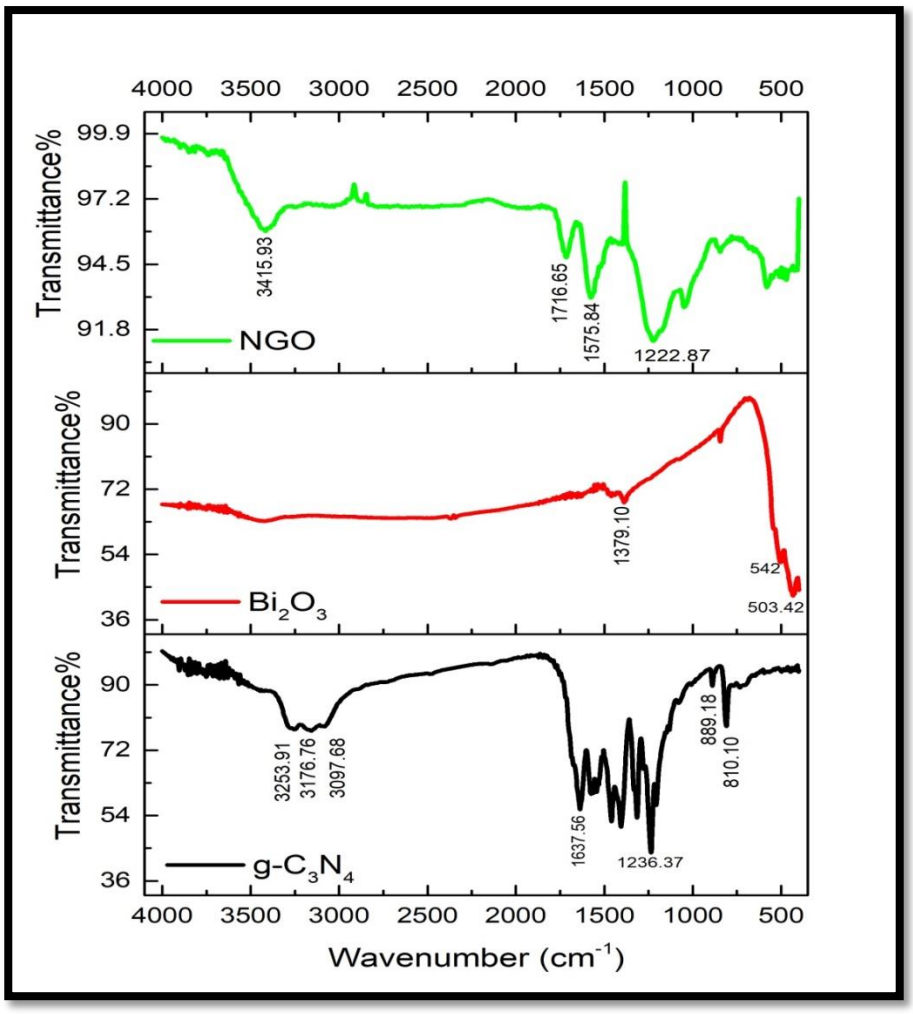

Fig. (3-4) FT-IR spectrums of g-C_3N_4, Bi_2O_3 and NGO

The FT-IR spectrums of (20%) g-C_3N_4 -Bi_2O_3, (40%) g-C_3N_4 -Bi_2O_3, (60%) g-C_3N_4 -Bi_2O_3 and (80%) g-C_3N_4 -Bi_2O_3 binary nano composites are shown in Fig. (3-5). The peaks at 503.42 and 543.93 cm^{-1} were associated with the Bi–O vibration of BiO_6 units appeared in (20%) g-C_3N_4 -Bi_2O_3, (40%) g-C_3N_4 -Bi_2O_3 and (60%) g-C_3N_4 -Bi_2O_3) while disappeared in (80%) g-C_3N_4 -Bi_2O_3. This is due to the difference in synthesis rates, The breathing mode of the heptazine ring system is assigned by the absorption band at 810.10 cm^{-1}, the deformation mode of N–H is assigned by the absorption band at 889.18 cm^{-1} , the stretching mode of C–N heterocycles as either trigonal C–N(–C)–C or bridging C–NH–C units is assigned by the absorption bands in the range of 1100–1700 cm^{-1}, and the broad bands in the range of the 3000–3700 cm^{-1} region are assigned to the adsorbed H_2O molecules and N–H vibration, the peaks appeared in((40%) g-C_3N_4 -Bi_2O_3 , (60%) g-C_3N_4 -Bi_2O_3 and (80%) g-C_3N_4 -Bi_2O_3), while the intensity of the peak is weak in (20%) g-C_3N_4 -Bi_2O_3 due to the difference in synthesis rates [158],[171] as shown in Table (3-5).

Table (3-5) The major peak bands of (20%) g-C_3N_4 -Bi_2O_3, (40%) g- C_3N_4 -Bi_2O_3, (60%) g-C_3N_4 -Bi_2O_3 and (80%) g-C_3N_4 -Bi_2O_3 binary nano composites

Functional Group	**Wavenumber (cm^{-1})**	**Functional Group**	**Wavenumber (cm^{-1})**
N–H, O-H	3000-3700	heptazine ring system	810.10
C–N(–C)–C, C–NH–C	1100-1700	Bi–O vibration	503.42 and 543.93
deformation mode of N–H	889.18		

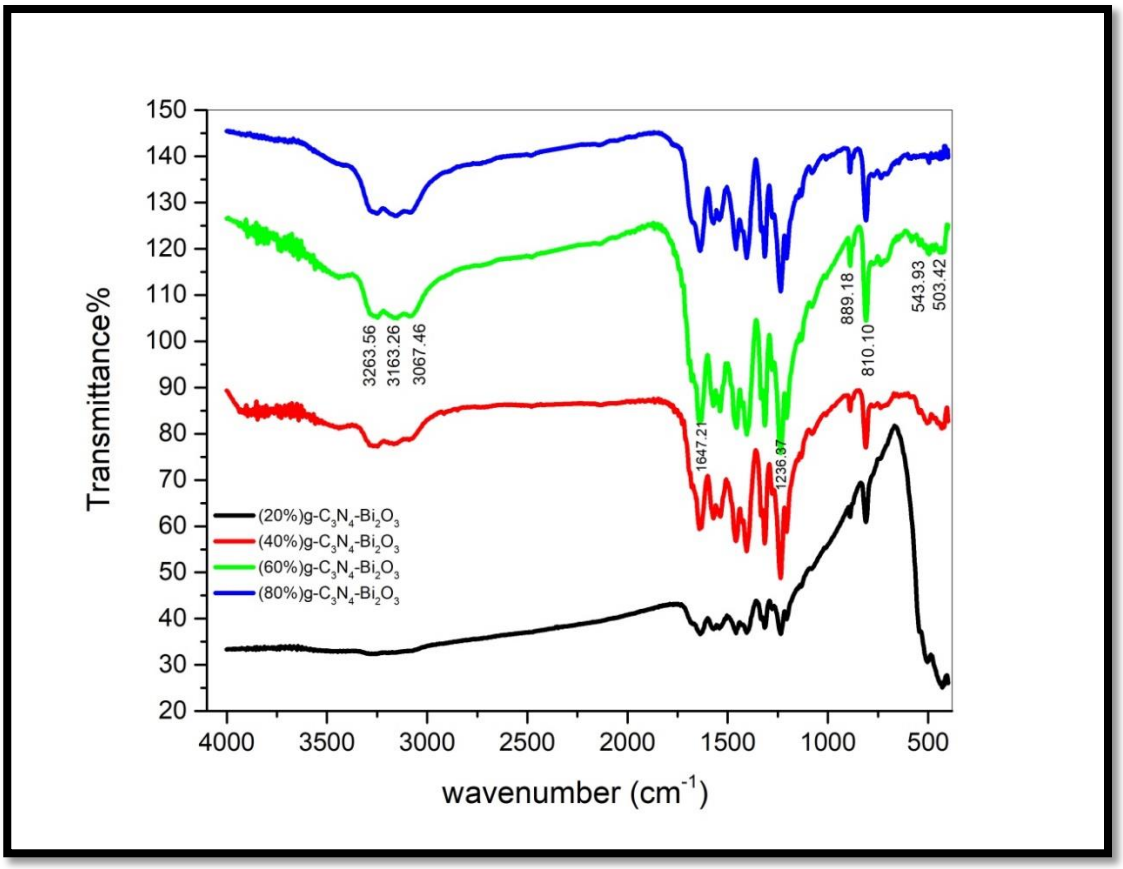

Fig. (3-5) FT-IR spectrum of (20%) g-C_3N_4 -Bi_2O_3, (40%) g-C_3N_4 -Bi_2O_3, (60%) g-C_3N_4 -Bi_2O_3 and (80%) g-C_3N_4 -Bi_2O_3 binary nanocomposites

The FT-IR spectrum of BiC_{80}/GO(10 mg) , BiC_{80}/GO(20 mg) , BiC_{80}/GO(30 mg) and BiC_{80}/GO(40 mg) ternary nano composites are shown in Fig. (3-6), The breathing mode of the heptazine ring system is assigned by the absorption band at 810.10 cm^{-1}, the deformation mode of N–H is assigned by the absorption band at 889.18 cm^{-1} , the stretching mode of C–N heterocycles as either trigonal C–N(–C)–C or bridging C–NH–C units is assigned by the absorption bands in the range

of 1100–1700 cm^{-1}, and broad band observed at 3000-3700 cm^{-1} represents the stretching vibration of -OH in carboxylic and alcohol groups and N–H vibration as shown in Table (3-6).

Table (3-6) The major peak bands of BiC_{80}/GO (10 mg), BiC_{80}/GO (20 mg), BiC_{80}/GO (30 mg) and BiC_{80}/GO (40 mg) ternary nano composites

Functional Group	Wavenumber (cm^{-1})	Functional Group	Wavenumber (cm^{-1})
N–H, O-H	3000-3700	deformation mode of N–H	889.18
C–N(–C)–C, C–NH–C	1100-1700	heptazine ring system	810.10

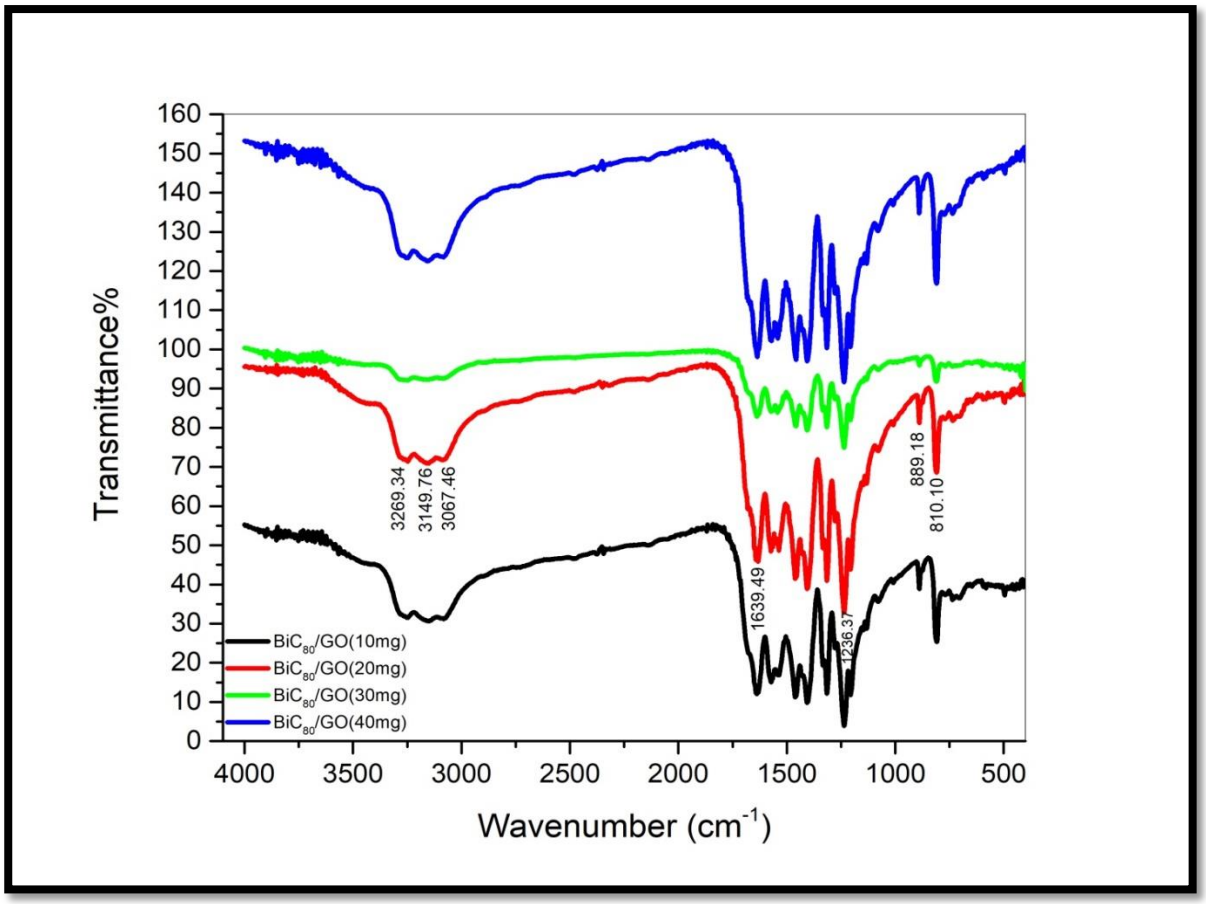

Fig. (3-6) FT-IR spectrum of BiC_{80}/GO (10 mg), BiC_{80}/GO (20 mg), BiC_{80}/GO (30 mg) and BiC_{80}/GO (40 mg) ternary nanocomposites

3.1.3 Ultraviolet-Visible Spectrophotometry

Ultraviolet–visible (UV–Vis) spectroscopy is an effective and essential technique for the complete category of synthesized nanoparticle. The samples g-C_3N_4, Bi_2O_3 shows an intense broader absorption peak at the wavelength 265.5 nm ,309 nm

respectively belonging to the involvement of charge transfer transitions [160]. The visible-light absorption behavior of g-C_3N_4 reflects the n-π* transition of the nitrogen atom lone pair electrons of the heptazine unit [172]. The sample of NGO shows an intense sharp absorption peak at the wavelength 253 nm and a shoulder peak 256.5 nm which were the absorption bands corresponding to π→π* electron transitions of poly aromatic C=C bonds and n→π* electron transitions of C=O bonds respectively [129] as show in Fig. (3-7).

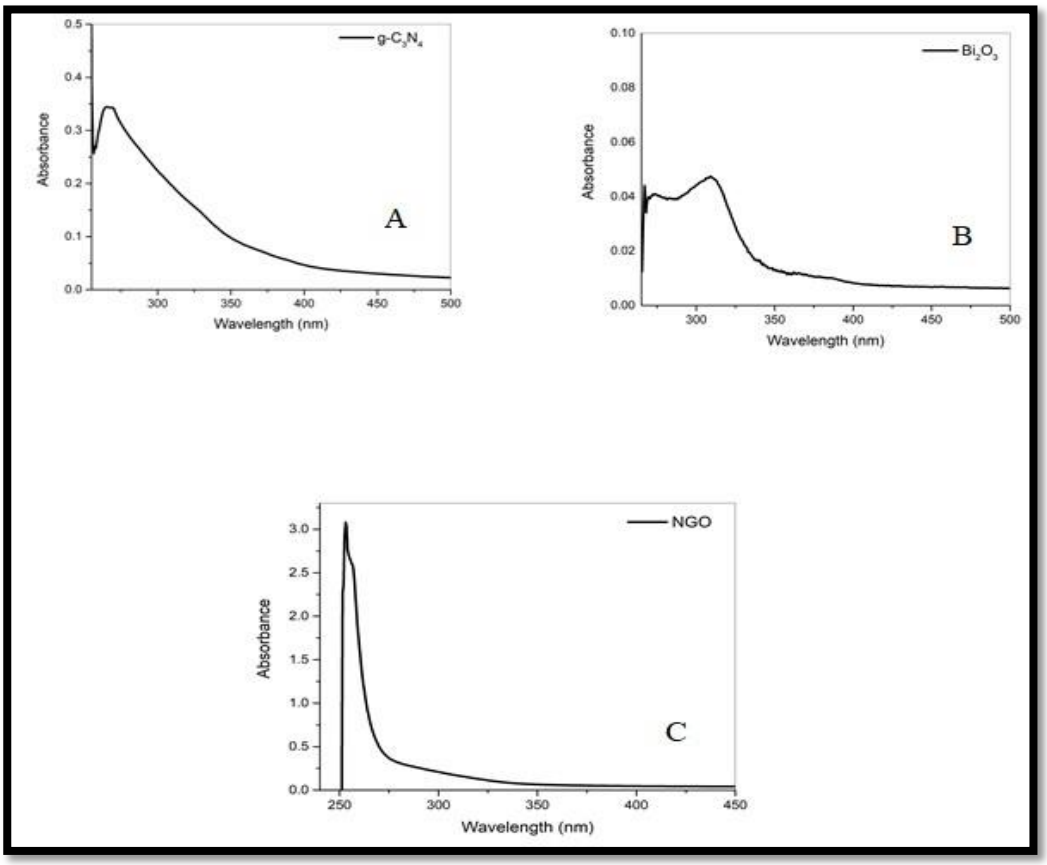

Fig. (3-7) Absorption spectrums of (A)g-C_3N_4, (B) Bi_2O_3 and(C) NGO

The samples of (20%) g-C_3N_4 -Bi_2O_3, (40%) g-C_3N_4 -Bi_2O_3, (60%) g-C_3N_4 -Bi_2O_3 and (80%) g-C_3N_4 -Bi_2O_3 binary nano composites shows an intense broader absorption peak at the wavelength 309 nm, 309 nm ,310nm and 309 nm respectively, there are differences in absorption between the nanocomposites. It is noticed that the absorption wavelength of the binary nanocomposites exhibits red shift compared to the pure g-C_3N_4 as shown in Fig. (3-8).

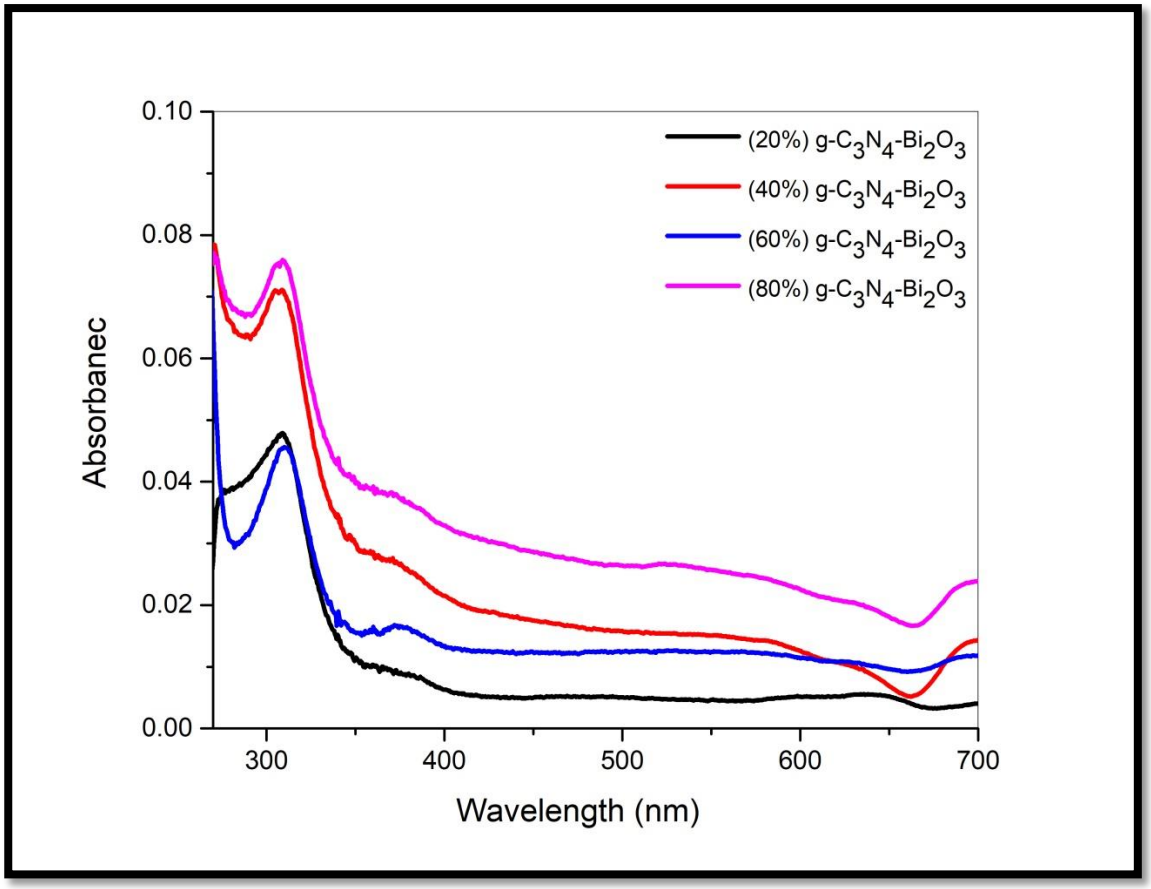

Fig. (3-8) Absorption spectrums of (20%) g-C_3N_4 -Bi_2O_3, (40%) g-C_3N_4 -Bi_2O_3, (60%) g-C_3N_4-Bi_2O_3 and (80%) g-C_3N_4 -Bi_2O_3 binary nanocomposites

The samples of BiC_{80}/GO (10 mg), BiC_{80}/GO (20 mg), BiC_{80}/GO (30 mg) and BiC_{80}/GO (40 mg) ternary nano composites shows an intense broader absorption peak at the wavelength 311.5 nm, 312 nm ,308.5nm and 304.5 nm respectively, there are differences in absorption between the nanocomposites. The absorption wavelengths of the ternary nanocomposites exhibit red shift compared to the pure g-C_3N_4 and NGO while BiC_{80}/GO (10 mg), BiC_{80}/GO (20 mg) red shift, BiC_{80}/GO (30 mg) and BiC_{80}/GO (40 mg) shows blue shift compared to Bi_2O_3 as show in Fig. (3-9).

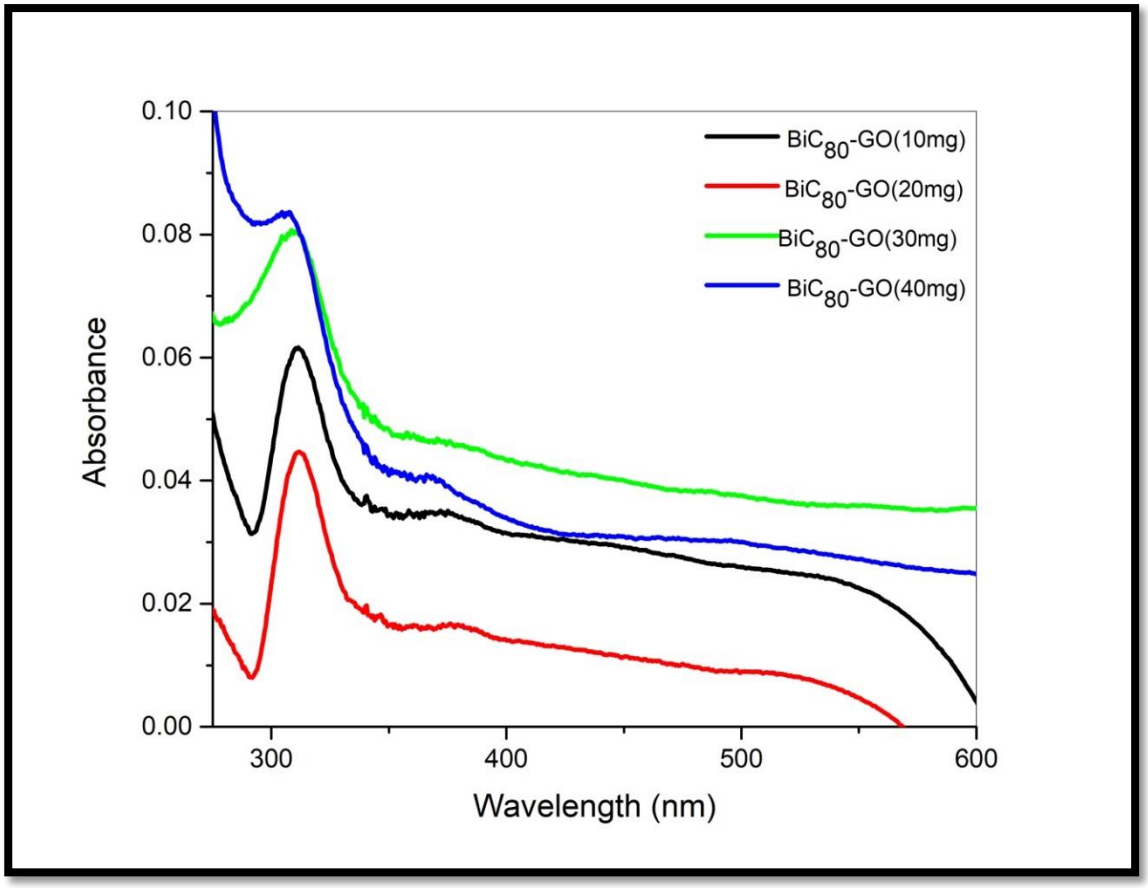

Fig. (3-9) Absorption spectrums of BiC_{80}/GO (10 mg), BiC_{80}/GO (20 mg), BiC_{80}/GO (30 mg) and BiC_{80}/GO (40 mg) ternary nanocomposites

3.1.4 Photoluminescence Spectral Analysis (PL)

The PL technique is useful to reveal the migration, transfer, and recombination process of photo-generated electron–hole pairs in semiconductors. Therefore, the PL spectra for; pure g-C_3N_4 with an excitation wavelength of 265.5 nm, Bi_2O_3 with an excitation wavelength of 309 nm, and NGO with an excitation wavelength of 253 nm were obtained. The main emission peak is centered at the range 360 nm and the other peak in 550 nm for the pure g-C_3N_4 sample, which can be attributed to the band-band PL phenomenon with the energy of light approximately equal to the band gap energy of g-C_3N_4 [173]. The main emission peak is centered at 386 nm and the other peak in 623 nm for the Bi_2O_3 sample and 357 nm for the NGO sample as shown in Fig. (3-10).

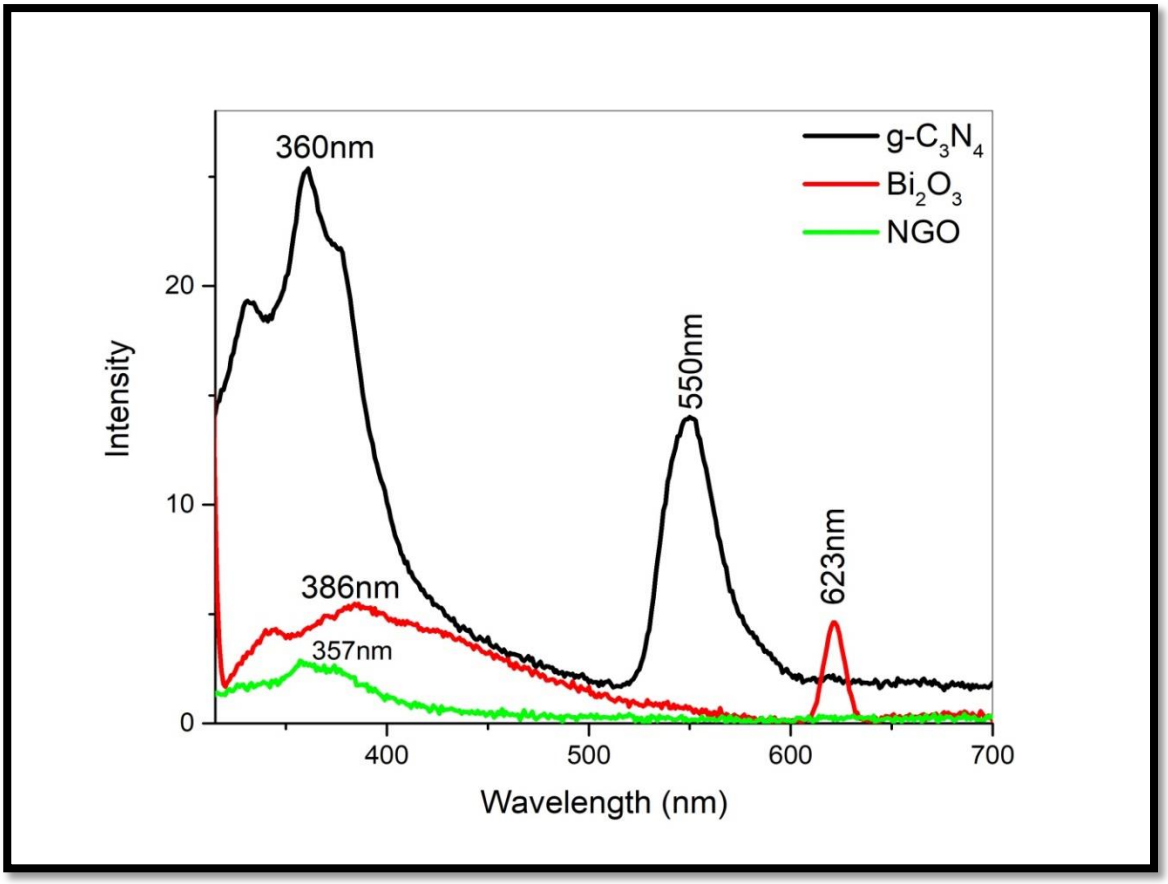

Fig. (3-10) Photoluminescence (PL) spectra of g-C_3N_4, Bi_2O_3 and NGO

The PL spectra for (20%) g-C_3N_4 -Bi_2O_3, (40%) g-C_3N_4 -Bi_2O_3, (60%) g-C_3N_4 -Bi_2O_3 and (80%) g-C_3N_4 -Bi_2O_3 binary nanocomposites with an excitation wavelength of 309 nm ,309 nm ,310 nm and 309 nm respectively were obtained. The results are shown in Fig. (3-11) The main emission peak is centered at the range 339 -550 nm and the other peak in 616 nm.

The PL spectra for BiC_{80}/GO (10 mg), BiC_{80}/GO (20 mg), BiC_{80}/GO (30 mg) and BiC_{80}/GO (40 mg) ternary nanocomposites with an excitation wavelength of 311.5 nm ,312 nm ,308.5 nm and 304.5 nm respectively were obtained. The results are shown in Fig. (3-12) The main emission peak is centered at about 328 - 550 nm and the other peak in (623,623,615 and 608nm) respectively.

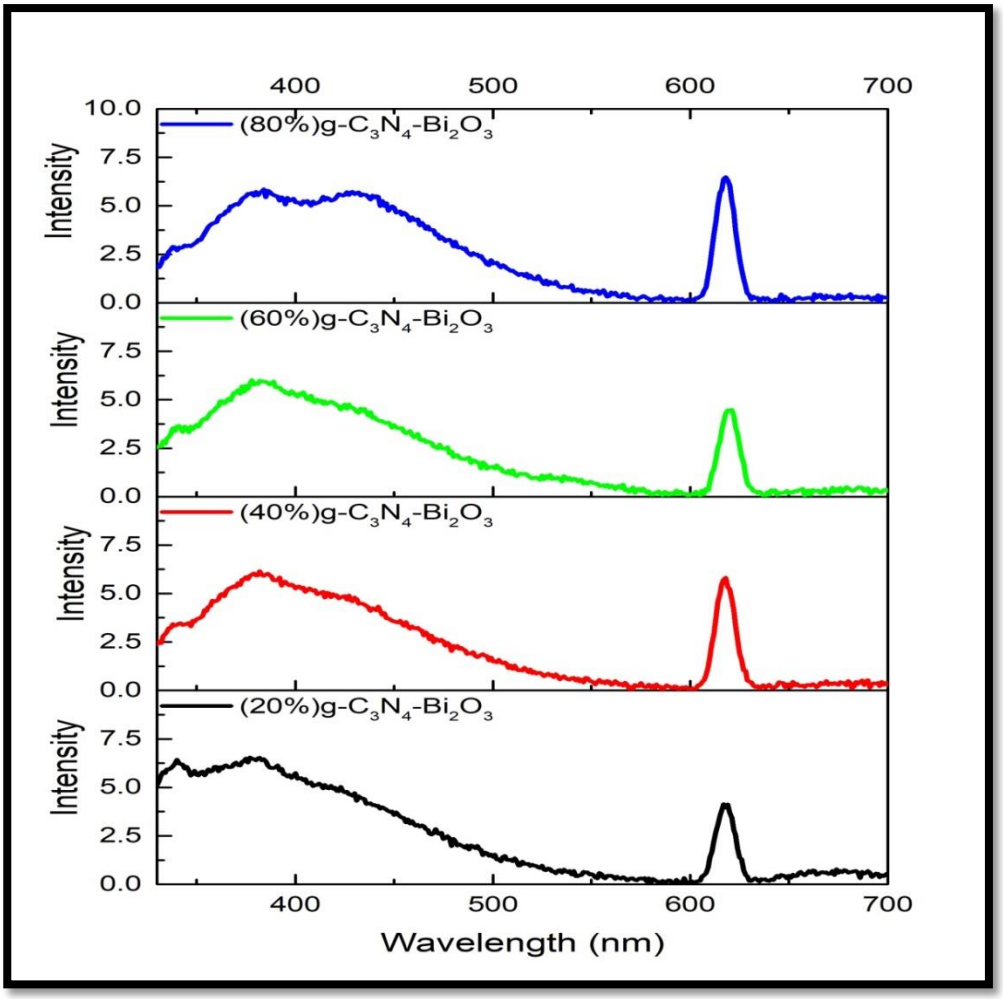

Fig. (3-11) Photoluminescence (PL) spectra of (20%) g-C_3N_4 -Bi_2O_3, (40%) g-C_3N_4 -Bi_2O_3, (60%) g-C_3N_4 -Bi_2O_3 and (80%) g-C_3N_4 -Bi_2O_3 binary nanocomposites

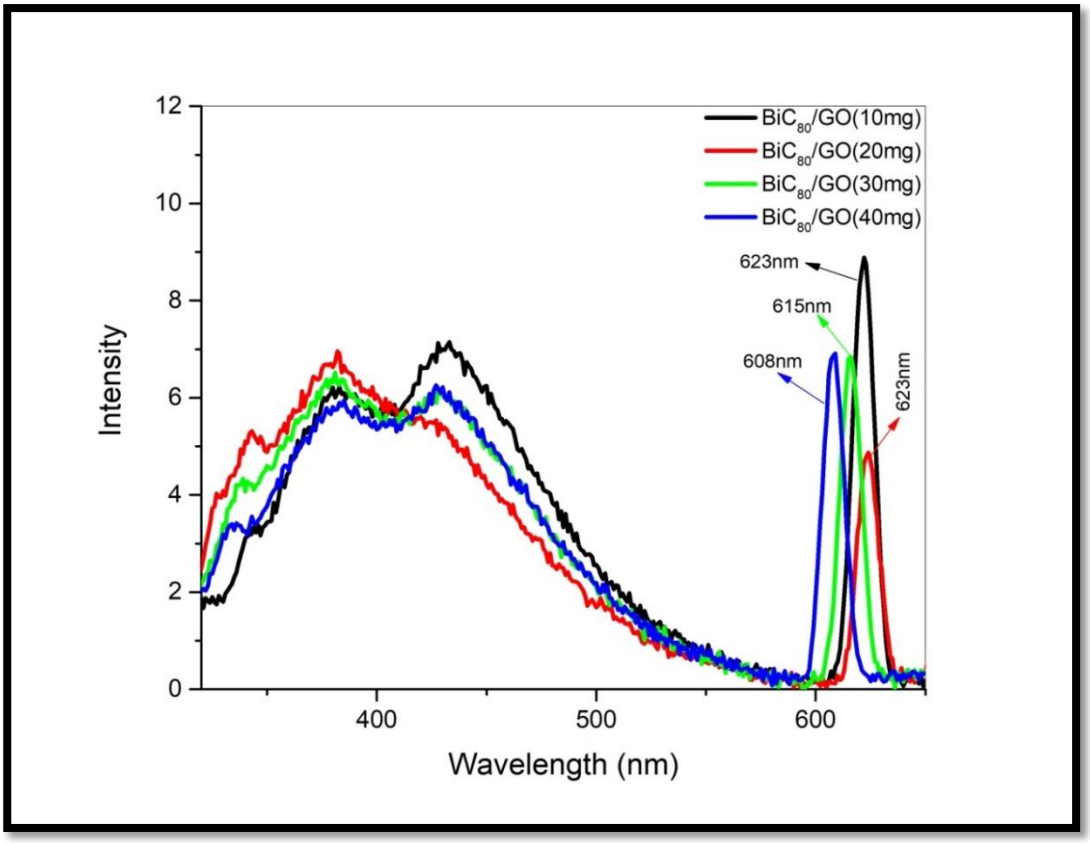

Fig. (3-12) Photoluminescence (PL) spectra of BiC_{80}/GO (10 mg), BiC_{80}/GO (20 mg), BiC_{80}/GO (30 mg) and BiC_{80}/GO (40 mg) ternary nanocomposites

3.1.5 Thermogravimetric Analysis (TGA)

TGA was performed for investigating the thermal stability of the samples. For g-C_3N_4, a sharp weight loss occurred from 530 to 722 °C, which could be attributed to the burning of g-C_3N_4 in the form of gases, such as ammonia and hydrogen cyanide, [143],[174]. Bi_2O_3 showed a sharp weight loss occurred from 370 to 800°C. For NGO, three weight loss processes, namely, from 70 to 120 °C, from 150 to 330 °C and from 350 to750 °C which could be assigned the loss of surface absorbed water, due to the removal of oxygen functional groups and NGO burning as shown in Fig. (3-13).

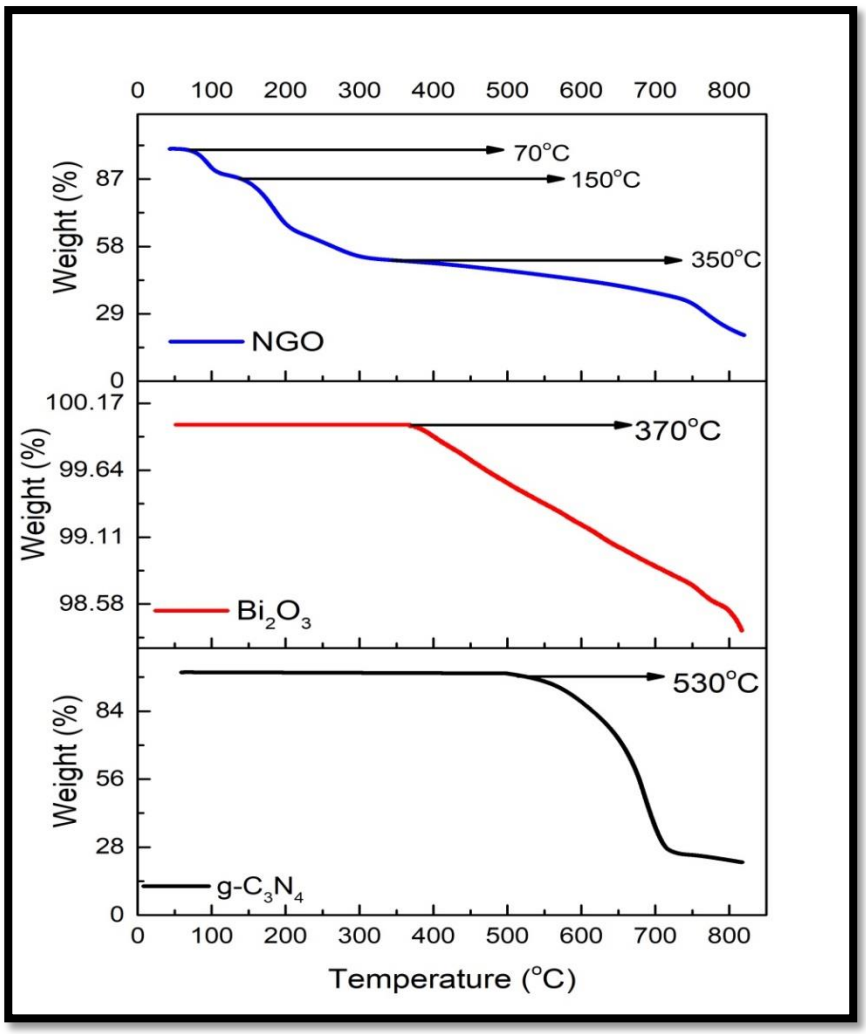

Fig. (3-13) Thermogravimetric analysis (TGA) of g-C_3N_4, Bi_2O_3 and NGO

For (20%) g-C_3N_4 -Bi_2O_3 a sharp weight loss occurred from 400 to 600 °C, (40%) g-C_3N_4 -Bi_2O_3 a sharp weight loss occurred from 440 to 500 °C, (60%) g-C_3N_4 -Bi_2O_3 a sharp weight loss occurred from 450 to 590 °C and (80%) g-C_3N_4 -Bi_2O_3 a sharp weight loss occurred from 475 to 630 °C [160]. as shown in Fig. (3-14).

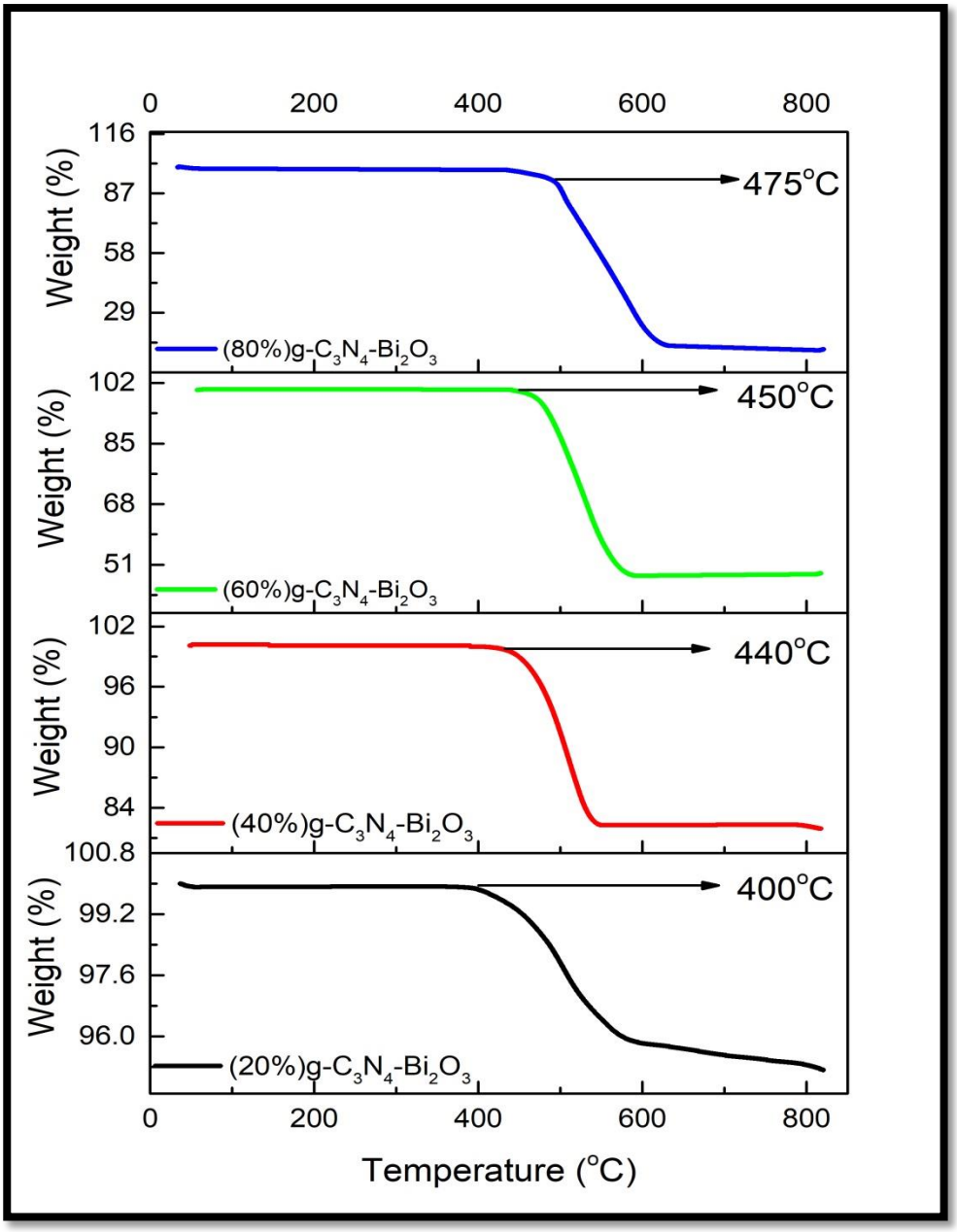

Fig. (3-14) Thermogravimetric analysis (TGA) of (20%) g-C_3N_4 -Bi_2O_3, (40%) g-C_3N_4 – Bi_2O_3, (60%) g-C_3N_4 -Bi_2O_3 and (80%) g-C_3N_4 -Bi_2O_3 binary nanocomposites

Sharp weight loss occurred for, BiC_{80}/GO (10 mg) at the range 450 - 655 °C, BiC_{80}/GO (20 mg) at the range 485 - 640 °C, BiC_{80}/GO (30 mg) at the range 450 - 645 °C and BiC_{80}/GO (40 mg) at the range 415- 800 °C as shown in Fig. (3-15).

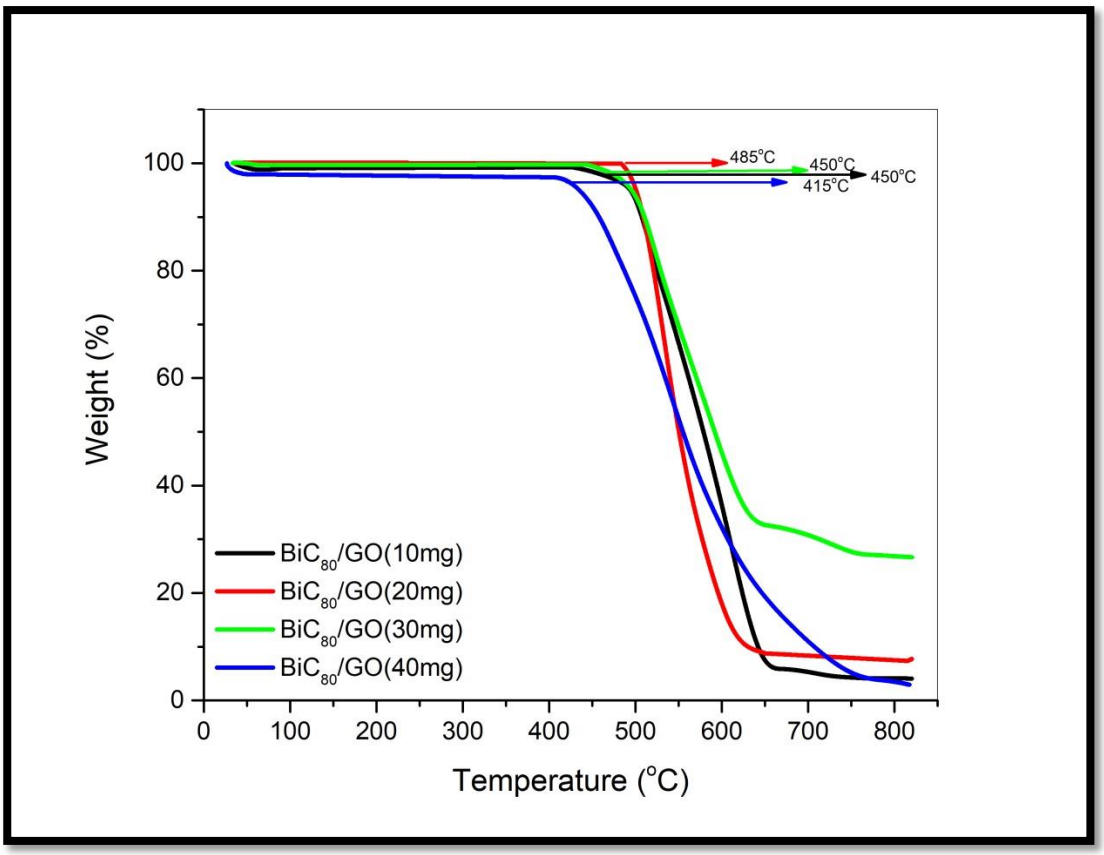

Fig. (3-15) Thermogravimetric analysis (TGA) of BiC_{80}/GO (10 mg), BiC_{80}/GO (20 mg), BiC_{80}/GO (30 mg) and BiC_{80}/GO (40 mg) ternary nanocomposites

3.1.6 Field Emission Scanning Electron Microscopy (FESEM)

The morphology of the synthesized samples was examined by FESEM analysis as shown in Fig. (3-16) (A) FESEM images of g-C_3N_4 ,(B) Size distribution. The FESEM image of g-C_3N_4 describes that it has a stacked nanosheet structure and well matched with the literature [175], crystal size was (7.643 – 212 nm).

The EDS spectrum and elemental distribution micrographs show the presence of C, N, and O in the g-C_3N_4. The Energy Dispersive Spectroscopy (EDS) spectrum does not show any other peaks other than the above-mentioned elements as show in Fig. (3-17).

A B

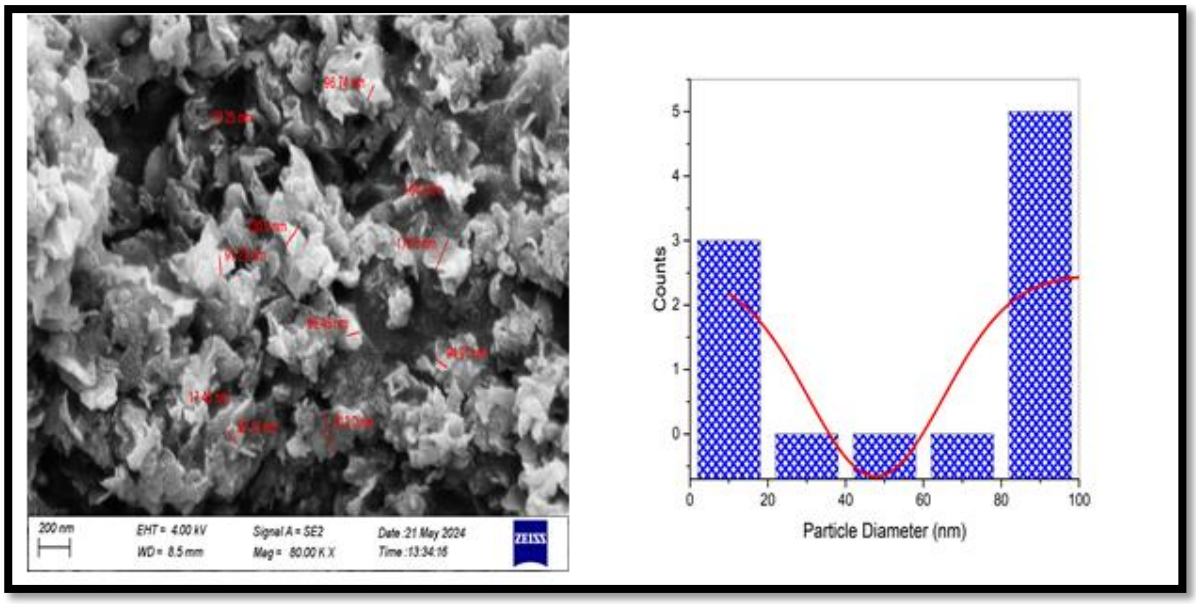

Fig. (3-16) (A) FESEM images of g-C_3N_4, (B) Size distribution

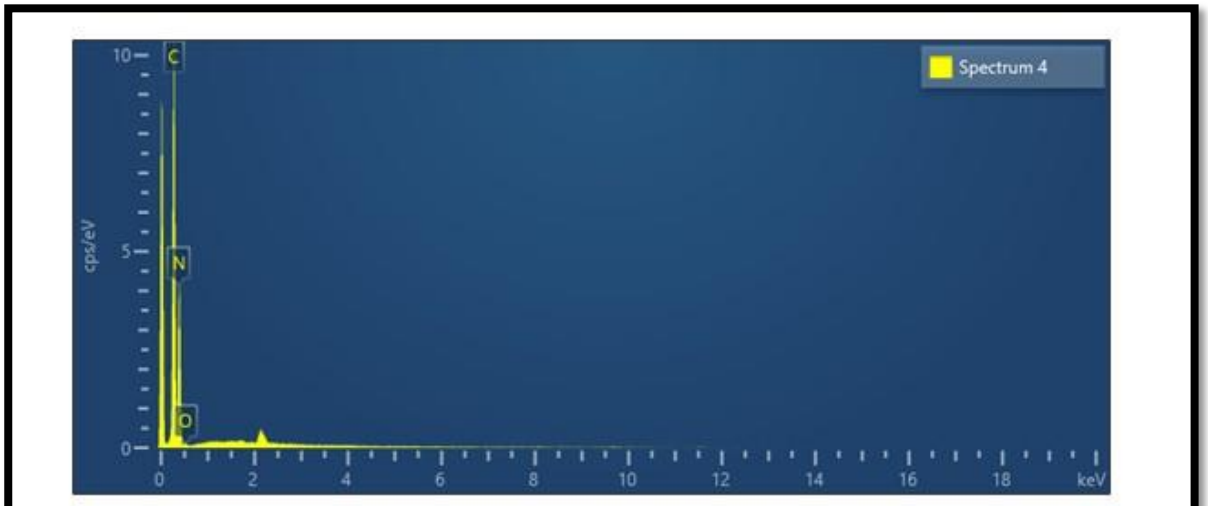

Spectrum 4				
Element	Line Type	Weight %	Weight % Sigma	Atomic %
N	K series	64.22	0.61	60.79
O	K series	1.07	0.32	0.88
C	K series	34.72	0.57	38.33
Total		100.00		100.00

Fig. (3-17) EDS spectrum of g-C_3N_4

The FESEM image of Bi_2O_3 the pristine exhibited a flower-like microsphere, well matched the literature [176], crystal size was (9.667 – 417.4 nm) as shown in Fig. (3-18) (A) FESEM images of Bi_2O_3 ,(B) Size distribution.

The EDS spectrum and the elemental distribution micrographs shows the presence of Bi, and O in the Bi_2O_3. The EDS spectrum does not show any other peaks except the above-mentioned elements, which indicates the purity of the synthesized samples as shown in Fig. (3-19).

A B

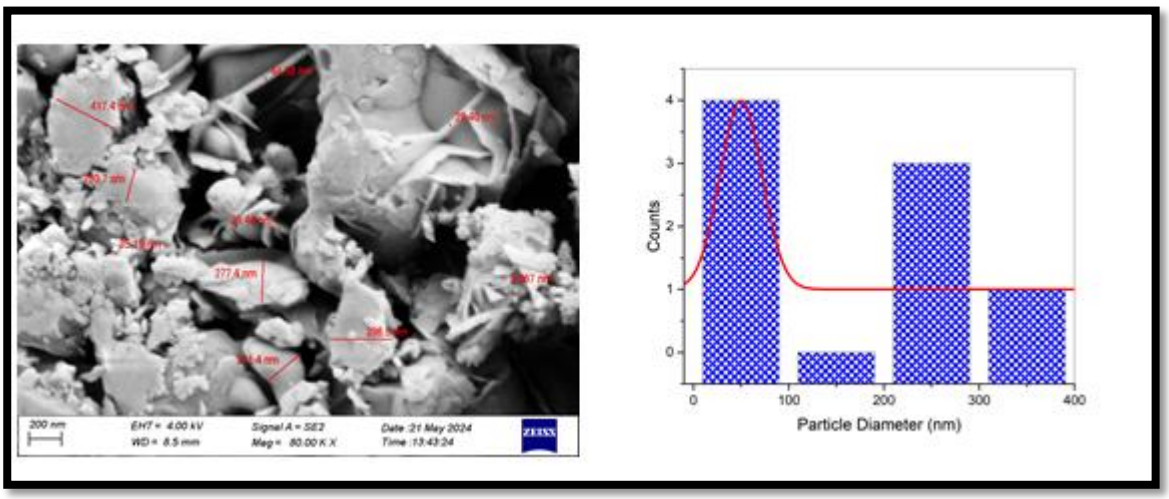

Fig. (3-18)(A) FESEM images of Bi_2O_3 ,(B) Size distribution

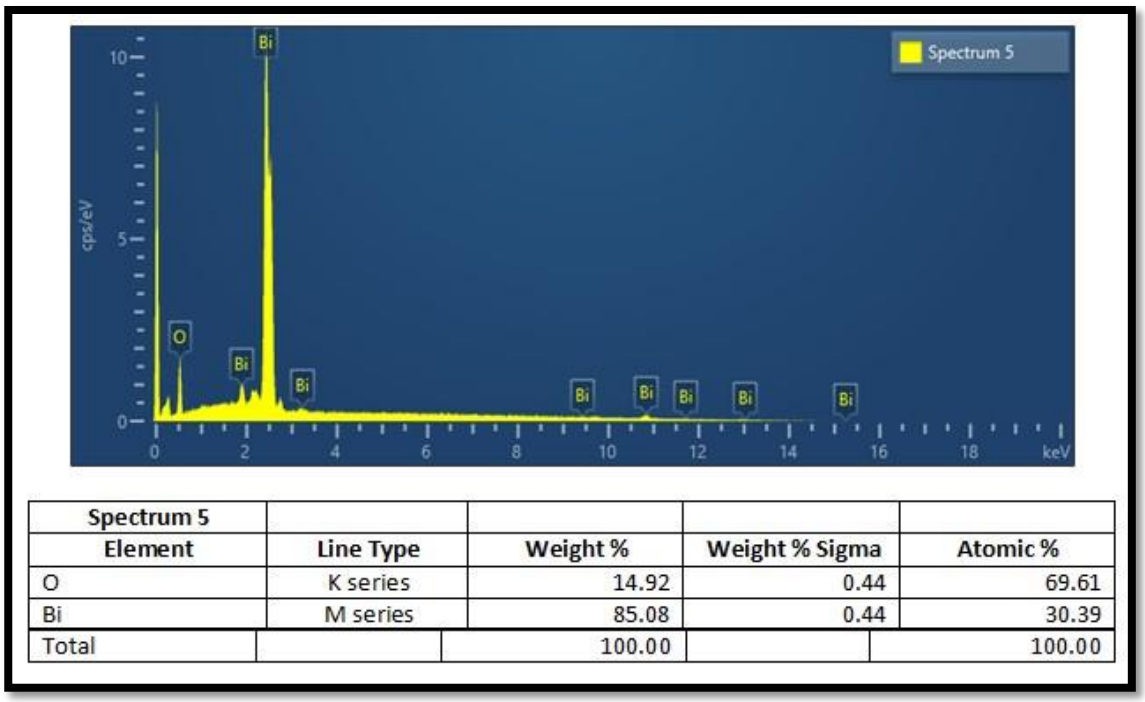

Spectrum 5				
Element	Line Type	Weight %	Weight % Sigma	Atomic %
O	K series	14.92	0.44	69.61
Bi	M series	85.08	0.44	30.39
Total		100.00		100.00

Fig. (3-19) EDS spectrum of Bi_2O_3

The FESEM used to study the surface morphology of NGO as shown in Fig. (3-20) (A) FESEM images of NGO,(B) Size distribution, the corrugation shape observed, crystal size was (13.94 – 38.86 nm) as it was clear, low wrinkled on NGO surface are more sensitive and shows better recovery ability [177].

The (EDS) spectrum (attached with the FESEM), used to identify the elements involved in the NGO formation as shown in Fig. (3-21), the appearance of a peak at energy (0.18 keV) to carbon atoms, and another peak at energy (0.5 keV) to oxygen atoms, this evidence proved the presence of carbon and oxygen atoms only in pure synthesized NGO. The obtained results agree well with the previous studies [178].

A B

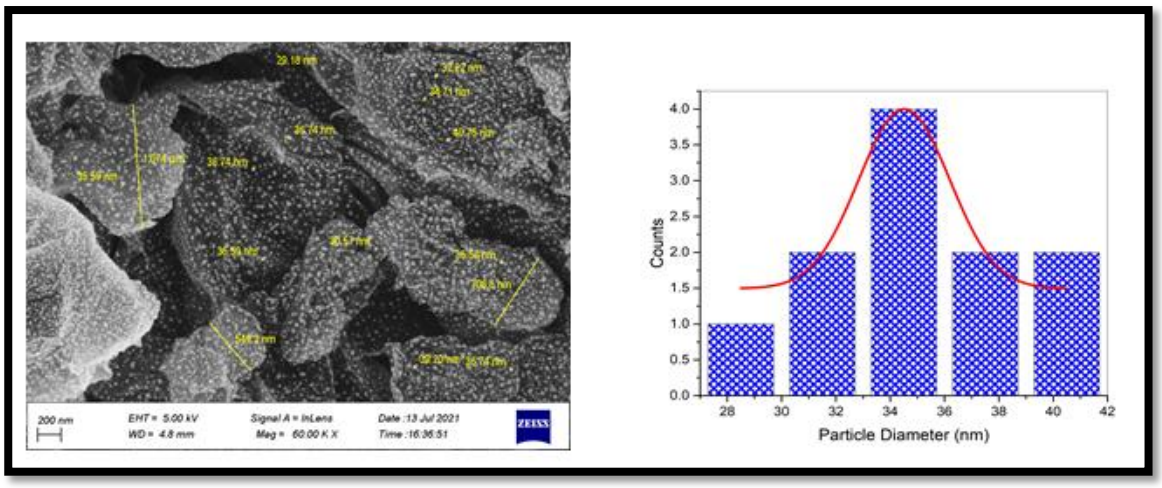

Fig. (3-20) (A) FESEM images of NGO,(B) Size distribution

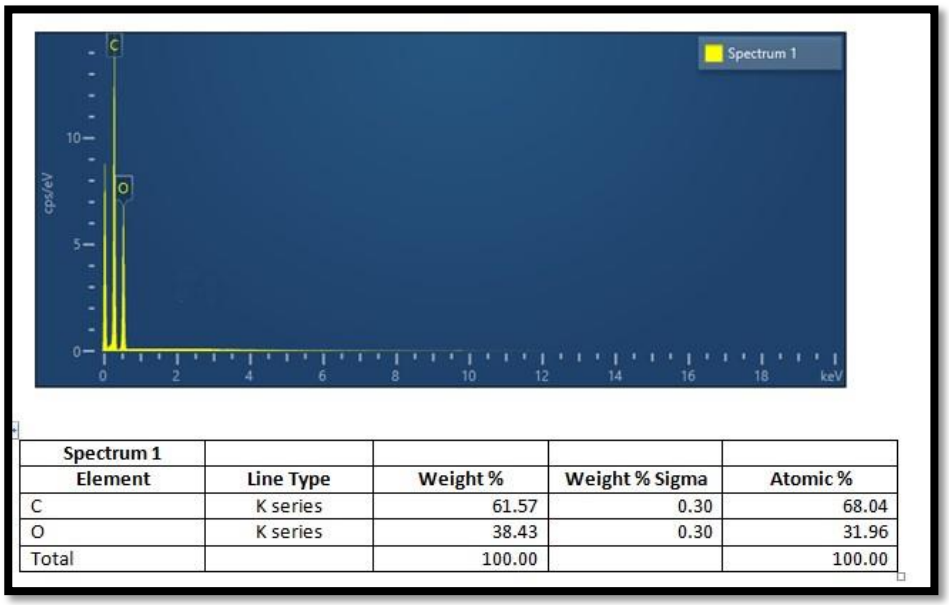

Spectrum 1				
Element	Line Type	Weight %	Weight % Sigma	Atomic %
C	K series	61.57	0.30	68.04
O	K series	38.43	0.30	31.96
Total		100.00		100.00

Fig. (3-21) EDS spectrum of NGO

The FESEM image of (20%) g-C_3N_4 - Bi_2O_3 binary nanocomposites as shown in Fig. (3-22), the introduction of Bi_2O_3 into porous g-C_3N_4 can be seen as small irregular particles on top of g-C_3N_4 surface sheets [179], crystal size was (37.60 – 509.8 nm).

The EDS spectrum and elemental distribution micrographs shows only the presence of C, N, Bi and O in the (20%) g-C_3N_4 - Bi_2O_3 binary nanocomposite. The EDS spectrum does not show any other peaks other than the above-mentioned elements, which indicates the purity of the synthesized sample as show in Fig. (3-23).

A B

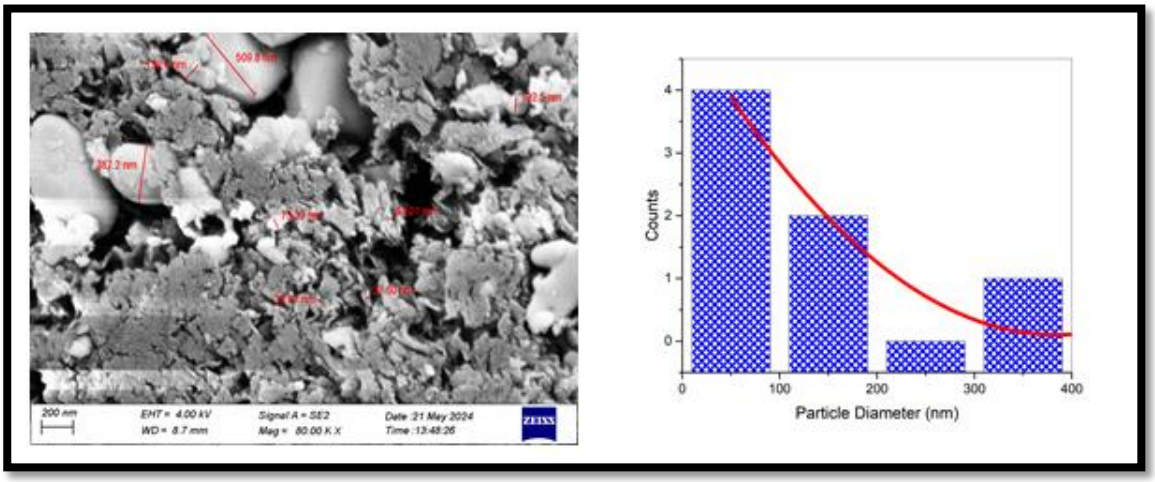

Fig. (3-22)(A) FESEM images of (20%) g-C_3N_4 - Bi_2O_3 binary nanocomposite,(B) Size distribution

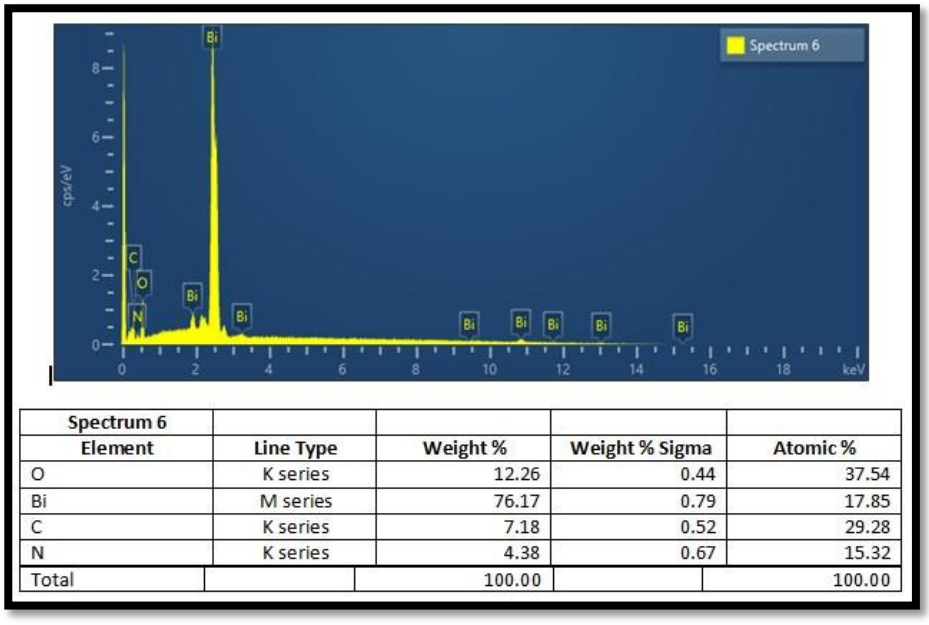

Spectrum 6				
Element	Line Type	Weight %	Weight % Sigma	Atomic %
O	K series	12.26	0.44	37.54
Bi	M series	76.17	0.79	17.85
C	K series	7.18	0.52	29.28
N	K series	4.38	0.67	15.32
Total		100.00		100.00

Fig. (3-23) EDS spectrum of (20%) g-C_3N_4 - Bi_2O_3 binary nanocomposite

The FESEM image of (40%) g-C_3N_4 - Bi_2O_3 binary nanocomposite as shown in Fig. (3-24),the introduction of Bi_2O_3 into porous g-C_3N_4 can be seen as small irregular particles on top of g-C_3N_4 surface sheets [179], crystal size was (12.32 – 339.1 nm).

The EDS spectrum and elemental distribution micrographs show the presence of C, N, Bi and O in the (40%) g-C_3N_4 - Bi_2O_3 binary Nano Composites. The EDS spectrum does not show any other peaks than the above-mentioned elements, which indicates the purity of the synthesized sample. The changes in the weight% and atomic% of the elements is due to the difference of the reactant's percentage of the binary nanocomposite as show in Fig. (3-25).

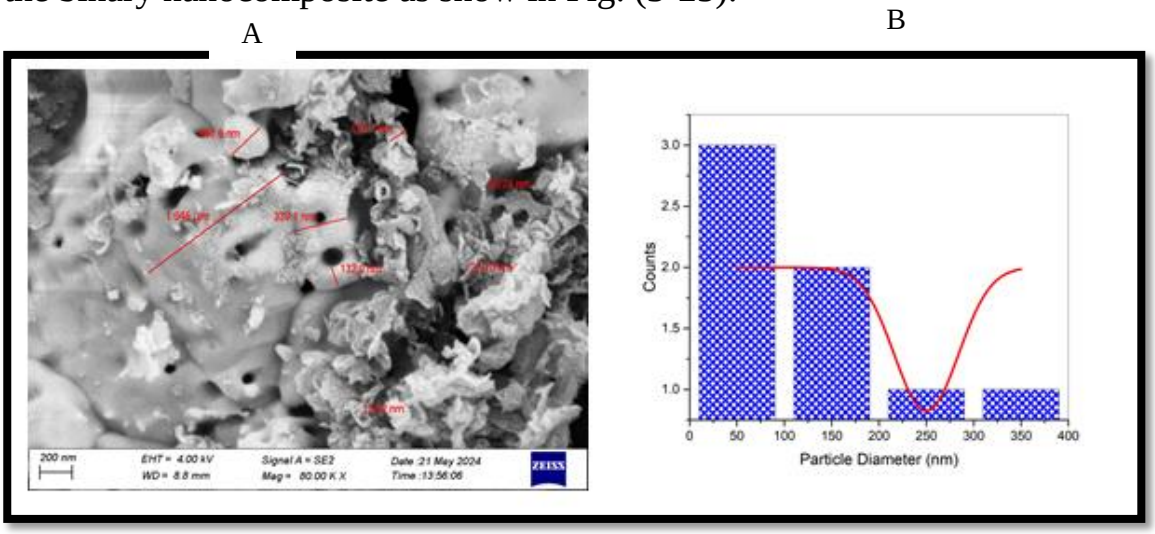

Fig. (3-24)(A) FESEM images of (40%) g-C_3N_4 - Bi_2O_3 binary nanocomposite ,(B) Size distribution

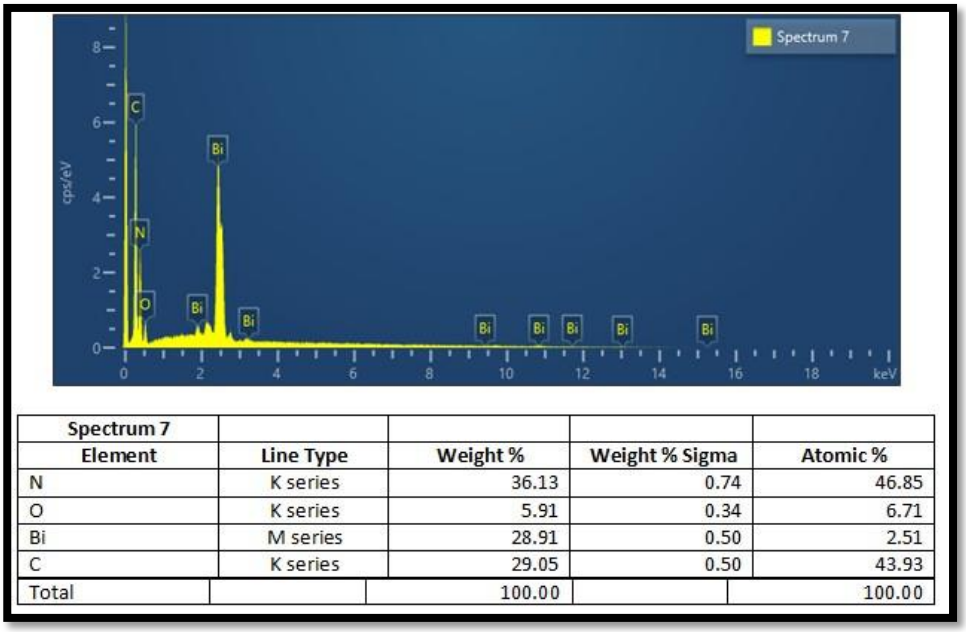

Spectrum 7				
Element	Line Type	Weight %	Weight % Sigma	Atomic %
N	K series	36.13	0.74	46.85
O	K series	5.91	0.34	6.71
Bi	M series	28.91	0.50	2.51
C	K series	29.05	0.50	43.93
Total		100.00		100.00

Fig. (3-25) EDS spectrum of (40%) g-C_3N_4 - Bi_2O_3 binary nanocomposite

The FESEM image of (60%) g-C_3N_4 - Bi_2O_3 binary nanocomposites as shown in Fig. (3-26), the introduction of Bi_2O_3 into porous g-C_3N_4 can be seen as small irregular particles on top of g-C_3N_4 surface sheets [179], crystal size was (44.56 – 845.6 nm).

The EDS spectrum and elemental distribution micrographs show the presence of C, N, Bi and O in the (60%) g-C_3N_4 - Bi_2O_3 binary nanocomposite. The EDS spectrum does not show any other peaks than the above-mentioned elements, which indicates the purity of the synthesized sample. The differences in the weight% and atomic% of the elements is due to the variance of the reactant's percentage of binary nanocomposites as show in Fig. (3-27).

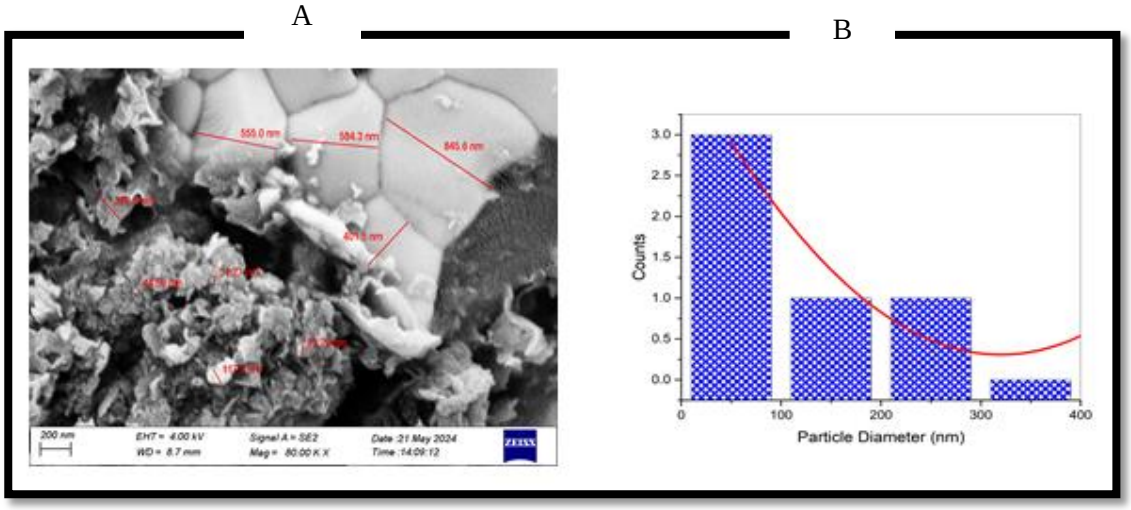

Fig. (3-26)(A) FESEM images of (60%) g-C_3N_4 - Bi_2O_3 binary nanocomposite,(B) Size distribution

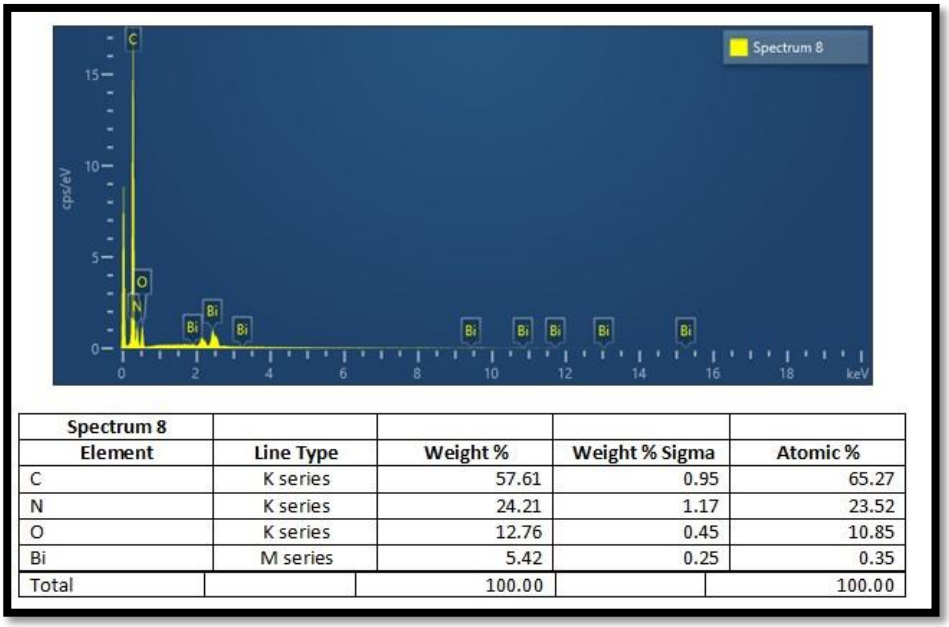

Spectrum 8				
Element	Line Type	Weight %	Weight % Sigma	Atomic %
C	K series	57.61	0.95	65.27
N	K series	24.21	1.17	23.52
O	K series	12.76	0.45	10.85
Bi	M series	5.42	0.25	0.35
Total		100.00		100.00

Fig. (3-27) EDS spectrum of (60%) g-C_3N_4 - Bi_2O_3 binary nanocomposite

The FESEM image of (80%) g-C_3N_4 - Bi_2O_3 binary nanocomposites as shown in Fig. (3-28), the introduction of Bi_2O_3 into porous g-C_3N_4 can be seen as small irregular particles on top of g-C_3N_4 surface sheets [179], crystal size was (27.34 – 796.1 nm).

The EDS spectrum and elemental distribution micrographs shows only the presence of C, N, Bi and O in the (80%) g-C_3N_4 - Bi_2O_3 binary nanocomposite. The EDS spectrum does not show any other peaks than the above-mentioned elements, which indicates the purity of the synthesized sample. The changes in the weight% and atomic% of the elements is due to the variance in reactant's percentage of the binary nanocomposite as show in Fig. (3-29).

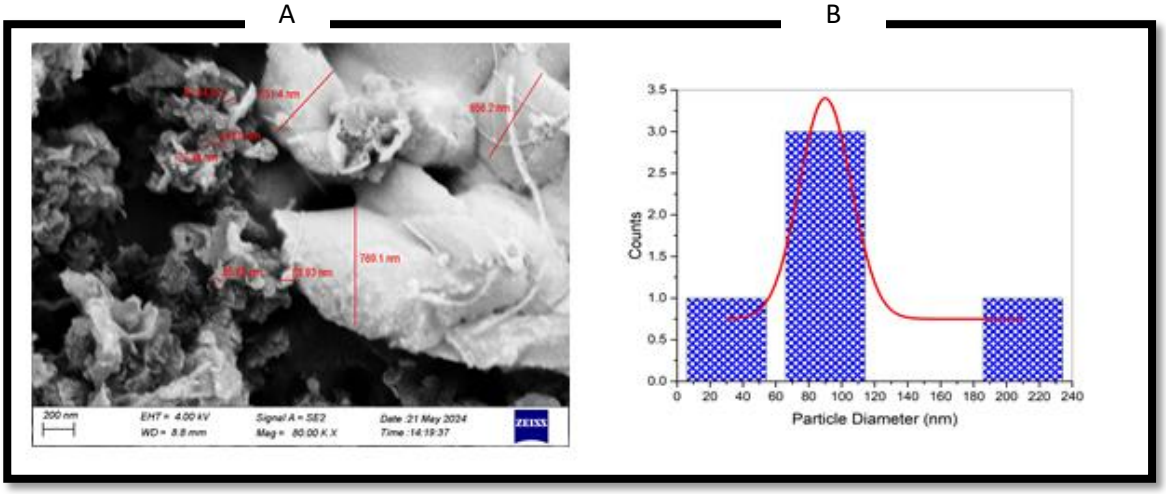

Fig. (3-28)(A) FESEM images of (80%) g-C_3N_4 - Bi_2O_3 binary nanocomposite,(B) Size distribution

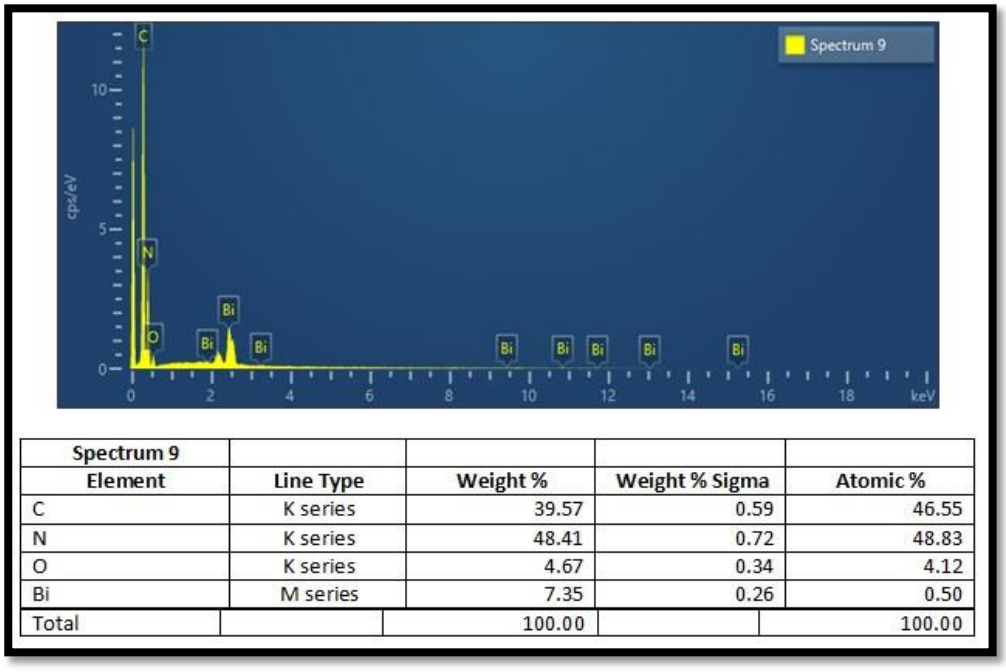

Spectrum 9				
Element	Line Type	Weight %	Weight % Sigma	Atomic %
C	K series	39.57	0.59	46.55
N	K series	48.41	0.72	48.83
O	K series	4.67	0.34	4.12
Bi	M series	7.35	0.26	0.50
Total		100.00		100.00

Fig. (3-29) EDS spectrum of (80%) g-C_3N_4 - Bi_2O_3 binary nanocomposite

The FESEM image of BiC_{80}/GO (10 mg) ternary nanocomposite as shown in Fig. (3-30), Bi_2O_3 interference can be seen with the surface sheets of both g-C_3N_4 and NGO, crystal size was (39.86 – 597.9 nm).

The EDS spectrum and elemental distribution micrographs shows only the presence of C, N, Bi and O in the BiC_{80}/GO (10 mg) ternary nanocomposite. The EDS spectrum does not show any other peaks than the above-mentioned elements, which indicates the purity of the synthesized sample. The changes in the weight% and atomic% of the elements is due to the difference of reactant's percentage of the ternary nanocomposites as show in Fig. (3-31).

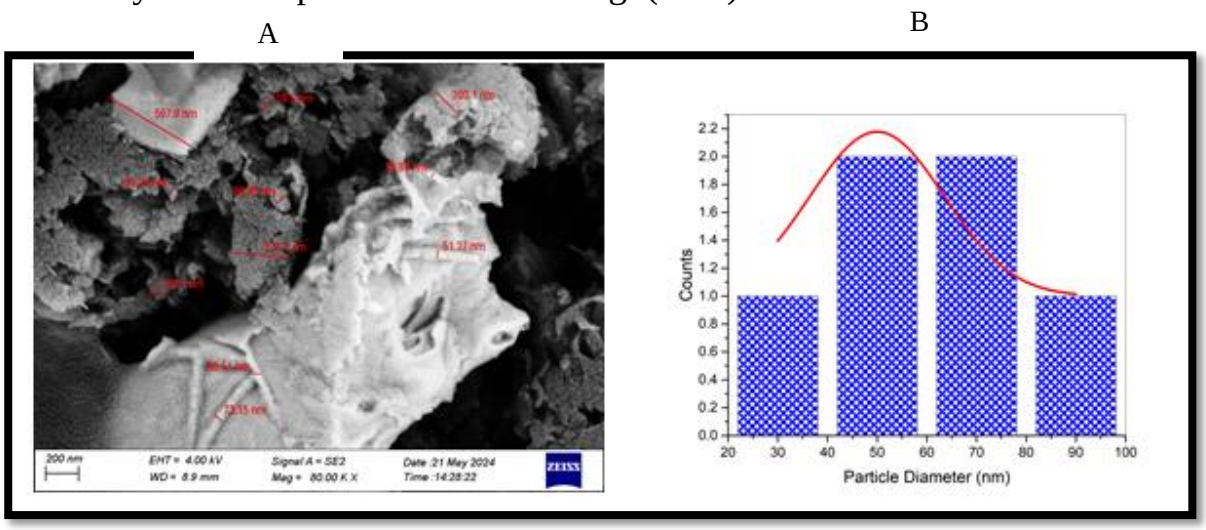

Fig. (3-30)(A) FESEM images of BiC_{80}/GO (10 mg) ternary nanocomposite,(B) Size distribution

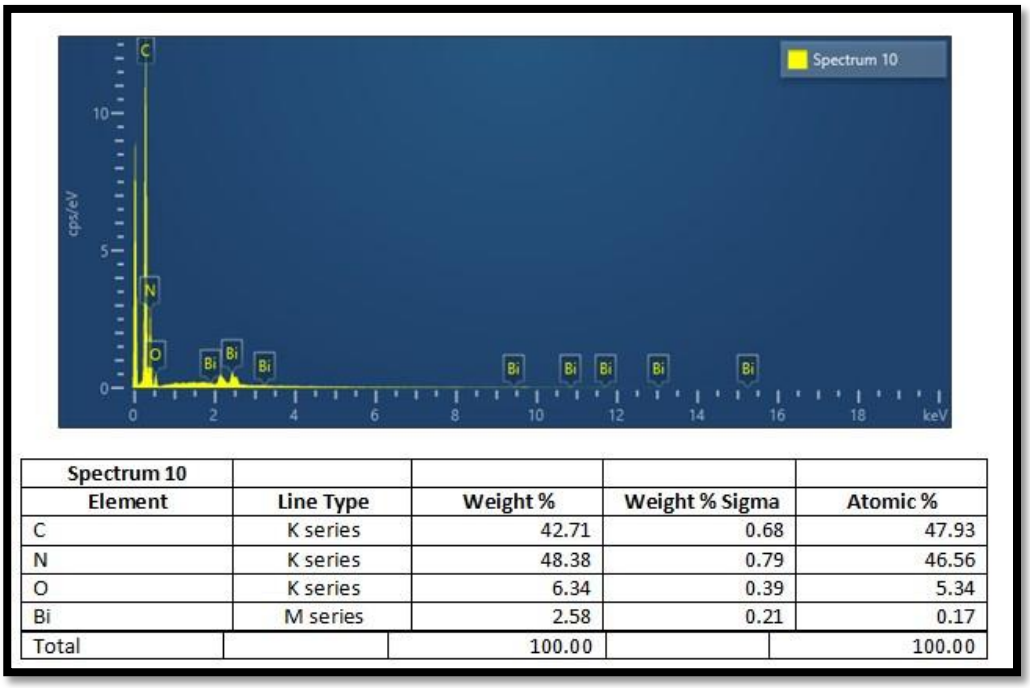

Spectrum 10				
Element	Line Type	Weight %	Weight % Sigma	Atomic %
C	K series	42.71	0.68	47.93
N	K series	48.38	0.79	46.56
O	K series	6.34	0.39	5.34
Bi	M series	2.58	0.21	0.17
Total		100.00		100.00

Fig. (3-31) EDS spectrum of BiC_{80}/GO (10 mg) ternary nanocomposite

The FESEM image of BiC_{80}/GO (20 mg) ternary nanocomposites as shown in Fig. (3-32), Bi_2O_3 interference can be seen with the surface sheets of both g-C_3N_4 and NGO, crystal size was (21.62 – 587 nm).

The EDS spectrum and elemental distribution micrographs shows only the presence of C, N, Bi and O in the BiC_{80}/GO (20 mg) ternary nanocomposite. The EDS spectrum does not show any other peaks than the above-mentioned elements, which indicates the purity of the synthesized sample. The changes in the weight% and atomic% of the elements is due to the difference of the reactant's percentage of ternary nanocomposites as show in Fig. (3-33).

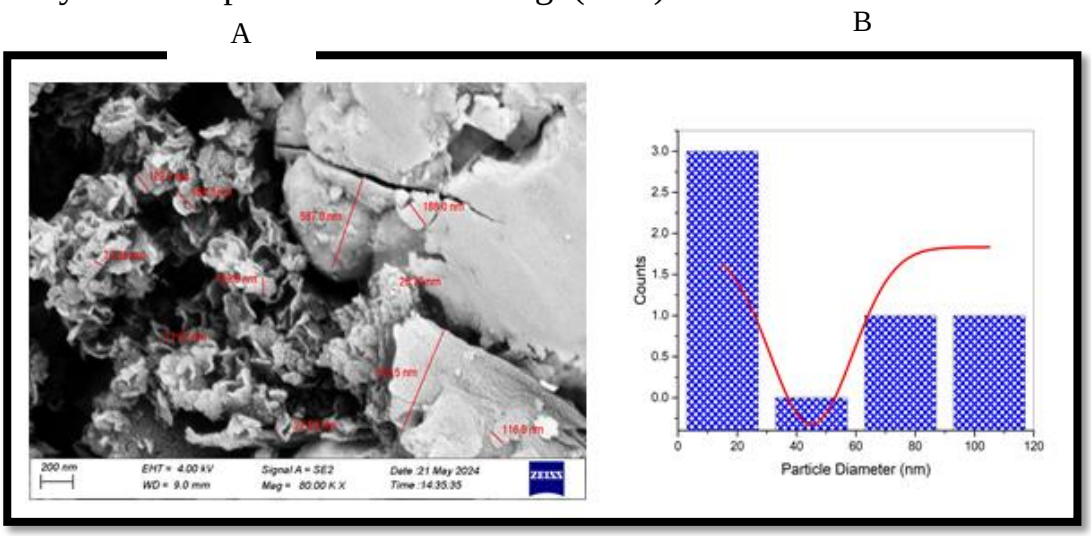

Fig.(3-32)(A) FESEM images of BiC_{80}/GO (20 mg) ternary nanocomposite ,(B) Size distribution

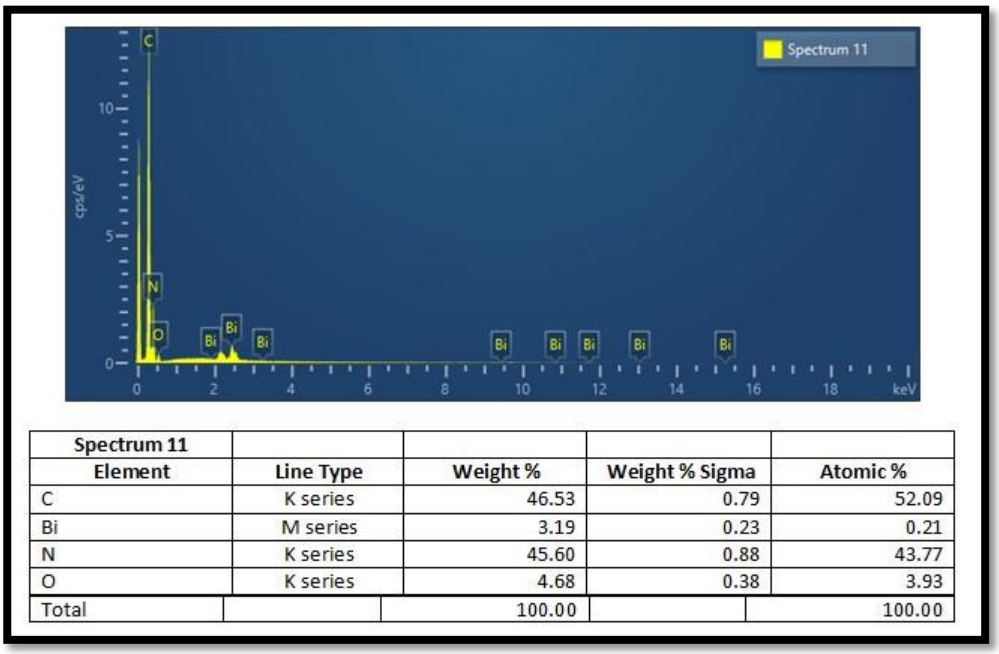

Spectrum 11				
Element	Line Type	Weight %	Weight % Sigma	Atomic %
C	K series	46.53	0.79	52.09
Bi	M series	3.19	0.23	0.21
N	K series	45.60	0.88	43.77
O	K series	4.68	0.38	3.93
Total		100.00		100.00

Fig. (3-33) EDS spectrum of BiC_{80}/GO (20 mg) ternary nanocomposite

The FESEM image of BiC_{80}/GO (30 mg) ternary nanocomposites as shown in Fig. (3-34), Bi_2O_3 interference can be seen with the surface sheets of both g-C_3N_4 and NGO, crystal size was (27.34– 369.2 nm).

The EDS spectrum and elemental distribution micrographs shows only the presence of C, N, Bi and O in the BiC_{80}/GO (30 mg) ternary nanocomposite. The EDS spectrum does not show any other peaks than the above-mentioned elements, which indicates the purity of the synthesized sample. The changes in the weight% and atomic% of the elements is due to the difference of the reactant's percentage of the ternary nanocomposites as show in Fig. (3-35).

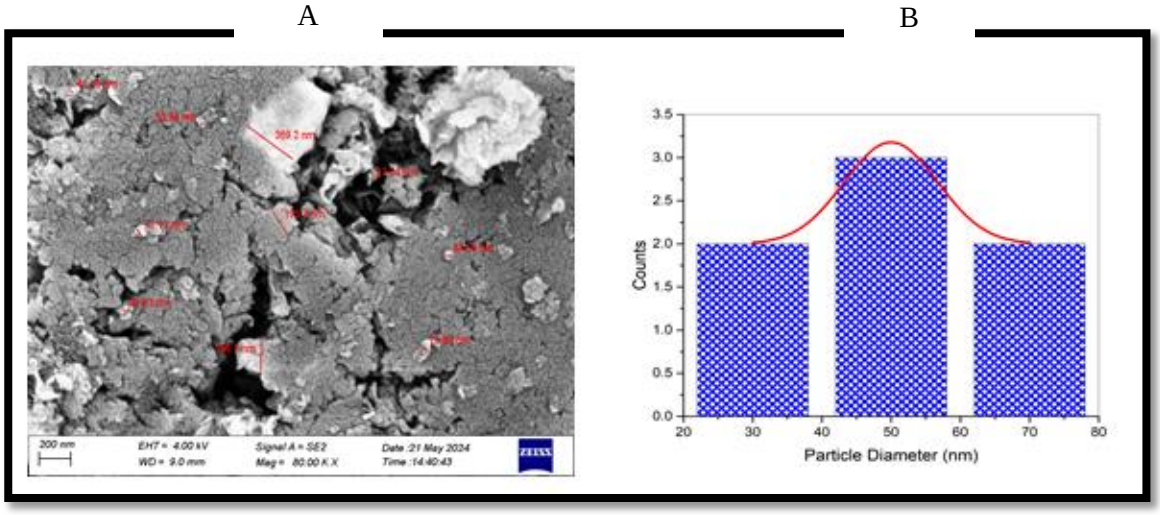

Fig. (3-34)(A) FESEM images of BiC_{80}/GO (30 mg) ternary nanocomposite,(B) Size distribution

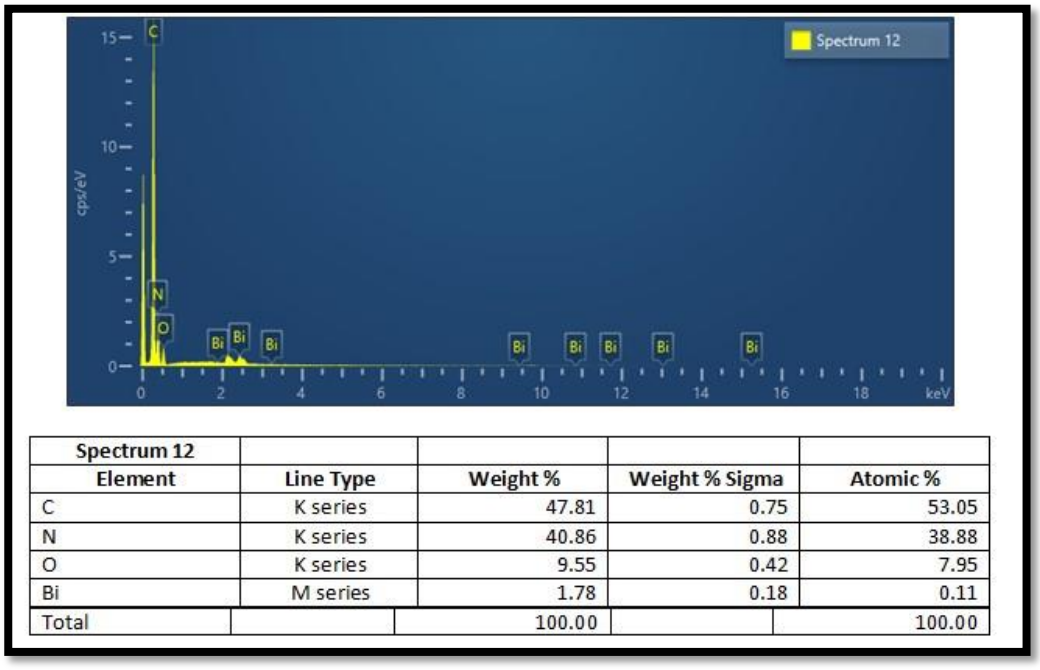

Spectrum 12				
Element	Line Type	Weight %	Weight % Sigma	Atomic %
C	K series	47.81	0.75	53.05
N	K series	40.86	0.88	38.88
O	K series	9.55	0.42	7.95
Bi	M series	1.78	0.18	0.11
Total		100.00		100.00

Fig. (3-35) EDS spectrum of BiC_{80} /GO (30 mg) ternary nanocomposite

The FESEM image of BiC_{80}/GO (40 mg) ternary nano composites as shown in Fig. (3-36), Bi_2O_3 interference can be seen with the surface sheets of both g-C_3N_4 and NGO, crystal size was (24.65– 258.7 nm).

The EDS spectrum and elemental distribution micrographs shows only the presence of C, N, Bi and O in the BiC_{80}/GO (40 mg) ternary nanocomposite. The EDS spectrum does not show any other peaks than the above-mentioned elements, which indicates the purity of the prepared sample. The changes in the weight% and atomic% of the elements is due to the difference of the reactant's percentage of ternary nanocomposites as shown in Fig. (3-37).

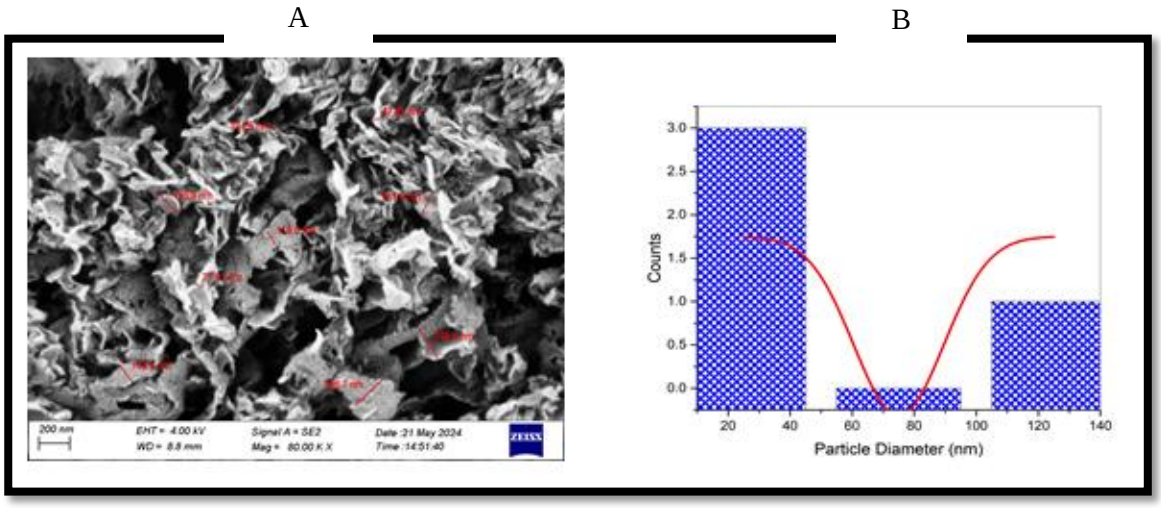

Fig. (3-36)(A) FESEM images of BiC_{80}/GO (40 mg) ternary nanocomposite,(B) Size distribution

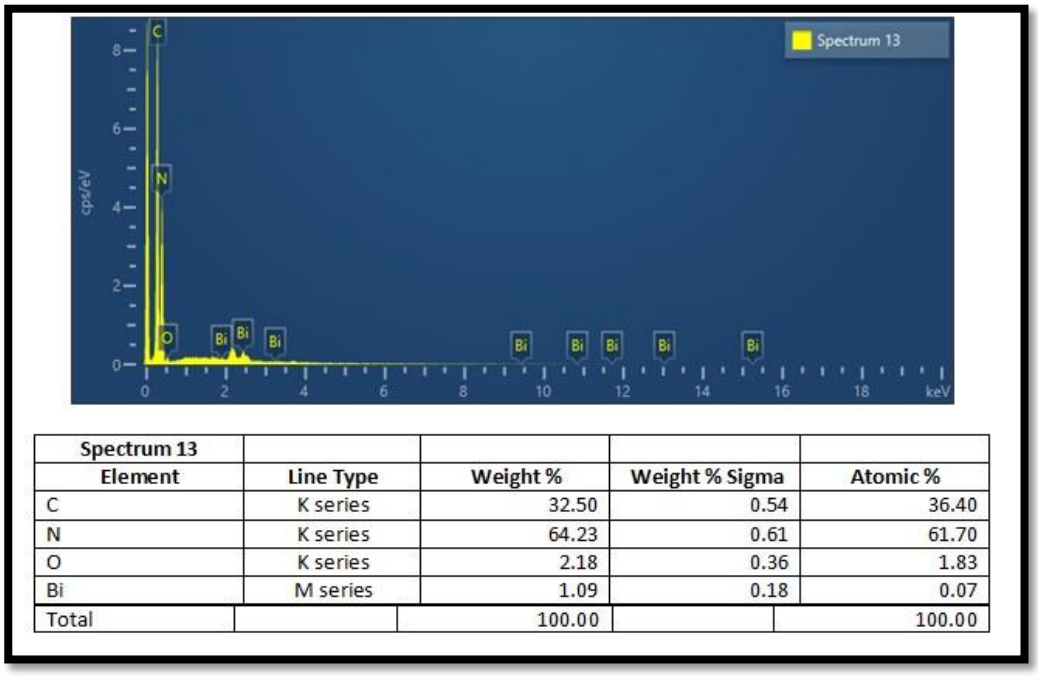

Spectrum 13				
Element	Line Type	Weight %	Weight % Sigma	Atomic %
C	K series	32.50	0.54	36.40
N	K series	64.23	0.61	61.70
O	K series	2.18	0.36	1.83
Bi	M series	1.09	0.18	0.07
Total		100.00		100.00

Fig. (3-37) EDS spectrum of BiC_{80}/GO (40 mg) ternary nanocomposite

3.2 Photocatalytic Degradation of the methylene blue (MB)

3.2.1 Photocatalytic Degradation of the MB dye by g-C_3N_4, Bi_2O_3 and NGO

Photocatalytic activity of g-C_3N_4, Bi_2O_3 and NGO was tested against MB dye. The MB dye solution was prepared (10 mg.L^{-1}), the absorption spectrum was obtained as shown in the Fig. (3-38) λ_{max}=664.50 nm, the catalyst mixed with the MB dye in the dark for 30 minutes before being exposure to the visible light (Tungsten lamp 300 watt) as shown in Fig. (3-39). Plotting C/C_o versus irradiation time. The concentration of the dye when subjected to photolysis was calculated using Eq. (3-2).

$A_1/C_1=A_2/C_2$ ….. (3-2)

Where A_1 represents the absorbance of the dye before the photolysis and C_1 is the initial concentration of the dye solution, While A_2 represents the absorbance of the dye after photolysis and C_2 is the concentration of the dye solution measured at different time interval during the photocatalytic reaction. Photocatalytic degradation percentage (D%) was calculated from the Eq.

$D\% = (C_o - C/C_o) \times 100$ …….(1-4)

where, C_o is the initial concentration of the dye solution and C is the concentration of the dye solution measured at different time interval during the photocatalytic reaction as shown in the tables (3-7), (3-8), (3-9) respectively. In the dark the adsorption process of the dye occurred only. The degradation efficiency D% of Bi_2O_3, g-C_3N_4, NGO was, 0.95, 93.34, and 98.335 respectively on the MB dye solution 10 mg.L^{-1} (g-C_3N_4 and Bi_2O_3) and 100 mg.L^{-1} for NGO in a time period of 180 min. The results show that the degradation efficiency of NGO> g-C_3N_4 > Bi_2O_3.

Demethylation is the first step in the photodegradation of MB. Next, the central aromatic ring of the molecule is broken, followed by the side aromatic rings. Finally, the fragments from the first two steps are converted to intermediate species, such as R-NH_3^+, phenol, aniline, and aldehydic/carboxylate species. Finally, these intermediates are converted to the final products, which include CO_2, H_2O, SO_4^{2-}, and NH_4^+ [180]. The majority of the reaction intermediates are produced when the MB dye's aromatic ring breaks. In the end, the dye fragments are broken down into H_2O, CO_2, ammonium ions, and sulfate ions via subsequent chemical intermediates such as aldehyde, carboxylic species, phenols, and amines [181].

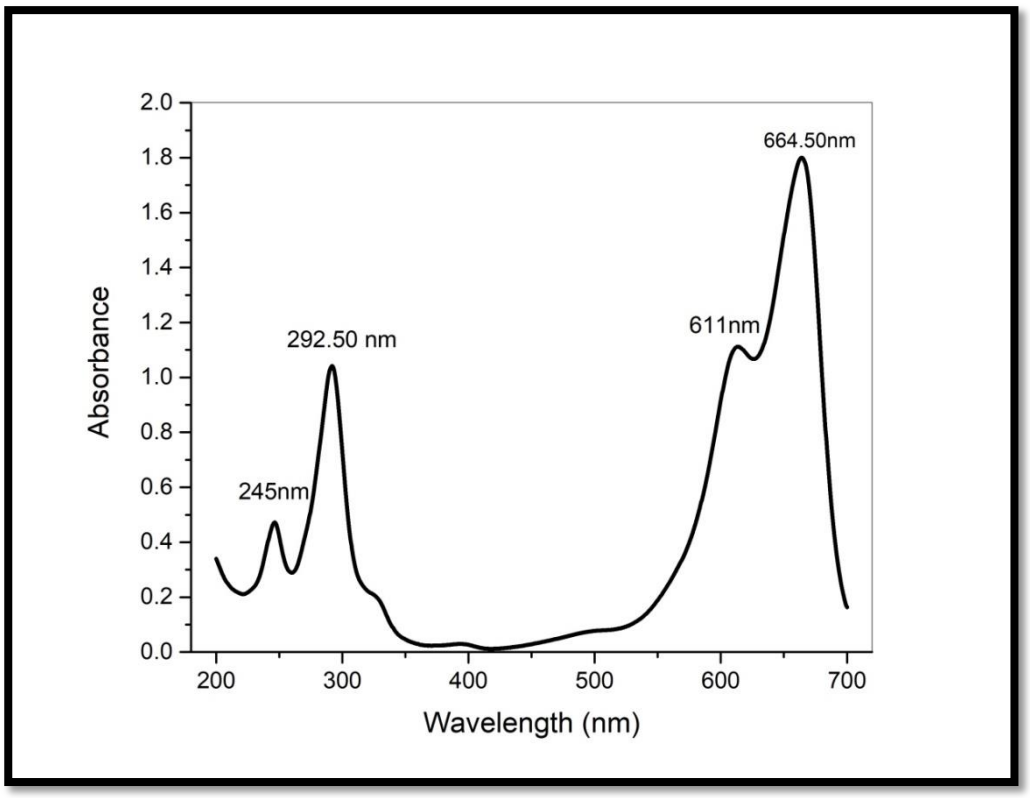

Fig. (3-38) Absorption spectrum of MB dye (10 mg.L^{-1})

Table (3-7) Photocatalytic degradation of MB (10 mg.L^{-1}), Vol.=50 ml by g-C_3N_4 wt.=50 mg

Time (min)	**Absorption n=3**	**SD**	**RSD**	**Concentration (mg.L^{-1})**	**D%**	**C/C_o**	**Note**
30	0.679	±0.001732	0.255088	3.057	69.43	0.3057	In dark
30	0.612	±0.021071	3.443024	2.755	72.45	0.2755	Visible light
60	0.534	±0.012124	2.270479	2.404	75.96	0.2404	Visible light
90	0.387	±0.012897	3.332565	1.745	82.55	0.1745	Visible light
120	0.254	±0.001	0.393701	1.143	88.57	0.1143	Visible light
150	0.223	±0.001732	0.776704	1.004	89.96	0.1004	Visible light
180	0.148	±0.001732	1.170305	0.666	93.34	0.0666	Visible light

Table (3-8) Photocatalytic degradation of MB (10 mg.L^{-1}), Vol.=50 ml by Bi_2O_3 wt.=50 mg

Time (min)	**Absorption** n=3	**SD**	**RSD**	**Concentration (mg.L^{-1})**	**D%**	**C/C_o**	**Note**
30	2.3250	±0.002646	0.113796	9.978	0.22	0.9978	In dark
30	2.3246	±0.004041	0.173856	9.976	0.24	0.9976	Visible light
60	2.3230	±0.004	0.172191	9.969	0.31	0.9969	Visible light
90	2.3203	±0.006506	0.280412	9.958	0.42	0.9958	Visible light
120	2.3166	±0.005508	0.237744	9.942	0.58	0.9942	Visible light
150	2.3086	±0.003512	0.152122	9.908	0.92	0.9908	Visible light
180	2.3080	±0.004583	0.198552	9.905	0.95	0.9905	Visible light

Table (3-9) Photocatalytic degradation of MB (100 mg.L^{-1}), Vol.=50 ml by NGO wt.=50 mg

Time (min)	Absorption n=3	SD	RDS	Concentration (mg.L^{-1})	D%	C/C$_o$	Note
30	3.4076	±0.004041	0.118601	97.332	2.668	0. 97332	In dark
30	1.5710	±0.001	0.063654	44.872	55.128	0.44872	Visible light
60	0.4010	±0.001	0.249377	11.453	88.547	0.11453	Visible light
90	0.1863	±0.000577	0.309904	5.321	94.679	0.05321	Visible light
120	0.1176	±0.000577	0.490944	3.359	96.641	0.03359	Visible light
150	0.0780	±0.001	1.282051	2.227	97.773	0.02227	Visible light
180	0.0583	±0.000577	0.990309	1.665	98.335	0.01665	Visible light

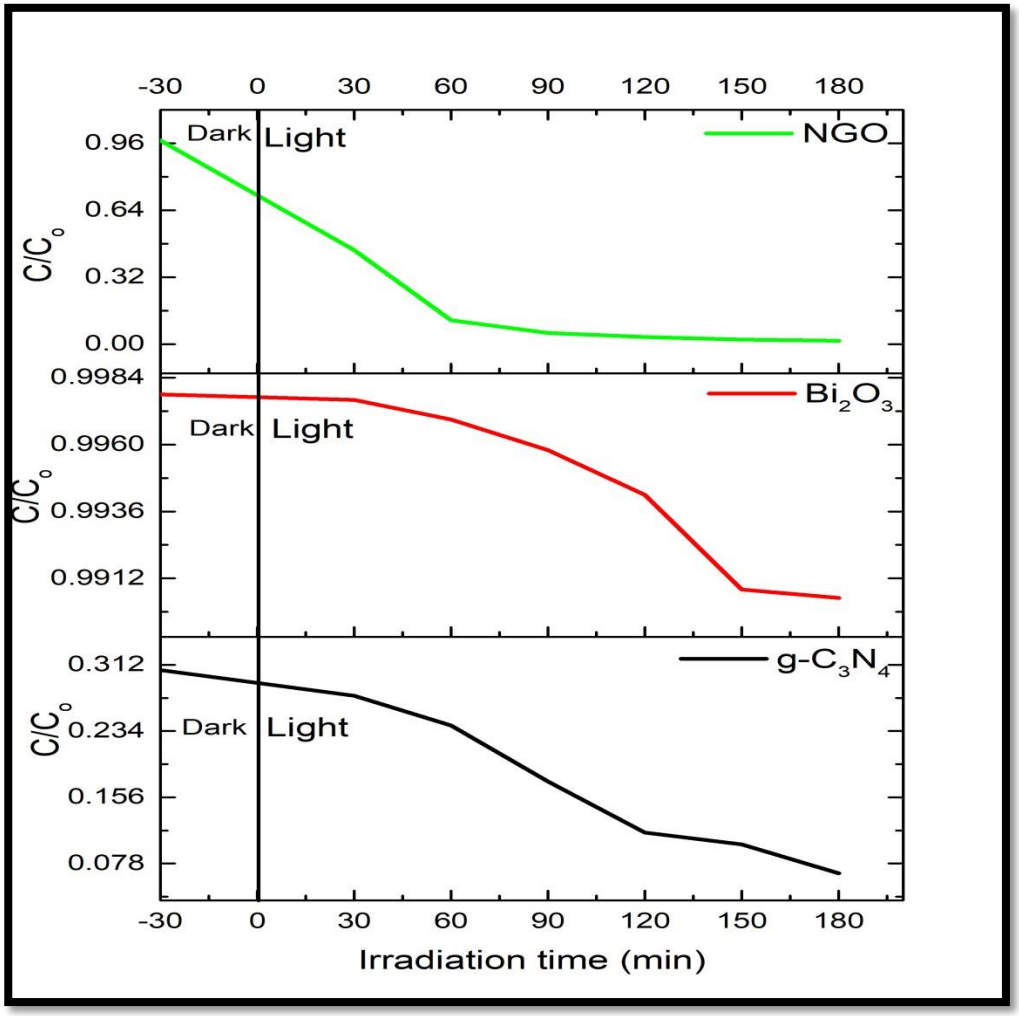

Fig, (3-39) Photocatalytic degradation efficiency of MB dye by g-C_3N_4, Bi_2O_3 and NGO under visible light irradiation

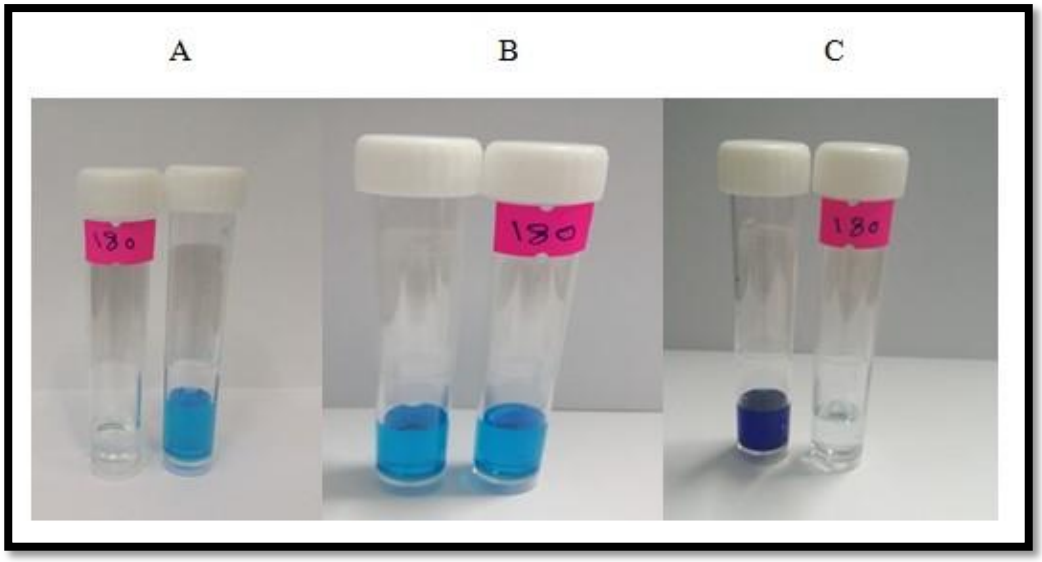

Fig, (3-40) MB dye before and after Photocatalytic degradation by (A) g-C_3N_4, (B) Bi_2O_3 (C) NGO

3.2.2 Photocatalytic Degradation of the MB dye by g-C_3N_4 -Bi_2O_3 binary nanocomposites

Photocatalytic activity of (20%) g-C_3N_4 -Bi_2O_3, (40%) g-C_3N_4 -Bi_2O_3, (60%) g-C_3N_4 -Bi_2O_3 and (80%) g-C_3N_4 -Bi_2O_3 binary nanocomposites was tested against MB dye. The dye solution (10 mg.L^{-1}) mixed with the catalyst, placed in the dark for 30 minutes (adsorption) of the MB dye, before being exposure to visible light and the results are shown in Fig. (3-41). By plotting C/C_o versus irradiation time, the results shown in the table, (3-10), (3-11), (3-12) and (3-13) respectively. The efficiency D% of (20%) g-C_3N_4 -Bi_2O_3, (40%) g-C_3N_4 -Bi_2O_3, (60%) g-C_3N_4 -Bi_2O_3 and (80%) g-C_3N_4 -Bi_2O_3 was, 21.77 ,35. 4, 41.48 and 98.38 respectively in a time period of 180 min. The best photo catalytic degradation was (80%) g-C_3N_4 -Bi_2O_3 compared to the other binary nanocomposites.

Table (3-10) Photocatalytic degradation of MB (10 mg.L^{-1}), Vol.=50 ml by (20%) g-C_3N_4-Bi_2O_3 wt.=50 mg

Time (min)	Absorption n=3	SD	RSD	Concentration (mg.L^{-1})	D%	C/C_o	Note
30	1.9256	±0.012583	0.653462	8.898	11.02	0.8898	In dark
30	1.902	±0.005	0.262881	8.789	12.11	0.8789	Visible light
60	1.827	±0.007	0.383142	8.442	15.58	0.8442	Visible light
90	1.7953	±0.004041	0.225113	8.296	17.04	0.8296	Visible light
120	1.753	±0.004	0.22818	8.100	19.00	0.8100	Visible light
150	1.7206	±0.005508	0.320096	7.951	20.49	0.7951	Visible light
180	1.693	±0.003	0.1772	7.823	21.77	0.7823	Visible light

Table (3-11) Photocatalytic degradation of MB (10 mg.L^{-1}), Vol.=50 ml by (40%) g-C_3N_4-Bi_2O_3 wt.=50 mg

Time (min)	Absorption n=3	SD	RSD	Concentration (mg.L^{-1})	D%	C/C_o	Note
30	1.795	±0.001732	0.096493	7.824	21.76	0.7824	In dark
30	1.749	±0.001	0.057176	7.624	23.76	0.7624	Visible light
60	1.692	±0.003464	0.204734	7.375	26.25	0.7375	Visible light
90	1.614	±0.002	0.123916	7.035	29.65	0.7035	Visible light
120	1.5626	±0.002517	0.161053	6.811	31.89	0.6811	Visible light
150	1.5216	±0.001528	0.100389	6.632	33.68	0.6632	Visible light
180	1.4820	±0.003	0.202429	6.460	35.40	0.6460	Visible light

Table (3-12) Photocatalytic degradation of MB (10 mg.L^{-1}), Vol.=50 ml by (60%) g-C_3N_4-Bi_2O_3 wt.=50 mg

Time(min)	Absorption n=3	SD	RSD	Concentration (mg.L^{-1})	D%	C/C_o	Note
30	1.7060	±0.001	0.058617	7.334	26.66	0.7334	In dark
30	1.6680	±0.002	0.119904	7.171	28.29	0.7171	Visible light
60	1.6116	±0.000577	0.035825	6.928	30.72	0.6928	Visible light
90	1.5676	±0.001528	0.097444	6.739	32.61	0.6739	Visible light
120	1.4513	±0.001155	0.079563	6.239	37.61	0.6239	Visible light
150	1.3946	±0.002082	0.149266	5.995	40.05	0.5995	Visible light
180	1.3613	±0.002309	0.169647	5.852	41.48	0.5852	Visible light

Table (3-13) Photocatalytic degradation of MB (10 mg.L^{-1}), Vol.=50 ml by (80%) g-C_3N_4-Bi_2O_3 wt.=50 mg

Time (min)	Absorption n=3	SD	RSD	Concentration (mg.L^{-1})	D%	C/C_o	Note
30	0.9023	±0.00577	0.063987	3.859	61.41	0.3859	In dark
30	0.6943	±0.00577	0.083156	2.969	70.31	0.2969	Visible light
60	0.5043	±0.00577	0.114485	2.156	78.61	0.2156	Visible light
90	0.3366	±0.00577	0.171524	1.439	85.61	0.1439	Visible light
120	0.2030	±0	0	0.868	91.32	0.0868	Visible light
150	0.1056	±0.00577	0.546733	0.451	95.49	0.0451	Visible light
180	0.0380	±0.001	2.631579	0.162	98.38	0.0162	Visible light

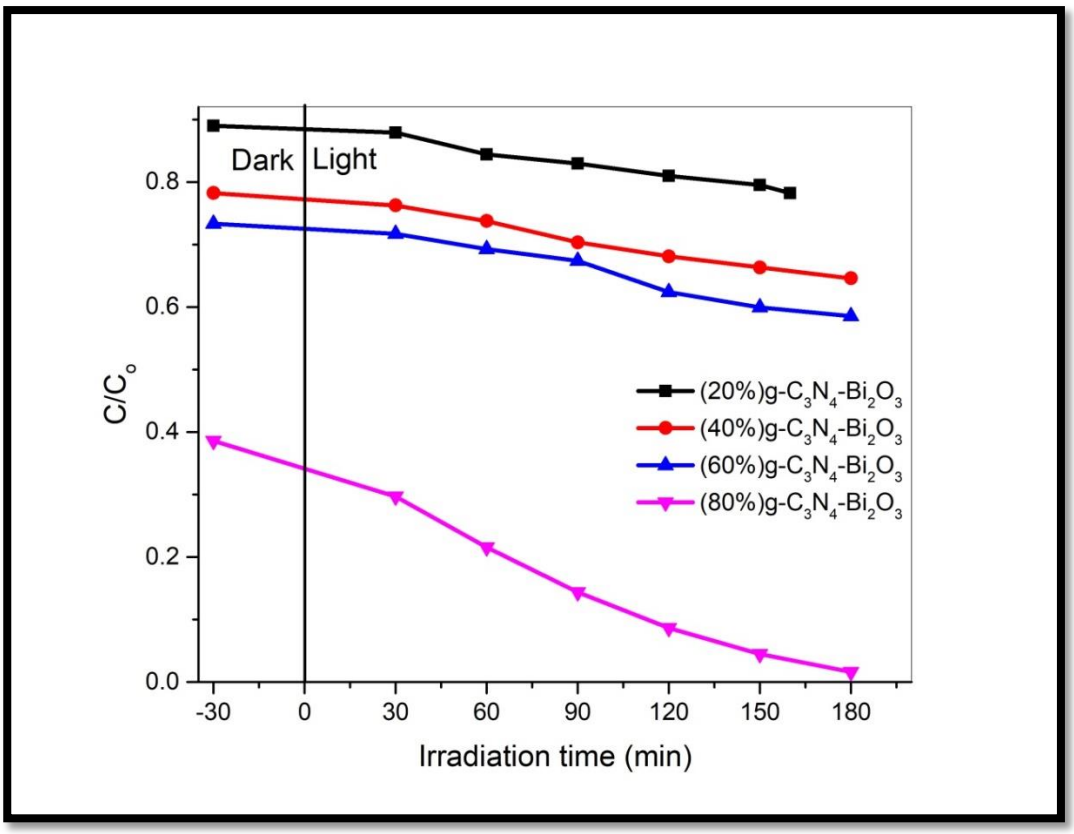

Fig. (3-41) Photocatalytic degradation of MB dye by (20%) g-C_3N_4 -Bi_2O_3, (40%) g-C_3N_4 – Bi_2O_3, (60%) g-C_3N_4 -Bi_2O_3 and (80%) g-C_3N_4 -Bi_2O_3 binary nanocomposites

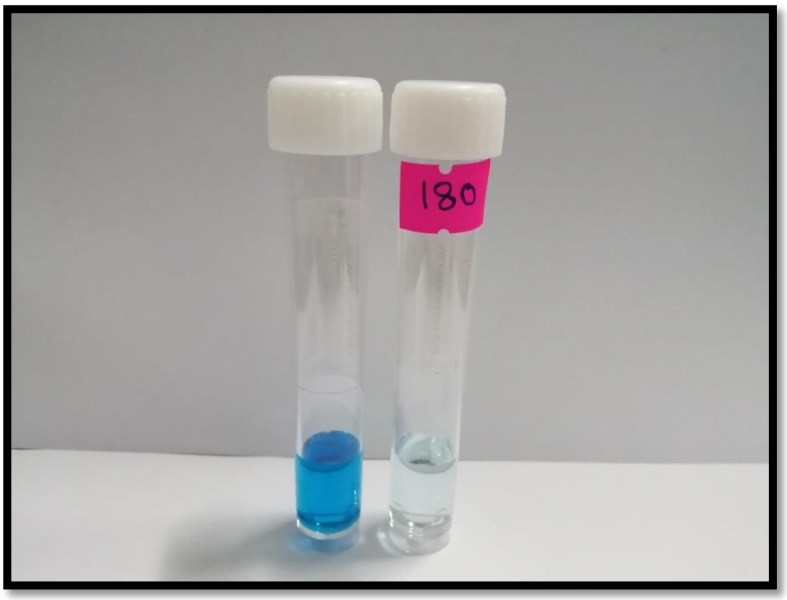

Fig. (3-42) MB dye before and after photocatalytic degradation by (80%) g-C_3N_4 -Bi_2O_3 binary nanocomposite

3.2.3 Photocatalytic Degradation of the MB dye by novel BiC_{80}/GO (x mg) ternary nanocomposites

Photocatalytic activity of BiC_{80}/GO (10 mg), BiC_{80}/GO (20 mg), BiC_{80}/GO (30 mg) and BiC_{80}/GO (40 mg) ternary nanocomposites was tested against MB dye. The MB dye solution (10 $mg.L^{-1}$) was mixed with each catalyst, placed in the dark for 30 minutes (adsorption) of MB dye, as shown in Fig. (3-43). By plotting C/C_o versus the irradiation time, the results are shown in the table (3-14), (3-15), (3-16), (3-17) respectively. The degradation efficiency %D of the catalysts, BiC_{80}/GO (10 mg), BiC_{80}/GO (20 mg), BiC_{80}/GO (30 mg) and BiC_{80}/GO (40 mg), 88.98, 97.81, 96.65 and 91.58 respectively, on the MB dye solution in a time period of 180 min. The result shows that BiC_{80}/GO (20 mg) is more efficient in terms of MB dye degradation compared to the other ternary nanocomposites.

Table (3-14) Photocatalytic degradation of MB (10 $mg.L^{-1}$), Vol.=50 ml by BiC_{80}/GO (10mg), wt.=50 mg

Time (min)	Absorption n=3	SD	RSD	Concentration ($mg.L^{-1}$)	D%	C/C_o	Note
30	1.1476	±0.000577	0.050309	4.891	51.09	0.4891	In dark
30	0.9953	±0.000577	0.058008	4.242	57.58	0.4242	Visible light
60	0.8253	±0.000577	0.069956	3.517	64.83	0.3517	Visible light
90	0.6966	±0.000577	0.082881	2.969	70.31	0.2969	Visible light
120	0.5483	±0.001155	0.210596	2.337	76.63	0.2337	Visible light
150	0.3966	±0.000577	0.145575	1.690	83.1	0.1690	Visible light
180	0.2586	±0.000577	0.22326	1.102	88.98	0.1102	Visible light

Table (3-15) Photocatalytic degradation of MB (10 $mg.L^{-1}$), Vol.=50 ml by BiC_{80}/GO (20mg), wt.=50 mg

Time (min)	Absorption n=3	SD	RSD	Concentration ($mg.L^{-1}$)	D%	C/C_o	Note
30	0.9903	±0.000577	0.058301	4.257	57.43	0.4257	In dark
30	0.6930	±0	0	2.979	70.21	0.2979	Visible light
60	0.4536	±0.000577	0.127282	1.950	80.5	0.1950	Visible light
90	0.2813	±0.000577	0.205244	1.209	87.91	0.1209	Visible light
120	0.1553	±0.000577	0.371765	0.668	93.32	0.0668	Visible light
150	0.0706	±0.000577	0.817777	0.303	96.97	0.0303	Visible light
180	0.0510	±0	0	0.219	97.81	0.0219	Visible light

Table (3-16) Photocatalytic degradation of MB (10 mg.L^{-1}), Vol.=50 ml by BiC_{80}/GO (30mg), wt.=50 mg

Time (min)	Absorption n=3	SD	RSD	Concentration (mg.L^{-1})	D%	C/C_o	Note
30	1.2030	±0.001	0.083126	4.880	51.2	0.4880	In dark
30	0.9503	±0.000577	0.060755	3.855	61.45	0.3855	Visible light
60	0.7436	±0.000577	0.077643	3.016	69.84	0.3016	Visible light
90	0.5396	±0.001528	0.283085	2.189	78.11	0.2189	Visible light
120	0.3456	±0.001528	0.441992	1.402	85.98	0.1402	Visible light
150	0.1790	±0.001	0.558659	0.726	92.74	0.0726	Visible light
180	0.0826	±0.001528	1.849304	0.335	96.65	0.0335	Visible light

Table (3-17) Photocatalytic degradation of MB (10 mg.L^{-1}), Vol.=50 ml BiC_{80}/GO (40mg), wt.=50 mg

Time (min)	Absorption n=3	SD	RSD	Concentration (mg.L^{-1})	D%	C/C_o	Note
30	1.2973	±0.001155	0.089008	5.506	44.94	0.5506	In dark
30	1.1120	±0.001	0.089928	4.719	52.81	0.4719	Visible light
60	0.9250	±0	0	3.926	60.74	0.3926	Visible light
90	0.7390	±0	0	3.136	68.64	0.3136	Visible light
120	0.5496	±0.000577	0.105049	2.332	76.68	0.2332	Visible light
150	0.3756	±0.000577	0.153714	1.594	84.06	0.1594	Visible light
180	0.1986	±0.000577	0.29071	0.842	91.58	0.0842	Visible light

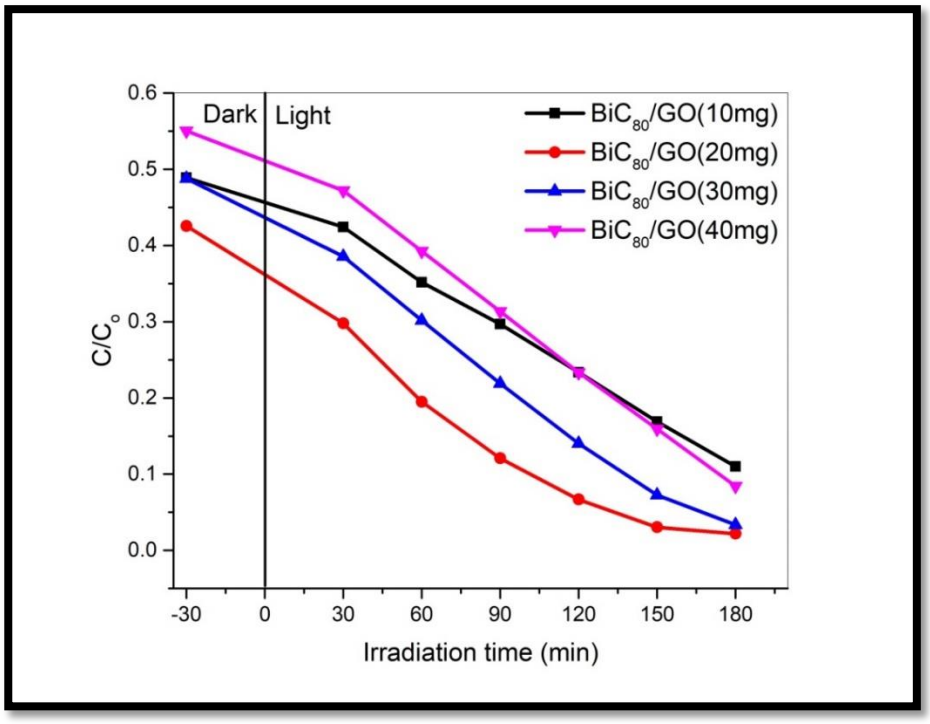

Fig, (3-43) Photocatalytic degradation MB dye by of BiC_{80}/GO (10 mg), BiC_{80}/GO (20 mg), BiC_{80}/GO (30 mg) and BiC_{80}/GO (40 mg) ternary nanocomposites under visible light irradiation

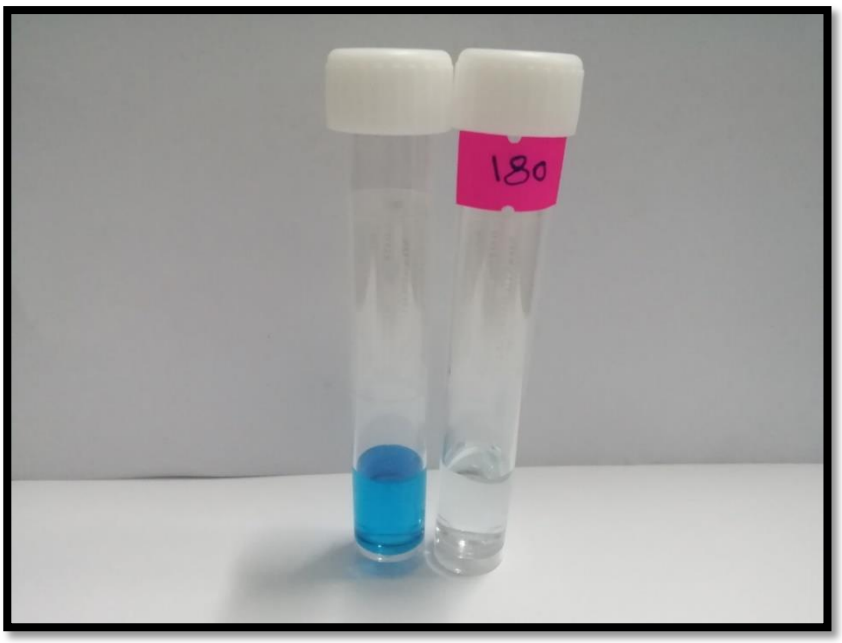

Fig. (3-44) MB dye before and after photocatalytic degradation by BiC_{80}/GO (20 mg) ternary nanocomposite under visible light irradiation

3.2.4 Recycle Process

Recycle process up to two cycles and the results are shown in Fig. (3-45). In the first cycle, (80%) g-C_3N_4 -Bi_2O_3 binary nanocomposites shows 71.154% of photocatalytic degradation efficiency in a time period of 180 min. Then the binary nanocomposites were separated by centrifugation, dried in oven then used for the next cycle. In the second cycle (80%) g-C_3N_4 -Bi_2O_3 binary nano composites shows 23.608% of degradation in a time period of 180 min. Thus, the results evidently show that the synthesized binary nanocomposites can be reused.

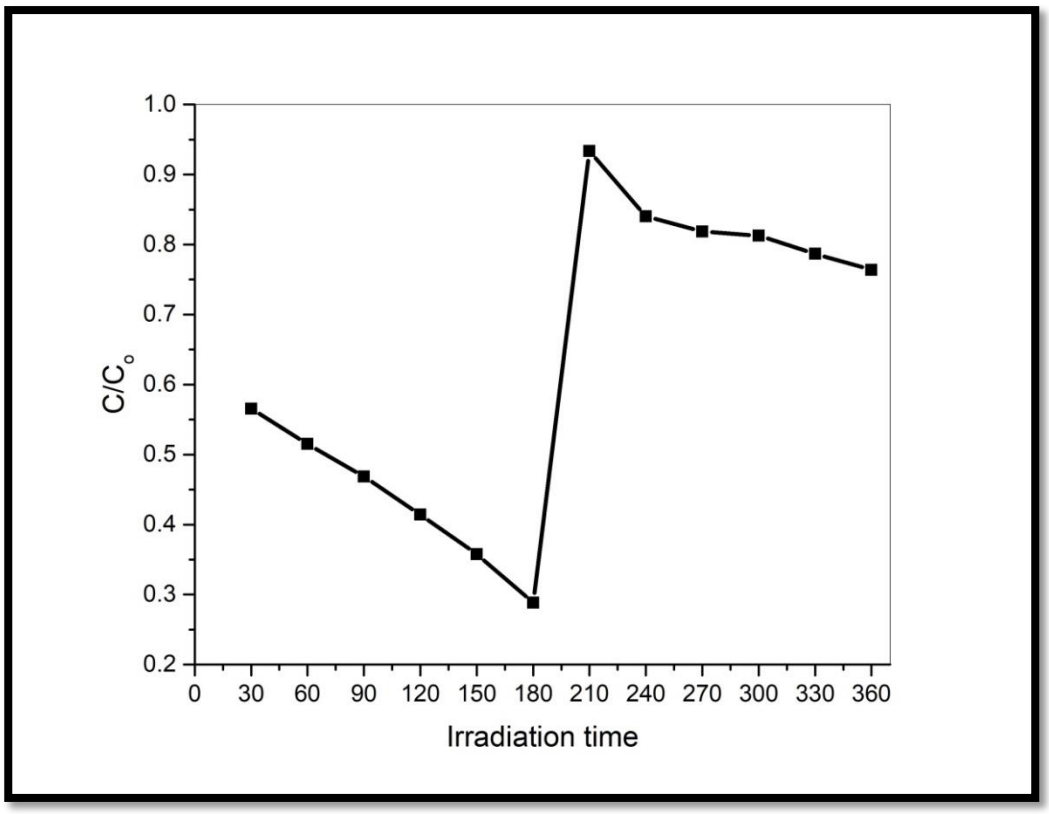

Fig. (3-45) Recycle process of (80%) g-C_3N_4 -Bi_2O_3 binary nanocomposite against MB dye for two cycles

recycle process up to tow cycles and the results are shown in Fig. (3-46). In the first cycle, BiC_{80}/GO (20 mg) ternary nanocomposites show 82.66% of photocatalytic degradation efficiency in a time period of 180 min. Then the ternary nanocomposite was separated by centrifugation, dried in oven, then used for the next cycles. In the second cycle BiC_{80}/GO (20 mg) ternary nano composites shows 28.38% of degradation in a time period of 180 min. Thus, the results evidently show that the synthesized ternary nanocomposites can be reused.

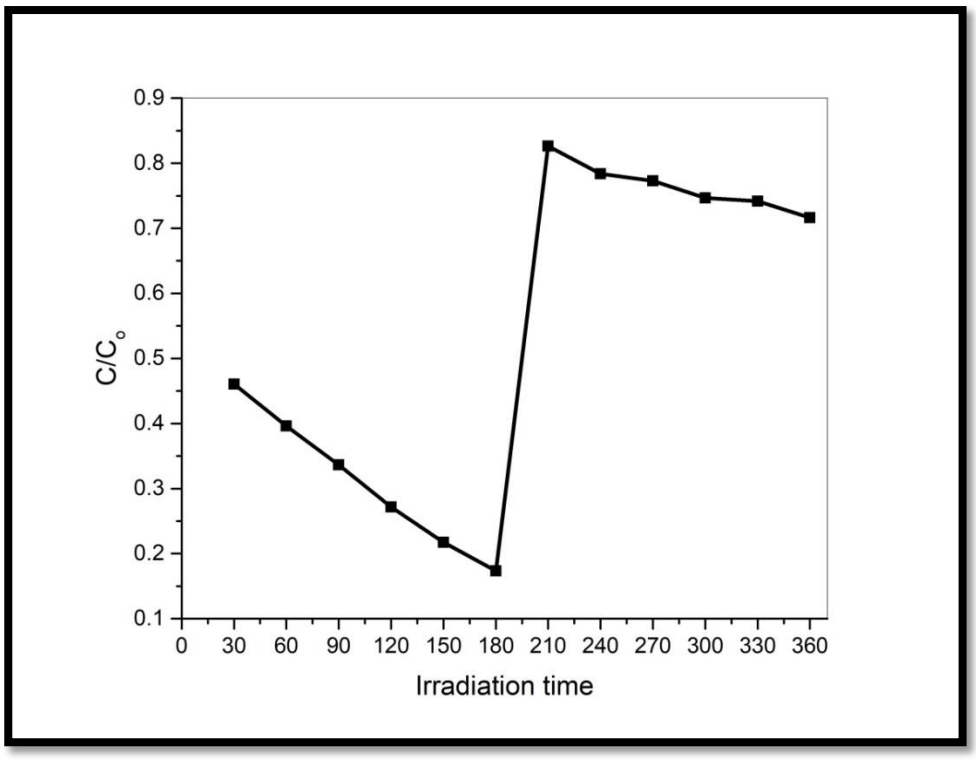

Fig. (3-46) Recycle process of BiC_{80}/GO (20 mg) ternary nanocomposite against MB dye for two cycles

3.3 Optimum Conditions of photocatalytic degradation of MB dye

3.3.1 Effect of catalyst weight

The effect of the catalyst weight of (80%) g-C_3N_4 -Bi_2O_3 binary nano composite and BiC_{80}/GO (20 mg) ternary nanocomposite on the photocatalytic degradation of MB dye was studied by using different weights of composites (40 ,50 and 60 mg). Photocatalytic activity of (80%) g-C_3N_4 -Bi_2O_3 binary nanocomposite was tested against MB dye. The dye solution (10 mg.L^{-1}), under visible light (Tungsten lamp 300 watt) irradiation for a time period of 180 min, when the catalyst mixed with the MB dye, placed in the dark for 30 minutes before being exposure to visible light and the results are shown in Fig. (3-47). By plotting the C/C_o versus irradiation time which based on the results in the tables (3-18), (3-19), (3-20) respectively. The efficiency D% of 40, 50 and 60 mg of (80%) g-C_3N_4 -Bi_2O_3 was 53.653, 98.38 and 83.133 respectively in degradation the MB dye 10 ppm. This means that wt.=50mg is more efficient in terms of MB dye degradation compared to the other weights.

Table (3-18) Photocatalytic degradation of MB (10 mg.L^{-1}), Vol.=50 ml by (80%) g-C_3N_4 - Bi_2O_3 wt.=40 mg binary nanocomposite at 25^oC

Time (min)	Absorption n=3	SD	RSD	Concentration (mg.L^{-1})	D%	C/C_o	Note
30	1.8706	±0.001528	0.08166	7.2307	27.696	0.7230	In dark
30	1.772	±0.003606	0.203474	6.8496	31.504	0.6849	Visible light
60	1.637	±0.001	0.061087	6.3277	36.723	0.6327	Visible light
90	1.501	±0.001732	0.115393	5.8020	41.98	0.5802	Visible light
120	1.4033	±0.003215	0.229071	5.4244	45.756	0.5424	Visible light
150	1.3126	±0.001528	0.116374	5.0738	49.262	0.5073	Visible light
180	1.199	±0.001732	0.144458	4.6347	53.653	0.4634	Visible light

Table (3-19) Photocatalytic degradation of MB (10 mg.L^{-1}), Vol.=50 ml by (80%) g-C_3N_4 - Bi_2O_3 wt.=50 mg binary nanocomposite at 25^oC

Time (min)	Absorption n=3	SD	RSD	Concentration (mg.L^{-1})	D%	C/C_o	Note
30	0.9023	±0.000577	0.063987	3.859	61.41	0.3859	In dark
30	0.6943	±0.000577	0.083156	2.969	70.31	0.2969	Visible light
60	0.5043	±0.000577	0.114485	2.156	78.61	0.2156	Visible light
90	0.3366	±0.000577	0.171524	1.439	85.61	0.1439	Visible light
120	0.2030	±0	0	0.868	91.32	0.0868	Visible light
150	0.1056	±0.000577	0.546733	0.451	95.49	0.0451	Visible light
180	0.0380	±0.001	2.631579	0.162	98.38	0.0162	Visible light

Table (3-20) Photocatalytic degradation of MB (10 mg.L^{-1}), Vol.=50 ml by (80%) g-C_3N_4 - Bi_2O_3 wt.=60 mg binary nanocomposite at 25^oC

Time (min)	Absorption n=3	SD	RSD	Concentration (mg.L^{-1})	D%	C/C_o	Note
30	1.3376	±0.000577	0.043163	5.1092	48.908	0.5109	In dark
30	1.2303	±0.001528	0.124159	4.6993	53.007	0.4699	Visible light
60	1.0636	±0.000577	0.054283	4.0626	59.374	0.4062	Visible light
90	0.9020	±0.001	0.110865	3.4453	65.547	0.3445	Visible light
120	0.7616	±0.000577	0.075808	2.9090	70.91	0.2909	Visible light
150	0.6063	±0.001528	0.343339	2.3158	76.842	0.2315	Visible light
180	0.4416	±0.000577	0.130741	1.6867	83.133	0.1686	Visible light

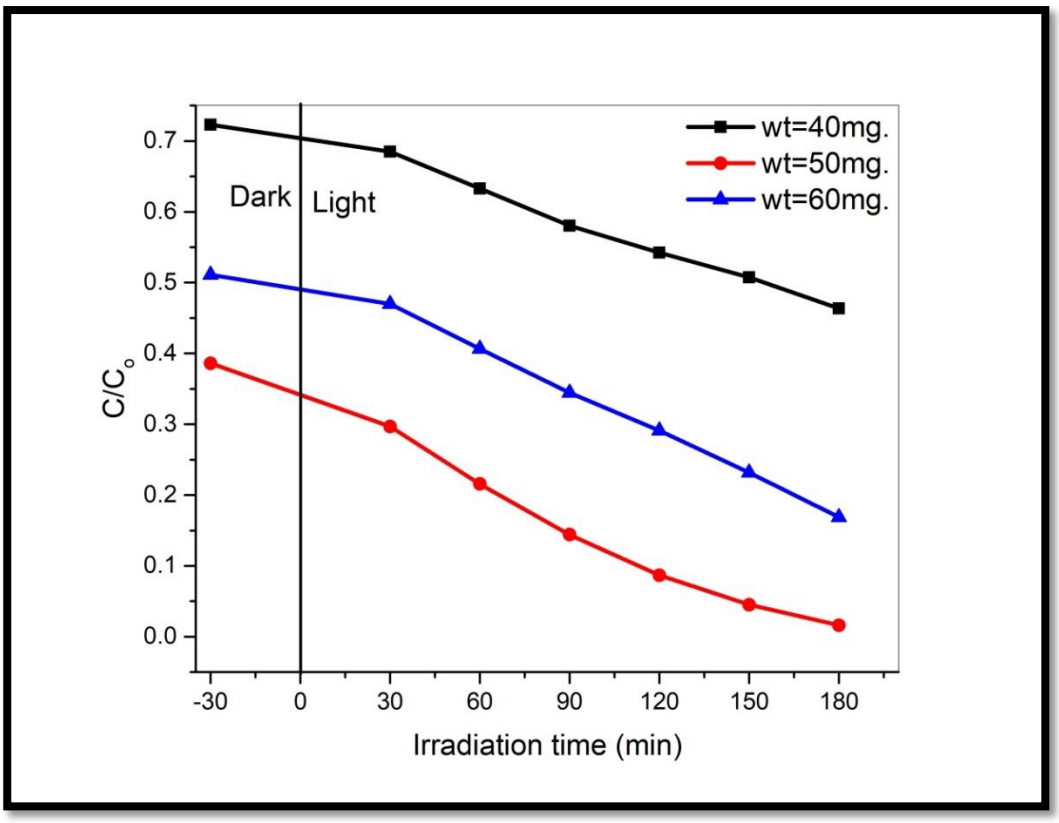

Fig. (3-47) Effect of catalyst weight on photocatalytic degradation of MB dye by (80%) g-C_3N_4 -Bi_2O_3 binary nanocomposite (composite weight=40, 50 and 60 mg)

Photocatalytic activity of BiC_{80}/GO (20 mg) ternary nanocomposites was tested against MB dye. The dye solution (10 mg.L^{-1}), the catalyst mixed with the MB dye solution placed in the dark for 30 minutes (adsorption) only for each composite before being exposure to visible light and the results are shown in Fig. (3-48). By plotting the C/C_o versus irradiation time, based on the results in the tables (3-21), (3-22), (3-23) respectively. The efficiency (D%) of variable weights 40, 50, and 60 mg of BiC_{80}/GO (20 mg) on degradation the MB dye 10 ppm, was 63.875, 97.81 and 85.029 respectively at time period of 180 min. This means that wt.=50 mg is more efficient in terms of MB dye degradation compared to the other nanocomposite catalytic weights.

Table (3-21) Photocatalytic degradation of MB (10 mg.L^{-1}), Vol.=50 ml by BiC_{80}/GO (20 mg) wt.=40 mg ternary nanocomposite at 25^{o}C

Time (min)	Absorption n=3	SD	RSD	Concentration (mg.L^{-1})	D%	C/C_o	Note
30	1.6003	±0.001528	0.095452	6.4789	35.211	0.6478	In dark
30	1.4680	±0.001	0.06812	5.9433	40.567	0.5943	Visible light
60	1.3543	±0.001528	0.112791	5.4829	45.171	0.5482	Visible light
90	1.2260	±0	0	4.9635	50.365	0.4963	Visible light
120	1.0990	±0.000577	0.052534	4.4518	55.482	0.4451	Visible light
150	0.9920	±0.001	0.100806	4.0161	59.839	0.4016	Visible light
180	0.8923	±0.001155	0.129407	3.6125	63.875	0.3612	Visible light

Table (3-22) Photocatalytic degradation of MB (10 mg.L^{-1}), Vol.=50 ml by BiC_{80}/GO (20 mg) wt.=50 mg ternary nanocomposite at 25^{o}C

Time (min)	Absorption n=3	SD	RSD	Concentration (mg.L^{-1})	D%	C/C_o	Note
30	0.9903	±0.000577	0.058301	4.257	57.43	0.4257	In dark
30	0.6930	±0	0	2.979	70.21	0.2979	Visible light
60	0.4536	±0.000577	0.127282	1.950	80.5	0.1950	Visible light
90	0.2813	±0.000577	0.205244	1.209	87.91	0.1209	Visible light
120	0.1553	±0.000577	0.371765	0.668	93.32	0.0668	Visible light
150	0.0706	±0.000577	0.817777	0.303	96.97	0.0303	Visible light
180	0.0510	±0	0	0.219	97.81	0.0219	Visible light

Table (3-23) Photocatalytic degradation of MB (10 mg.L^{-1}), Vol.=50 ml by BiC_{80}/GO (20 mg) wt.=60 mg ternary nanocomposite at 25^{o}C

Time (min)	Absorption n=3	SD	RSD	Concentration (mg.L^{-1})	D%	C/C_o	Note
30	1.1310	±0	0	4.5276	54.724	0.4527	In dark
30	0.9520	±0.001	0.105042	3.8110	61.89	0.3811	Visible light
60	0.8850	±0	0	3.5428	64.572	0.3542	Visible light
90	0.7653	±0.001155	0.150882	3.0564	69.436	0.3056	Visible light
120	0.6316	±0.001155	0.182821	2.5284	74.716	0.2528	Visible light
150	0.4963	±0.000577	0.116331	1.9867	80.133	0.1986	Visible light
180	0.3740	±0	0	1.4971	85.029	0.1497	Visible light

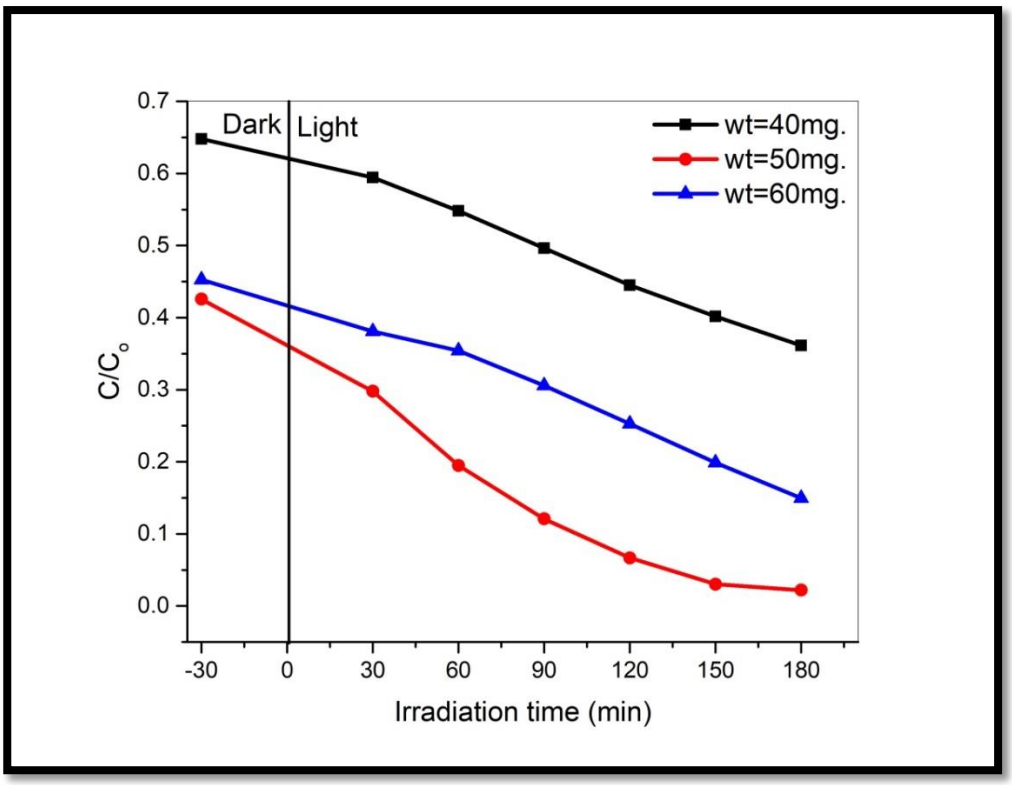

Fig. (3-48) Effect of catalyst weight on photocatalytic degradation of MB dye by BiC_{80}/GO (20 mg) ternary nanocomposite (composite weight=40, 50 and 60 mg)

3.3.2 Effect of the MB dye concentration

Studying the effect of the concentration of MB dye on the photo catalytic degradation on to (80%) g-C_3N_4 -Bi_2O_3 binary nanocomposite and novel BiC_{80}/GO (20 mg) ternary nanocomposite was studied by using different concentration of MB dye solution (5 ,10 and 15 mg.L^{-1}).

Photocatalytic activity of (80%) g-C_3N_4 -Bi_2O_3 binary nanocomposites was tested against MB dye. The dye solution was prepared at concentrations (5,10 and 15 mg.L^{-1}), under visible light (Tungsten lamp 300 watt) irradiation for a time period of 180 min. The catalyst mixed with the MB dye placed in the dark for 30 minutes (adsorption) before being exposure to visible light and the results are shown in Fig. (3-49). Plotting C/C_o versus irradiation time, based on the results in the tables (3-24), (3-25), (3-26) respectively. The efficiency D% of (80%) g-C_3N_4 -Bi_2O_3 (50 mg) at variable concentrations (5, 10 and 15 mg.L^{-1}) of MB dye solution was, 98.022, 98.38 and 66.582 respectively in a time period of 180 min. This means that the degradation efficient (80%) g-C_3N_4 -Bi_2O_3 of MB dye at 5 mg.L^{-1} is better than 10 mg.L^{-1} and 15 mg.L^{-1} during irradiation time 180 min.

Table (3-24) Photocatalytic degradation of MB(5 $mg.L^{-1}$), Vol.=50 ml by (80%) g-C_3N_4 -Bi_2O_3 wt.=50 mg binary nanocomposite at 25^oC

Time (min)	Absorption n=3	SD	RSD	Concentration ($mg.L^{-1}$)	D%	C/C_o	Note
30	0.2493	±0.000577	0.231589	1.0915	78.17	0.2183	In dark
30	0.1220	±0.001	0.819672	0.5341	89.317	0.1068	Visible light
60	0.0693	±0.002082	3.003847	0.3034	93.932	0.0606	Visible light
90	0.0320	±0.001	3.125	0.1401	97.198	0.0280	Visible light
120	0.0290	±0	0	0.1269	97.461	0.0253	Visible light
150	0.0266	±0.000577	2.17049	0.1164	97.671	0.0232	Visible light
180	0.0226	±0.000577	2.554647	0.0989	98.022	0.0197	Visible light

Table (3-25) Photo catalytic degradation of MB (10 $mg.L^{-1}$), Vol.=50 ml by (80%) g-C_3N_4 - Bi_2O_3 wt.=50 mg binary nanocomposite at 25^oC

Time (min)	Absorption n=3	SD	RSD	Concentration ($mg.L^{-1}$)	D%	C/C_o	Note
30	0.9023	±0.000577	0.063987	3.859	61.41	0.3859	In dark
30	0.6943	±0.000577	0.083156	2.969	70.31	0.2969	Visible light
60	0.5043	±0.000577	0.114485	2.156	78.61	0.2156	Visible light
90	0.3366	±0.000577	0.171524	1.439	85.61	0.1439	Visible light
120	0.2030	±0	0	0.868	91.32	0.0868	Visible light
150	0.1056	±0.000577	0.546733	0.451	95.49	0.0451	Visible light
180	0.0380	±0.001	2.631579	0.162	98.38	0.0162	Visible light

Table (3-26) Photo catalytic degradation of MB (15 $mg.L^{-1}$), Vol.=50 ml by (80%) g-C_3N_4 - Bi_2O_3 wt.=50 mg binary nanocomposite at 25^oC

Time (min)	Absorption n=3	SD	RSD	Concentration ($mg.L^{-1}$)	D%	C/C_o	Note
30	1.719	±0.001	0.058173	9.4589	36.941	0.6305	In dark
30	1.637	±0.002	0.122175	9.0077	39.949	0.6005	Visible light
60	1.488	±0.002	0.134409	8.1878	45.415	0.5458	Visible light
90	1.358	±0.001	0.073638	7.4724	50.184	0.4981	Visible light
120	1.213	±0	0	6.6746	55.503	0.4449	Visible light
150	1.064	±0.001155	0.108494	5.8563	60.958	0.3904	Visible light
180	0.911	±0.001	0.109769	5.0128	66.582	0.3341	Visible light

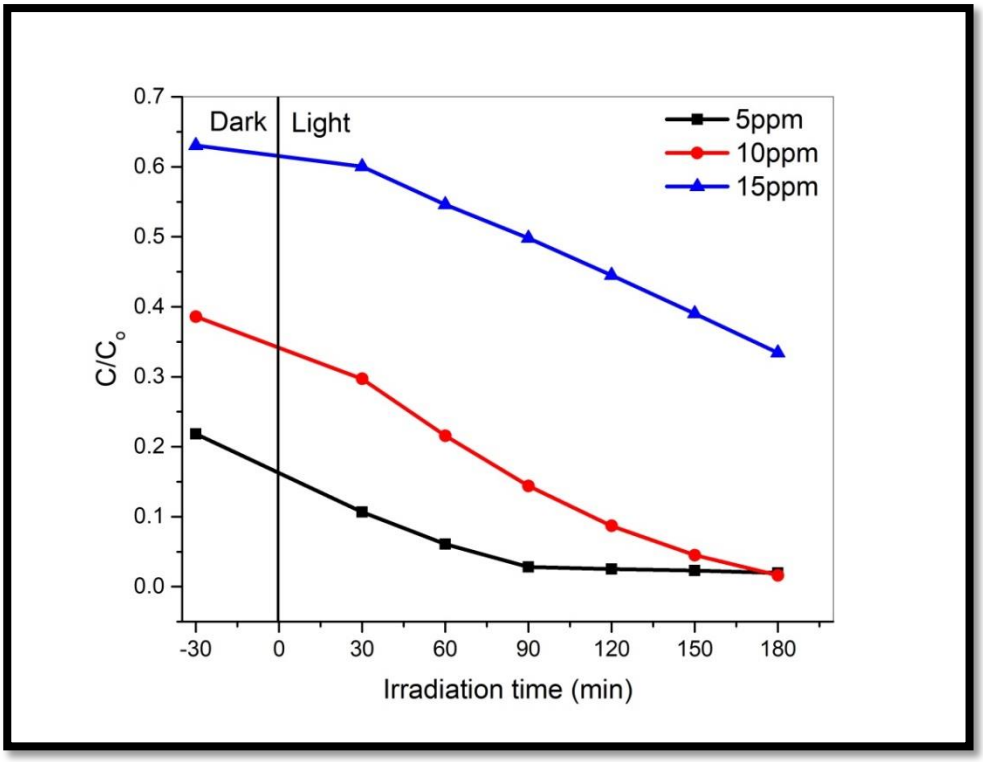

Fig. (3-49) Effect of MB dye concentrations on photocatalytic degradation by (80%) g-C_3N_4 -Bi_2O_3, wt.=50 mg binary nanocomposite (MB dye concentration =5,10 and 15 mg.L^{-1})

Photocatalytic activity of novel BiC_{80}/GO (20 mg) ternary nanocomposites was tested against MB dye. The dye solution prepared at the concentrations (5,10 and 15 mg.L^{-1}), under visible light (Tungsten lamp 300 watt) irradiation for a time period of 180 min. The catalyst mixed with the MB dye solution placed in the dark for 30 minutes (adsorption) before being exposure to the visible light, the results are shown in Fig. (3-50). Plotting C/C_o versus irradiation time, based on the results in the tables (3-27), (3-28), (3-29) respectively. The D% efficiency of BiC_{80}/GO (20 mg) on variable concentrations of MB solution, 5, 10 and 15 mg.L^{-1} were 98.514, 97.81 and 66.967 respectively at time period of 180 min. This means that the degradation efficient of BiC_{80}/GO (20 mg) on MB dye at a (5 mg.L^{-1}) is slightly better than (10 mg.L^{-1}) and significantly better than(15 mg.L^{-1}).

Table (3-27) Photocatalytic degradation of MB (5 $mg.L^{-1}$), Vol.=50 ml by BiC_{80}/GO (20 mg), wt.=50 mg ternary nanocomposite at 25°C

Time (min)	Absorption n=3	SD	RSD	Concentration ($mg.L^{-1}$)	D%	C/C_o	Note
30	0.260	±0.001	0.384615	1.0734	78.531	0.2146	In dark
30	0.169	±0.001	0.591716	0.6977	86.045	0.1395	Visible light
60	0.096	±0	0	0.3963	92.073	0.0792	Visible light
90	0.056	±0.000577	1.020053	0.2336	95.327	0.0467	Visible light
120	0.034	±0	0	0.1403	97.193	0.0280	Visible light
150	0.031	±0	0	0.1279	97.441	0.2558	Visible light
180	0.018	±0	0	0.0743	98.514	0.0148	Visible light

Table (3-28) Photo catalytic degradation of MB (10 $mg.L^{-1}$), Vol.=50 ml by BiC_{80}/GO (20 mg) wt.=50 mg ternary nanocomposite at 25°C

Time (min)	Absorption n=3	SD	RSD	Concentration ($mg.L^{-1}$)	D%	C/C_o	Note
30	0.9903	±0.000577	0.058301	4.257	57.43	0.4257	In dark
30	0.6930	±0	0	2.979	70.21	0.2979	Visible light
60	0.4536	±0.000577	0.127282	1.950	80.5	0.1950	Visible light
90	0.2813	±0.000577	0.205244	1.209	87.91	0.1209	Visible light
120	0.1553	±0.000577	0.371765	0.668	93.32	0.0668	Visible light
150	0.0706	±0.000577	0.817777	0.303	96.97	0.0303	Visible light
180	0.0510	±0	0	0.219	97.81	0.0219	Visible light

Table (3-29) Photo catalytic degradation of MB (15 $mg.L^{-1}$), Vol.=50 ml by BiC_{80}/GO (20 mg) wt.=50 mg ternary nanocomposite at 25°C

Time (min)	Absorption n=3	SD	RSD	Concentration ($mg.L^{-1}$)	D%	C/C_o	Note
30	1.6930	±0.001	0.059067	9.4510	36.993	0.6301	In dark
30	1.5736	±0.001528	0.097072	8.7845	41.437	0.5856	Visible light
60	1.4563	±0.001528	0.104891	8.1296	45.803	0.5419	Visible light
90	1.3000	±0	0	7.2571	51.619	0.4838	Visible light
120	1.1676	±0.000577	0.049448	6.5180	56.547	0.4345	Visible light
150	1.0436	±0.000577	0.055323	5.8258	61.162	0.3883	Visible light
180	0.8887	±0.57735	0.000650	4.9549	66.967	0.3303	Visible light

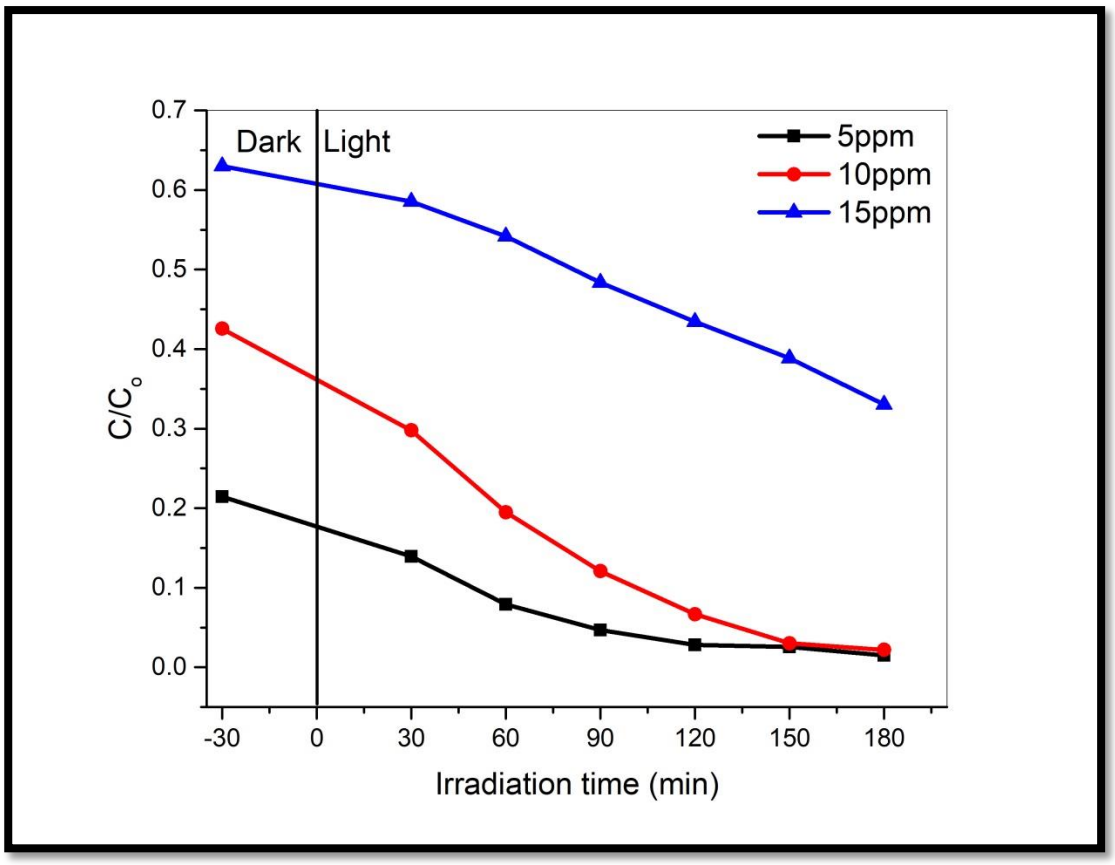

Fig. (3-50) Effect of MB dye concentration on photocatalytic degradation of BiC_{80}/GO (20 mg) ternary nanocomposite, (MB dye concentration =5,10 and 15 $mg.L^{-1}$)

3.3.3 Effect of Temperature

Studying the effect of the temperature on the photo catalytic degradation MB dye on to (80%) g-C_3N_4 -Bi_2O_3 binary nanocomposite and novel BiC_{80}/GO (20 mg) ternary nanocomposite by using different temperatures (25 ,35 and 40 ^oC).
Photocatalytic activity of (80%) g-C_3N_4 -Bi_2O_3 binary nanocomposites was tested against MB dye. The visible light (Tungsten lamp 300 watt) above the dye solution 10 ppm, irradiation for a time period of 180 min, the catalyst mixed with the MB dye, placed in the dark for 30 minutes (adsorption) before being exposure to the visible, the results are shown in Fig. (3-51). Plotting the C/C_o versus and irradiation time based on the results in the tables (3-30), (3-31), (3-32) respectively, MB10 $mg.L^{-1}$, catalyst wt.=50 mg. The efficiency D% of (80%) g-C_3N_4 -Bi_2O_3 for the degradation the MB dye 10 $mg.L^{-1}$, at temperature, 25^oC, 35 and 40^oC were, 98.38, 95.249 and 95.201respectively in a time period of 180 min. This means that the degradation of MB dye at temperature 25^oC is better than a 35^oC and 40^oC.

Table (3-30) Photocatalytic degradation of MB (10 mg.L^{-1}), Vol.=50 ml by (80%) g-C_3N_4 - Bi_2O_3 wt.=50 mg binary nanocomposite at 25^oC

Time (min)	Absorption n=3	SD	RSD	Concentration (mg.L^{-1})	D%	C/C_o	Note
30	0.9023	±0.00577	0.063987	3.859	61.41	0.3859	In dark
30	0.6943	±0.00577	0.083156	2.969	70.31	0.2969	Visible light
60	0.5043	±0.00577	0.114485	2.156	78.61	0.2156	Visible light
90	0.3366	±0.00577	0.171524	1.439	85.61	0.1439	Visible light
120	0.2030	±0	0	0.868	91.32	0.0868	Visible light
150	0.1056	±0.00577	0.546733	0.451	95.49	0.0451	Visible light
180	0.0380	±0.001	2.631579	0.162	98.38	0.0162	Visible light

Table (3-31) Photocatalytic degradation of MB (10 mg.L^{-1}), Vol.=50 ml by (80%) g-C_3N_4 - Bi_2O_3 wt.=50 mg binary nanocomposite at 35^oC

Time (min)	Absorption n=3	SD	RSD	Concentration (mg.L^{-1})	D%	C/C_o	Note
30	0.8703	±0.002309	0.265357	4.2063	57.937	0.4206	In dark
30	0.6953	±0.166072	0.166072	3.3605	66.395	0.3361	Visible light
60	0.5450	±0	0	2.6341	73.659	0.2634	Visible light
90	0.4343	±0.00577	0.132938	2.0990	79.01	0.2099	Visible light
120	0.2740	±0	0	1.3243	86.757	0.1324	Visible light
150	0.1760	±0.001	0.568182	0.8506	91.494	0.0851	Visible light
180	0.0983	±0.00577	0.587335	0.4751	95.249	0.0475	Visible light

Table (3-32) Photocatalytic degradation of MB (10 mg.L^{-1}), Vol.=50 ml by (80%) g-C_3N_4 - Bi_2O_3 wt.=50 mg binary nanocomposite at 40^oC

Time (min)	Absorption n=3	SD	RSD	Concentration (mg.L^{-1})	D%	C/C_o	Note
30	0.9870	±0	0	4.7089	52.911	0.4708	In dark
30	0.8230	±0.001	0.121507	3.9265	60.735	0.3926	Visible light
60	0.6146	±0.001155	0.187878	2.9322	70.678	0.2932	Visible light
90	0.5196	±0.002676	0.515096	2.4790	75.21	0.2479	Visible light
120	0.2886	±0.00577	0.200052	1.3769	86.231	0.1376	Visible light
150	0.1770	±0.001	0.564972	0.8444	91.556	0.0844	Visible light
180	0.1006	±0.00577	0.573907	0.4799	95.201	0.0479	Visible light

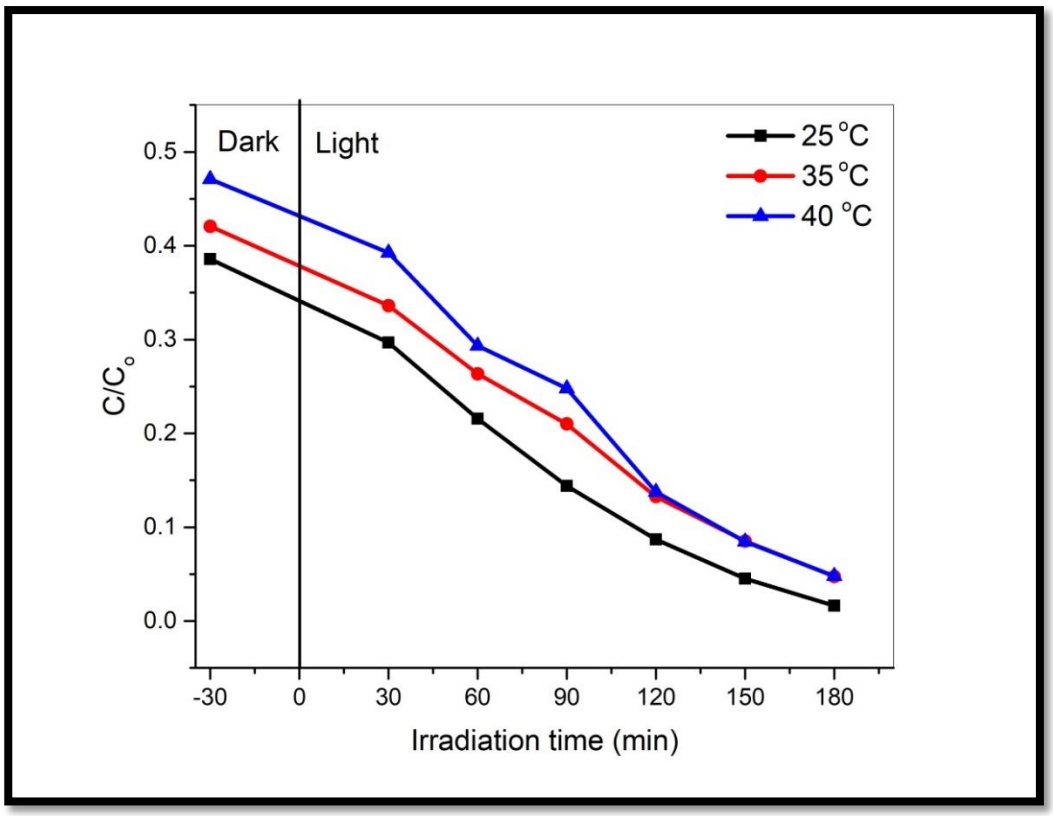

Fig. (3-51) Effect of temperature on photocatalytic degradation of MB (10 mg.L^{-1}) by (80%) g-C_3N_4 -Bi_2O_3 binary nanocomposite at 25,35 and 40^{o}C

Photocatalytic activity of BiC_{80}/GO (20 mg) ternary nanocomposites was tested against MB dye. The visible light (Tungsten lamp 300 watt) above the dye solution 5 ppm, irradiation for a time period of 180 min, the catalyst mixed with the MB dye, placed in the dark for 30 minutes (adsorption) before being exposure to the visible, the results are shown in Fig. (3-52). Plotting the C/C_o versus and irradiation time based on the results in the tables (3-33), (3-34), (3-35) respectively, MB 5 mg.L^{-1}, catalyst wt.=50 mg. The efficiency D% of BiC_{80}/GO (20 mg) for the degradation MB dye 5 mg.L^{-1}, at temperature, 25^{o}C, 35 and 40^{o}C were, 98.514, 97.762 and 97.994 respectively in a time period of 180 min. This means that the degradation of MB dye at temperature 35^{o}C is better than a 25^{o}C and 40^{o}C.

Table (3-33) Photocatalytic degradation of MB(5 mg.L^{-1}), Vol.=50 ml by BiC_{80}/GO (20 mg), wt.=50 mg ternary nanocomposite at 25^{o}C

Time (min)	Absorption n=3	SD	RSD	Concentration (mg.L^{-1})	D%	C/C_o	Note
30	0.260	±0.001	0.384615	1.0734	78.531	0.2146	In dark
30	0.169	±0.001	0.591716	0.6977	86.045	0.1395	Visible light
60	0.096	±0	0	0.3963	92.073	0.0792	Visible light
90	0.056	±0.000577	1.020053	0.2336	95.327	0.0467	Visible light
120	0.034	±0	0	0.1403	97.193	0.0280	Visible light
150	0.031	±0	0	0.1279	97.441	0.2558	Visible light
180	0.018	±0	0	0.0743	98.514	0.0148	Visible light

Table (3-34) Photocatalytic degradation of MB(5 mg.L^{-1}), Vol.=50 ml by BiC_{80}/GO (20 mg) wt.=50 mg ternary nanocomposite at 35^{o}C

Time (min)	Absorption n=3	SD	RSD	Concentration (mg.L^{-1})	D%	C/C_o	Note
30	0.1830	±0.000346	0.18929	0.7980	84.04	0.1596	In dark
30	0.1116	±0.000577	0.517339	0.4806	90.388	0.0961	Visible light
60	0.0503	±0.000577	1.147814	0.2166	95.668	0.0433	Visible light
90	0.0446	±0.000577	1.294507	0.1920	96.16	0.0384	Visible light
120	0.0276	±0.000577	2.091849	0.1188	97.624	0.0237	Visible light
150	0.0263	±0.000577	2.195248	0.1132	97.736	0.0226	Visible light
180	0.0260	±0	0	0.1119	97.762	0.0223	Visible light

Table (3-35) Photo catalytic degradation of MB(5 mg.L^{-1}), Vol.=50 ml by BiC_{80}/GO (20 mg) wt.=50 mg ternary nanocomposite at 40^{o}C

Time (min)	Absorption n=3	SD	RSD	Concentration (mg.L^{-1})	D%	C/C_o	Note
30	0.1957	±0.002	1.021972	0.8747	82.505	0.1749	In dark
30	0.0966	±0.001155	1.195342	0.4289	91.421	0.0857	Visible light
60	0.0486	±0.000577	1.187964	0.2158	95.684	0.0431	Visible light
90	0.0400	±0.001	2.5	0.1776	96.448	0.0355	Visible light
120	0.0246	±0.000577	2.346952	0.1092	97.816	0.0218	Visible light
150	0.0233	±0.000577	2.477898	0.1034	97.932	0.0206	Visible light
180	0.0226	±0.000577	2.554647	0.1003	97.994	0.0201	Visible light

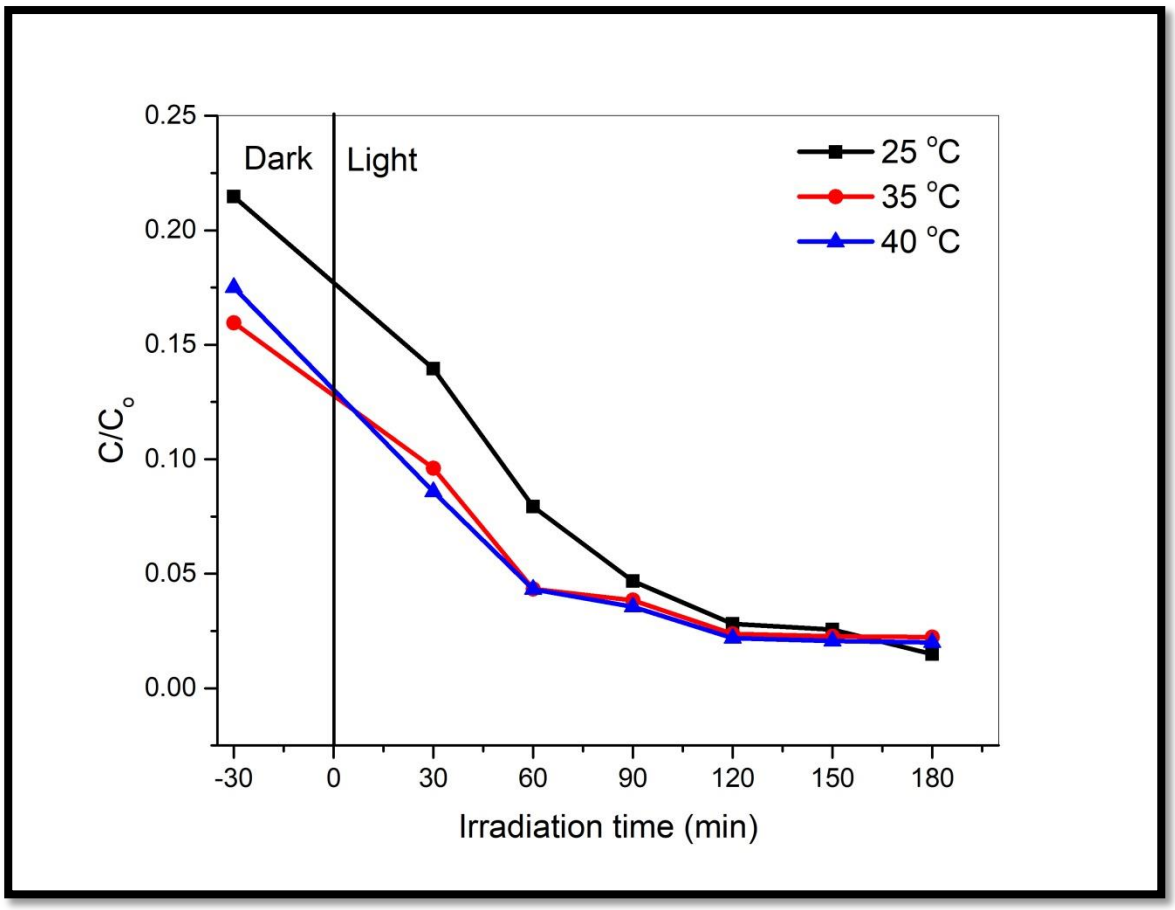

Fig. (3-52) Effect of temperature on photocatalytic degradation of MB by BiC_{80}/GO (20 mg) ternary nanocomposite at 25,35 and 40^{o}C

3.3.4 Effect of pH

The effect of pH on the photocatalytic degradation of MB dye by, (80%) g-C_3N_4 - Bi_2O_3 binary nanocomposite and BiC_{80}/GO (20 mg) ternary nanocomposite at pH range (2-14) was studied. The absorption spectrums of MB dye without catalyst were measured as shown in the Fig. (3-53).

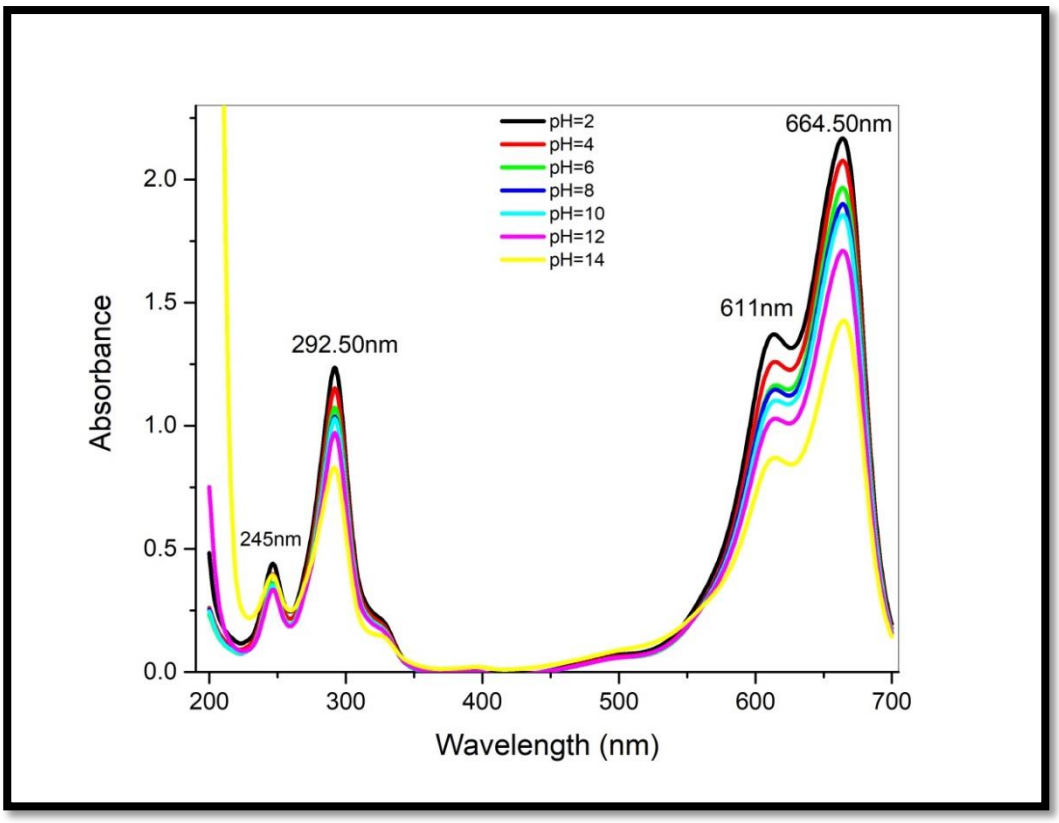

Fig. (3-53) Absorption spectrums of MB dye (10 mg.L^{-1}) at pH 2-14

Photocatalytic activity of (80%) g-C_3N_4 -Bi_2O_3 (50 mg) binary nanocomposite was tested against MB dye, the dye solution (10 mg.L^{-1}), under visible light (Tungsten lamp 300 watt) irradiation for a time period of 180 min, in the beginning the catalyst mixed with the MB dye solution in the dark for 30 minutes (adsorption) only before being exposure to visible light; in order to find out the effect of pH on the MB degradation, results are shown in Fig. (3-54). Plotting the C/C_o versus irradiation time which based on the results in the tables (3-36), (3-37), (3-38), (3-39), (3-40), (3-41), (3-42) respectively, at MB concentration 10 mg.L^{-1}, catalyst wt.=50mg at 25^{o}C The efficiency D% of (80%) g-C_3N_4 -Bi_2O_3 for the degradation the MB dye, at pH=2, 4, 6, 8, 10, 12 and 14 in the order 73.856, 94.784, 95.548, 94.589, 96.311, 99.038 and 98.492 respectively. This means that the degradation efficiency of (80%) g-C_3N_4 -Bi_2O_3 binary nanocomposite for MB dye at pH=14 is the best because it took minimum degradation time 30 min. under visible light.

Table (3-36) Photocatalytic degradation of MB (10 mg.L^{-1}) at pH= 2, Vol.=50 ml by (80%) g-C_3N_4 -Bi_2O_3 wt.=50 mg binary nanocomposite at 25^oC

Time (min)	Absorption n=3	SD	RSD	Concentration (mg.L^{-1})	D%	C/C_o	Note
30	0.6920	±0	0	3.2656	67.344	0.3265	In dark
30	0.6906	±0.000577	0.08360125	3.2590	67.41	0.3259	Visible light
60	0.6746	±0.000577	0.0855840	3.1835	68.165	0.3183	Visible light
90	0.6476	±0.000577	0.08915229	3.0561	69.439	0.3056	Visible light
120	0.6260	±0	0	2.9542	70.458	0.2954	Visible light
150	0.5976	±0.000577	0.09661149	2.8201	71.799	0.2820	Visible light
180	0.5540	±0	0	2.6144	73.856	0.2614	Visible light

Table (3-37) Photocatalytic degradation of MB (10 mg.L^{-1}) at pH= 4, Vol.=50 ml by (80%) g-C_3N_4 -Bi_2O_3 wt.=50 mg binary nanocomposite at 25^oC

Time (min)	Absorption n=3	SD	RSD	Concentration (mg.L^{-1})	D%	C/C_o	Note
30	0.4730	±0.000513	0.108491	2.6265	73.735	0.2626	In dark
30	0.4616	±0.000577	0.545193	2.5615	74.385	0.2561	Visible light
60	0.3256	±0.002517	0.177319	1.8068	81.932	0.1806	Visible light
90	0.2630	±0.001	0.380228	1.4594	85.406	0.1459	Visible light
120	0.1990	±0.001	0.502513	1.1043	88.957	0.1104	Visible light
150	0.1496	±0.000577	0.385929	0.8301	91.699	0.0830	Visible light
180	0.0940	±0	0	0.5216	94.784	0.0521	Visible light

Table (3-38) Photocatalytic degradation of MB (10 mg.L^{-1}) at pH= 6, Vol.=50 ml by (80%) g-C_3N_4 -Bi_2O_3 wt.=50 mg binary nanocomposite at 25^oC

Time (min)	Absorption n=3	SD	RSD	Concentration (mg.L^{-1})	D%	C/C_o	Note
30	0.529	±0.000577	0.109078	2.6597	73.403	0.2659	In dark
30	0.407	±0.001	0.2457	2.0452	79.548	0.2045	Visible light
60	0.329	±0	0	1.6532	83.468	0.1653	Visible light
90	0.239	±0.000577	0.241266	1.2025	87.975	0.1202	Visible light
120	0.173	±0	0	0.8693	91.307	0.0869	Visible light
150	0.114	±0.001	0.877193	0.5728	94.272	0.0572	Visible light
180	0.088	±0.000577	0.651637	0.4452	95.548	0.0445	Visible light

Table (3-39) Photocatalytic degradation of MB (10 mg.L^{-1}) at pH= 8, Vol.=50 ml by (80%) g-C_3N_4 -Bi_2O_3 wt.=50 mg binary nanocomposite at 25^oC

Time (min)	Absorption n=3	SD	RSD	Concentration (mg.L^{-1})	D%	C/C_o	Note
30	0.6756	±0.000577	0.085457	3.4663	65.337	0.3466	In dark
30	0.5363	±0.001155	0.215309	2.7516	72.484	0.2751	Visible light
60	0.4300	±0	0	2.2062	77.938	0.2206	Visible light
90	0.3510	±0.001	0.2849	1.8009	81.991	0.1801	Visible light
120	0.2523	±0.000577	0.228835	1.2945	87.055	0.1294	Visible light
150	0.1740	±0.001	0.574713	0.8927	91.073	0.0892	Visible light
180	0.1053	±0.001528	1.450641	0.5402	94.598	0.0540	Visible light

Table (3-40) Photocatalytic degradation of MB (10 mg.L^{-1}) at pH= 10, Vol.=50 ml by (80%) g-C_3N_4 -Bi_2O_3 wt.=50 mg binary nanocomposite at 25^oC

Time (min)	Absorption n=3	SD	RSD	Concentration (mg.L^{-1})	D%	C/C_o	Note
30	0.5930	±0.001732	0.292083	3.2036	67.964	0.3203	In dark
30	0.4473	±0.001539	0.344172	2.4165	75.835	0.2416	Visible light
60	0.3036	±0.001155	0.380336	1.6401	83.599	0.1640	Visible light
90	0.1896	±5.77E-05	0.030451	1.0243	89.757	0.1024	Visible light
120	0.1120	±0.002	1.785714	0.6050	93.95	0.0605	Visible light
150	0.0806	±0.000577	0.716315	0.4354	95.646	0.0435	Visible light
180	0.0683	±0.000577	0.845315	0.3689	96.311	0.0368	Visible light

Table (3-41) Photocatalytic degradation of MB (10 mg.L^{-1}) at pH= 12, Vol.=50 ml by (80%) g-C_3N_4 -Bi_2O_3 wt.=50 mg binary nanocomposite at 25^oC

Time (min)	Absorption n=3	SD	RSD	Concentration (mg.L^{-1})	D%	C/C_o	Note
30	0.1283	±0.002517	1.961505	0.7714	92.286	0.0771	In dark
30	0.0880	±0.003	3.409091	0.5291	94.709	0.0529	Visible light
60	0.0826	±0.001155	1.397943	0.4966	95.034	0.0496	Visible light
90	0.0300	±0	0	0.1803	98.197	0.0180	Visible light
120	0.0160	±0.001732	10.82532	0.0962	99.038	0.0096	Visible light

Table (3-42) Photocatalytic degradation of MB (10 mg.L^{-1}) at pH= 14, Vol.=50 ml by (80%) g-C_3N_4 -Bi_2O_3 wt.=50 mg binary nanocomposite at 25^oC

Time (min)	Absorption n=3	SD	RSD	Concentration (mg.L^{-1})	D%	C/C_o	Note
30	0.0566	±0.004619	8.160428	0.4008	95.992	0.0401	In dark
30	0.0213	±0.000577	2.710565	0.1508	98.492	0.0151	Visible light

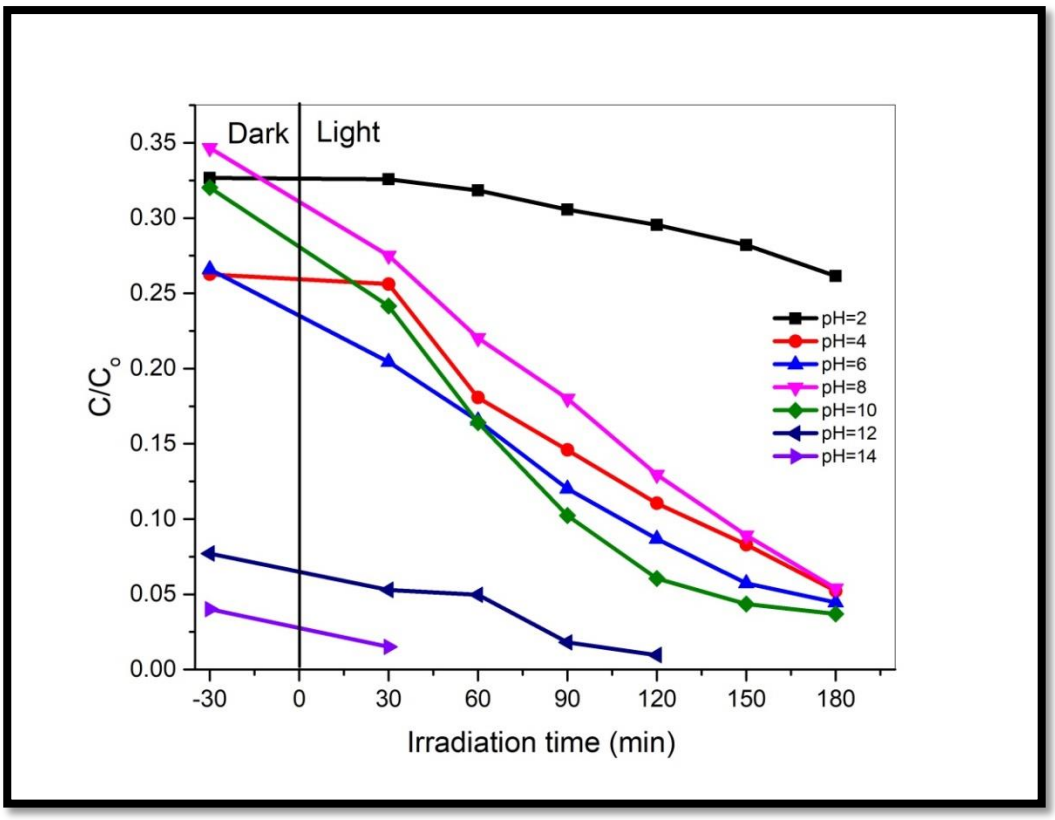

Fig. (3-54) Effect of pH (2-14) on photocatalytic degradation of MB dye 10 mg.L^{-1}, by (80%) g-C_3N_4 -Bi_2O_3 (50 mg) binary nanocomposite

Photocatalytic activity of BiC_{80}/GO(20 mg) ternary nanocomposite (50 mg) was tested against MB dye, the dye solution (10 mg.L^{-1}), under visible light (Tungsten lamp 300 watt) irradiation for a time period of 180 min, in the beginning the catalyst mixed with the MB dye solution in the dark for 30 minutes (adsorption) only before being exposure to visible light; in order to find out the effect of pH on the MB degradation, results are shown in Fig. (3-55). Plotting the C/C_o versus irradiation time which based on the results in the tables (3-43), (3-44), (3-45), (3-46), (3-47) and (3-48) respectively, at MB concentration 10 mg.L^{-1}, catalyst wt.=50mg, temperature25^{o}C.

The efficiency D% of BiC_{80}/GO (20 mg) for the degradation the MB dye, at pH=2, 4, 6, 8, 10 and12 was in the order 84.371, 84.933, 96.022, 99.133, 97.925 and 99.541 respectively. This means that the degradation efficiency of BiC_{80}/GO (20 mg) ternary nanocomposites on MB dye at pH=12 is the best, while it was 100% at pH =14 in the dark, adsorption only.

Lower pH (acidic) causes less MB molecules adsorption on the photocatalyst surface because H^+, the dominating species, competes with the cationic MB dye. The reaction between the $^{\bullet}OH$ and MB is lessened because MB does not adsorb on the photocatalyst surface. Higher pH values prevent OH^- and MB from competing because OH^- will be repelled by the negatively charged surface of the photocatalyst and will persist in the mixture in significant amounts [101],[102].

Table (3-43) Photocatalytic degradation of MB (10 $mg.L^{-1}$) at pH= 2, Vol.=50 ml by (BiC_{80}/GO-20 mg), wt.=50 mg ternary nanocomposite at 25°C

Time (min)	Absorption n=3	SD	RSD	Concentration ($mg.L^{-1}$)	D%	C/C_o	Note
30	0.6176	±0.001528	0.247332	2.8592	71.408	0.2859	In dark
30	0.5566	±0.000577	0.103728	2.5768	74.232	0.2576	Visible light
60	0.5110	±0.001	0.195695	2.3657	76.343	0.2365	Visible light
90	0.4670	±0	0	2.1620	78.38	0.2162	Visible light
120	0.4106	±0.000577	0.140611	1.9009	80.991	0.1901	Visible light
150	0.3746	±0,001	0.266951	1.7342	82.658	0.1734	Visible light
180	0.3376	±0.000577	0.171016	1.5629	84.371	0.1563	Visible light

Table (3-44) Photocatalytic degradation of MB (10 $mg.L^{-1}$) at pH= 4, Vol.=50 ml by (BiC_{80}/GO-20 mg), wt.=50 mg ternary nanocomposite at 25°C

Time (min)	Absorption n=3	SD	RSD	Concentration ($mg.L^{-1}$)	D%	C/C_o	Note
30	0.9540	±0.001	0.104822	4.5777	54.223	0.4577	In dark
30	0.8436	±0.000577	0.068439	4.0479	59.521	0.4047	Visible light
60	0.6880	±0	0	3.3013	66.987	0.3301	Visible light
90	0.6006	±0.000577	0.096129	2.8819	71.181	0.2881	Visible light
120	0.5030	±0.001	0.198807	2.4136	75.864	0.2413	Visible light
150	0.4150	±0	0	1.9913	80.087	0.1991	Visible light
180	0.3140	±0	0	1.5067	84.933	0.1506	Visible light

Table (3-45) Photocatalytic degradation of MB (10 $mg.L^{-1}$) at pH= 6, Vol.=50 ml by (BiC_{80}/GO-20 mg), wt.=50 mg ternary nanocomposite at 25°C

Time (min)	Absorption n=3	SD	RSD	Concentration ($mg.L^{-1}$)	D%	C/C_o	Note
30	0.6900	±0.001	0.144928	3.4311	65.689	0.3431	In dark
30	0.5686	±0.001528	0.268647	2.8274	71.726	0.2827	Visible light
60	0.4450	±0	0	2.2128	77.726	0.2212	Visible light
90	0.3296	±0.000577	0.175167	1.6389	83.611	0.1638	Visible light
120	0.2443	±0.000577	0.236328	1.2148	87.852	0.1214	Visible light
150	0.1493	±0.000577	0.386705	0.7424	92.576	0.0742	Visible light
180	0.0800	±0.002646	3.307189	0.3978	96.022	0.0397	Visible light

Table (3-46) Photocatalytic degradation of MB (10 mg.L^{-1}) at pH= 8, Vol.=50 ml by (BiC_{80}/GO-20 mg), wt.=50 mg ternary nanocomposite at 25^{o}C

Time (min)	Absorption n=3	SD	RSD	Concentration (mg.L^{-1})	D%	C/C_o	Note
30	0.358	±0.003	0.837989	1.8274	81.726	0.1827	In dark
30	0.225	±0.001	0.444444	1.1485	88.515	0.1148	Visible light
60	0.163	±0.001528	0.93541	0.8335	91.665	0.0833	Visible light
90	0.107	±0.001	0.934579	0.05461	94.539	0.0546	Visible light
120	0.065	±0.001	1.538462	0.3318	96.682	0.0331	Visible light
150	0.031	±0.001	3.225806	0.1582	98.418	0.0158	Visible light
180	0.017	±0.001	5.882353	0.0867	99.133	0.0086	Visible light

Table (3-47) Photocatalytic degradation of MB (10 mg.L^{-1}) at pH= 10, Vol.=50 ml by (BiC_{80}/GO-20 mg), wt.=50 mg ternary nanocomposite at 25^{o}C

Time (min)	Absorption n=3	SD	RSD	Concentration (mg.L^{-1})	D%	C/C_o	Note
30	0.4703	±0.005033	1.070215	2.5954	74.046	0.2595	In dark
30	0.3293	±0.001155	0.350653	1.8173	81.827	0.1817	Visible light
60	0.2323	±0.000577	0.248536	1.2820	87.18	0.1282	Visible light
90	0.1776	±0.001528	0.860093	0.9801	90.199	0.0980	Visible light
120	0.1280	±0	0	0.7064	92.936	0.0706	Visible light
150	0.0720	±0	0	0.3973	96.027	0.0397	Visible light
180	0.0376	±0.000577	1.535506	0.2075	97.925	0.0207	Visible light

Table (3-48) Photocatalytic degradation of MB (10 mg.L^{-1}) at pH= 12, Vol.=50 ml by (BiC_{80}/GO-20 mg), wt.=50 mg ternary nanocomposite at 25^{o}C

Time (min)	Absorption n=3	SD	RSD	Concentration (mg.L^{-1})	D%	C/C_o	Note
30	0.1363	±0.001528	1.120708	0.7824	92.176	0.07824	In dark
30	0.1003	±0.003786	3.774615	0.5757	94.243	0.05757	Visible light
60	0.0760	±0.001	1.315789	0.4362	95.638	0.04362	Visible light
90	0.0493	±0.000577	1.171096	0.2830	97.17	0.02830	Visible light
120	0.0080	±0	0	0.0459	99.541	0.00459	Visible light

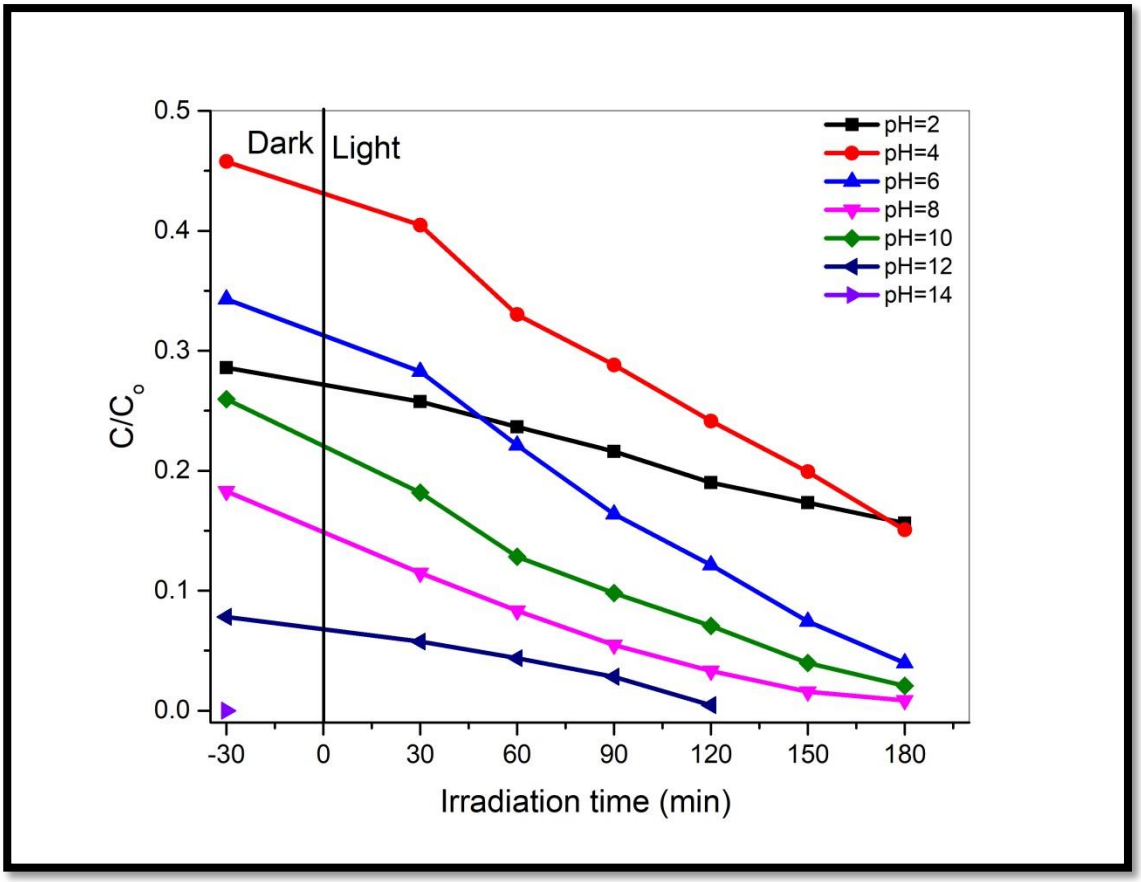

Fig. (3-55) Effect of the pH (2-14) on the photocatalytic degradation of MB dye by (BiC_{80}/GO-20 mg) ternary nanocomposite

The obtained optimum conditions for the best efficient (80%) g-C_3N_4 -Bi_2O_3 are (catalyst weight =50 mg, dye concentration= 5 mg.L^{-1}, temperature= 25°C, pH =14), while the optimum conditions for ternary nanocomposites BiC_{80}/GO (20 mg) are (catalyst weight =50 mg, dye concentration= 5 mg.L^{-1}, temperature = 35°C, pH=12).

3.4 Energy Gap

The indirect optical band gap is calculated by plotting the value of $(\alpha h\nu)^{1/2}$ (y-axis) as a function of hν (x-axis) and extrapolating the straight line portion to $(\alpha h\nu)^{1/2}$ =0 .The band gap of g-C_3N_4 was 2.60eV as shown in the Fig.(3-56), It was 2.7eV in the previous studies [158] . The band gap of Bi_2O_3 was 3.24eV as shown in the Fig.(3-57), in the previous studies was 2.82eV[160] . The band gap of NGO was about 4.47eV as shows in the Fig. (3-58), in the previous studies was 3.11eV [182]. The band gap energy depends on the synthesis method and conditions. The results are shown in the table (3-49).

Table (3-49) Energy gap of g-C_3N_4, Bi_2O_3 and NGO

Nanomaterial	Band gap energy (eV)	Band gap energy in references (eV)
g-C_3N_4	2.60	2.70 [158]
Bi_2O_3	3.24	2.82 [160]
NGO	4.47	3.10 [182]

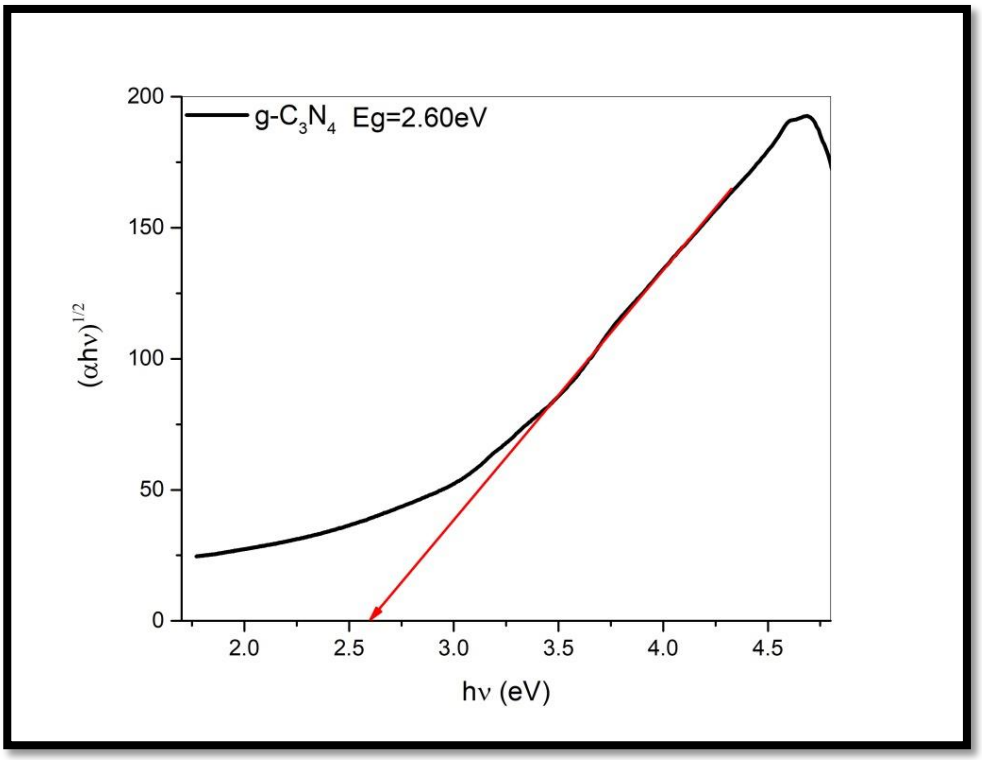

Fig. (3-56) Tauc plot for band gap energy of g-C_3N_4

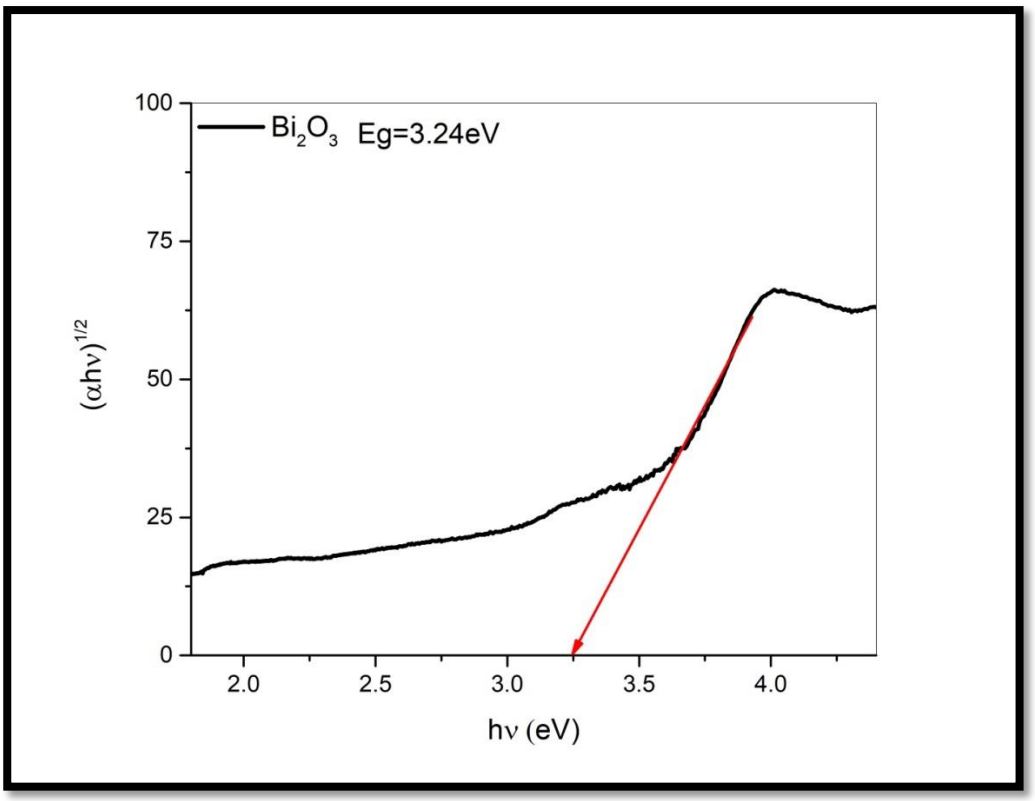

Fig. (3-57) Tauc plot for band gap energy of Bi_2O_3

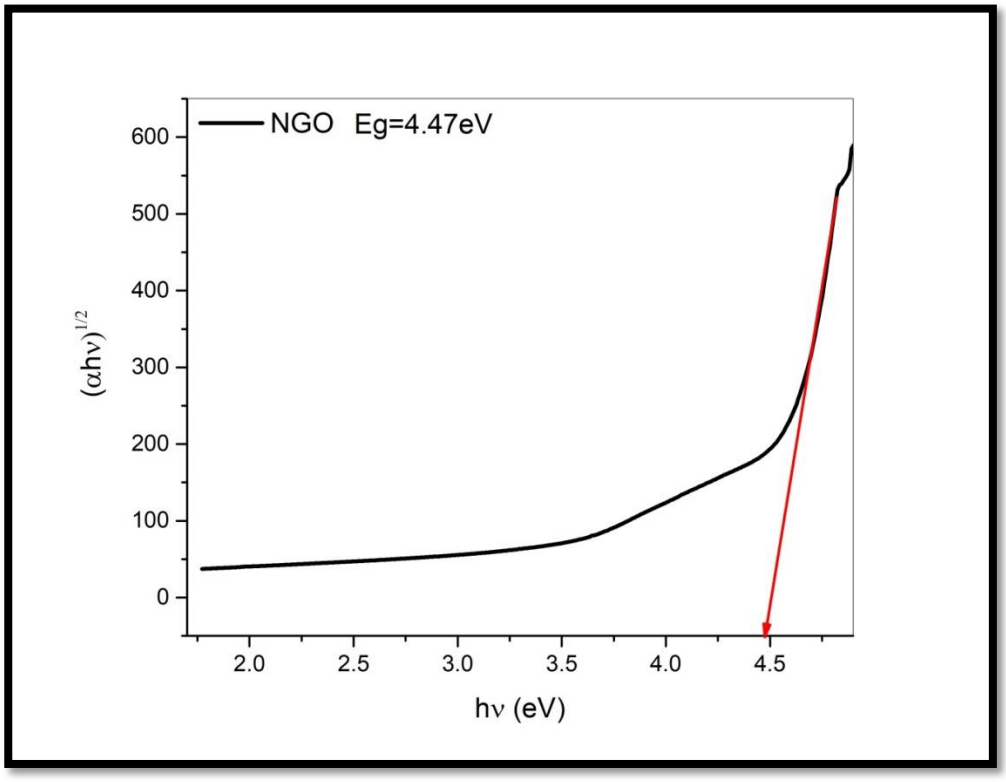

Fig. (3-58) Tauc plot for band gap energy of NGO

The (20%) g-C_3N_4 -Bi_2O_3, (40%) g-C_3N_4 -Bi_2O_3, (60%) g-C_3N_4 -Bi_2O_3 and (80%) g-C_3N_4 -Bi_2O_3 binary nanocomposites shows the band gap (3.30,3.14,3.23 and2.88eV) respectively, as shown in the Fig (3-59), while in the previous studies was 2.42eV [176]. The band gap energy depends on the synthesis method and conditions, the results are shown in the table (3-50).

Table (3-50) Energy gap of (20%) g-C_3N_4 -Bi_2O_3, (40%) g-C_3N_4 -Bi_2O_3, (60%) g-C_3N_4 -Bi_2O_3 and (80%) g-C_3N_4 -Bi_2O_3 binary nanocomposites

nanocomposites	Band gap energy (eV)	Band gap energy in references (eV)
(80%) g-C_3N_4 -Bi_2O_3	2.88	2.42 [176]
(40%) g-C_3N_4 -Bi_2O_3	3.14	2.42 [176]
(60%) g-C_3N_4 -Bi_2O_3	3.23	2.42 [176]
(20%) g-C_3N_4 -Bi_2O_3	3.30	2.42 [176]

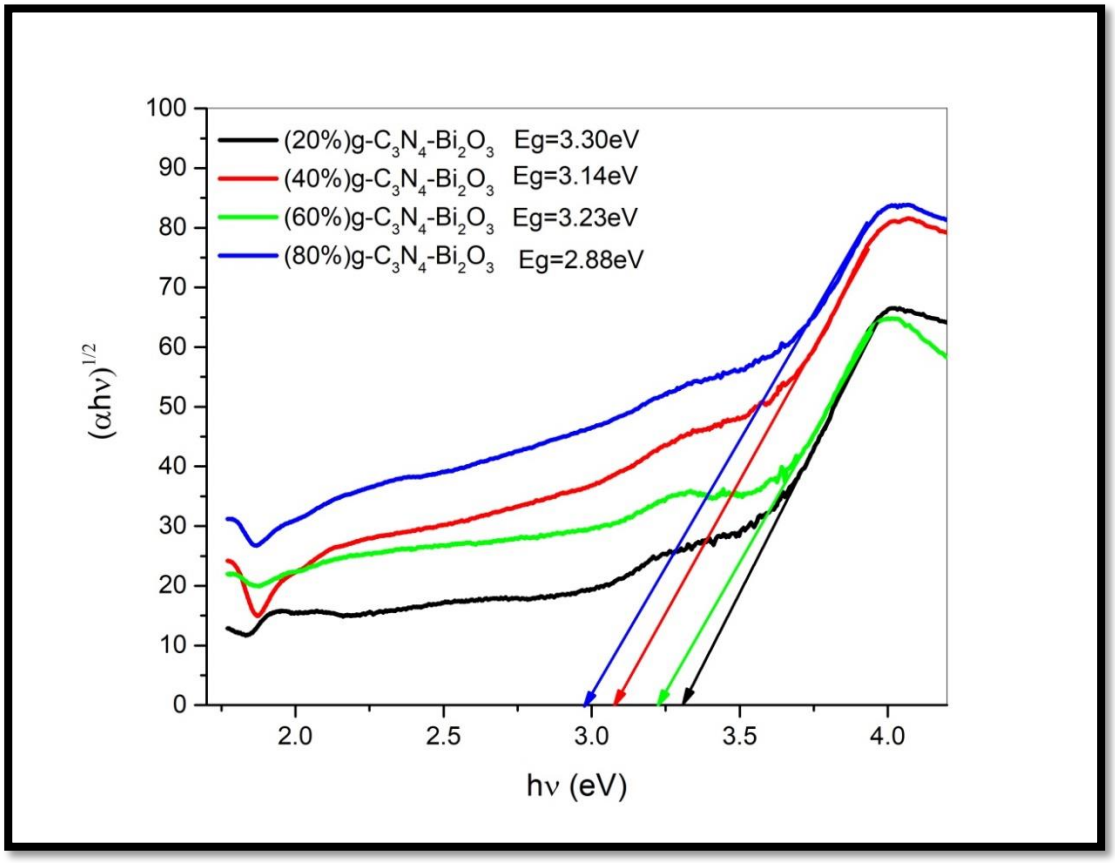

Fig. (3-59) Tauc plots for band gap energy of (20%) g-C_3N_4-Bi_2O_3, (40%) g-C_3N_4-Bi_2O_3, (60%) g-C_3N_4-Bi_2O_3 and (80%) g-C_3N_4-Bi_2O_3 binary nanocomposites

The BiC_{80}/GO (10 mg), BiC_{80}/GO (20 mg), BiC_{80}/GO (30 mg) and BiC_{80}/GO (40 mg) the ternary nanocomposites have band gaps (3,3.22,2.72 and 2.997eV) respectively, as shown in the Fig. (3-60). The band gap energy depends on the synthesis method and conditions. The results are shown in the table (3-51)

Table (3-51) Energy gap values of BiC_{80}/GO (10 mg), BiC_{80}/GO (20 mg), BiC_{80}/GO (30 mg) and BiC_{80}/GO (40 mg) ternary nanocomposites

Nanocomposites	Band gap energy (eV)
BiC_{80}/GO (30 mg)	2.72
BiC_{80}/GO (40 mg)	2.99
BiC_{80}/GO (10 mg)	3.00
BiC_{80}/GO (20 mg)	3.22

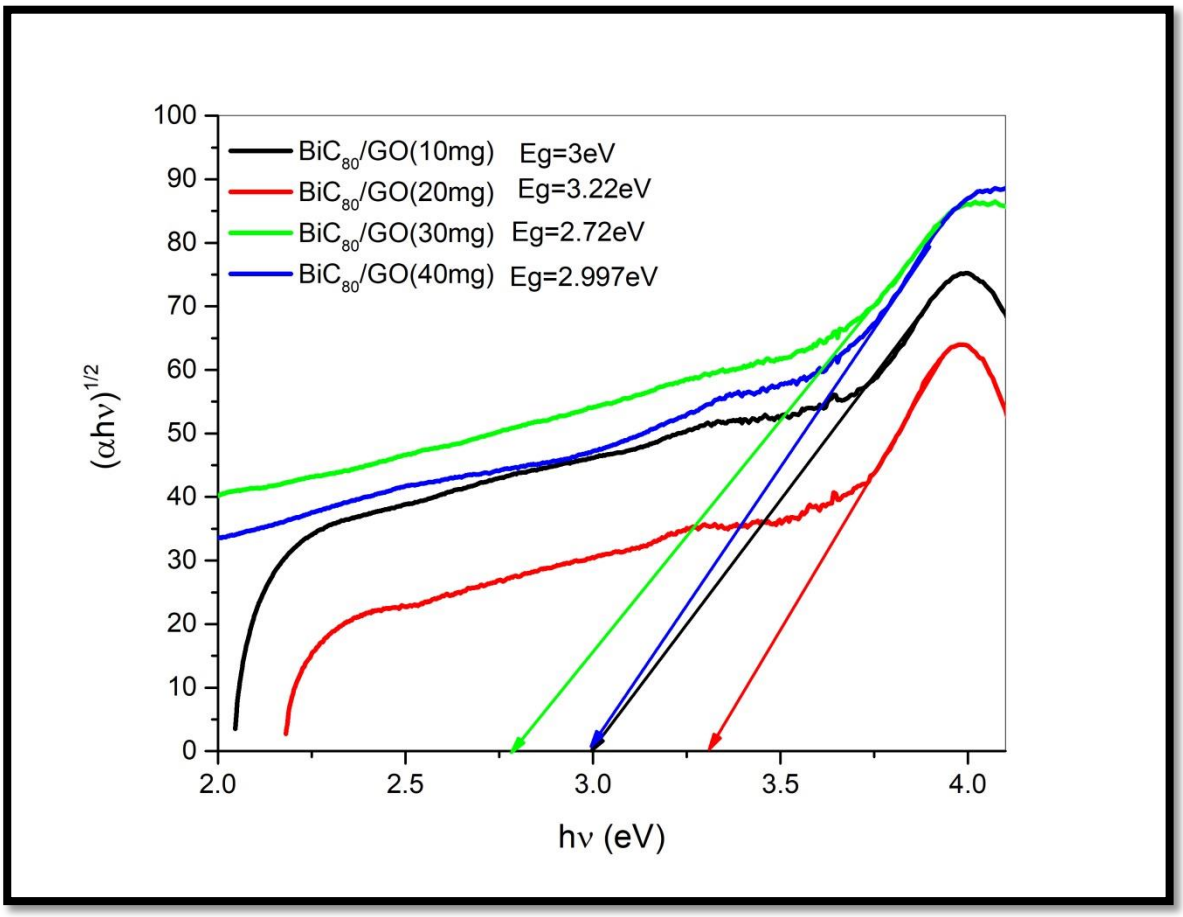

Fig. (3-60) Tauc plot for band gaps energy of BiC_{80}/GO (10 mg), BiC_{80}/GO (20 mg), BiC_{80}/GO (30 mg) and BiC_{80}/GO (40 mg) ternary nanocomposites

3.5 Photocatalytic mechanism of nanocomposites

3.5.1 Electron transfer mechanism of catalytic binary nanocomposites

The photoluminesence mechanism is explained as follows, when the g-C_3N_4 was excited by wavelength (265.50 nm), electrons from the valance band transferred to the conduction band leaving the holes in the former. The transferred electrons in conduction band recombine with holes in the valance band after releasing photones as PL emission. The observed higher photolumiesence intensity indicates the higher recombination rate of photoindued electron-hole pairs in the g-C_3N_4 sample. In the case of Bi_2O_3/g-C_3N_4 binary nanocomposites, the photoinduced electrons from the conduction band of g-C_3N_4 trasferred to the conduction band of Bi_2O_3, [183],[184], in the mean time, the holes in the valance band of Bi_2O_3 transferred to the valance band of g-C_3N_4 as shown in Fig. (3-61). This separation and transfer of charge carriers in Bi_2O_3/g-C_3N_4 nanocomposites effectively inhibit the recombination process leading to observed lower PL intensity. The minimal intensity of all Bi_2O_3/g-C_3N_4 binary nanocomposites indicating that the luminescence is quenched more effectively which in turn suggests the promoted photoinduced electron-hole pair separation and transfer.
The photoinduced electrons in the CB of Bi_2O_3 will reacts with O_2 molecules to form super oxide anion radicals $O_2/•O^{-2}$ (-0.05 eV NHE) and O_2/H_2O_2 (+0.69 eV NHE) while the holes in VB of g-C_3N_4 react with OH^{-1} ion to form hydroxyl radical (H_2O/•OH (2.28 eV NHE) and OH^{-1}/•OH (1.99 eV NHE). These reactive oxidative agents decompose the MB molecule to CO_2 and H_2O.

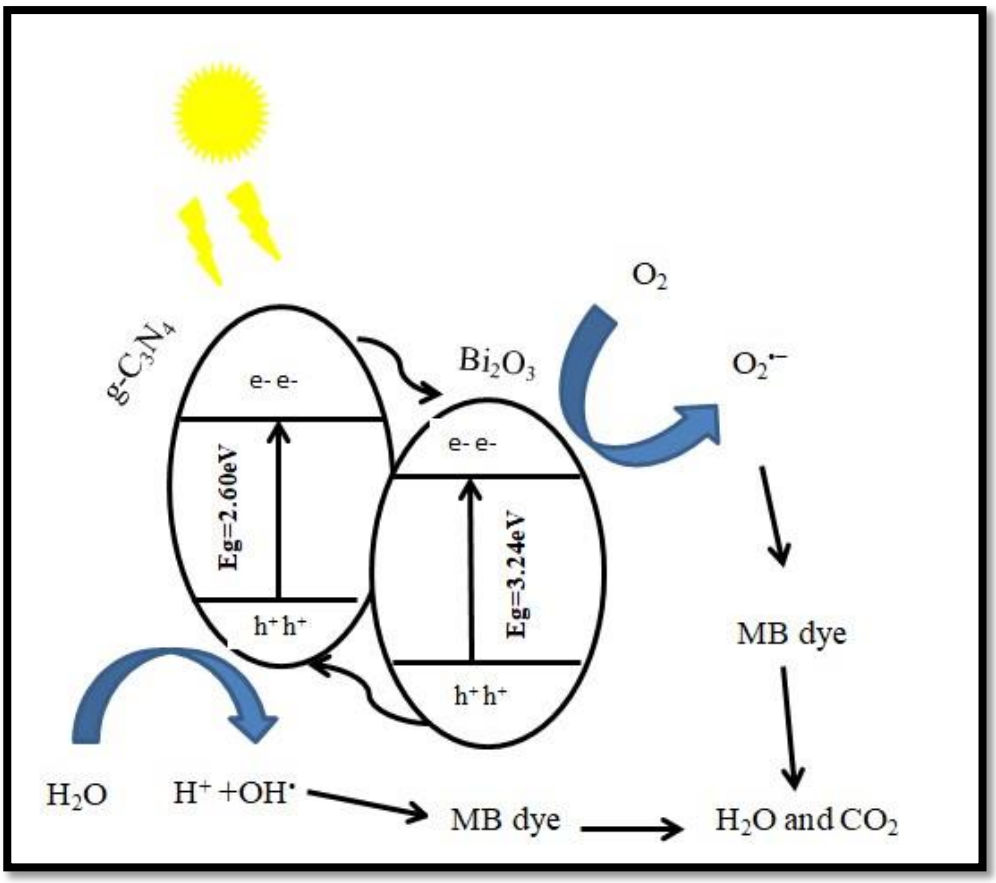

Fig. (3-61) Proposed mechanism for the photodegradation of MB dye by g-C_3N_4 -Bi_2O_3 binary nanocomposite catalyst

3.5.2 Electron transfer mechanism of catalytic ternary nanocomposites

The photocatalytic mechanism of BiC_{80}/GO (x mg), light irradiates g-C_3N_4 and Bi_2O_3 at the same time and excites to generate e^- and h^+ pairs. The electrons migrate from CB of g-C_3N_4 to CB of Bi_2O_3, while holes migrate from VB of Bi_2O_3 to VB of g-C_3N_4, thereby reduction recombination [185]. Moreover, electrons will flow spontaneously from CB of Bi_2O_3 and then gradually flow to NGO [186],[187],[188]. This process effectively separated electrons and holes and increase the lifetime of the charge [189], which directly leads to fluorescence quenching Fig. (3-62). As the accepter of electrons, strengthens the transfer of electric charge and makes the carrier react with water and dissolved oxygen on the surface of the composite to produce $\bullet O^{-2}$ and •OH [190]. Finally, the pollutants are completely oxidized into CO_2 and H_2O.

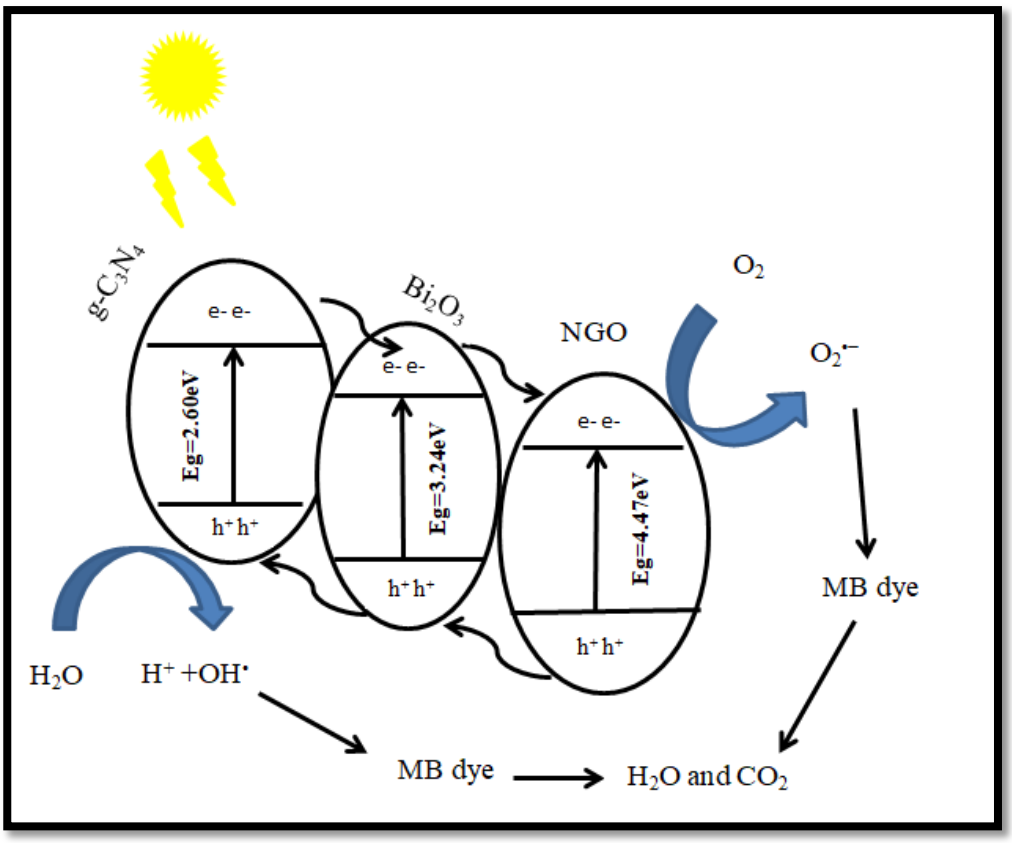

Fig. (3-62) Proposed mechanism for the photodegradation of MB dye by (BiC_{80}/GO (x mg) ternary nanocomposite catalyst

3.6 Kinetics of photocatalytic degradation of MB dye

The effect of initial concentration of MB dye on the degradation rate by 50 mg of (80%) g-C_3N_4-Bi_2O_3 binary nanocomposite catalyst compound was studied in the concentration range 5-15 mg.L^{-1}. A plot of the negative log of the ratio of concentration to the original concentration as described by Eq. (3-3) will produce a straight line for -ln(C/C_o) vs. time (t) and describes a pseudo-first-order kinetic relationship [191].

$-\ln C/C_o = kt$……. (3-3)

Pseudo-first-order degradation lines are depicted in Fig. (3-63), the correlation coefficients (R^2) are 0.81114 ,0.94452 and 0.9862 for 5, 10 and 15 mg.L^{-1} respectively of MB dye concentrations, indicating that the degradation of MB dye followed a pseudo-first-order kinetic model.

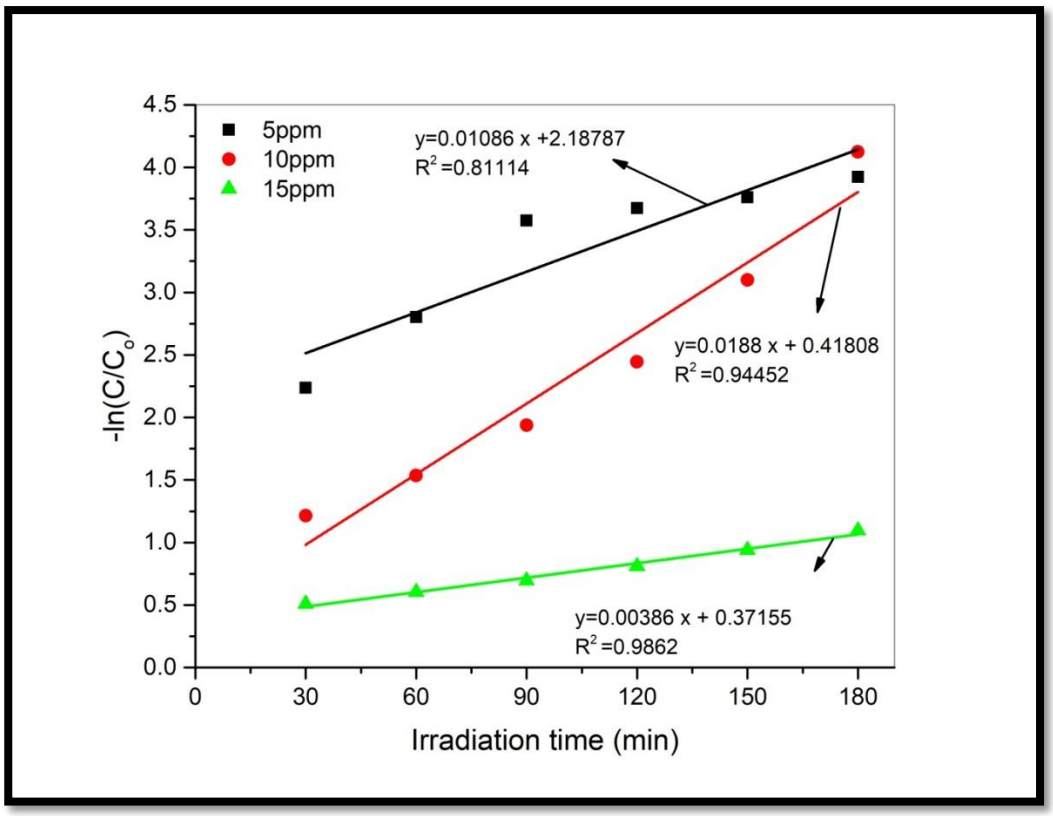

Fig. (3-63) First-order plots for photocatalytic degradation of MB dye (5-15 mg.L^{-1}) by 50 mg of (80%) g-C_3N_4 - Bi_2O_3 binary nanocomposite catalyst

A plot of the negative log of the degradation ratio of MB dye concentration to the original concentration by using 50 mg of BiC_{80}/GO (20 mg) ternary nanocomposite as a catalyst described by Eq. (3-3) will produce a straight line for $-\ln(C/C_o)$ vs. time (t) and describes a pseudo-first-order kinetic relationship [191]. Pseudo-first-order degradation lines are depicted in Fig. (3-64), the correlation coefficients (R^2) are 0.96764 ,0,9862 and 0.98682 for 5, 10 and 15 mg.L^{-1} respectively of MB dye concentrations, indicating the degradation of MB dye by BiC_{80}/GO (20 mg) ternary nanocomposites catalyst followed a pseudo-first-order kinetic model. In general, pseudo-first-order kinetic process in this case of photocatalytic degradation of MB dye follow the Langmuir-Hinshelwood mechanism, the reaction rate is proportional to amount of photocatalytic material covered with the pollutant MB dye. Since photocatalytic reaction can occur only when organic pollutant molecules are adsorbed onto the surface of the catalyst.

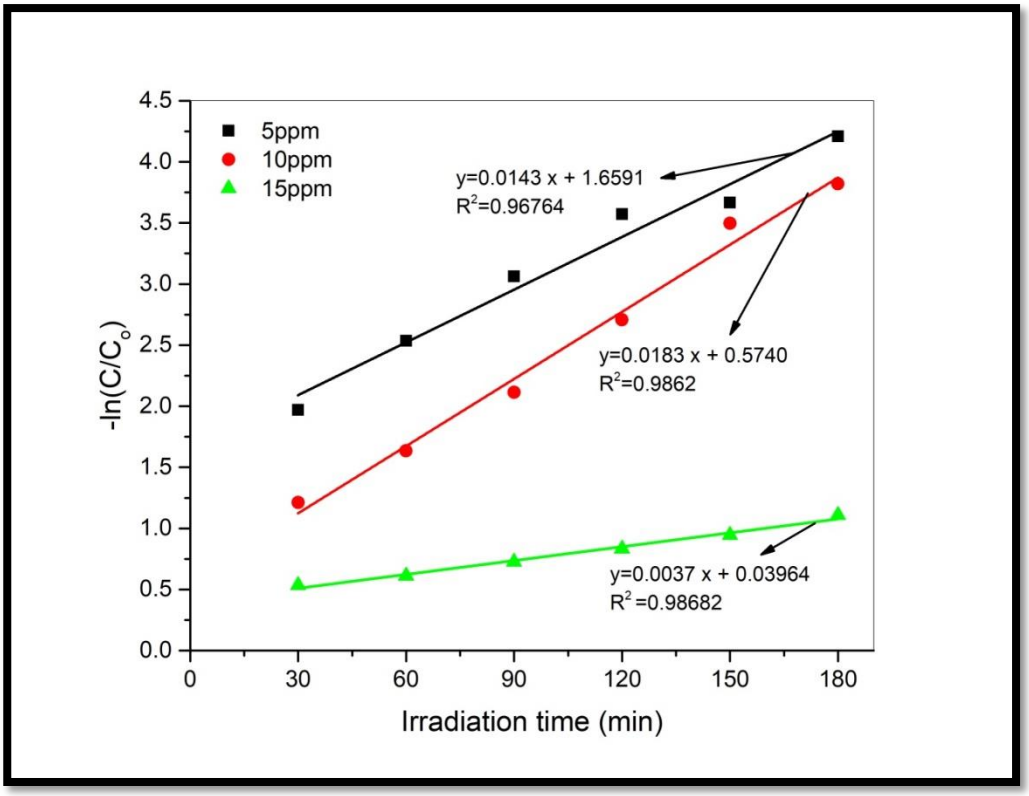

Fig. (3-64) First-order plots for photocatalytic degradation of MB dye (5-15 mg.L^{-1}) by 50 mg of BiC_{80}/GO (20 mg) ternary nanocomposite catalyst

3.7 Membrane Synthesis

3.7.1 Separation of MB dye by g-C_3N_4, Bi_2O_3 and NGO membranes

The experimental data shows the removal of MB dye by the membranes in the order g-C_3N_4 > NGO > Bi_2O_3, the best membrane is g-C_3N_4, R% (62.872 %), as show in Fig. (3-65). The removal efficiency (R%) of MB was calculated by using Eq. (3-4)

$R\%=C_o- C_e /C_o$ x100 ……. (3-4)

Where R represents the removal efficiency of MB, C_o (mg.L^{-1}) and C_e (mg.L^{-1}) are the initial and equilibrium concentrations, respectively.The separation mechanism indicated that this membrane adsorbed dyes mainly through physical sieving, electrostatic interaction, and hydrogen bonds[192].

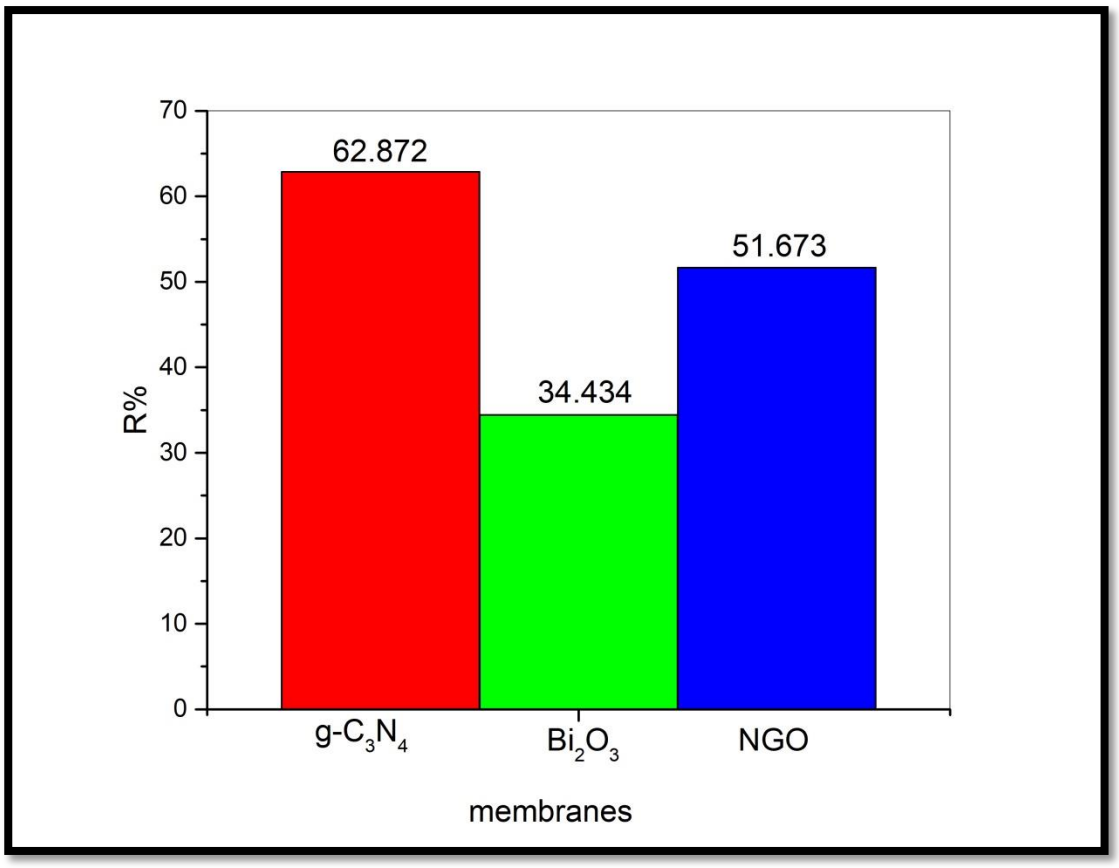

Fig. (3-65): Removal percentage of MB dye by g-C_3N_4, Bi_2O_3 and NGO membranes

3.7.2 Separation of MB dye by (20%) g-C_3N_4 -Bi_2O_3, (40%) g-C_3N_4 -Bi_2O_3, (60%) g-C_3N_4 -Bi_2O_3 and (80%) g-C_3N_4 -Bi_2O_3 binary nanocomposites membranes

The experimental data shows the removal % of MB dye by the membranes in the order (80%) g-C_3N_4 -Bi_2O_3 > (60%) g-C_3N_4 -Bi_2O_3 > (40%) g-C_3N_4 -Bi_2O_3> (20%) g-C_3N_4 -Bi_2O_3, the best membrane is (80%) g-C_3N_4 -Bi_2O_3, where R% (70.819 %), as show in Fig. (3-66). The mechanism analysis indicated that this membrane adsorbed dyes mainly through physical sieving, electrostatic interaction, and hydrogen bonds[192].

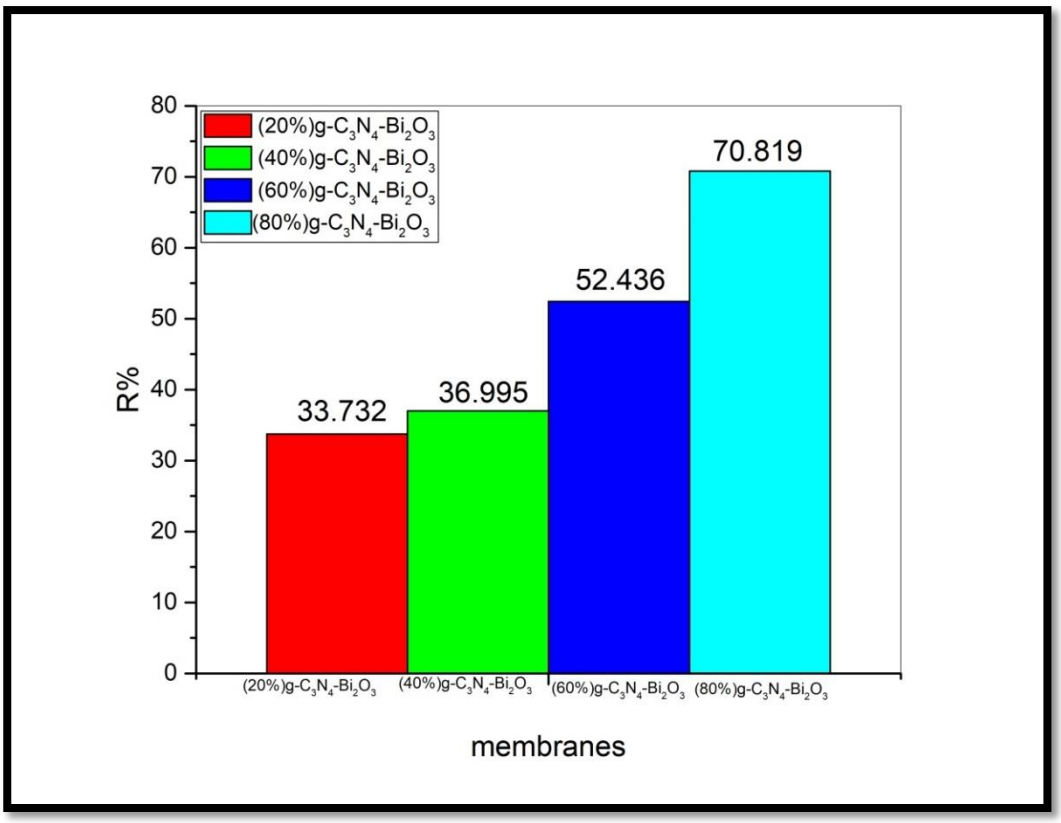

Fig. (3-66): Removal percentage of MB dye by (20%) g-C_3N_4 -Bi_2O_3, (40%) g-C_3N_4 -Bi_2O_3, (60%) g-C_3N_4 -Bi_2O_3 and (80%) g-C_3N_4 -Bi_2O_3 binary nanocomposites membranes

3.7.3 Separation of MB Dye by BiC_{80}/GO (10 mg), BiC_{80}/GO (20 mg), BiC_{80}/GO (30 mg) and BiC_{80}/GO (40 mg) ternary nanocomposites membranes

The experimental data shows the removal R% of MB dye by the membranes in the order BiC_{80}/GO (30mg) > BiC_{80}/GO (20mg) > BiC_{80}/GO (40mg) > BiC_{80}/GO (10 mg), the best membrane is BiC_{80}/GO (30 mg), where R% (49.265 %), as show in Fig. (3-67). The mechanism analysis indicated that this membrane adsorbed dyes mainly through physical sieving, electrostatic interaction, and hydrogen bonds[192].

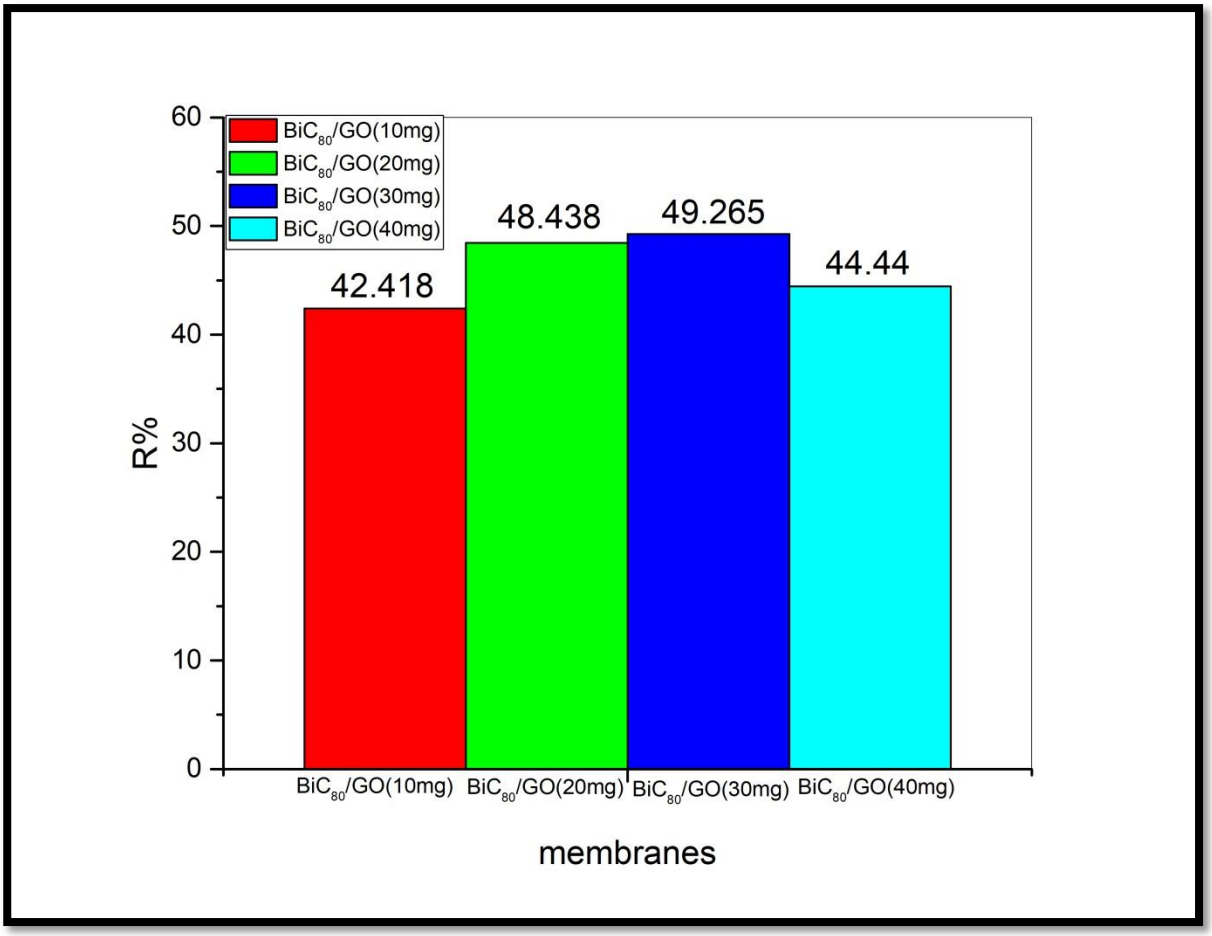

Fig. (3-67): Removal percentage of MB dye by BiC_{80}/GO (10 mg), BiC_{80}/GO (20 mg), BiC_{80}/GO (30 mg) and BiC_{80}/GO (40 mg) ternary nanocomposite membranes

Conclusion and Recommendations

Conclusion

This study includes synthesis; nano graphitic carbon nitride(g-C_3N_4), nano bismuth oxide (Bi_2O_3) and, nano-graphene oxide (NGO). Synthesis binary nanocomposites (20%) g-C_3N_4 -Bi_2O_3, (40%) g-C_3N_4 -Bi_2O_3, (60%) g-C_3N_4 -Bi_2O_3, (80%) g-C_3N_4 -Bi_2O_3. In addition to synthesis a novel ternary nanocomposites BiC_{80}/GO (10 mg), BiC_{80}/GO (20 mg), BiC_{80}/GO (30 mg) and BiC_{80}/GO (40 mg) by high temperature calcination method. The particle size was calculated by Debye-Scherrer equation, the average particles size of synthesized g-C_3N_4, $Bi_2O_3$and NGO (5.209, 24.972 and 6.476 nm) respectively. Binary nanocomposites (20%) g-C_3N_4 -Bi_2O_3. (40%) g-C_3N_4 -Bi_2O_3, (60%) g-C_3N_4 -Bi_2O_3, and (80%) g-C_3N_4 -Bi_2O_3 (29.775, 28.306, 24.245 and 29.533 nm) respectively. While the ternary nano composites are BiC_{80}/GO (10 mg), BiC_{80}/GO (20 mg), BiC_{80}/GO (30 mg) and BiC_{80}/GO (40 mg) (17.468, 18.169, 21.097 and 20.397 nm) respectively.

The degradation efficiency D% of MB dye by g-C_3N_4, Bi_2O_3 and NGO (93.34%,0.95% and 98.335%) respectively, under the visible light irradiation in a time period of 180 min. The degradation efficiency D% of MB dye by Binary nanocomposites (20%) g-C_3N_4 -Bi_2O_3, (40%) g-C_3N_4 -Bi_2O_3, (60%) g-C_3N_4 -Bi_2O_3 and (80%) g-C_3N_4 -Bi_2O_3 (21.77%, 35.4%, 41.48% and 98.38%) respectively, under the visible light irradiation in a time period of 180 min. The degradation efficiency D% of MB dye by ternary nanocomposites BiC_{80}/GO (10 mg), BiC_{80}/GO (20 mg), BiC_{80}/GO (30 mg) and BiC_{80}/GO (40 mg) (88.98%,97.81%,96.65 and 91.58%) respectively, under visible light irradiation in a time period of 180 min. Therefore, these nanocomposites can be used to remove the organic pollutants from river and sea water which exposure to sunlight.

The nano membranes were fabricated, g-C_3N_4, Bi_2O_3 and NGO by vacuum filtration. The removal R% of methylene blue was, (62.872%, 34.434% and 51.673%) respectively. Binary nanocomposites, (20%) g-C_3N_4 -Bi_2O_3, (40%) g-C_3N_4 -Bi_2O_3, (60%) g-C_3N_4 -Bi_2O_3, (80%) g-C_3N_4 -Bi_2O_3 were fabricated as membranes by vacuum filtration, the removal R% was (33.268%, 36.995%, 52.436% and 70.819%) respectively. Ternary nanocomposites BiC_{80}/GO (10 mg), BiC_{80}/GO (20 mg), BiC_{80}/GO (30 mg) and BiC_{80}/GO (40 mg) were fabricated as membranes by vacuum filtration, the removal R% are (42.418%, 48.438%, 49.265% and 44.44%) respectively.

Recommendations

1. Studying the biological activity of (20%) g-C_3N_4 -Bi_2O_3, (40%) g-C_3N_4 -Bi_2O_3, (60%) g-C_3N_4 -Bi_2O_3, (80%) g-C_3N_4 -Bi_2O_3 binary nanocomposites, BiC_{80}/GO (10 mg), BiC_{80}/GO (20 mg), BiC_{80}/GO (30 mg) and BiC_{80}/GO (40 mg) ternary nanocomposites against bacteria and fungi.
2. Study of electrical conductivity for (20%) g-C_3N_4 -Bi_2O_3, (40%) g-C_3N_4 -Bi_2O_3, (60%) g-C_3N_4 -Bi_2O_3, (80%) g-C_3N_4 -Bi_2O_3 binary nanocomposites, BiC_{80}/GO (10 mg), BiC_{80}/GO (20 mg), BiC_{80}/GO (30 mg) and BiC_{80}/GO (40 mg) ternary nanocomposites.
3. Study of the mechanical properties of these (20%) g-C_3N_4 -Bi_2O_3, (40%) g-C_3N_4 -Bi_2O_3, (60%) g-C_3N_4 -Bi_2O_3, (80%) g-C_3N_4 -Bi_2O_3 binary nano composites, BiC_{80}/GO (10 mg), BiC_{80}/GO (20 mg), BiC_{80}/GO (30 mg) and BiC_{80}/GO (40 mg) ternary nanocomposites.
4. Synthesis of other Graphitic Carbon Nitride(g-C_3N_4) composites by using other metal oxides.
5. Using g-C_3N_4, Bi_2O_3, NGO, (20%) g-C_3N_4 -Bi_2O_3, (40%) g-C_3N_4 -Bi_2O_3, (60%) g-C_3N_4 -Bi_2O_3, (80%) g-C_3N_4 -Bi_2O_3 binary nanocomposites, BiC_{80}/GO (10 mg), BiC_{80}/GO (20 mg), BiC_{80}/GO (30 mg) and BiC_{80}/GO (40 mg) ternary nanocomposites and membranes to remove other organic pollutants and heavy metals.

References

[1] F. J. Heiligtag and M. Niederberger, “The fascinating world of nanoparticle research,” *Mater. Today*, vol. 16, no. 7–8, pp. 262–271, Jul. 2013, doi: 10.1016/j.mattod.2013.07.004.
[2] A. R. Singh, “Nanotechnology-based approaches applied to nutraceuticals,” *Drug Deliv. Transl. Res.*, vol. 12, no. 3, pp. 485–499, Mar. 2022, doi: 10.1007/s13346-021-00960-3.
[3] S. S. Shah, M. N. Shaikh, M. Y. Khan, M. A. Alfasane, M. M. Rahman, and M. A. Aziz, “Present Status and Future Prospects of Jute in Nanotechnology: A Review,” *Chem. Rec.*, vol. 21, no. 7, pp. 1631–1665, Jul. 2021, doi: 10.1002/tcr.202100135.
[4] V. Harish *et al.*, “Review on Nanoparticles and Nanostructured Materials: Bioimaging, Biosensing, Drug Delivery, Tissue Engineering, Antimicrobial, and Agro-Food Applications,” *Nanomaterials*, vol. 12, no. 3, p. 457, Jan. 2022, doi: 10.3390/nano12030457.
[5] A. Santamaria, “Historical Overview of Nanotechnology and Nanotoxicology,” 2012, pp. 1–12. doi: 10.1007/978-1-62703-002-1_1.
[6] P. Khanna, A. Kaur, and D. Goyal, “Algae-based metallic nanoparticles: Synthesis, characterization and applications,” *J. Microbiol. Methods*, vol. 163, p. 105656, Aug. 2019, doi: 10.1016/j.mimet.2019.105656.
[7] S. Zhuang, E. S. Lee, L. Lei, B. B. Nunna, L. Kuang, and W. Zhang, “Synthesis of nitrogen-doped graphene catalyst by high-energy wet ball milling for electrochemical systems,” *Int. J. Energy Res.*, vol. 40, no. 15, pp. 2136–2149, Dec. 2016, doi: 10.1002/er.3595.
[8] H. Lyu, B. Gao, F. He, C. Ding, J. Tang, and J. C. Crittenden, “Ball-Milled Carbon Nanomaterials for Energy and Environmental Applications,” *ACS Sustain. Chem. Eng.*, vol. 5, no. 11, pp. 9568–9585, Nov. 2017, doi: 10.1021/acssuschemeng.7b02170.
[9] C. C. Koch and J. D. Whittenberger, “Mechanical milling/alloying of intermetallics,” *Intermetallics*, vol. 4, no. 5, pp. 339–355, Jan. 1996, doi: 10.1016/0966-9795(96)00001-5.
[10] R. JANOT and D. GUERARD, “Ball-milling in liquid mediaApplications to the preparation of anodic materials for lithium-ion batteries,” *Prog. Mater. Sci.*, vol. 50, no. 1, pp. 1–92, Jan. 2005, doi: 10.1016/S0079-6425(03)00050-1.
[11] R. Ostermann, J. Cravillon, C. Weidmann, M. Wiebcke, and B. M. Smarsly, “Metal–organic framework nanofibers viaelectrospinning,” *Chem. Commun.*, vol. 47, no. 1, pp. 442–444, 2011, doi: 10.1039/C0CC02271C.
[12] P. S. Kumar, “Hierarchical electrospun nanofibers for energy harvesting, production and environmental remediation,” *Energy Environ. Sci.*, vol. 7, no. 10, pp. 3192–3222, 2014, doi: 10.1039/C4EE00612G.

[13] P. Du., “Coaxial electrospun TiO_2/ZnO core–sheath nanofibers film: Novel structure for photoanode of dye-sensitized solar cells,” *Electrochim. Acta*, vol. 78, pp. 392–397, Sep. 2012, doi: 10.1016/j.electacta.2012.06.034.
[14] A. Pimpin and W. Srituravanich, “Review on Micro- and Nanolithography Techniques and their Applications,” *Eng. J.*, vol. 16, no. 1, pp. 37–56, Jan. 2012, doi: 10.4186/ej.2012.16.1.37.
[15] Y. Yin, B. Gates, and Y. Xia, “A Soft Lithography Approach to the Fabrication of Nanostructures of Single Crystalline Silicon with Well-Defined Dimensions and Shapes,” *Adv. Mater.*, vol. 12, no. 19, pp. 1426–1430, Oct. 2000, doi: 10.1002/1521-4095(200010)12:19<1426::AID-ADMA1426>3.0.CO;2-B.
[16] V. Garg, R. G. Mote, and J. Fu, “Facile fabrication of functional 3D micro-nano architectures with focused ion beam implantation and selective chemical etching,” *Appl. Surf. Sci.*, vol. 526, p. 146644, Oct. 2020, doi: 10.1016/j.apsusc.2020.146644.
[17] P. Pieranski, “Two-Dimensional Interfacial Colloidal Crystals,” *Phys. Rev. Lett.*, vol. 45, no. 7, pp. 569–572, Aug. 1980, doi: 10.1103/PhysRevLett.45.569.
[18] G. Zhang and D. Wang, “Colloidal Lithography—The Art of Nanochemical Patterning,” *Chem. – An Asian J.*, vol. 4, no. 2, pp. 236–245, Feb. 2009, doi: 10.1002/asia.200800298.
[19] P. Ayyub, R. Chandra, P. Taneja, A. K. Sharma, and R. Pinto, “Synthesis of nanocrystalline material by sputtering and laser ablation at low temperatures,” *Appl. Phys. A Mater. Sci. Process.*, vol. 73, no. 1, pp. 67–73, Jul. 2001, doi: 10.1007/s003390100833.
[20] H. H. Son, G. H. Seo, U. Jeong, D. Y. Shin, and S. J. Kim, “Capillary wicking effect of a Cr-sputtered superhydrophilic surface on enhancement of pool boiling critical heat flux,” *Int. J. Heat Mass Transf.*, vol. 113, pp. 115–128, Oct. 2017, doi: 10.1016/j.ijheatmasstransfer.2017.05.055.
[21] J. Mu oz-Garc a., “Toward functional nanomaterials,” *ZM Wang. sl Springer, Dordr.*, p. 323, 2009.
[22] J. H. Nam., “Room-temperature sputtered electrocatalyst WSe2 nanomaterials for hydrogen evolution reaction,” *J. Energy Chem.*, vol. 47, pp. 107–111, Aug. 2020, doi: 10.1016/j.jechem.2019.11.027.
[23] M. Nie, K. Sun, and D. D. Meng, “Formation of metal nanoparticles by short-distance sputter deposition in a reactive ion etching chamber,” *J. Appl. Phys.*, vol. 106, no. 5, Sep. 2009, doi: 10.1063/1.3211326.
[24] D. Zhang., “Controllable synthesis of carbon nanomaterials by direct current arc discharge from the inner wall of the chamber,” *Carbon N. Y.*, vol. 142, pp. 278–284, Feb. 2019, doi: 10.1016/j.carbon.2018.10.062.

[25] A. D. Liehr, “Solid State Physics. Advances in Research and Applications.,” *J. Am. Chem. Soc.*, vol. 82, no. 10, pp. 2658–2659, May 1960, doi: 10.1021/ja01495a084.
[26] V. Amendola and M. Meneghetti, “Laser ablation synthesis in solution and size manipulation of noble metal nanoparticles,” *Phys. Chem. Chem. Phys.*, vol. 11, no. 20, p. 3805, 2009, doi: 10.1039/b900654k.
[27] J. S. Duque, B. M. Madrigal, H. Riascos, and Y. P. Avila, “Colloidal Metal Oxide Nanoparticles Prepared by Laser Ablation Technique and Their Antibacterial Test,” *Colloids and Interfaces*, vol. 3, no. 1, p. 25, Feb. 2019, doi: 10.3390/colloids3010025.
[28] J. Zhang, M. Chaker, and D. Ma, “Pulsed laser ablation based synthesis of colloidal metal nanoparticles for catalytic applications,” *J. Colloid Interface Sci.*, vol. 489, pp. 138–149, Mar. 2017, doi: 10.1016/j.jcis.2016.07.050.
[29] J. Chrzanowska., “Synthesis of carbon nanotubes by the laser ablation method: Effect of laser wavelength,” *Phys. status solidi*, vol. 252, no. 8, pp. 1860–1867, Aug. 2015, doi: 10.1002/pssb.201451614.
[30] R. A. Ismail, M. H. Mohsin, A. K. Ali, K. I. Hassoon, and S. Erten-Ela, “Preparation and characterization of carbon nanotubes by pulsed laser ablation in water for optoelectronic application,” *Phys. E Low-dimensional Syst. Nanostructures*, vol. 119, p. 113997, May 2020, doi: 10.1016/j.physe.2020.113997.
[31] T. E. Itina, “On nanoparticle formation by laser ablation in liquids,” *J. Phys. Chem. C*, vol. 115, no. 12, pp. 5044–5048, 2011.
[32] A. C. Jones and M. L. Hitchman, *Chemical vapour deposition: precursors, processes and applications*. Royal society of chemistry, 2009.
[33] K. A. Shah and B. A. Tali, “Synthesis of carbon nanotubes by catalytic chemical vapour deposition: A review on carbon sources, catalysts and substrates,” *Mater. Sci. Semicond. Process.*, vol. 41, pp. 67–82, Jan. 2016, doi: 10.1016/j.mssp.2015.08.013.
[34] H. Ago, “CVD Growth of High-Quality Single-Layer Graphene,” in *Frontiers of Graphene and Carbon Nanotubes*, Tokyo: Springer Japan, 2015, pp. 3–20. doi: 10.1007/978-4-431-55372-4_1.
[35] P. Machac, S. Cichon, L. Lapcak, and L. Fekete, “Graphene prepared by chemical vapour deposition process,” *Graphene Technol.*, vol. 5, no. 1–2, pp. 9–17, Jun. 2020, doi: 10.1007/s41127-019-00029-6.
[36] Q. Wu., “In situ chemical vapor deposition of graphene and hexagonal boron nitride heterostructures,” *Curr. Appl. Phys.*, vol. 16, no. 9, pp. 1175–1191, Sep. 2016, doi: 10.1016/j.cap.2016.04.024.
[37] X. Wu, G. Q. (Max) Lu, and L. Wang, “Shell-in-shell TiO_2 hollow spheres synthesized by one-pot hydrothermal method for dye-sensitized solar cell application,” *Energy Environ. Sci.*, vol. 4, no. 9, p. 3565, 2011, doi: 10.1039/c0ee00727g.

[38] S. Cao, C. Zhao, T. Han, and L. Peng, “Hydrothermal synthesis, characterization and gas sensing properties of the WO_3 nanofibers,” *Mater. Lett.*, vol. 169, pp. 17–20, Apr. 2016, doi: 10.1016/j.matlet.2016.01.053.
[39] H. K. Bisoyi and Q. Li, “Liquid Crystalline Anisotropic Nanoparticles: From Metallic and Semiconducting Nanoparticles to Carbon Nanomaterials,” 2015, pp. 209–240. doi: 10.1007/978-3-319-18293-3_6.
[40] A. Chen and P. Holt-Hindle, “Platinum-Based Nanostructured Materials: Synthesis, Properties, and Applications,” *Chem. Rev.*, vol. 110, no. 6, pp. 3767–3804, Jun. 2010, doi: 10.1021/cr9003902.
[41] K. Sue., “Size-controlled synthesis of metal oxide nanoparticles with a flow-through supercritical water method,” *Green Chem.*, vol. 8, no. 7, p. 634, 2006, doi: 10.1039/b518291c.
[42] K. Byrappa and T. Adschiri, “Hydrothermal technology for nanotechnology,” *Prog. Cryst. Growth Charact. Mater.*, vol. 53, no. 2, pp. 117–166, Jun. 2007, doi: 10.1016/j.pcrysgrow.2007.04.001.
[43] A. E. Danks, S. R. Hall, and Z. Schnepp, “The evolution of ‘sol–gel’ chemistry as a technique for materials synthesis,” *Mater. Horizons*, vol. 3, no. 2, pp. 91–112, 2016, doi: 10.1039/C5MH00260E.
[44] T. K. Tseng, Y. S. Lin, Y. J. Chen, and H. Chu, “A Review of Photocatalysts Prepared by Sol-Gel Method for VOCs Removal,” *Int. J. Mol. Sci.*, vol. 11, no. 6, pp. 2336–2361, May 2010, doi: 10.3390/ijms11062336.
[45] M. Parashar, V. K. Shukla, and R. Singh, “Metal oxides nanoparticles via sol–gel method: a review on synthesis, characterization and applications,” *J. Mater. Sci. Mater. Electron.*, vol. 31, no. 5, pp. 3729–3749, Mar. 2020, doi: 10.1007/s10854-020-02994-8.
[46] L. Znaidi, “Sol–gel-deposited ZnO thin films: A review,” *Mater. Sci. Eng. B*, vol. 174, no. 1–3, pp. 18–30, Oct. 2010, doi: 10.1016/j.mseb.2010.07.001.
[47] C. cero de Coelho Escobar and J. o H. Z. dos Santos, “Effect of the sol‑gel route on the textural characteristics of silica imprinted with Rhodamine B,” *J. Sep. Sci.*, vol. 37, no. 7, pp. 868–875, 2014.
[48] Y. Liu, J. Goebl, and Y. Yin, “Templated synthesis of nanostructured materials,” *Chem. Soc. Rev.*, vol. 42, no. 7, pp. 2610–2653, 2013, doi: 10.1039/C2CS35369E.
[49] W. Li and D. Zhao, “An overview of the synthesis of ordered mesoporous materials,” *Chem. Commun.*, vol. 49, no. 10, pp. 943–946, 2013, doi: 10.1039/C2CC36964H.
[50] R. R. Poolakkandy and M. M. Menamparambath, “Soft-template-assisted synthesis: a promising approach for the fabrication of transition metal oxides,” *Nanoscale Adv.*, vol. 2, no. 11, pp. 5015–5045, 2020, doi: 10.1039/D0NA00599A.

[51] Y. Yamauchi and K. Kuroda, “Rational Design of Mesoporous Metals and Related Nanomaterials by a Soft-Template Approach,” *Chem. – An Asian J.*, vol. 3, no. 4, pp. 664–676, Apr. 2008, doi: 10.1002/asia.200700350.
[52] S. J. Hurst, E. K. Payne, L. Qin, and C. A. Mirkin, “Multisegmented One-Dimensional Nanorods Prepared by Hard-Template Synthetic Methods,” *Angew. Chemie Int. Ed.*, vol. 45, no. 17, pp. 2672–2692, Apr. 2006, doi: 10.1002/anie.200504025.
[53] H. Fereidoun, M. S. Nourddin, N. A. Rreza, A. Mohsen, R. Ahmad, and H. Pouria, “The effect of long-term exposure to particulate pollution on the lung function of Teheranian and Zanjanian students,” *Pakistan J. Physiol.*, vol. 3, no. 2, 2007.
[54] A. Daly and P. Zannetti, “An introduction to air pollution‐definitions, classifications, and history,” *Ambient Air Pollut. P Zannetti, D Al-Ajmi S Al-Rashied, Arab Sch. Sci. Technol. EnviroComp Inst.*, pp. 1–14, 2007.
[55] D. L. Karlen, S. S. Andrews, B. J. Wienhold, and T. M. Zobeck, “Soil quality assessment: Past, present and future,” 2008.
[56] Q. Y. Ma, S. J. Traina, T. J. Logan, and J. A. Ryan, “In situ lead immobilization by apatite,” *Environ. Sci. Technol.*, vol. 27, no. 9, pp. 1803–1810, Sep. 1993, doi: 10.1021/es00046a007.
[57] P. Kristensen, C. Whalley, F. N. N. Zal, and T. Christiansen, “European waters assessment of status and pressures 2018.,” 2018.
[58] S. Sharma and A. Bhattacharya, “Drinking water contamination and treatment techniques,” *Appl. Water Sci.*, vol. 7, no. 3, pp. 1043–1067, Jun. 2017, doi: 10.1007/s13201-016-0455-7.
[59] F. L. Braghiroli, H. Bouafif, C. M. Neculita, and A. Koubaa, “Activated Biochar as an Effective Sorbent for Organic and Inorganic Contaminants in Water,” *Water, Air, Soil Pollut.*, vol. 229, no. 7, p. 230, Jul. 2018, doi: 10.1007/s11270-018-3889-8.
[60] P. E. Greeson, *Organic substances in water*, no. 848. US Geological Survey, 1981.
[61] N. R. Council, D. on Earth, L. Studies, C. on L. Sciences, and S. D. W. Committee, “Drinking Water and Health: Volume 1,” 1977.
[62] E. Diamanti-Kandarakis., “Endocrine-Disrupting Chemicals: An Endocrine Society Scientific Statement,” *Endocr. Rev.*, vol. 30, no. 4, pp. 293–342, Jun. 2009, doi: 10.1210/er.2009-0002.
[63] A. S. Kesselheim, M. S. Sinha, J. Avorn, and A. Sarpatwari, “Pharmaceutical policy in the United States in 2019: An overview of the landscape and avenues for improvement,” *Stan. L. Pol’y Rev.*, vol. 30, p. 421, 2019.
[64] E. Forgacs, T. Cserháti, and G. Oros, “Removal of synthetic dyes from wastewaters: a review,” *Environ. Int.*, vol. 30, no. 7, pp. 953–971, Sep. 2004, doi: 10.1016/j.envint.2004.02.001.

[65] S. Parsons, *Advanced oxidation processes for water and wastewater treatment*. IWA publishing, 2004.
[66] F. Vázquez-Ortega, I. Lagunes, and Á. Trigos, "Cosmetic dyes as potential photosensitizers of singlet oxygen generation," *Dye. Pigment.*, vol. 176, p. 108248, May 2020, doi: 10.1016/j.dyepig.2020.108248.
[67] A. Rehman., "The application of cationic-nonionic mixed micellar media for enhanced solubilization of Direct Brown 2 dye," *J. Mol. Liq.*, vol. 301, p. 112408, Mar. 2020, doi: 10.1016/j.molliq.2019.112408.
[68] M. Derudi, G. Venturini, G. Lombardi, G. Nano, and R. Rota, "Biodegradation combined with ozone for the remediation of contaminated soils," *Eur. J. Soil Biol.*, vol. 43, no. 5–6, pp. 297–303, Nov. 2007, doi: 10.1016/j.ejsobi.2007.03.001.
[69] M. RAUF, S. ASHRAF, and S. ALHADRAMI, "Photolytic oxidation of Coomassie Brilliant Blue with HO," *Dye. Pigment.*, vol. 66, no. 3, pp. 197–200, Sep. 2005, doi: 10.1016/j.dyepig.2004.09.006.
[70] A. D. LAURENT, V. WATHELET, M. BOUHY, D. JACQUEMIN, and E. PERP TE, "Simulation de la perception des couleurs de colorants organiques," 2010.
[71] E. A. Azzopardi *et al.*, "Chromophores in operative surgery: Current practice and rationalized development," *J. Control. Release*, vol. 249, pp. 123–130, Mar. 2017, doi: 10.1016/j.jconrel.2016.12.044.
[72] A. Benaissa, "Etude de la faisabilit dlimination de certains colorants textiles par certains mat-riaux dchets d-origine naturelle," 2012.
[73] F. Temesgen, N. Gabbiye, and O. Sahu, "Biosorption of reactive red dye (RRD) on activated surface of banana and orange peels: economical alternative for textile effluent," *Surfaces and interfaces*, vol. 12, pp. 151–159, 2018.
[74] S. ONG, E. TOORISAKA, M. HIRATA, and T. HANO, "Biodegradation of redox dye Methylene Blue by up-flow anaerobic sludge blanket reactor," *J. Hazard. Mater.*, vol. 124, no. 1–3, pp. 88–94, Sep. 2005, doi: 10.1016/j.jhazmat.2005.03.054.
[75] H. Patel and R. T. Vashi, "Fixed-bed column studies of dyeing mill wastewater treatment using naturally prepared adsorbents," *Charact. Treat. Text. wastewater*, pp. 127–145, 2015.
[76] A. Ahmad, N. Khan, B. S. Giri, P. Chowdhary, and P. Chaturvedi, "Removal of methylene blue dye using rice husk, cow dung and sludge biochar: Characterization, application, and kinetic studies," *Bioresour. Technol.*, vol. 306, p. 123202, Jun. 2020, doi: 10.1016/j.biortech.2020.123202.
[77] X.-J. Liu, M.-F. Li, and S. K. Singh, "Manganese-modified lignin biochar as adsorbent for removal of methylene blue," *J. Mater. Res. Technol.*, vol. 12, pp. 1434–1445, May 2021, doi: 10.1016/j.jmrt.2021.03.076.

[78] R. Dalefield, *Veterinary Toxicology for Australia and New Zealand*. Elsevier, 2017.
[79] C. Ponraj, V. G., and J. Daniel, "A review on the visible light active $BiFeO_3$ nanostructures as suitable photocatalyst in the degradation of different textile dyes," *Environ. Nanotechnology, Monit. Manag.*, vol. 7, pp. 110–120, May 2017, doi: 10.1016/j.enmm.2017.02.001.
[80] G. D. Shanks, "Control and elimination of Plasmodium vivax," *Adv. Parasitol.*, vol. 80, pp. 301–341, 2012.
[81] D. Bosoy, J. Axelband, R. Pursell, J. Lukaszczyk, and S. Stawicki, "Utilization of methylene blue in the setting of hypotension associated with concurrent renal and hepatic failure: A concise review," *Int. J. Acad. Med.*, vol. 3, no. 3, p. 101, 2017, doi: 10.4103/IJAM.IJAM_88_16.
[82] I. W. G. on the E. of the C. R. of C. to Humans, *IARC Monographs on the Evaluation of the Carcinogenic Risk of Chemicals to Humans*, vol. 30. International Agency for Research on Cancer, 1983.
[83] O. S. Bayomie, H. Kandeel, T. Shoeib, H. Yang, N. Youssef, and M. M. H. El-Sayed, "Novel approach for effective removal of methylene blue dye from water using fava bean peel waste," *Sci. Rep.*, vol. 10, no. 1, p. 7824, 2020.
[84] B. Dalal-Clayton and S. Bass, "National Strategies for Sustainable Development: the Challenge Ahead," Oct. 2011.
[85] K. Takanabe, "Solar water splitting using semiconductor photocatalyst powders," *Sol. Energy Fuels*, pp. 73–103, 2016.
[86] N. J. Turro, V. Ramamurthy, and J. C. Scaiano, *Modern molecular photochemistry of organic molecules*, vol. 188. University Science Books Sausalito, CA, 2010.
[87] K. Takanabe, "Photocatalytic Water Splitting: Quantitative Approaches toward Photocatalyst by Design," *ACS Catal.*, vol. 7, no. 11, pp. 8006–8022, Nov. 2017, doi: 10.1021/acscatal.7b02662.
[88] U. G. Akpan and B. H. Hameed, "Parameters affecting the photocatalytic degradation of dyes using TiO2-based photocatalysts: A review," *J. Hazard. Mater.*, vol. 170, no. 2–3, pp. 520–529, Oct. 2009, doi: 10.1016/j.jhazmat.2009.05.039.
[89] M. Ikram, A. Raza, S. Ali, and S. Ali, "Electrochemical exfoliation of 2D advanced carbon derivatives," *21st Century Adv. Carbon Mater. Eng. Appl. Compr. Handb.*, 2020.
[90] M. Shaban, F. A. Elwahab, A. E. Ghitas, and M. Y. El Zayat, "Efficient and recyclable photocatalytic degradation of methylene blue dye in aqueous solutions using nanostructured Cd 1- x Co x S films of different doping levels," *J. Sol-Gel Sci. Technol.*, vol. 95, pp. 276–288, 2020.
[91] K. Saeed and I. Khan, "Efficient photodegradation of neutral red chloride dye in aqueous medium using graphene/cobalt-manganese oxides nanocomposite," *Turkish J. Chem.*, vol. 41, no. 3, pp. 391–398, 2017.

[92] I. Khan, M. Sadiq, I. Khan, and K. Saeed, “Manganese dioxide nanoparticles/activated carbon composite as efficient UV and visible-light photocatalyst,” *Environ. Sci. Pollut. Res.*, vol. 26, pp. 5140–5154, 2019.
[93] K. Saeed, I. Khan, T. Gul, and M. Sadiq, “Efficient photodegradation of methyl violet dye using TiO_2/Pt and TiO_2/Pd photocatalysts,” *Appl. Water Sci.*, vol. 7, pp. 3841–3848, 2017.
[94] S. Shahabuddin, N. Muhamad Sarih, S. Mohamad, and J. Joon Ching, “$SrTiO_3$ nanocube-doped polyaniline nanocomposites with enhanced photocatalytic degradation of methylene blue under visible light,” *Polymers (Basel).*, vol. 8, no. 2, p. 27, 2016.
[95] T. Soltani and M. H. Entezari, “Photolysis and photocatalysis of methylene blue by ferrite bismuth nanoparticles under sunlight irradiation,” *J. Mol. Catal. A Chem.*, vol. 377, pp. 197–203, 2013.
[96] K. Saeed, I. Khan, and S.-Y. Park, “TiO_2/amidoxime-modified polyacrylonitrile nanofibers and its application for the photodegradation of methyl blue in aqueous medium,” *Desalin. Water Treat.*, vol. 54, no. 11, pp. 3146–3151, 2015.
[97] M. A. Fox and M. T. Dulay, “Heterogeneous photocatalysis,” *Chem. Rev.*, vol. 93, no. 1, pp. 341–357, 1993.
[98] F. Azeez., “The effect of surface charge on photocatalytic degradation of methylene blue dye using chargeable titania nanoparticles,” *Sci. Rep.*, vol. 8, no. 1, pp. 1–9, 2018.
[99] K. Saeed, N. Zada, I. Khan, and M. Sadiq, “Synthesis, characterization and photodegradation application of Fe-Mn and F-MWCNTs supported Fe-Mn oxides nanoparticles,” *Desalin. Water Treat*, vol. 108, pp. 362–368, 2018.
[100] T. Nguyen Thi Thu, N. Nguyen Thi, V. Tran Quang, K. Nguyen Hong, T. Nguyen Minh, and N. Le Thi Hoai, “Synthesis, characterisation, and effect of pH on degradation of dyes of copper-doped TiO2,” *J. Exp. Nanosci.*, vol. 11, no. 3, pp. 226–238, 2016.
[101] R. Hejazi, A. R. Mahjoub, A. H. C. Khavar, and Z. Khazaee, “Fabrication of novel type visible-light-driven TiO_2@ MIL-100 (Fe) microspheres with high photocatalytic performance for removal of organic pollutants,” *J. Photochem. Photobiol. A Chem.*, vol. 400, p. 112644, 2020.
[102] N. R. Hendekhale and A. Mohammad-Khah, “A novel synthesis of Co_2ZrO_5 and m-ZrO_2 nanoparticles by sono-precipitation and hydrothermal methods and their application in UV/Visible-photocatalytic studies,” *J. Environ. Chem. Eng.*, vol. 8, no. 5, p. 104065, 2020.
[103] A. Salama, A. Mohamed, N. M. Aboamera, T. A. Osman, and A. Khattab, “Photocatalytic degradation of organic dyes using composite nanofibers under UV irradiation,” *Appl. Nanosci.*, vol. 8, pp. 155–161, 2018.

[104] S. Alkaykh, A. Mbarek, and E. E. Ali-Shattle, "Photocatalytic degradation of methylene blue dye in aqueous solution by $MnTiO_3$ nanoparticles under sunlight irradiation," *Heliyon*, vol. 6, no. 4, 2020.
[105] E. M. Elsayed, M. S. Elnouby, M. H. Gouda, N. A. Elessawy, and D. M. F. Santos, "Effect of the morphology of tungsten oxide embedded in sodium alginate/polyvinylpyrrolidone composite beads on the photocatalytic degradation of methylene blue dye solution," *Materials (Basel).*, vol. 13, no. 8, p. 1905, 2020.
[106] L. A. Chanu, W. J. Singh, K. J. Singh, and K. N. Devi, "Effect of operational parameters on the photocatalytic degradation of Methylene blue dye solution using manganese doped ZnO nanoparticles," *Results Phys.*, vol. 12, pp. 1230–1237, 2019.
[107] H. Ashrafi, M. Akhond, and G. Absalan, "Adsorption and photocatalytic degradation of aqueous methylene blue using nanoporous carbon nitride," *J. Photochem. Photobiol. A Chem.*, vol. 396, p. 112533, 2020.
[108] A. Prasert, S. Sontikaew, D. Sriprapai, and S. Chuangchote, "Polypropylene/ZnO nanocomposites: Mechanical properties, photocatalytic dye degradation, and antibacterial property," *Materials (Basel).*, vol. 13, no. 4, p. 914, 2020.
[109] K. A. Isai and V. S. Shrivastava, "Photocatalytic degradation of methylene blue using ZnO and 2% Fe/ZnO semiconductor nanomaterials synthesized by sol-gel method: a comparative study," *SN Appl. Sci.*, vol. 1, pp. 1–11, 2019.
[110] B. Janani., "The effect of various capping agents on surface modifications of CdO NPs and the investigation of photocatalytic performance, antibacterial and anti-biofilm activities," *J. Inorg. Organomet. Polym. Mater.*, vol. 30, pp. 1865–1876, 2020.
[111] A. B. Ali Baig, V. Rathinam, and J. Palaninathan, "Photodegradation activity of yttrium-doped SnO_2 nanoparticles against methylene blue dye and antibacterial effects," *Appl. Water Sci.*, vol. 10, no. 2, p. 76, 2020.
[112] K. M. Reza, A. S. W. Kurny, and F. Gulshan, "Parameters affecting the photocatalytic degradation of dyes using TiO_2: a review," *Appl. Water Sci.*, vol. 7, pp. 1569–1578, 2017.
[113] P. Birnal, M. C. M. de Lucas, I. Pochard, B. Domenichini, and L. Imhoff, "Photocatalytic properties of atomic layer deposited TiO_2 inverse opals and planar films for the degradation of dyes," *Appl. Surf. Sci.*, vol. 512, p. 145693, 2020.
[114] B. Gao, Y. Ma, Y. Cao, W. Yang, and J. Yao, "Great enhancement of photocatalytic activity of nitrogen-doped titania by coupling with tungsten oxide," *J. Phys. Chem. B*, vol. 110, no. 29, pp. 14391–14397, 2006.
[115] J. M. Hermann, "Heterogeneous photocatalysis: an emerging discipline involving multiphase system," *Catal. today*, vol. 24, no. 1–2, pp. 157–164, 1995.

[116] M. Ismael, "A review on graphitic carbon nitride (g-C_3N_4) based nanocomposites: synthesis, categories, and their application in photocatalysis," *J. Alloys Compd.*, vol. 846, p. 156446, 2020.
[117] H.Wang.,"A sensitive photoelectrochemical immunoassay of N6-methyladenosine based on dual-signal amplification strategy: Ru doped in SiO2 nanosphere and carboxylated g-C3N4," *Biosens. Bioelectron.*, vol. 99, pp. 281–288, 2018.
[118] Y. Zheng, J. Liu, J. Liang, M. Jaroniec, and S. Z. Qiao, "Graphitic carbon nitride materials: controllable synthesis and applications in fuel cells and photocatalysis," *Energy Environ. Sci.*, vol. 5, no. 5, pp. 6717–6731, 2012.
[119] M. Ismael and Y. Wu, "A mini-review on the synthesis and structural modification of gC_3 N_4-based materials, and their applications in solar energy conversion and environmental remediation," *Sustain. Energy Fuels*, vol. 3, no. 11, pp. 2907–2925, 2019.
[120] J. Mao, T. Peng, X. Zhang, K. Li, L. Ye, and L. Zan, "Effect of graphitic carbon nitride microstructures on the activity and selectivity of photocatalytic CO_2 reduction under visible light," *Catal. Sci. Technol.*, vol. 3, no. 5, pp. 1253–1260, 2013.
[121] W.-J. Ong, L.-L. Tan, Y. H. Ng, S.-T. Yong, and S.-P. Chai, "Graphitic carbon nitride (g-C_3N_4)-based photocatalysts for artificial photosynthesis and environmental remediation: are we a step closer to achieving sustainability?," *Chem. Rev.*, vol. 116, no. 12, pp. 7159–7329, 2016.
[122] J. Vasiljevi, I. Jerman, and B. Simon i, "Graphitic carbon nitride as a new sustainable photocatalyst for textile functionalization," *Polymers (Basel).*, vol. 13, no. 15, p. 2568, 2021.
[123] S. Cao and J. Yu, "g-C_3N_4-based photocatalysts for hydrogen generation," *J. Phys. Chem. Lett.*, vol. 5, no. 12, pp. 2101–2107, 2014.
[124] A. Thomas., "Graphitic carbon nitride materials: variation of structure and morphology and their use as metal-free catalysts," *J. Mater. Chem.*, vol. 18, no. 41, pp. 4893–4908, 2008.
[125] M. Groenewolt and M. Antonietti, "Synthesis of g C_3N_4 nanoparticles in mesoporous silica host matrices," *Adv. Mater.*, vol. 17, no. 14, pp. 1789–1792, 2005.
[126] G. Lofrano, *Emerging compounds removal from wastewater: natural and solar based treatments*. Springer Science & Business Media, 2012.
[127] C. Berger *et al.*, "Ultrathin epitaxial graphite: 2D electron gas properties and a route toward graphene-based nanoelectronics," *J. Phys. Chem. B*, vol. 108, no. 52, pp. 19912–19916, 2004.
[128] R. R. Nair., "Fine structure constant defines visual transparency of graphene," *Science (80-.).*, vol. 320, no. 5881, p. 1308, 2008.

[129] Safaa. Sabri. Najim. and H. H. Radi. Ahmed Abd ulwahid Mohammed, "Using Solid Phase Micro Extraction Method to Separate The Trace Elements from Crude Oil Samples by Nano Graphene Oxide as a Sorbent," *Turkish J. Physiother. Rehabil.*, vol. 32, no. 3, pp. 23182–23191, 2021.

[130] R. Samiee, B. Ramezanzadeh, M. Mahdavian, E. Alibakhshi, and G. Bahlakeh, "Graphene oxide nano-sheets loading with praseodymium cations: Adsorption-desorption study, quantum mechanics calculations and dual active-barrier effect for smart coatings fabrication," *J. Ind. Eng. Chem.*, vol. 78, pp. 143–154, 2019.

[131] S. Sohni., "Highly efficient removal of acid red 17 and bromophenol blue dyes from industrial wastewater using graphene oxide functionalized magnetic chitosan composite," *Polym. Compos.*, vol. 39, no. 9, pp. 3317–3328, 2018.

[132] L. Yin, J. Niu, Z. Shen, and J. Chen, "Mechanism of reductive decomposition of pentachlorophenol by Ti-doped -Bi_2O_3 under visible light irradiation," *Environ. Sci. Technol.*, vol. 44, no. 14, pp. 5581–5586, 2010.

[133] S. Dong., "Fabrication of 3D ultra-light graphene aerogel/Bi_2WO_6 composite with excellent photocatalytic performance: A promising photocatalysts for water purification," *J. Taiwan Inst. Chem. Eng.*, vol. 97, pp. 288–296, 2019.

[134] S. Park, H. Ko, S. Lee, H. Kim, and C. Lee, "Light-activated gas sensing of Bi_2O_3-core/ZnO-shell nanobelt gas sensors," *Thin Solid Films*, vol. 570, pp. 298–302, 2014.

[135] Y. Lu., "Induced aqueous synthesis of metastable -Bi_2O_3 microcrystals for visible-light photocatalyst study," *Cryst. Growth Des.*, vol. 15, no. 3, pp. 1031–1042, 2015.

[136] A. Gasmi., "Chloroquine and hydroxychloroquine in the treatment of COVID-19: the never-ending story," *Appl. Microbiol. Biotechnol.*, vol. 105, pp. 1333–1343, 2021.

[137] H. Fischer, "Polymer nanocomposites: from fundamental research to specific applications," *Mater. Sci. Eng. C*, vol. 23, no. 6–8, pp. 763–772, Dec. 2003, doi: 10.1016/j.msec.2003.09.148.

[138] P. H. C. Camargo, K. G. Satyanarayana, and F. Wypych, "Nanocomposites: synthesis, structure, properties and new application opportunities," *Mater. Res.*, vol. 12, pp. 1–39, 2009.

[139] C. Zhu, D. Du, A. Eychmu ller, and Y. Lin, "Engineering ordered and nonordered porous noble metal nanostructures: synthesis, assembly, and their applications in electrochemistry," *Chem. Rev.*, vol. 115, no. 16, pp. 8896–8943, 2015.

[140] S. Cao,Z.Jiao,H.Chen, F. Jiang, and X. Wang,"Carboxylic acid-functionalized cadmium sulfide/graphitic carbon nitride composite photocatalyst with well-combined interface for sulfamethazine degradation," *J. Photochem. Photobiol. A Chem.*, vol. 364, pp. 22–31, 2018.

[141] R. He, J. Zhou, H. Fu, S. Zhang, and C. Jiang, "Room-temperature in situ fabrication of Bi_2O_3/g-C_3N_4 direct Z-scheme photocatalyst with enhanced photocatalytic activity," *Appl. Surf. Sci.*, vol. 430, pp. 273–282, 2018.

[142] Q. Xu, L. Zhang, J. Yu, S. Wageh, A. A. Al-Ghamdi, and M. Jaroniec, "Direct Z-scheme photocatalysts: Principles, synthesis, and applications," *Mater. Today*, vol. 21, no. 10, pp. 1042–1063, 2018.

[143] L. Zhang, G. Wang, Z. Xiong, H. Tang, and C. Jiang, "Fabrication of flower-like direct Z-scheme -Bi_2O_3/g-C_3N_4 photocatalyst with enhanced visible light photoactivity for Rhodamine B degradation," *Appl. Surf. Sci.*, vol. 436, pp. 162–171, 2018.

[144] J. Zhao, Y. Liu, Y. Wang, H. Li, J. Wang, and Z. Li, "Boron doped graphitic carbon nitride dots dispersed on graphitic carbon nitride/graphene hybrid nanosheets as high performance photocatalysts for hydrogen evolution reaction," *Appl. Surf. Sci.*, vol. 470, pp. 923–932, Mar. 2019, doi: 10.1016/j.apsusc.2018.11.138.

[145] Z. Zhao, Y. Sun, and F. Dong, "Graphitic carbon nitride based nanocomposites: a review," *Nanoscale*, vol. 7, no. 1, pp. 15–37, 2015.

[146] Y. Wang, Z. Li, H. Yu, and C. Feng, "Facile and one-pot solution synthesis of several kinds of 3D hierarchical flower-like -Bi2O3 microspheres," *Funct. Mater. Lett.*, vol. 9, no. 05, p. 1650059, 2016.

[147] J. Fang., "Au@ TiO_2/CdS ternary nanostructures for efficient visible-light-driven hydrogen generation," *ACS Appl. Mater. Interfaces*, vol. 5, no. 16, pp. 8088–8092, 2013.

[148] U. Caudillo-Flores., "Hydrogen photogeneration using ternary $CuGaS_2$-TiO_2-Pt nanocomposites," *Int. J. Hydrogen Energy*, vol. 45, no. 3, pp. 1510–1520, 2020.

[149] T. Robinson, G. McMullan, R. Marchant, and P. Nigam, "Remediation of dyes in textile effluent: A critical review on current treatment technologies with a proposed alternative," *Bioresour. Technol.*, vol. 77, no. 3, pp. 247–255, 2001, doi: 10.1016/S0960-8524(00)00080-8.

[150] Z. Karim, A. P. Mathew, M. Grahn, J. Mouzon, and K. Oksman, "Nanoporous membranes with cellulose nanocrystals as functional entity in chitosan: Removal of dyes from water," *Carbohydr. Polym.*, vol. 112, pp. 668–676, 2014, doi: 10.1016/j.carbpol.2014.06.048.

[151] X. Gao., "Dual-scaled porous nitrocellulose membranes with underwater superoleophobicity for highly efficient oil/water separation.," *Adv. Mater.*, vol. 26, no. 11, pp. 1771–1775, 2013.

[152] J. R. Werber, C. O. Osuji, and M. Elimelech, “Materials for next-generation desalination and water purification membranes,” *Nat. Rev. Mater.*, vol. 1, 2016, doi: 10.1038/natrevmats.2016.18.
[153] D. Kanakaraju, B. D. Glass, and M. Oelgem ller, “Titanium dioxide photocatalysis for pharmaceutical wastewater treatment,” *Environ. Chem. Lett.*, vol. 12, pp. 27–47, 2014.
[154] P. Zhang., “Graphene film doped with silver nanoparticles: self-assembly formation, structural characterizations, antibacterial ability, and biocompatibility,” *Biomater. Sci.*, vol. 3, no. 6, pp. 852–860, 2015.
[155] M. S. Rahaman, C. D. Vecitis, and M. Elimelech, “Electrochemical carbon-nanotube filter performance toward virus removal and inactivation in the presence of natural organic matter,” *Environ. Sci. Technol.*, vol. 46, no. 3, pp. 1556–1564, 2012.
[156] G. Wei., “Self-assembling peptide and protein amyloids: from structure to tailored function in nanotechnology,” *Chem. Soc. Rev.*, vol. 46, no. 15, pp. 4661–4708, 2017.
[157] J. Yin and B. Deng, “Polymer-matrix nanocomposite membranes for water treatment,” *J. Memb. Sci.*, vol. 479, pp. 256–275, 2015.
[158] F. Dong, L. Wu, Y. Sun, M. Fu, Z. Wu, and S. C. Lee, “Efficient synthesis of polymeric g-C3N4 layered materials as novel efficient visible light driven photocatalysts,” *J. Mater. Chem.*, vol. 21, no. 39, p. 15171, 2011, doi: 10.1039/c1jm12844b.
[159] F. Dong, Z. Wang, Y. Sun, W.-K. Ho, and H. Zhang, “Engineering the nanoarchitecture and texture of polymeric carbon nitride semiconductor for enhanced visible light photocatalytic activity,” *J. Colloid Interface Sci.*, vol. 401, pp. 70–79, Jul. 2013, doi: 10.1016/j.jcis.2013.03.034.
[160] Y. Li., “g-C3N4 modified Bi_2O_3 composites with enhanced visible-light photocatalytic activity,” *J. Phys. Chem. Solids*, vol. 76, pp. 112–119, 2015.
[161] J. Chen, B. Yao, C. Li, and G. Shi, “An improved Hummers method for eco-friendly synthesis of graphene oxide,” *Carbon N. Y.*, vol. 64, pp. 225–229, Nov. 2013, doi: 10.1016/j.carbon.2013.07.055.
[162] Z. Kalaycıoğlu, B. Özuğur Uysal, Ö. Pekcan, and F. B. Erim, “Efficient Photocatalytic Degradation of Methylene Blue Dye from Aqueous Solution with Cerium Oxide Nanoparticles and Graphene Oxide-Doped Polyacrylamide,” *ACS Omega*, vol. 8, no. 14, pp. 13004–13015, 2023, doi: 10.1021/acsomega.3c00198.
[163] S. N. Ghazi, Safaa. Sabri. Najim, and A. M. Abbas, “Synthesis and Characterization of Hybrid-Nano Graphene Oxide Composites Membranes for Water Treatment,” *J. Nanostructures*, vol. 13, no. 2, pp. 597–607, 2023, doi: 10.22052/JNS.2023.02.030.

[164] Z. Xie., "Construction of carbon dots modified MoO_3/g-C_3N_4 Z-scheme photocatalyst with enhanced visible-light photocatalytic activity for the degradation of tetracycline," *Appl. Catal. B Environ.*, vol. 229, pp. 96–104, 2018.
[165] S. P. S. David, S. Veeralakshmi, J. Sandhya, S. Nehru, and S. Kalaiselvam, "Room temperature operatable high sensitive toluene gas sensor using chemiresistive Ag/Bi2O3 nanocomposite," *Sensors Actuators B Chem.*, vol. 320, p. 128410, 2020.
[166] W. Liu, J. Cai, Z. Ding, and Z. Li, "TiO_2/RGO composite aerogels with controllable and continuously tunable surface wettability for varied aqueous photocatalysis," *Appl. Catal. B Environ.*, vol. 174, pp. 421–426, 2015.
[167] S. Mustapha., "Comparative study of crystallite size using Williamson-Hall and Debye-Scherrer plots for ZnO nanoparticles," *Adv. Nat. Sci. Nanosci. Nanotechnol.*, vol. 10, no. 4, 2019, doi: 10.1088/2043-6254/ab52f7.
[168] A. Sewnet., "Single-Step Synthesis of Graphitic Carbon Nitride Nanomaterials by Directly Calcining the Mixture of Urea and Thiourea: Application for Rhodamine B (RhB) Dye Degradation," *Nanomaterials*, vol. 13, no. 4, p. 762, Feb. 2023, doi: 10.3390/nano13040762.
[169] A. Bari., "Evaluation of bactericidal potential and catalytic dye degradation of multiple morphology based chitosan/polyvinylpyrrolidone-doped bismuth oxide nanostructures," *Nanoscale Adv.*, vol. 4, no. 12, pp. 2713–2728, 2022, doi: 10.1039/d2na00105e.
[170] A. N. Shafawi, R. A. Mahmud, K. A. Ali, L. K. Putri, N. I. M. Rosli, and A. R. Mohamed, "Bi_2O_3 particles decorated on porous g-C_3N_4 sheets: enhanced photocatalytic activity through a direct Z-scheme mechanism for degradation of Reactive Black 5 under UV-vis light," *J. Photochem. Photobiol. A Chem.*, vol. 389, p. 112289, 2020.
[171] T. H. T. Vinh, C. M. Thi, and P. Van Viet, "Enhancing photocatalysis of NO gas degradation over g-C_3N_4 modified -Bi_2O_3 microrods composites under visible light," *Mater. Lett.*, vol. 281, p. 128637, 2020.
[172] B. Palanivel, M. Shkir, T. Alshahrani, and A. Mani, "Novel $NiFe_2O_4$ deposited S-doped g-C_3N_4 nanorod: Visible-light-driven heterojunction for photo-Fenton like tetracycline degradation," *Diam. Relat. Mater.*, vol. 112, p. 108148, 2021.
[173] K. Maeda, X. Wang, Y. Nishihara, D. Lu, M. Antonietti, and K. Domen, "Photocatalytic activities of graphitic carbon nitride powder for water reduction and oxidation under visible light," *J. Phys. Chem. C*, vol. 113, no. 12, pp. 4940–4947, 2009.

[174] P. Ke, D. Zeng, J. Cui, X. Li, and Y. Chen, “Improvement in Structure and Visible Light Catalytic Performance of g-C3N4 Fabricated at a Higher Temperature,” *Catalysts*, vol. 12, no. 3, p. 247, Feb. 2022, doi: 10.3390/catal12030247.

[175] J. Zhang, Y. Hu, X. Jiang, S. Chen, S. Meng, and X. Fu, “Design of a direct Z-scheme photocatalyst: preparation and characterization of Bi2O3/g-C3N4 with high visible light activity,” *J. Hazard. Mater.*, vol. 280, pp. 713–722, 2014.

[176] Y. Gao, T. Song, X. Guo, Y. Zhang, and Y. Yang, “Electronic interaction and oxgen vacancy engineering of g-C_3N_4/ -Bi_2O_3 Z-scheme heterojunction for enhanced photocatalytic aerobic oxidative homo-/hetero-coupling of amines to imines in aqueous phase,” *Green Carbon*, vol. 1, no. 2, pp. 105–117, 2023.

[177] S. Drewniak, R. Muzyka, A. Stolarczyk, T. Pustelny, M. Kotyczka-Mora ska, and M. Setkiewicz, “Studies of reduced graphene oxide and graphite oxide in the aspect of their possible application in gas sensors,” *Sensors*, vol. 16, no. 1, p. 103, 2016.

[178] Y. Xu., “Synthesis and characterization of additive graphene oxide nanoparticles dispersed in water: experimental and theoretical viscosity prediction of non Newtonian nanofluid,” *Math. Methods Appl. Sci.*, 2020.

[179] S. Liu, J. Chen, D. Xu, X. Zhang, and M. Shen, “Enhanced photocatalytic activity of direct Z-scheme Bi_2O_3/g-C_3N_4 composites via facile one-step fabrication,” *J. Mater. Res.*, vol. 33, no. 10, pp. 1391–1400, 2018.

[180] Z. Yu and S. S. C. Chuang, “Probing methylene blue photocatalytic degradation by adsorbed ethanol with in situ IR,” *J. Phys. Chem. C*, vol. 111, no. 37, pp. 13813–13820, 2007.

[181] M. I. Din, R. Khalid, J. Najeeb, and Z. Hussain, “Fundamentals and photocatalysis of methylene blue dye using various nanocatalytic assemblies-a critical review,” *J. Clean. Prod.*, vol. 298, p. 126567, 2021.

[182] B. A. Aragaw, “Reduced graphene oxide-intercalated graphene oxide nano-hybrid for enhanced photoelectrochemical water reduction,” *J. Nanostructure Chem.*, vol. 10, pp. 9–18, 2020.

[183] S. C. Yan, S. B. Lv, Z. S. Li, and Z. G. Zou, “Organic‐inorganic composite photocatalyst of gC_3 N_4 and TaON with improved visible light photocatalytic activities,” *Dalt. Trans.*, vol. 39, no. 6, pp. 1488–1491, 2010.

[184] H. Qin., “Z-Scheme MoS_2/gC_3 N_4 heterojunction for efficient visible light photocatalytic CO_2 reduction,” *Dalt. Trans.*, vol. 47, no. 42, pp. 15155–15163, 2018.

[185] J. Liu., “Light-assisted preparation of heterostructured g-C_3N_4/ZnO nanorods arrays for enhanced photocatalytic hydrogen performance,” *Catal. Today*, vol. 355, pp. 932–936, 2020.

[186] Waseem and M. Faraz, "Novel g-C_3N_4/Fe-ZnO/RGO nanocomposites with boosting visible light photocatalytic activity for MB, Cr (VI), and outstanding catalytic activity toward para-nitrophenol reduction," *Nanotechnology*, vol. 31, no. 32, p. 325603, 2020.

[187] J. Wang, G. Wang, J. Jiang, Z. Wan, Y. Su, and H. Tang, "Insight into charge carrier separation and solar-light utilization: rGO decorated 3D ZnO hollow microspheres for enhanced photocatalytic hydrogen evolution," *J. Colloid Interface Sci.*, vol. 564, pp. 322–332, 2020.

[188] D. Akyz, "rGO-TiO_2-CdO-ZnO-Ag photocatalyst for enhancing photocatalytic degradation of methylene blue," *Opt. Mater. (Amst).*, vol. 116, p. 111090, 2021.

[189] J. Xiao, X. Zhang, and Y. Li, "A ternary g-C_3N_4/Pt/ZnO photoanode for efficient photoelectrochemical water splitting," *Int. J. Hydrogen Energy*, vol. 40, no. 30, pp. 9080–9087, 2015.

[190] B. Gupta, A. K. Gupta, P. S. Ghosal, and C. S. Tiwary, "Photo-induced degradation of bio-toxic Ciprofloxacin using the porous 3D hybrid architecture of an atomically thin sulfur-doped g-C_3N_4/ZnO nanosheet," *Environ. Res.*, vol. 183, p. 109154, 2020.

[191] D. Hou, L. Feng, J. Zhang, S. Dong, D. Zhou, and T.-T. Lim, "Preparation, characterization and performance of a novel visible light responsive spherical activated carbon-supported and Er^{3+}: $YFeO_3$-doped TiO_2 photocatalyst," *J. Hazard. Mater.*, vol. 199, pp. 301–308, 2012.

[192] Z. Wang, A. Wu, L. C. Ciacchi, and G. Wei, "Recent advances in Nanoporous Membranes for Water Purification," *Nanomaterials*, vol. 8, no. 2, 2018, doi: 10.3390/nano8020065.

الخلاصة

يعد تلوث المياه مشكلة واسعة النطاق في جميع أنحاء العالم. ففي الوقت الحاضر، أدت الأنشطة الصناعية المتنامية إلى توليد كميات هائلة من المواد الخطرة؛ النفايات الصناعية غير المعالجة والملوثات غير الخاضعة للرقابة التي تنطلق في المياه البيئية. من بينها، تولد الأصباغ الناتجة عن الصناعات النسيجية كمية كبيرة من مياه الصرف الصناعي بسبب الطلب الكبير على المياه ويتم تصريفها بشكل متكرر في البيئة طوال عملية الإنتاج ولها تأثير مباشر على صحة الإنسان، ونتيجة لذلك، تعد معالجة تلوث المياه أحد أهم الحلول. القضايا الحتمية التي أولىها المجتمع العلمي اهتمامًا كبيرًا بهدف أساسي هو حماية الموارد المائية الطبيعية والحفاظ عليها. تتضمن هذه الدراسة ثلاثة أجزاء تخليق، تشخيص و تطبيق متراكبات نيتريد الكربون الجرافيتي النانوي($g\text{-}C_3N_4$)، أكسيد البزموت النانوي(Bi_2O_3) وأكسيد الجرافين النانوي NGO) لإزالة صبغة المثلين الزرقاء.

القسم الاول يتضمن تخليق نيتريد الكربون الجرافيتي النانوي($g\text{-}C_3N_4$)، أكسيد البزموت النانوي(Bi_2O_3) وأكسيد الجرافين النانوي NGO). تم تخليق المتراكبات النانوية الثنائية بطريقة التكليس $g\text{-}C_3N_4$ -Bi_2O_3 (20%)، $g\text{-}C_3N_4$ -Bi_2O_3 (40%)، $g\text{-}C_3N_4$ -Bi_2O_3 (60%) ، $g\text{-}C_3N_4$ -Bi_2O_3 (80%). و المتراكبات النانوية الثلاثية الجديدة بطريقة التكليس
BiC_{80}/GO (10 mg)، BiC_{80}/GO (20 mg)، BiC_{80}/GO (30 mg) وBiC_{80}/GO (40 mg)

القسم الثاني يتضمن تشخيص هذه المتراكبات بواسطة (XRD) لمعرفة حجم الجسيمات من خلال معادلة ديباي-شيرير،(FT-IR)، (UV–Vis) التحليل الطيفي ،PL ، TGA لدراسة الثبات الحراري للعينات، FESEM و EDSلدراسة مورفولوجيا السطح للمتراكبات.

القسم الثالث يتضمن تطبيق إستخدام هذه المتراكبات في معالجة المياة وذلك بإزالة الملوثات العضوية(صبغة المثلين الزرقاء) وبطريقتين : الأولى التحلل الضوئي، كانت كفاءة التحلل الضوئي D%ل($g\text{-}C_3N_4$)،(Bi_2O_3) و(NGO) (93.34%،0.95% و98.335%)على التوالي، تحت إشعة الضوء المرئي في فترة زمنية قدرها ١٨٠ دقيقة. كفائة التحلل الضوئي D% للمتراكبات النانوية الثنائية $g\text{-}C_3N_4$ -Bi_2O_3 (20%)، $g\text{-}C_3N_4$ -Bi_2O_3 (40%)، $g\text{-}C_3N_4$ -Bi_2O_3 (60%) ،g- (80%) C_3N_4 -Bi_2O_3(21.77%،35.4%،41.48% و98.38%)على التوالي، تحت إشعة الضوء المرئي في فترة زمنية قدرها ١٨٠ دقيقة. تم إيجاد الظروف المثلى لأفضل كفاءةBi_2O_3 -$g\text{-}C_3N_4$ (80%) (وزن المحفز = ٥٠ ملجم، تركيز الصبغة = ٥ جزء في المليون، درجة الحرارة = ٢٥ درجة مئوية،الدالة الحامضية =١٤). كفائة التحلل%D للمتراكبات النانوية الثلاثية (BiC_{80}/GO (10 mg، BiC_{80}/GO (20 mg)، BiC_{80}/GO (30 mg) وBiC_{80}/GO (40 mg) (88.98% ، 96.65،97.81% و 91.58%)على التوالي، تحت إشعة الضوء المرئي في فترة زمنية قدرها ١٨٠ دقيقة. الظروف المثلى للمتراكبات النانوية الثلاثية (BiC_{80}/GO (20 mg هي (وزن المحفز = ٥٠ ملجم، تركيز الصبغة = ٥ جزء في المليون، درجة الحرارة = ٣٥ درجة مئوية،الدالة الحامضية =١٢)

الطريقة الثانية (الأغشية) حيثٌ صنعت أغشية، $g\text{-}C_3N_4$، (Bi_2O_3) و (NGO) بواسطة الترشيح الفراغي. وكانت نسبة الإزالة%R من صبغة الميثيلين الزرقاء(62.872%، 34.434% و51.673%)على التوالي.تم تصنيع المتراكبات النانوية الثنائية $g\text{-}C_3N_4$ -Bi_2O_3 (20%)، g- (40%) $g\text{-}C_3N_4$ -Bi_2O_3، C_3N_4 -Bi_2O_3، (60%) $g\text{-}C_3N_4$ -Bi_2O_3، (80%) $g\text{-}C_3N_4$ -Bi_2O_3 كاغشية عن طريق الترشيح الفراغي وكانت نسبة الإزالة%R(33.268%، 36.995%، 52.436% و70.819%) على التوالي. تم تصنيع المتراكبات النانوية الثلاثية (BiC_{80}/GO (10 mg)، (BiC_{80}/GO (20 mg)، BiC_{80}/GO (30 mg)و (BiC_{80}/GO (40 mg كاغشية عن طريق الترشيح الفراغي وكانت نسبة الإزالة%R (42.418%، 48.438%، 49.265% و44.44%)على التوالي.

جمهورية العراق
وزارة التعليم العالي و البحث العلمي
جامعة ميسان
كلية العلوم
قسم الكيمياء

دراسة خواص الإنحلال بالتحفيز الضوئي والأمتزاز لبعض المتراكبات النانوية الجديدة لإزالة صبغة المثلين الزرقاء من المحاليل المائية

رسالة مقدمة الى
كلية العلوم / جامعة ميسان كجزء من متطلبات نيل
شهادة الماجستير في العلوم – الكيمياء

الطالب

منتظر تحسين علي

بكالوريوس علوم كيمياء/ جامعة ميسان (2020)

بإشراف

الأستاذ المساعد

صفاء صبري نجم

٢٠٢٤ م **١٤٤٦ هـ**